

**STUDIES ON POROUS GRAPHENE,
OXIDES OF NICKEL AND THEIR
NANOCOMPOSITES FOR
SUPERCAPACITOR APPLICATION**

Thesis

Submitted in partial fulfilment of the requirements for the degree of

DOCTOR OF PHILOSOPHY

by

MEENAKETAN SETHI



DEPARTMENT OF CHEMISTRY

NATIONAL INSTITUTE OF TECHNOLOGY KARNATAKA,

SURATHKAL, MANGALORE-575025

JUNE, 2021

DECLARATION

I hereby *declare* that the Research Thesis entitled '**STUDIES ON POROUS GRAPHENE, OXIDES OF NICKEL AND THEIR NANOCOMPOSITES FOR SUPERCAPACITOR APPLICATION**' which is being submitted to the **National Institute of Technology Karnataka Surathkal**, in partial fulfilment of the requirements for the award of the Degree of **Doctor of Philosophy in Chemistry** is a *bonafide report of the research work carried out by me*. The material contained in this Research Thesis has not been submitted to any University or Institution for the award of any degree.

Meenaketan Sethi

Meenaketan Sethi

Reg. No.: 155093CY15F04

Department of Chemistry

Place: NITK-Surathkal

Date: 17/06/2021

CERTIFICATE

This is to *certify* that Research Thesis entitled '**STUDIES ON POROUS GRAPHENE, OXIDES OF NICKEL AND THEIR NANOCOMPOSITES FOR SUPERCAPACITOR APPLICATION**' submitted by **Mr. Meenaketan Sethi** (Register No: **155093CY15F04**) as the record of the research work carried out by him, *is accepted as the Research Thesis submission* in partial fulfilment of the requirements for the award of degree of **Doctor of Philosophy**.

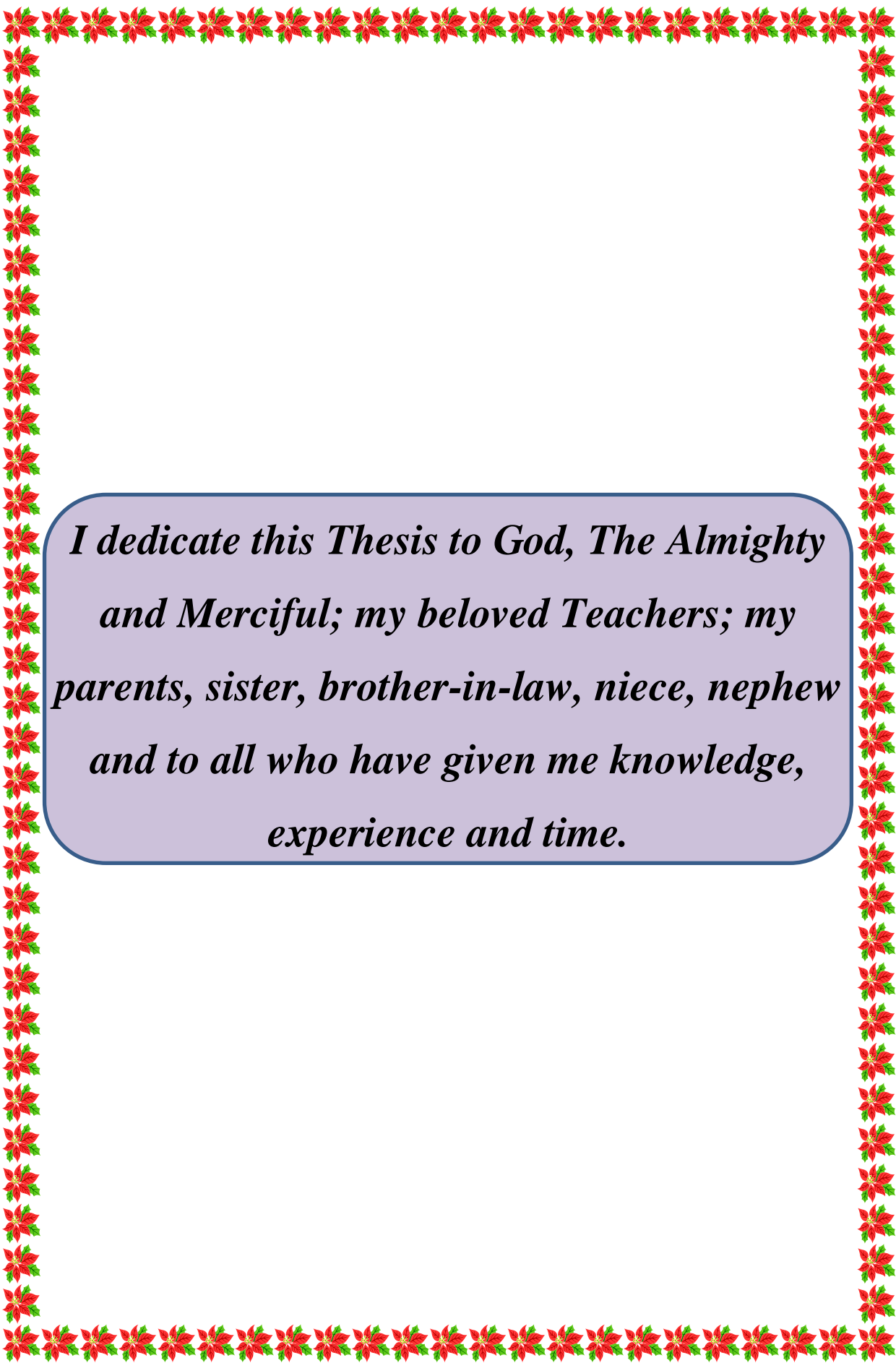


Research Guide



Chairman-DRPC

Dr. ARUN M. ISLOOR
Professor & Head
DEPARTMENT OF CHEMISTRY
National Institute of Technology Karnataka
Surathkal, Srinivasnagar
MANGALORE - 575 025, D.K., INDIA



*I dedicate this Thesis to God, The Almighty
and Merciful; my beloved Teachers; my
parents, sister, brother-in-law, niece, nephew
and to all who have given me knowledge,
experience and time.*

ACKNOWLEDGEMENT

“Experience is the best teacher”

It has been a great experience pursuing research dream at the *National Institute of Technology Karnataka (NITK), Surathkal* with proficient and magnanimous individuals who have helped me to achieve what I have attained up to this point. I would like to express my deepest appreciation and gratitude for the help and support of the kind people around me, only some of which is particularly mentioned here.

I would like to express my deep sense of gratitude to my research supervisor *Prof. D. Krishna Bhat*, Professor and Former Head, Dept. of Chemistry NITK, Surathkal for giving me an opportunity to carry out my research work under his guidance. His timely advice, patience, strong guidance, enthusiastic encouragement, and useful critiques helped me to grow in all directions. His guidance and continuous support through entire duration of my research work has helped me to write this thesis. I could not have imagined, nor can I imagine even today, having a better advisor and mentor than him for my Ph.D. work.

I am ever grateful to *NITK, Surathkal*, for the research infrastructure and fellowship that allowed me to carry out my research work at a smooth pace.

I would also like to pay my deep sense of gratitude to *Dr. Sandhya U. Shenoy* for her guidance and continuous support to complete the research work. Without her kind direction and persistent help, this research work would not have been possible.

Apart from my research advisor, I would like to profusely thank my Research Progress Assessment Committee members *Prof. Subba Rao*, Dept. of Applied Mechanics and Hydraulics and *Prof. Arun M. Isloor*, Head, Dept. of Chemistry for their insightful comments and encouragement. This helped me to gain knowledge in various research perspectives. My sincere thanks are due to *all the faculty members* of the Dept. of Chemistry, NITK, Surathkal for their support during my research journey.

My special thanks to my lab mate **Mr. Harsha** for always standing by my side and sharing a great relationship as a compassionate friend. I will always cherish the warmth shown by him.

A special mention of thanks to my friends **Dr. Archana Singh, Dr. Praveen Mishra, Dr. Viprabha K, Dr. Akshatha R Shetty** and all my batch mates and many more for their constant support and cooperation during my stay at NITK, Surathkal. Their timely help and friendship shall always be remembered.

I record my sincere thanks to **Mrs. Shamila Nandini, Mrs. Sharmila, Mrs. Deepa, Mrs. Rashmi, Mr. Prasanth, Mr. Santosh, Mr. Pradeep, Mr. Harish** and other office and non-teaching staff for their kind support and help throughout my stay at NITK, Surathkal.

I owe my deepest and sincere gratitude to my parents (Late) **Mrs. Rama Sethi and (Late) Mr. Abhimanyu Sethi** for their blessings from heaven, to my sisters **Mrs. Kalpana Sethi, Mrs. Bhagyalata Sethi** and my Brother-in-laws **Mr. Bidesi Sethi, Mr. Ratna Sethi** for their love and encouragement that motivated me to achieve this goal. Special thanks are due to my niece **Miss Jigyansha Sethi** and nephew **Mr. Debansha Sethi** for their love and good wishes. My sincere thanks to my fiancée **Banaja Basini Sethi** for her psychological support and encouragement during my thesis and defense preparation. Above all, I humbly thank **God Almighty**, without Whose Grace and Blessings my dream for completing the research work would have remained a dream.

Meenaketan Sethi

ABSTRACT

The research thesis entitled ‘**STUDIES ON POROUS GRAPHENE, OXIDES OF NICKEL AND THEIR NANOCOMPOSITES FOR SUPERCAPACITOR APPLICATION**’ deals with the synthesis, characterization and studies on supercapacitor application of some oxides of nickel and their nanocomposites with porous graphene. The work describes successful synthesis of seven different kinds of novel electrode materials such as PG, NiO, NF, NC, PGNiO, PGNF and PGNC using solvothermal method. All the synthesized electrode materials were carefully characterized for their structural, elemental and morphological properties by employing appropriate techniques such as XRD, Raman, XPS, FESEM, TEM, HRTEM and BET techniques. The electrode materials were investigated for their utility in the field of supercapacitors using an aqueous 2 M KOH electrolyte. The synthesized electrode materials exhibited high electrochemical activity due to the synergistic effects of the components of the nanocomposite materials. The nanocomposite electrode materials displayed high cyclic stability at a higher applied current density. The impressive electrochemical accomplishment is attributed to the presence of porous structure and good surface area of composites, which not only acted as an ion-buffering reservoir but also maintained the mechanical strength during the continuous charge-discharge cycles. The obtained results suggest that these novel nanostructured oxides and PG based nanocomposites are potential candidates as electrode materials for the application in supercapacitors.

Keywords: *Solvothermal method; Porous graphene; Hybrid composite; Specific capacitance; Cyclic stability; Energy density; Power density.*

CONTENTS

DECLARATION	
CERTIFICATE	
ACKNOWLEDGEMENT	
ABSTRACT	
CONTENTS	i
NOMENCLATURE	v
CHAPTER 1: INTRODUCTION AND A REVIEW OF LITERATURE	
1.1 INTRODUCTION TO SUPERCAPACITORS	02
1.2 REVIEW OF LITERATURE	06
1.2.1 PG	06
1.2.2 NiO AND PGNiO	07
1.2.3 NF AND PGNF	11
1.2.4 NC AND PGNC	14
1.3 SCOPE	18
1.4 OBJECTIVES	19
1.5 PRESENT WORK	20
CHAPTER 2: ECO-FRIENDLY SYNTHESIS OF POROUS GRAPHENE AND ITS UTILIZATION AS HIGH PERFORMANCE SUPERCAPACITOR ELECTRODE MATERIAL	
2.1 INTRODUCTION	23
2.2 EXPERIMENTAL SECTION	24
2.2.1 Synthesis of GO and PG	24
2.2.2 Characterization	24
2.2.3 Computational Details	26
2.2.4 Electrochemical Measurements	26
2.3 RESULTS AND DISCUSSION	29
2.3.1 Structural, Elemental and Morphological Analysis	29

2.3.2	Role of Solvent Mixture on the Reduction of GO to PG	37
2.3.3	Electronic Structure Analysis by DFT	38
2.3.4	Electrochemical Study of PG as an Electrode	44
2.3.5	Electrochemical Study of Fabricated Supercapacitor Using PG Electrodes	49
2.4	CONCLUSIONS	55
CHAPTER 3: SOLVOTHERMAL SYNTHESIS OF NiO NANOFLLAKES FOR SUPERCAPACITOR APPLICATION		
3.1	INTRODUCTION	58
3.2	EXPERIMENTAL SECTION	59
3.3	RESULTS AND DISCUSSION	59
3.3.1	Structural, Elemental and Morphological Analysis	59
3.3.2	Electrochemical Study of NiO as an Electrode	62
3.3.3	Electrochemical Study of Fabricated Supercapacitor Using NiO Electrodes	67
3.4	CONCLUSIONS	70
CHAPTER 4: SIMPLE SOLVOTHERMAL SYNTHESIS OF POROUS GRAPHENE-NiO NANOCOMPOSITES WITH HIGH CYCLIC STABILITY FOR SUPERCAPACITOR APPLICATION		
4.1	INTRODUCTION	72
4.2	EXPERIMENTAL SECTION	73
4.3	RESULTS AND DISCUSSION	73
4.3.1	Structural, Elemental and Morphological Analysis	73
4.3.2	Electrochemical Study of PGNiO Composite Electrodes	78
4.3.3	Electrochemical Study of 10 PGNiO Composite Electrode	80
4.3.4	Electrochemical Study of Fabricated Supercapacitor Using 10 PGNiO Composite Electrodes	85
4.4	CONCLUSIONS	90

**CHAPTER 5: SOLVOTHERMAL SYNTHESIS OF NiFe₂O₄
NANOPARTICLES FOR HIGH-PERFORMANCE SUPERCAPACITOR
APPLICATIONS**

5.1	INTRODUCTION	92
5.2	EXPERIMENTAL SECTION	93
5.3	RESULTS AND DISCUSSION	93
5.3.1	Structural, Elemental and Morphological Analysis	93
5.3.2	Electrochemical Study of NF as an Electrode	96
5.3.3	Electrochemical Study of Fabricated Supercapacitor Using NF Electrodes	101
5.4	CONCLUSIONS	105

**CHAPTER 6: A POROUS GRAPHENE-NiFe₂O₄ NANOCOMPOSITE
WITH HIGH ELECTROCHEMICAL PERFORMANCE AND HIGH
CYCLING STABILITY FOR ENERGY STORAGE APPLICATIONS**

6.1	INTRODUCTION	107
6.2	EXPERIMENTAL SECTION	108
6.3	RESULTS AND DISCUSSION	108
6.3.1	Structural, Elemental and Morphological Analysis	108
6.3.2	Electrochemical Study of PGNF Composite Electrodes	115
6.3.3	Electrochemical Study of 10 PGNF Composite Electrode	118
6.3.4	Electrochemical Study of Fabricated Supercapacitor Using 10 PGNF Composite Electrodes	125
6.4	CONCLUSIONS	129

**CHAPTER 7: SOLVOTHERMAL SYNTHESIS AND HIGH
SUPERCAPACITOR PERFORMANCE OF NiCo₂O₄ NANORODS**

7.1	INTRODUCTION	131
7.2	EXPERIMENTAL SECTION	132
7.3	RESULTS AND DISCUSSION	133
7.3.1	Structural, Elemental and Morphological Analysis	133
7.3.2	Electrochemical Study of NC as an Electrode	135

7.3.3	Electrochemical Study of Fabricated Supercapacitor Using NC Electrodes	138
7.4	CONCLUSIONS	143
CHAPTER 8: POROUS GRAPHENE-NiCo₂O₄ NANOROD HYBRID COMPOSITE AS A HIGH PERFORMANCE SUPERCAPACITOR ELECTRODE MATERIAL		
8.1	INTRODUCTION	145
8.2	EXPERIMENTAL SECTION	146
8.3	RESULTS AND DISCUSSION	146
8.3.1	Structural, Elemental and Morphological Analysis	146
8.3.2	Electrochemical Study of PGNC Composite Electrodes	151
8.3.3	Electrochemical Study of 10 PGNC Composite Electrode	154
8.3.4	Electrochemical Study of Fabricated Supercapacitor Using 10 PGNC Composite Electrodes	162
8.4	CONCLUSIONS	167
CHAPTER 9: SUMMARY AND CONCLUSIONS		
9.1	SUMMARY	169
9.2	CONCLUSIONS	172
9.3	SCOPE FOR FUTURE WORK	175
REFERENCES		177
RESEARCH PUBLICATIONS		209
BIO-DATA		212

NOMENCLATURE

ABBREVIATIONS

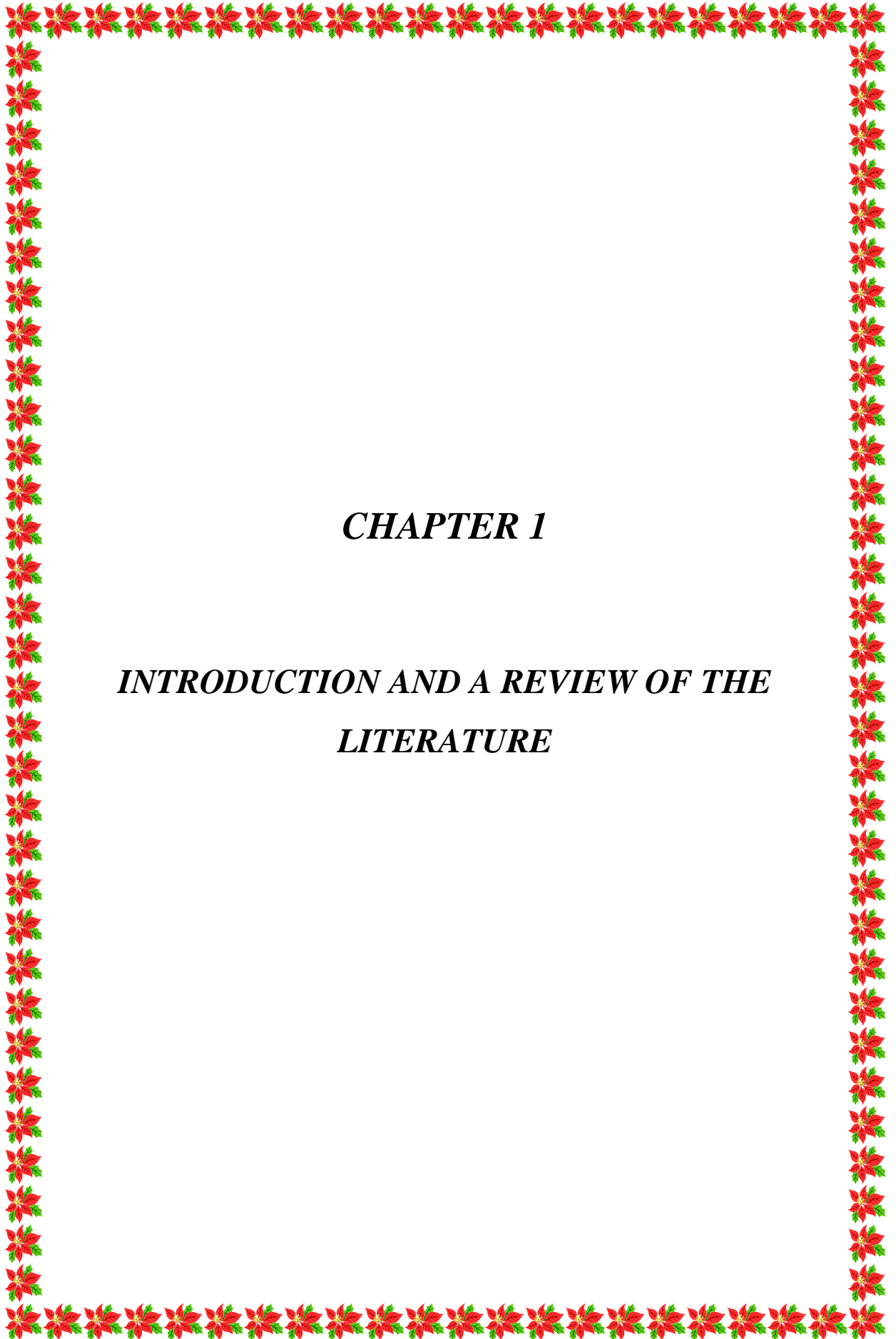
AC	Alternating Current
AFM	Atomic Force Microscopy
ALD	Atomic Layer Deposition
BET	Brunauer-Emmett-Teller
BJH	Barrett-Joyner-Halenda
CB	Conduction Band
CBM	Conduction Band Maximum
CNT	Carbon Nanotube
CV	Cyclic Voltammetry
DFT	Density Functional Theory
DMF	Dimethylformamide
DOS	Density of States
EDLCs	Electrochemical Double Layer Capacitors
EDX	Energy Dispersive X-ray
EIS	Electrochemical Impedance Spectra
EMIMBF ₄ /AN	1-Ethyl-3-Methylimidazolium Tetrafluoroborate/Acetonitrile
FESEM	Field Emission Scanning Electron Microscope

FTIR	Fourier Transform Infra-Red
GCD	Galvanostatic Charge-Discharge
GO	Graphene Oxide
NC	NiCo ₂ O ₄
NF	NiFe ₂ O ₄
NMP	N-Methyl-2-Pyrrolidone
NPs	Nano Particles
pDOS	Partial Density of States
PG	Porous Graphene
PVDF	Poly(Vinylidene Fluoride)
rGO	Reduced Graphene Oxide
SAED	Selected Area Electron Diffraction
TEABF ₄ /ACN	TetraethylAmmonium Tetrafluoroborate/Acetonitrile
TEM	Transmission Electron Microscope
VB	Valence Band
VBM	Valence Band Maximum
XPS	X-ray Photoelectron Spectroscopy
XRD	X-ray Diffraction

SYMBOLS AND UNITS

α	Alpha
\AA	Angstrom
β	Beta
cm	Centimeter
η	Coulombic efficiency
I	Current
$^{\circ}$	Degree
$^{\circ}\text{C}$	Degree Celsius
eV	Electron Volt
g	Gram
>	Greater than
Hz	Hertz
h	Hour
$^{-1}$	Inverse
K_{α}	K Alpha
kHz	Kilo Hertz
kV	Kilo Volt
λ	Lambda

<	Less than
μ	Micro
mL	milli liter
mmol	milli mole
min	Minute
M	Molarity
nm	Nanometer
Ω	Ohm
%	Percentage
θ	Theta
τ	Tau
V	Voltage



CHAPTER 1

***INTRODUCTION AND A REVIEW OF THE
LITERATURE***

Chapter 1 gives a brief introduction to the basic concepts of the study undertaken. It also gives a brief overview of the relevant works in the literature which focus upon porous graphene (PG), NiO, NiFe₂O₄ (NF), NiCo₂O₄ (NC), PGNiO, PGNF, PGNC hybrid composite synthesis and energy storage applications. Scope and objectives of the present research work have been given at the end.

1.1 INTRODUCTION TO SUPERCAPACITORS

The rapid depletion of the conventional energy sources and severe impact of pollution on the environment has led to increasing demand for the advancement of clean, efficient and environmentally benign energy storage systems to mitigate the energy crisis. Although batteries are used for the storage of large amount of charge, they lack fast charging and high cyclability (Fang et al., 2020). Tethering batteries with supercapacitors can ameliorate the charge storage capacity and can be used for future energy storage devices. The supercapacitors can be categorized into three types namely: electrochemical double layer capacitors (EDLCs), pseudocapacitors and hybrid capacitors (a type of capacitor made by blending of EDLC and pseudocapacitor materials). The charge storage mechanism decides the category of the supercapacitor.

In EDLC, generally carbonaceous materials of high surface area is used as electrode material, as EDLC phenomena is dependent on the electrode/electrolyte interface where ion transport takes place and leads to the creation of an electrochemically active layer (Tian et al., 2020). Graphene owing to its high surface area is a promising material to increase the double layer capacitance as it can accommodate electrolyte ions (Wu et al., 2020). But it suffers from a drawback of finite quantum capacitance. Quantum capacitance of the material depends on its electronic structure (Song et al., 2018). Hence, by tuning the electronic structure, the material's performance as a supercapacitor can be enhanced. Recently, PG, a type of graphenic material formed by the removal of sp² bonded carbon atoms from the parent graphene plane, has attracted a lot of attention due to its porous structure and high surface area (Hwang et al., 2020). The applicability of this material is restricted

due to the expensive synthetic techniques required for the production and poor yield (Eftekhari, 2018; Qiu et al., 2018).

In pseudocapacitors the charge is developed by the faradaic redox reactions at the electrode surface; this property is generally shown by oxides and sulphides of metals/polymers (Goel et al., 2018; Jiang et al., 2019; Nguyen et al., 2018). Among oxides of metals, RuO₂ is considered as the best electrode material for supercapacitor application, but the cost and toxicity issues limit its applicability. Recently mixed metal oxides/spinels are considered as superior electrode materials for supercapacitors as compared to the single oxides owing to the mixture of two metal domains, various oxidation states, easy synthesis and high electrochemical response (Chime et al., 2020; Gao et al., 2019).

NiO is an inorganic material that acquires the NaCl (rock salt) crystal structure in which the Ni²⁺ and O²⁻ occupy the octahedral sites. This material appears as a cubic crystal with a space group of Fm-3m and a space group number of 225 with a molecular mass of 74.6928 g mol⁻¹. NiO has been considered as a potential candidate for energy storage applications due to its high theoretical capacitance values of 3750 F g⁻¹ (Zhao et al., 2016). This material is widely used in supercapacitor applications owing to its abundant availability, environmental benignity, easy synthetic process and good electronic conductivity. NiO in the form of particles, nanoflakes, pyramidal structures, nanoflakes, belts, hollow NiO nanostructures and urchins (Edison et al., 2018; Goel et al., 2018; Kumar et al., 2017; Sannasi et al., 2020; Tan et al., 2018; Wang et al., 2019; Zhang et al., 2016) has been applied as an active electrode material for supercapacitor applications.

NF is a mixed metal oxide of nickel and iron, used as an electrode material for supercapacitor applications. NF is a spinel material with a space group of Fd-3m and the formula of AB₂O₄, which occurs in a mixed valence type structure with a cubic crystal system in which A and B atoms (cations) occupying some or all of the octahedral and tetrahedral sites. In contrast, O atoms (anions) are arranged in a cubic close packed lattice. NF is widely utilized as an electrode material for supercapacitor

application due to its high theoretical capacitance values, the mixture of 2 metal domains (Ni and Fe), high abundance, environmentally friendly nature (Bandgar et al., 2018) and more electronic conductivity compared to single NiO and Fe₃O₄. Many research groups have studied its electrochemical performance in supercapacitor applications where NF had different nano architectures such as nanopowders, nanoassemblies, nanoparticles, thin films, nanostructures, nanosheets and core-shell nanostructures (Anwar et al., 2011; Aparna et al., 2018; Askari et al., 2020; Bandgar et al., 2018; Bhojane et al., 2017; Gao et al., 2019; Zhang et al., 2018).

NC also crystallizes in an inverse spinel structure with similar structural properties like NF. NC is a widely utilized electrode material for supercapacitor application due to its high theoretical capacitance value i.e. more than 3000 F g⁻¹ (Wang et al., 2018; Yao et al., 2017), the mixture of 2 metal domains (Ni and Co), high abundance, environmentally friendly nature and electronic conductivity as compared to single NiO and Co₃O₄. There are various nano dimension structures of NC, reported by many authors which were potentially utilized as an active electrode material for supercapacitors and have displayed high electrochemical performance such as hexagonal NC nanostructures, NC nanoneedles, NC nanoparticles, NC nanofeathers, honey comb like NC, NC quantum dots, urchin and sheaf like nanostructures and firework-shaped NC (Bhagwan et al., 2019; Cao et al., 2020; Chatterjee et al., 2020; Gao et al., 2020; Kumar et al., 2020; Siwatch et al., 2020; Umeshbabu et al., 2014; Zhang et al., 2019).

The EDLC material, especially PG, which possesses high surface area and good electronic conductivity for the transport of electrolyte ions, provides good capacitance value and high cyclic stability but has low energy density and power density values. On the other side, oxides of nickel/polymers are utilized as an electrode for pseudocapacitors. They can be easily synthesized and provide high electronic conductivity due to the redox nature of pseudocapacitors. The rich redox property of pseudocapacitors can generate high capacitance and energy density value, but it lacks cyclic stability. To overcome the issues of EDLC and pseudocapacitive material, the best way is to design a hybrid supercapacitor. Hybrid supercapacitors are

excellent electrochemical energy storage devices that combine the advantages of both EDLC and pseudocapacitor (Li et al., 2019; Liu et al., 2019). By exhibiting high energy and power density, high specific capacitance and long life cycle they bridge the gap between conventional capacitors and batteries. PG is superior compared to the parent graphene structure, as it can provide higher surface area and facilitate high electrical conductivity due to the presence of pores/voids on the sheet, where electrolyte ions can move freely without any added restriction. On the other side, oxides of nickel like NiO, NF and NC are considered as celebrated oxides for supercapacitor applications owing to their high theoretical capacitance value, abundance, environmentally benignity, high thermal and chemical stability (Askari et al., 2020; Wang et al., 2018; Yao et al., 2017; Zhao et al., 2016). The NiO, NF and NC in the form of various nanostructures have been used as an electrode material for supercapacitors and has depicted good capacitance values. Therefore, a hybrid supercapacitor employing the combination of PG with NiO, NF and NC to form PGNiO, PGNF and PGNC composite is expected to produce enhanced capacitance value, energy/power density and longer cyclic stability at a high current range.

Many authors have reported the synthesis and electrochemical characterization of hybrid composites of PGNiO, PGNF and PGNC such as porous carbon sphere@NiO core-shell nanocomposite, graphene like foam/NiO nanocomposite, NF nanoparticles on a 3D graphene capsule, NF nanocubes on rGO cryogel, hierarchical reduced graphene hydrogel-NC nanowire composite and flower like N-doped porous carbon/NC hybrid composite (Vickraman et al., 2018; He et al., 2019; Shaymaa et al., 2018; Zhang et al., 2019; Li et al., 2019; Tang et al., 2019), which has delivered excellent electrochemical performance at beneficial current densities. Hence, the study of the PG composites would be of high interest in the field of supercapacitors.

1.2 REVIEW OF LITERATURE

1.2.1 PG

An overview of some reported literature on PG's synthesis and its utility in supercapacitor has been presented here.

Fan et al. (2012) successfully synthesized the PG nanosheets by using MnO_2 as an etching agent from graphene sheets. The PG, when utilized as an electrode material, displayed a capacitance value of 241 F g^{-1} compared to graphene of 195 F g^{-1} at a scan rate of 2 mV s^{-1} in 6 M KOH electrolyte. The PG also obtained 88% of its initial capacitance value after 5000 cycles.

Han et al. (2014) synthesized holey graphene using commercially available graphene as only the starting material. A single step produced the holey graphene by heating the graphene in an air atmosphere (acts as an oxidant). The obtained material produced a capacitance value of 45 F g^{-1} at a current density of 3 A g^{-1} in an ionic liquid electrolyte of potential 2.5 V and 98% initial capacitance retention value after 10000 cycles at a constant current density of 3 A g^{-1} .

Xu et al. (2014) fabricated holey graphene frameworks using graphene oxide (GO) as the starting precursor through the hydrothermal method by using H_2O_2 as an oxidizing agent. The synthesized holey graphene frameworks exhibited a capacitance value of 298 F g^{-1} at a current density of 1 A g^{-1} in an organic electrolyte, namely 1-ethyl-3-methylimidazolium tetrafluoroborate/acetonitrile ($\text{EMIMBF}_4/\text{AN}$) and 91% capacitance retention rate was observed after 10000 cycles at a current density of 20 A g^{-1} .

Bai et al. (2016) synthesized holey graphene using a hydrothermal method and GO as the starting precursor. The obtained holey graphene displayed a capacitance value of 251 F g^{-1} at a current density of 1 A g^{-1} in 6 M KOH electrolyte. It retained around 94% initial capacitance value after 6000 cycles at a current density of 5 A g^{-1} .

Kim et al. (2016) produced graphene nanomesh using GO as a starting precursor by following the chemical route. The as-prepared graphene nanomesh showed a capacitance value of 253 F g^{-1} at a current density of 1 A g^{-1} and 91% capacitance retention after 50000 cycles at a constant current density of 10 A g^{-1} in 1 M tetraethylammonium tetrafluoroborate/acetonitrile (TEABF₄/AN) electrolyte.

Liu et al. (2018) prepared 3D graphene hydrogel using GO as the starting precursor under the hydrothermal method. The obtained graphene hydrogel displayed a capacitance value of 202 F g^{-1} at a current density of 1 A g^{-1} with an 89% retention rate after 5000 cycles at a current density of 5 A g^{-1} in 1 M H₂SO₄ electrolyte.

Kang et al. (2019) prepared PG using exfoliated graphite through the microwave approach, followed by KOH activation. The as-synthesized PG displayed a capacitance value of 133 F g^{-1} at a current density of 1 A g^{-1} in 1 M Na₂SO₄ electrolyte.

Wang et al. (2019) synthesized PG through partial combustion of GO. The PG has displayed a capacitance value of 223 F g^{-1} at a current density of 1 A g^{-1} with an 83% retention rate after 5000 cycles at a current density of 1 A g^{-1} .

Hwang et al. (2020) designed a stacking free PG network using GO as a starting precursor under the hydrothermal method. The obtained PG network has displayed a capacitance value of 338 F g^{-1} at a current density of 1 A g^{-1} and a 100% capacitance retention rate after 10000 cycles at a current density of 1 A g^{-1} .

1.2.2 NiO AND PGNiO

An overview of a few reported literature about the synthesis of NiO, PGNiO and its utility in supercapacitor has been discussed here.

Kolathodi et al. (2015) synthesized NiO nanofibers by sol-gel based electrospinning method followed by calcination. The synthesized nanofibers delivered a capacitance value of 248 F g^{-1} at a current density of 1 A g^{-1} and 98% initial

capacitance value was retained after 1000 cycles at a current density of 5 A g^{-1} in 6 M KOH electrolyte. The good capacitance value obtained for the NiO was mainly attributed to the high crystallinity of the fibers, which provided the path for effective ion transport.

Zhang et al. (2016) synthesized mesoporous NiO nanourchins by a hydrothermal method followed by calcination in air. The electrochemical results depicted a capacitance value of 540 F g^{-1} at a current density of 1 A g^{-1} and 80% initial capacitance value was retained after 1000 cycles at a current density of 10 A g^{-1} . The excellent performance showed by the urchin nanostructure was mainly attributed to the large surface area, reduced diffusion path; also, the urchin like structure acted as an ion reservoir for the efficient redox reaction.

Kumar et al. (2017) synthesized NiO nanopyramidal thin films which were depicted a capacitance value of 72 F g^{-1} at a current density of 1 mA cm^{-2} with a capacitance retention rate of 91% after 1000 cycles at an applied current density of 1 mA cm^{-2} in 1 M KOH electrolyte solution. The obtained better electrochemical performance of the electrode material was primarily believed to the hydrophilic nature of the NiO surface.

Tan et al. (2018) synthesized NiO nanobelts through the hydrothermal method, followed by calcination. The as-prepared nanobelts executed a capacitance value of 517 F g^{-1} at a current density of 0.5 A g^{-1} with a 76% capacitance retention rate after 10000 cycles at a current density of 2 A g^{-1} in 2 M KOH electrolyte. The observed better capacitance value was mainly due to the good crystallinity and superior redox property of NiO.

Edison et al. (2018) prepared NiO nanoparticles onto a Ni-foam by electrochemical method followed by calcination. The nanoparticles, when utilized as an electrode material for supercapacitor application, displayed a capacity value of 112 C g^{-1} at a current density of 1 A g^{-1} . The better electrochemical performance was

primarily ascribed to the large surface area of NiO, which has provided more electroactive sites for the redox reactions.

Sun et al. (2019) prepared NiO nanocubes through the hydrothermal method, which has delivered a capacitance value of 1012 mF cm^{-2} at an applied current density of 1 mA cm^{-2} with a 70% retention rate after 6000 cycles at a current density of 10 mA cm^{-2} in 6 M KOH electrolyte. The excellent electrochemical performance obtained for the nanocubes was primarily believed to electrode material's high surface area.

Kitchamsetti et al. (2019) synthesized NiO nanobelt structures by adopting a hydrothermal approach. The as-synthesized material displayed a capacitance value of 794 F g^{-1} at a current density of 0.5 A g^{-1} with an 89% capacitance retention rate after 2500 cycles at a current density of 4 mA g^{-1} . The nanobelt morphology's excellent electrochemical performance was mainly ascribed to the mesoporous nature with large surface area and interconnected porous nanobelt network.

Sannasi et al. (2020) synthesized NiO nanoflakes through the microwave approach. The synthesized nanoflakes have delivered a capacitance value of 120 F g^{-1} at a current density of 1 A g^{-1} with good rate capability.

Jiang et al. (2013) synthesized PG/NiO nanocomposite through the hydrothermal method, followed by calcination. The obtained nanocomposite displayed a high surface area of $174 \text{ m}^2 \text{ g}^{-1}$ compared to NiO of $36 \text{ m}^2 \text{ g}^{-1}$. The composite structure displayed a capacitance value of 430 F g^{-1} compared to NiO of 125 F g^{-1} at a current density of 200 mA g^{-1} . The cyclic stability study displayed 86% (69%) retention rate for the nanocomposite (pure NiO) after 2000 cycles at a current density of 1 A g^{-1} . The enhanced electrochemical property in the composite was mainly ascribed to PG's porous nature, which acted as an ion buffering reservoir for the efficient electrochemical reaction.

Chen et al. (2014) synthesized NiO/nano PG composite through the atomic layer deposition (ALD) technique. The obtained composite sample displayed a capacitance value of 1006 F g^{-1} at a current density of 1 A g^{-1} and a retention rate of 94% after 1600 cycles at a current density of 2 A g^{-1} in 2 M KOH electrolyte. The incremental charge storage trait in the composite was believed to the nanoparticle structure of NiO and the presence of PG, which has enhanced the electron transport by shortening the ion/electron transport path.

Trung et al. (2015) synthesized 3D graphene/NiO nanoparticle composite structure through a high temperature calcination route. The obtained composite displayed a capacitance value of 1328 F g^{-1} at a current density of 1 A g^{-1} as compared to only reduced graphene oxide (rGO)/NiO composite of 632 F g^{-1} . The porous composite material retained 87% capacitance value compared to 67% for rGO/NiO composite after 2000 cycles at a current density of 2 A g^{-1} in 2 M KOH electrolyte. The composite structure's electrochemical performance was believed to the porous structure of graphene, which has provided high surface area along with the NiO nanoparticle to enhance conductivity and structural stability.

Lv et al. (2018) synthesized mesoporous NiO nanoflakes on graphene foam as an electrode material for supercapacitor applications. The electrode material displayed a capacitance value of 1062 F g^{-1} at a current density of 1 A g^{-1} with a 91% retention rate after 5000 cycles at a current density of 1 A g^{-1} compared to NiO nanoflakes. The improvement of the capacitance value in the composite sample was mainly ascribed to the better electronic conductivity and mesoporous nature of the composite material.

Vickraman et al. (2018) synthesized porous carbon sphere@NiO core-shell nanocomposite through the hydrothermal method. The prepared composite electrode material displayed a capacitance value of 825 F g^{-1} at a current density of 1 A g^{-1} compared to the bare NiO of 407 F g^{-1} . The composite electrode material also retained around 85% of the initial capacitance value after 3500 cycles at a current density of 10 A g^{-1} . The obtained good electrochemical behavior was primarily ascribed to the high surface area of the composite material.

He et al. (2019) prepared graphene like foam/NiO composite for supercapacitor applications. The composite material displayed a capacitance value of 539 F g^{-1} at a current density of 1 A g^{-1} compared to graphene like foam of 147 F g^{-1} at the same current density in 6 M KOH electrolyte. The composite material's good electrochemical performance compared to only graphene like foam is primarily ascribed to the large surface area, porous nature and synergistic effect of the composite materials.

1.2.3 NF AND PGNF

An overview of a few reported literature about the synthesis of NF, PGNF and its utility in supercapacitor has been discussed here.

Anwar et al. (2011) synthesized NF nanomaterials adopting different synthetic routes followed by high temperature calcination. Among the synthetic methods, the sol-gel mediated route displayed a capacitance value of 97 F g^{-1} in 0.1 N NaCl electrolyte. The enhanced capacitance value was primarily ascribed to the porous and interconnected structure of nanoparticles.

Liu et al. (2017) synthesized NF microspheres with hollow interiors through a hydrothermal route following calcination of the intermediates in air. The NF showed a capacitance value of 205 F g^{-1} at 1 A g^{-1} current density and 99% initial capacitance retention value was maintained after 2000 discharge curves at a current density of 1 A g^{-1} in 1 M KOH electrolyte. The electrode's good electrochemical performance was primarily believed to the hollow and hierarchical structure and good redox property of NF.

Bhojane et al. (2017) synthesized NF nanostructures by a wet chemical route. The active electrode displayed a capacitance value of 342 F g^{-1} at an applied 0.833 A g^{-1} current density with a deficient initial capacitance retention value after 1050 cycles. The good electrochemical performance of the electrodes was primarily

believed to the porous structure, which allowed the electrolyte ions for the better redox reaction.

Bandgar et al. (2018) synthesized NF thin films of different morphologies such as nanosheets ($47 \text{ m}^2 \text{ g}^{-1}$), nanoflowers ($25 \text{ m}^2 \text{ g}^{-1}$) and nanofeathers ($11 \text{ m}^2 \text{ g}^{-1}$) employing the wet chemical method for supercapacitor application. Among the prepared nanomaterials, the nanosheets displayed an excellent capacitance value of 1139 F g^{-1} compared to the nanoflowers (677 F g^{-1}) and nanofeathers (435 F g^{-1}) in 6 M KOH electrolyte along with 98% capacitance retention value after 7000 cycles. The better electrochemical execution obtained for the nanosheets was primarily ascribed to the formation of well interconnected and organized nanosheets, which provided high surface area and more active sites for electrochemical reactions.

Hua et al. (2018) synthesized NF nanocrystals of different sizes using hexamethylenetetramine (HMT) under the hydrothermal approach at different temperatures. Authors have reported that the high temperature reaction route leads to less crystal size than the low temperature route. The nanocrystal synthesized at $200 \text{ }^\circ\text{C}$ bearing the size of 46 nm presented a capacitance value of 562 F g^{-1} when coated on a Ni foam and in 2 M KOH electrolyte and 84% original capacitance value was retained after 1000 discharge rounds at a current density of 4 A g^{-1} . The nanocrystal's better electrochemical performance was primarily ascribed to the smaller nanocrystallite size and more exposed sites for electrochemical reaction.

Aparna et al. (2018) prepared the NF nanoassemblies through the hydrothermal method for supercapacitor application. The prepared nanoassemblies depicted a capacitance value of 109 F g^{-1} at a scan rate of 2 mV s^{-1} and 90% capacitance retention value after 1000 cycles at a scan rate of 10 mV s^{-1} . The good capacitance value observed for the nanoassemblies was mainly attributed to the good surface area and pore size distribution, which provided more active sites for the electrochemical reaction.

Gao et al. (2019) synthesized NF nanosheets ($128 \text{ m}^2 \text{ g}^{-1}$) and nanoparticles ($77 \text{ m}^2 \text{ g}^{-1}$) through the hydrothermal method followed by calcination of the intermediates in air. The Ni foam deposited active electrode showed a capacitance value of 241 and 174 F g^{-1} for nanosheets and nanoparticle morphology at a used current density of 1 A g^{-1} in 6 M KOH electrolyte and 130% of the initial capacitance value was maintained after 2000 discharge rounds at a current density of 1 A g^{-1} . The better electrochemical execution depicted by the nanosheet morphology was primarily attributed to the high surface area of nanosheets, good contact of electrode surface with the electrolyte, which has improved the electrical conductivity of the nanosheet sample.

Ge et al. (2016) synthesized porous carbon nanofibrous membranes incorporated with NF nanocrystals for supercapacitor applications. The nanocomposites displayed a capacitance value of 343 F g^{-1} at a current density of 1 A g^{-1} compared to only NF of 98 F g^{-1} in 1 M H_2SO_4 electrolyte. The composite material also delivered a 97% retention value after 10000 cycles at a current density of 1 A g^{-1} . The enhanced capacitance value and long term cyclic stability for the composite were primarily attributed to the 3D structure of carbon, which provided good ionic mobility. The presence of NF made the composite structure more stable owing to which the enhanced performance was observed.

Shaymaa et al. (2018) synthesized NF nanoparticles on a 3D graphene capsule through a hydrothermal route followed by calcination. The as-synthesized electrode material displayed a capacitance value of 1023 F g^{-1} at a current density of 2 A g^{-1} compared to only NF of 712 F g^{-1} in 2 M KOH electrolyte. The composite electrode material retained 94% of its initial capacitance value after 10000 cycles, whereas the NF electrode retained only 88% value. The composite material's enhanced electrochemical performance was primarily ascribed to the high surface area and increased electronic conductivity.

Zhang et al. (2019) synthesized NF nanocubes anchored on rGO cryogel through a hydrothermal method and the prepared electrode material displayed a

capacitance value of 488 F g^{-1} at a current density of 1 A g^{-1} and 90% retention value as compared to NF of 79% after 10000 cycles at a constant current density of 3 A g^{-1} . The increment in the electrochemical performance of the composite sample was mainly ascribed to the 3D porous network, which helped in the efficient transport of electrolyte ions. The incorporation of NF nanostructures reduced the strain produced during the electrolyte insertion/de-insertion process, which ultimately reduced the agglomeration of graphene sheets increasing the conductivity of the graphene and reducing the ion diffusion path for the improvement of electrochemical performance.

1.2.4 NC AND PGNC

An overview of a few reported literature about the synthesis of NC, PGNC and its utility in supercapacitor has been discussed here.

Mondal et al. (2015) followed the microwave approach for the synthesis of NC nanosheets, which has shown a capacitance value of 560 F g^{-1} at a current density of 2 A g^{-1} with 95% retention value after 5000 cycles at a current density of 10 A g^{-1} in 2 M KOH electrolyte. The good electrochemical performance executed by the electrode material was ascribed to the high surface area and porous nature of the electrode material, which has provided efficient electron transport and the contact area between the electrode/electrolyte surface.

Xu et al. (2018) synthesized hollow NC nanospheres with a large specific surface area. The prepared nanospheres as an electrode have displayed a capacitance value of 1229 F g^{-1} at a current density of 1 A g^{-1} with 86% retention value after 3000 cycles at a scan rate of 50 mV s^{-1} . The electrode material's excellent electrochemical performance was mainly attributed to the hollow structure with a large surface area that provided more active sites for the fast electrochemical redox reaction.

Yan et al. (2018) prepared NC nanosheets by electrodeposition method followed by thermal treatment. Then vacancies were created in the nanosheets by soaking the NC nanosheets in different concentrations of NaBH_4 . The electrochemical

result showed an enhancement in the capacitance value (1590 F g^{-1}) in the vacancy created sample compared to the normal nanosheets (898 F g^{-1}) at a constant current density of 1 A g^{-1} . The better electrochemical execution showed by the vacancy created sample was mainly ascribed to the enhanced electrical conductivity, improved redox reaction and faster kinetics.

Li et al. (2018) prepared a diamond-shaped hexahedron structure of NC through the hydrothermal method. The as-prepared NC has shown a capacitance value of 691 F g^{-1} at a current density of 1 mA cm^{-2} with a 96% initial capacitance retention value after 5000 cycles at a current density of 6 A g^{-1} in 6 M KOH electrolyte. The better electrochemical execution was mainly ascribed to the increased contact area between the electrode and electrolyte interface.

Bhagwan et al. (2019) synthesized hexagonal NC nanostructures through the co-precipitation method followed by calcination. The prepared electrode material depicted a capacitance value of 1525 F g^{-1} at a current density of 1 A g^{-1} with a 98% retention rate after 2000 cycles at a current density of 10 A g^{-1} . The sample's excellent electrochemical execution was mainly ascribed to the effective utilization of the electroactive surface area, reduced ion diffusion path and improved redox reaction.

Zhang et al. (2019) synthesized firework-shaped NC microspheres through a simple hydrothermal method, followed by calcination in air. The NC electrode material displayed a capacitance value of 696 F g^{-1} at a current density of 1 A g^{-1} with 86% capacitance retention value after 10000 cycles at a scan rate of 50 mV s^{-1} . The sample's excellent electrochemical execution was mainly ascribed to the maximum utilization of the electroactive surface area, reduced ion diffusion path and improved electrochemical reaction.

Gao et al. (2020) synthesized NC nanofeathers through the hydrothermal method, followed by calcination. The obtained material displayed a capacitance value of 1797 F g^{-1} at 1 A g^{-1} current density with an 87% retention value after 5000 cycles at a current density of 10 A g^{-1} . The obtained good electrochemical performance of

the electrode material was primarily ascribed to the short ion diffusion, faster kinetics and effective utilization of electrode material.

Lamiel et al. (2016) synthesized 3D graphene@NC arrays on nickel foam as an electrode material for supercapacitor applications. The as-synthesized material displayed a capacitance value of 2356 F g^{-1} at a current density of 2 A g^{-1} and 123% initial capacitance retention value after 1500 cycles at a current density of 10 A g^{-1} in 6 M KOH electrolyte. The extraordinary electrochemical execution of the composite material was mainly ascribed to the increased electronic conductivity of the composite sample.

Foo et al. (2016) synthesized 3D hierarchical rGO/NC nanostructures through the hydrothermal method. The electrode material displayed a capacitance value of 613 F g^{-1} at a current density of 1 A g^{-1} and 76% initial capacitance value was retained after 2000 cycles at an applied current density of 1 A g^{-1} in 2 M KOH electrolyte solution. The enhanced electrochemical performance of the composite sample was mainly attributed to the high surface area of the composite, which significantly reduced the diffusion path length and provided enough active sites for the electrochemical redox process.

Sun et al. (2016) synthesized NC/3D graphene composite through the hydrothermal method. The obtained composite displayed a high capacitance value of 2300 F g^{-1} at a current density of 1 A g^{-1} along with a 92% initial capacitance retention value after 4000 cycles at a current density of 10 A g^{-1} . The composite material's excellent electrochemical execution was mainly ascribed to the synergistic effect of the 3D porous structure of the graphene and nanoparticle structure of NC.

Fang et al. (2018) synthesized N-doped mesoporous carbon@NC nanocomposites through the hydrothermal method, followed by calcination. The as-synthesized composite electrode material showed a capacitance value of 1624 F g^{-1} at a current density of 1 A g^{-1} compared to NC nanostructure of 1038 F g^{-1} . The composite material retained a 94% capacitance value after 10000 cycles at a current

density of 1 A g^{-1} . The composite material's extraordinary electrochemical execution was mainly ascribed to the synergistic effect of the component materials.

Dong et al. (2019) synthesized NC nanorods incorporated in 3D porous ultrathin carbon networks as an electrode material for supercapacitor applications. The as-synthesized material displayed a capacitance value of 1256 F g^{-1} at a current density of 1 A g^{-1} , which may be ascribed to the fast electron transport and high utilization of active material for redox reaction.

Tang et al. (2019) prepared flower-like N-doped porous carbon/NC hybrid electrode material through a physical mixing method followed by a calcination process. The composite electrode displayed a capacitance value of 948 F g^{-1} compared to 603 F g^{-1} for NC nanostructures. The composite electrode material retained an initial capacitance value of 87% compared to the NC of only 68% after 2000 cycles at a constant current density of 10 A g^{-1} . The improved electrochemical performance in the composite sample was mainly ascribed to the good surface area, numerous porous channels for fast and efficient ion transportation and good electrical conductivity.

Li et al. (2019) synthesized hierarchical reduced graphene hydrogel-NC nanowire composites through a hydrothermal method for supercapacitor applications. The electrode material depicted a capacitance value of 1178 F g^{-1} at a current density of 1 A g^{-1} , while only NC has shown a capacitance value of 705 F g^{-1} at the same current density. The composite and NC electrode material displayed a capacitance retention rate of 87% and 82%, respectively, after 5000 cycles at a constant current density of 5 A g^{-1} in 3 M KOH electrolyte. The composite sample's improved performance was mainly ascribed to the high surface area, enhanced conductivity and porous nature.

Jiu et al. (2019) synthesized 3D graphene aerogel-NC nanowire composites under the hydrothermal method followed by calcination. The composite material displayed a capacitance value of 720 F g^{-1} at a current density of 1 A g^{-1} , while NC was displayed a capacitance value of 512 F g^{-1} at the same current density. The

amelioration in the capacitance value of the composite was attributed to the introduction of graphene aerogel, which provided good electrical conductivity and effective transport of electrolyte ions in the porous framework. The composite material retained 84% of the initial value after 1000 cycles at a current density of 1 A g⁻¹.

1.3 SCOPE

The present world needs flexible, lightweight, mechanically strong and highly efficient energy storage devices due to applications in portable and wearable consumer electronic devices. It is also evident that there is a growing demand for these devices as they provide higher power density, longer cycling life, faster charge/discharge rates and safer operation conditions than lithium ion batteries and thus are considered as the most promising energy storage devices. PG could be a suitable replacement for graphene as an EDLC material due to the characteristics of highly porous structure, ability to act as an ion-buffering reservoir and reduction in the transport path length leading to the amelioration of electrochemical traits. Till date, the preparation of PG includes chemical bottom up approach via the surface assisted aryl-aryl coupling reaction and physical methods include high energy techniques such as electron beam irradiation, helium ion bombardment, laser irradiation and carbothermal etching on graphene film. In such methods the porous network is developed on a conductive substrate, which is very costly and the yield is also very poor, which limits its applicability in a real-world market. In most of the cases, the planar graphene sheets readily agglomerate owing to either van der Waals or capillary forces due to which it hinders the efficient transport of electrons across the channels and hence, the effective utilization of the planar sheet is not possible to improve the electrochemical performance of the material. On the other side, oxides of nickel are considered as a celebrated oxide for supercapacitor applications owing to its high theoretical capacitance value, high abundance, environmentally benignity, high thermal and chemical stability. Various oxides of nickel in the form of different nanostructures have been used as an electrode material for supercapacitors but owing to their poor conductance values they exhibit mediocre capacitance values. Therefore,

a hybrid supercapacitor employing the combination of PG and oxides of nickel is expected to produce enhanced capacitance value, energy/power density and longer cyclic stability at a high current range. There are several reports on the synthesis of hybrid composites of oxides of nickel with different graphenic forms. However, the obtained high specific capacitance values are mainly due to the utilization of 6 M KOH electrolyte or Ni foam as current collector. Although the use of Ni foam along with the concentrated KOH electrolyte increases the specific capacitance value due to the presence of interlinked pores in the Ni foam, the high cost and tedious procedure of its usage have limited its utility. Also despite the higher capacitance value, the cyclic stability performance of the composites reported were not satisfactory even after the use of Ni foam current collector, due to the use of concentrated KOH electrolyte (4 M - 6 M) which triggers the delamination of electroactive material leading to the hampering of long term cyclic stability at higher current densities.

It is well agreed that supercapacitors form an important class of energy storage devices catering to a variety of needs. However, designing the same using eco-friendly and earth abundant materials with high performance is still the dire need of the day. The synthesis of hybrid supercapacitors involving nanocomposites of PG and oxides of nickel by a low-cost and eco-friendly method for mass production looks promising and is of importance. Employing a solvent system consisting of a mixture of 1:1 ethylene glycol and water (EG+H₂O) would be promising to obtain materials of high surface area and porous structure. Also it is worthwhile to investigate the electrochemical performance of these materials with lower concentrations of KOH and by using economic current collector in the form of Ni sheet. Based on these considerations the present study was carried out.

1.4 OBJECTIVES

The objectives of the proposed work are as follows:

- 1) To synthesize PG and oxides of Ni viz. NiO, NF and NC.
- 2) To synthesize nanocomposites of PG and oxides of Ni.

- 3) To characterize the synthesized materials using diffraction, microscopy, spectroscopy techniques and carry out elemental and surface area analysis.
- 4) To study the electrochemical performance of these materials as an electrode and as symmetrical supercapacitor device in aqueous 2 M KOH electrolyte.

1.5 PRESENT WORK

The present thesis reports the successful synthesis of seven different kinds of electrode materials namely PG, NiO, PGNiO, NF, PGNF, NC and PGNC via facile, eco-friendly solvothermal method using mixed solvents. All the synthesized electrode materials were thoroughly characterized for their structural, morphological, elemental, spectroscopic and surface area properties by employing appropriate techniques such as X-ray diffraction (XRD), field emission scanning electron microscopy (FESEM), transmission electron microscopy (TEM), energy dispersive X-ray analysis (EDX), Raman spectroscopy and BET surface area analysis. Thereafter, each electrode material was investigated for the energy storage applications. The electrochemical characterizations such as cyclic voltammetry (CV), galvanostatic charge discharge (GCD) analysis, electrochemical impedance spectroscopy (EIS) and cyclic stability test were performed in an aqueous 2 M KOH electrolyte using economic Ni sheet as current collector.

The contents presented in the thesis have been broadly divided into nine chapters with several sections in each chapter.

Chapter 1 gives a brief introduction to the basic concepts of the study undertaken. It also gives a brief overview of the relevant works in the literature which focus upon PG, NiO, NF, NC, PGNiO, PGNF and PGNC, their synthesis methods and their role in supercapacitor application. Scope and objectives of the present research work have been given at the end.

Chapter 2 - Chapter 8 deals with the synthesis, characterization and electrochemical studies of PG, NiO, PGNiO, NF, PGNF, NC and PGNC, respectively.

The electrochemical performance of the as-synthesized materials were studied thoroughly as an electrode material and by fabricating a symmetrical supercapacitor device.

Chapter 9 outlines the summary of the work presented in the thesis along with important conclusions drawn from the study. The results of the experimental investigation presented in the thesis are compared with the reported literature. Scope for further research has also been included in this chapter.

References used have been listed at the end followed by Bio-data.



CHAPTER 2

***ECO-FRIENDLY SYNTHESIS OF POROUS
GRAPHENE AND ITS UTILIZATION AS HIGH
PERFORMANCE SUPERCAPACITOR ELECTRODE
MATERIAL***

Chapter 2 presents an eco-friendly approach for the synthesis of PG employing a mixed solvent system under a facile solvothermal route and its thorough characterization to know the formation of PG. First principles calculations were implemented to study the effect of pore formation on the electronic structure. PG's electrochemical performance was studied as an electrode and in a supercapacitor device and is discussed thoroughly in this chapter.

2.1 INTRODUCTION

PG is a type of spongy graphenic material, which possesses different properties compared to that of graphene. After the discovery of graphene, many researchers have tried to modify the parent graphene structure and created a new type of planar sheet structure consisting of pores viz PG, formed by the removal of sp^2 bonded carbon atoms. Depending on their pore diameters they are classified as microporous (diameter < 2 nm), mesoporous (diameter from 2-50 nm) and macroporous (diameter > 50 nm) materials (Zdravkov et al., 2007). The pore sizes also vary from atomic to nanoscale dimensions, based on the fabrication methods used. Microporous structures can be used in catalysis, water and air purification, whereas the mesoporous and macroporous structures are generally used in adsorption of large hydrophobic molecules, chromatographic separations and electrochemical capacitors (Russo et al., 2013).

Although there are several reports on the synthesis of PG and its utilization for charge storage, they involve the use of strong oxidants, templates, or chemical activation. An overview of the recent literature reveals that in such methods, the production cost is high, the yield is poor, the capacitance is less or capacitance retention is low apart from lower energy and power densities (Bai et al., 2019; Chai et al., 2019; Ghosh et al., 2018a; Kang et al., 2019; Liu et al., 2018; Meng et al., 2018). These factors limit its applicability in a real-world market.

2.2 EXPERIMENTAL SECTION

2.2.1 Synthesis of GO and PG

All the chemicals used here were of analytical grade and used without any further purification process. Deionized water was used for washing and preparation of GO suspension and PG.

GO was synthesized according to the improved Hummers' method, reported elsewhere (Marcano et al., 2010). A calculated amount of graphite was mixed with 9:1 mixture of H₂SO₄:H₃PO₄. KMnO₄ was added in batches of little amount with continuous stirring to avoid overheating and then the reaction mixture was maintained at 50 °C for 12 h. The dark brown suspension formed was poured into 200 mL ice water followed by the addition of 30% H₂O₂ till the effervescence ceases, changing the color of the suspension from dark brown to brilliant yellow. The suspension was successively washed with water, 30% HCl and ethanol and finally dried at 50 °C for 10 h to get GO.

The obtained GO was dispersed in a mixture of 1:1 ethylene glycol + water (1 mg mL⁻¹) and was ultrasonicated for 2 to 3 h in an ultrasonic bath. Then, the exfoliated GO dispersion was put into a stainless-steel autoclave of 100 mL capacity and further heated to 160 °C for 16 to 32 h (these samples were named as PG 16 to PG 32, respectively). After the autoclave gets cooled down to room temperature, the black products were collected and were repeatedly washed with water. Finally, the products were dried at 80 °C for 6 h to obtain PG (Figure 2.1).

2.2.2 Characterization

The structural and morphological characterizations of GO and PG were done by XRD (Rigaku MiniFlex 600 X-Ray diffractometer) with Cu-K_α radiation ($\lambda=1.5418 \text{ \AA}$) with a scan rate of 2° per minute in the range of 5° - 80°, FESEM (Zeiss Ultra 55 field emission scanning electron microscope) equipped with EDX (Oxford instruments), TEM images were recorded on Fei Tecnai G2 operated at an acceleration voltage of 200 kV. Raman spectra were recorded on an STR 500

confocal micro Raman spectrometer (Airix Corporation, Japan) using a 532 nm laser source. BET surface area analysis was done by recording nitrogen adsorption/desorption isotherms at 77 K (BEL SORP II, Japan). Prior to the analysis, samples were degassed at 200 °C in vacuum for 2 h. The pore size distribution of the materials was determined by using Barrett-Joyner-Halenda (BJH) method. X-ray photoelectron spectroscopy (XPS) data were taken in the range of 1-1200 eV (Omicron Nanotechnology) with monochromatic Al-K α radiation (1486.7 eV) to investigate the surface chemical composition of the PG sheets. All the XPS spectra were corrected with the C 1s line at 284.5 eV. The Fourier transform infrared (FTIR) spectra were recorded in the wavenumber range of 400 - 4000 cm $^{-1}$ using Bruker, model-Alpha instrument. For the FTIR analysis, pellets were made by mixing KBr and synthesized samples to make a homogeneous pellet. AFM analysis was done by using SPM 9600 atomic force microscopy (Shimadzu) in tapping mode.

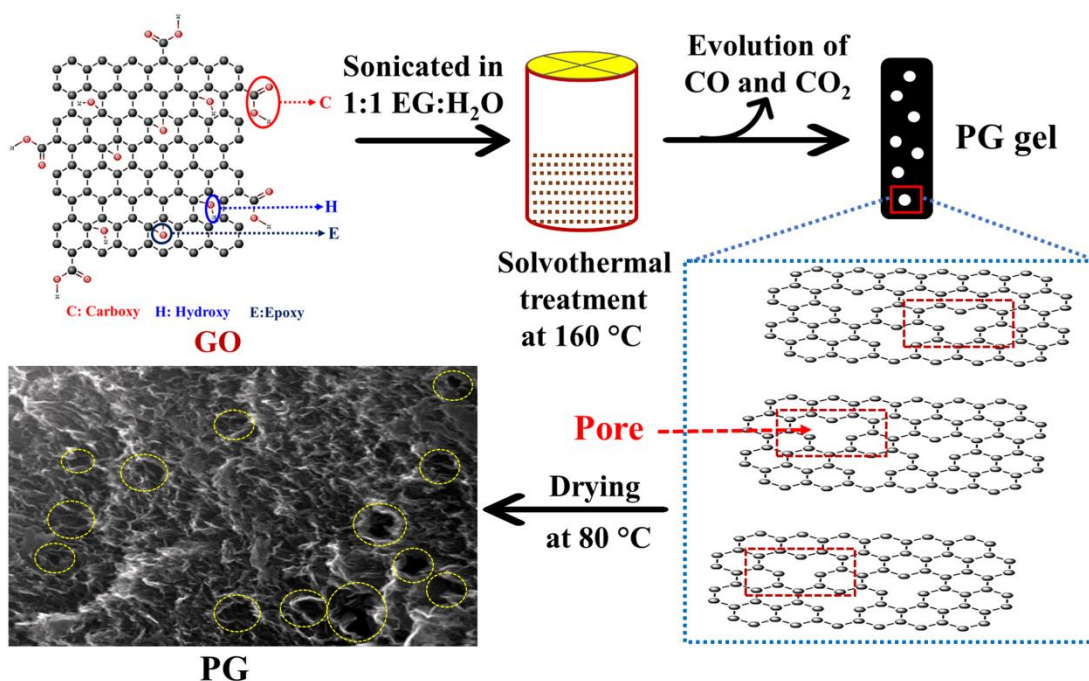


Figure 2.1 Mechanism of formation of PG.

2.2.3 Computational Details

First principles electronic structure and density of states (DOS) calculations of pristine graphene and PG were carried out within the framework of density functional theory (DFT) using Quantum ESPRESSO package (Giannozzi et al., 2009). Ultra-soft scalar relativistic pseudopotentials with parametrized functional of Perdew, Burke and Erzenhoff were used to approximate the exchange-correlation energy functional (Perdew et al., 1996). The pseudopotential representing the ionic core implements a generalized gradient approximation considering $2s^22p^2$ as valence electrons of carbon. Fully relaxed supercells of $5 \times 5 \times 1$ and $10 \times 10 \times 1$ dimensions of primitive cell were used to simulate various pore concentrations. A vacuum layer of 15 \AA was maintained to separate the adjacent periodic images of the sheet. K mesh of $9 \times 9 \times 1$ (for self consistent field calculations) and a denser grid of $36 \times 36 \times 1$ (for obtaining DOS) were used to sample integrations over the Brillouin zone of the supercell. Electronic wave functions represented by plane wave basis set were truncated with an energy cutoff of 50 Ry and charge density cutoff of 400 Ry. Gaussian smearing with a width of 0.01 eV was used to smear the discontinuity in occupation numbers of electronic states. The electronic structure of the 2D sheet was determined along $\Gamma - M - K - \Gamma$ high symmetry path.

2.2.4 Electrochemical Measurements

The working electrodes were made by mixing the active material (PG), acetylene black and PVDF binder in a weight ratio of 8:1:1. Initially, active material and acetylene black were mechanically mixed using a mortar and pestle and later a few drops of PVDF binder dissolved in NMP was added and mixed to get a slurry-like ink. The slurry-like ink was coated on one side of a Ni sheet of $1 \times 1 \text{ cm}^2$ area using the Doctor's blade technique followed by drying and employing a 3-electrode method. The mass deposited on the sheet was approximately 1 mg, as measured by a high precision weighing balance with a readability of 0.0001 g. Here, the coated Ni sheet served as the working electrode, saturated calomel as reference electrode and platinum wire as counter electrode. The symmetrical supercapacitor was fabricated by

coating the above prepared slurry-like ink on one side of a Toray carbon paper of 2×2 cm² area using layer by layer brush coating technique. The coated carbon paper was heated at 60 °C for 8 h to reduce the effect of the binder used. The supercapacitor setup consisted of coated PG as working electrode material, 2 M KOH as an electrolyte, a filter paper soaked in the electrolyte as a separator and stainless-steel panels as current collectors (Mishra et al., 2011; Subramanya et al., 2015a). The mass deposited on single carbon paper was found to be approximately equal to 3 mg. The electrochemical properties of the 3-electrode and supercapacitor device were evaluated by CV, GCD and EIS in the frequency range of 10⁵ Hz – 0.01 Hz (by impressing an AC perturbation of 10 mV) using a computer controlled IVIUMstat potentiostat/galvanostat electrochemical workstation BV Co., The Netherlands (Model: Vertex). The specific capacitance values from the CV curves were calculated according to equation 2.1 (Feng et al., 2018; Mishra et al., 2011; Sethi et al., 2019a).

$$C_s = \frac{nA}{\Delta V \times m \times \nu} \quad (2.1)$$

Where C_s = specific capacitance (F g⁻¹), A is the integrated area of the CV curve, ΔV is the maximum potential window (V), m is the deposited mass on one single electrode (g) and ν is the scan rate (V s⁻¹). For 3-electrode system, $n = 1$. A factor of $n = 2$ is multiplied owing to the formation of series capacitance in a 2-electrode cell (symmetrical supercapacitor device).

The specific capacitance values from the GCD curves were calculated using equation 2.2.

$$C_s = n \times \frac{I \times \Delta t}{m \times \Delta V} \quad (2.2)$$

Where C_s = specific capacitance (F g⁻¹), $\frac{I}{m}$ is the applied current density, Δt is the discharging time, ΔV is the maximum potential window to discharge the cell, $n = 1$ for 3-electrode system and $n = 2$ for 2-electrode cell.

The specific capacity Q_s ($C\ g^{-1}$) values were also calculated from the GCD data for 3-electrode system by using equation 2.3 (Zhang et al., 2019).

$$Q_s = \frac{I \times \Delta t}{m} \quad (2.3)$$

The energy density E ($Wh\ kg^{-1}$) and power density P ($W\ kg^{-1}$) of the prepared electrode and supercapacitor device were calculated according to equation 2.4 and 2.5, respectively (Hwang et al., 2020; Sethi et al., 2019a; Zhang et al., 2019).

$$E = \frac{1}{2} C_s \Delta V^2 \frac{1000}{3600} \quad (2.4)$$

Where C_s = specific capacitance ($F\ g^{-1}$), V is the maximum potential window, E is the applied energy density, t_d is the discharging time.

$$P = \frac{E}{t_d} \times 3600 \quad (2.5)$$

The specific capacity ($C\ g^{-1}$) values for the supercapacitor device were also calculated from the GCD data according to equation 2.6 (Brousse et al., 2015; Zhang et al., 2019).

$$Q_s = C \times \Delta U \quad (2.6)$$

Where Q_s is the specific capacity, C is the capacitance obtained from GCD curve and ΔU is the potential window.

The coulombic efficiency η (%) from the GCD curves were calculated using equation 2.7.

$$\eta (\%) = \frac{\Delta t_d}{\Delta t_c} \times 100 \quad (2.7)$$

Where Δt_d and Δt_c are the discharging time and charging time, respectively.

The double layer capacitance (C_{EDL}) and pseudocapacitance (C_P) contribution from the total capacitance were estimated by using the equation 2.8 (Biswas et al., 2020; Sharma et al., 2019).

$$C_s(T) = C_{EDL} + C_P \quad (2.8)$$

Where $C_s(T)$ is the total specific capacitance, C_{EDL} and C_P is the double layer capacitance and pseudocapacitance contribution, respectively.

2.3 RESULTS AND DISCUSSION

2.3.1 Structural, Elemental and Morphological Analysis

Figure 2.2(a) shows the XRD patterns of the synthesized GO and PGs. In GO there is a characteristic peak at 9.4° corresponding to the (001) crystal planes. The interlayer spacing of the GO is around 0.94 nm as compared to the pristine graphite of 0.34 nm, which clearly indicates that the high degree of oxygenation has occurred in the sample. In PG, the (001) crystal planes disappear and new peaks are observed at $20\text{--}25^\circ$ and $40\text{--}45^\circ$ range, which correspond to the characteristic (002) and (100) planes of the PG, respectively (Sadiq et al., 2017e). The calculated d-spacings from the Bragg's law is given in Table 2.1 and the d-spacings are close to the value of graphite i.e. 0.34 nm depicting the restoration of the graphite moiety. The XRD peaks of the PG are broad in nature, suggesting the stacked nature of the sheets and thickness of few layers. From the XRD peaks and Scherrer's equation, the average number of layers was calculated using equation 2.9 (Subramanya et al., 2015b).

$$N = \frac{L}{d} + 1 \quad (2.9)$$

Where N is the number of layers, L is the crystallite size obtained from Scherrer's equation and d is the d-spacing between the planes. The number of layers calculated using the formula was found to be $\sim 4\text{--}6$.

Raman spectroscopy is a potent technique to characterize the graphene samples in terms of crystal disorders, defects and hybridization (Mohamed et al.,

2017b; Sadiq et al., 2018b). The Raman spectra of GO and PG samples are shown in Figure 2.2(b). In all the samples the D band (formed due to the breathing mode of κ -point phonons of A_{1g} symmetry) and G band (formed due to the first order scattering of the E_{2g} mode) are present confirming the defect formation and restoration of graphite moiety in the PG samples (Sadiq et al., 2017c).

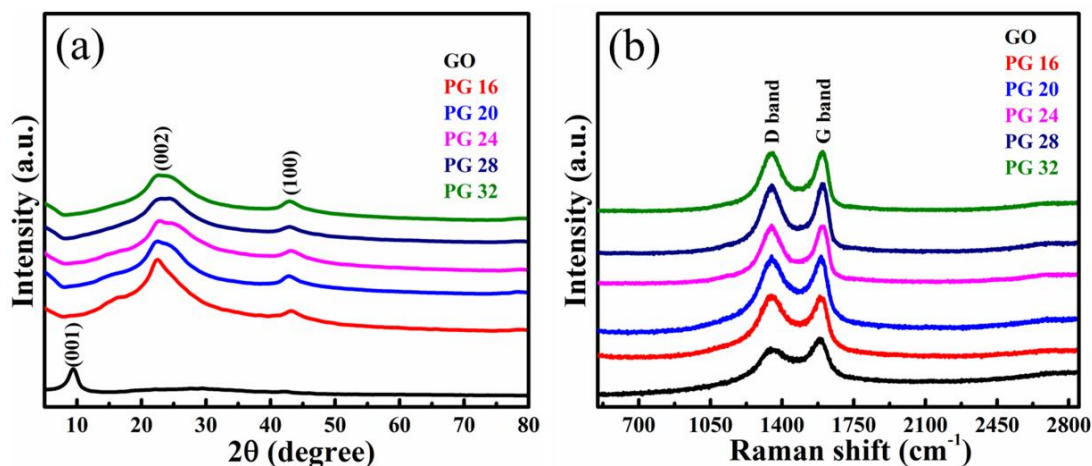


Figure 2.2 (a) XRD patterns, (b) Raman spectra of the prepared GO and PG samples showing D and G bands.

Table 2.1 2θ values and their corresponding d-spacing values for synthesized GO and PG.

Sample name	2θ values ($^{\circ}$)	d-spacing (nm)
GO	9.40	0.94
PG 16	22.42	0.396
PG 20	22.90	0.388
PG 24	23.00	0.386
PG 28	23.61	0.376
PG 32	22.53	0.394

In the Raman spectra of GO, the very low intensity of D band indicates lesser number of defects in GO sample. After the onset of the reduction process, the

progressive increase in the intensity of the D band, the broadening of G band and blue shifting of the peak from 1580 cm⁻¹ for GO to 1590-1599 cm⁻¹ for PG samples indicate the formation of defects and decrease in the number of layers in the samples (Sadiq et al., 2017c). The relative intensity ratio (I_D/I_G) of the D and G bands is a measure of the defects formed in the sample and is inversely proportional to the average size of the sp² domains (Sadiq et al., 2017e). The calculated (I_D/I_G) values for GO and PG samples are tabulated in Table 2.2.

Table 2.2 D and G band positions and their corresponding I_D/I_G ratio values for GO and PG.

Sample name	D band position	G band position	I_D/I_G ratio
GO	1351.0	1580.0	0.76
PG 16	1347.4	1590.0	0.94
PG 20	1347.4	1590.0	1.01
PG 24	1351.0	1594.0	1.07
PG 28	1351.0	1599.0	1.10
PG 32	1347.4	1594.8	1.05

Analysis of values in Tables 2.1 and 2.2 reveals that there is an inverse trend in the D and G band positions of Raman spectrum and XRD traces of PG 32 sample. This may be explained as follows: Compared to other samples, PG 32 was formed with a reaction time of 32 hours. This larger duration of reaction can cause better exfoliation and hence increased distance between planes of graphene crystallite. Accordingly, XRD trace of this sample showed higher d-spacing and reduction in the 2-theta value. Due to the same reason, the sample undergoes better reduction and possesses lesser extent of defects. This will result in a lower value of D-band in the Raman spectrum. However, the variation of these values is not regular or linear and there can also be several other reasons contributing to these effects. More detailed studies are needed to understand this behavior and to make any conclusive remarks on this trend.

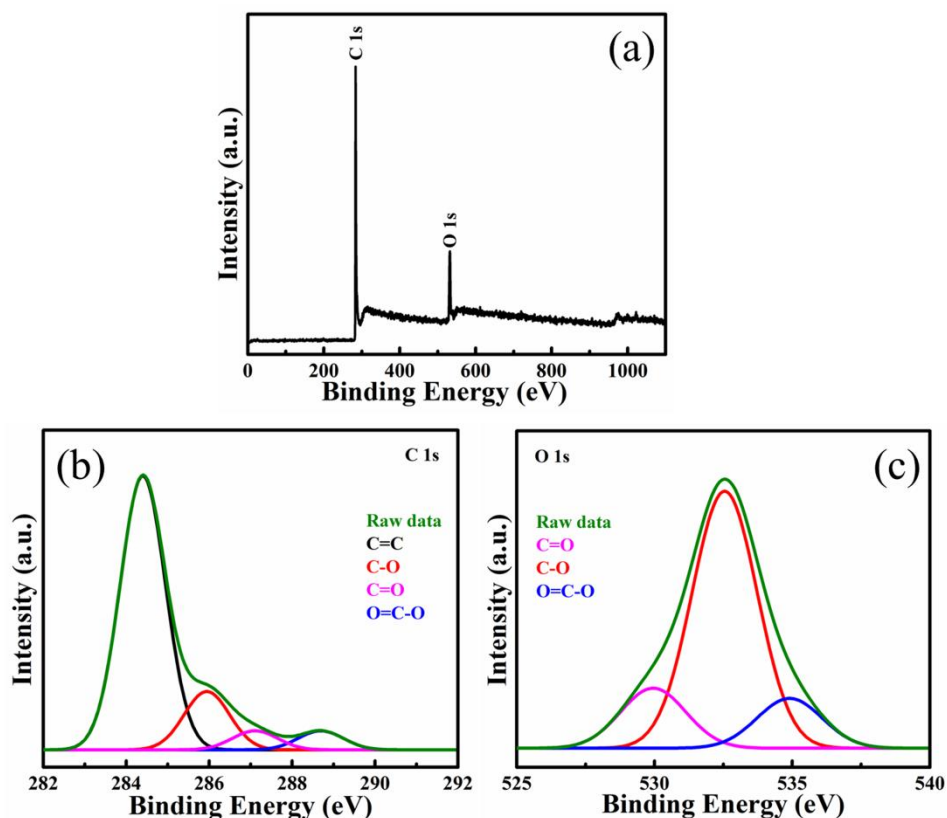


Figure 2.3 (a) XPS survey spectrum of PG 28, deconvoluted spectrum (b) C 1s and (c) O 1s.

The chemical composition of the PG 28 sample was analyzed by XPS technique. The survey spectrum of the PG 28 sample is shown in Figure 2.3(a), wherein only carbon (87.7 at. %) and oxygen (12.3 at. %) were present suggesting the high purity of the sample. The low content of the oxygen in the sample indicates that appreciable reduction has occurred in the PG 28 sample. The deconvoluted C 1s spectrum in Figure 2.3(b) shows the existence of a sharp peak at 284.5 with a flat tail towards higher binding energy, depicting the restoration of sp^2 moiety in the sample (Sadiq et al., 2017d). The peaks at binding energies of 285.9 and 288.5 eV correspond to the C-O and C=O species, respectively in the sample (Mohamed et al., 2017a; Srivastava et al., 2014). The deconvoluted O 1s spectrum in Figure 2.3(c) reveals two peaks at binding energies of 531.2 and 532.8 eV, which may be ascribed to the C=O and C-O species, respectively (Sadiq et al., 2016; Sadiq et al., 2017c).

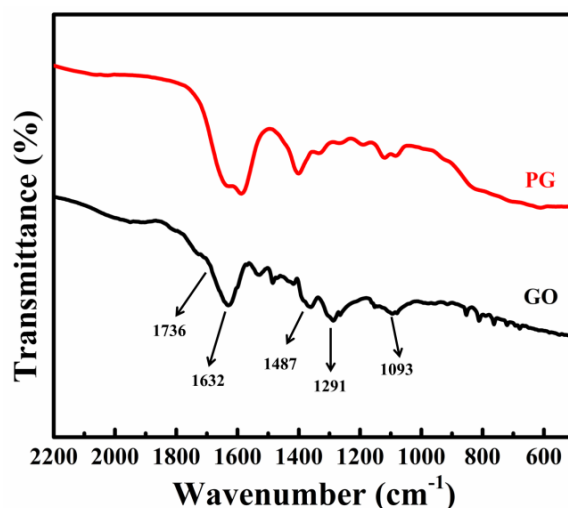


Figure 2.4 FTIR spectra of GO and PG.

The FTIR spectra of GO and PG are displayed in Figure 2.4. The FTIR analysis tells the presence of chemical bonding and functional groups in the as-synthesized materials. The FTIR spectrum of GO shows the presence of peaks at 1093 cm^{-1} corresponding to C-O-C stretching vibrations, 1291 cm^{-1} corresponding to C-OH stretching vibration, 1487 cm^{-1} corresponding to the O-H deformation of the C-OH group, 1632 cm^{-1} corresponding to the C=C stretching mode and the C-O stretching vibrations of the COOH group, 1736 cm^{-1} corresponding to the C=O stretching vibration from carbonyl group and a broad band at 3447 cm^{-1} corresponding to the absorption of water or O-H groups. In the spectrum of PG, the intensity corresponding to the peaks involving oxygen containing groups decreased suggesting the removal of oxygen moieties from GO to transform it to PG during the solvothermal process.

The FESEM and TEM images of GO are shown in Figure 2.5(a) and (b). The FESEM image shows the agglomeration of GO sheets without any void/pores on the sheet. The TEM image of a GO layer indicates the absence of defects on the GO sheet. The FESEM image of the PG sheets in Figure 2.5(c) shows the crumpled and wrinkled structure indicating the soft, flexible and porous morphology (pores are marked with yellow circles) and stacked nature consistent with XRD results. The EDX pattern is given in Figure 2.5(c) inset showing only C and O as elements present, suggests the purity of the PG material. In order to confirm the generation of

pores on the sheets, The TEM analysis was done, which reveals the porous nature in Figure 2.5(d) and selected area electron diffraction (SAED) pattern of the PG sheet is shown in inset of Figure 2.5(d).

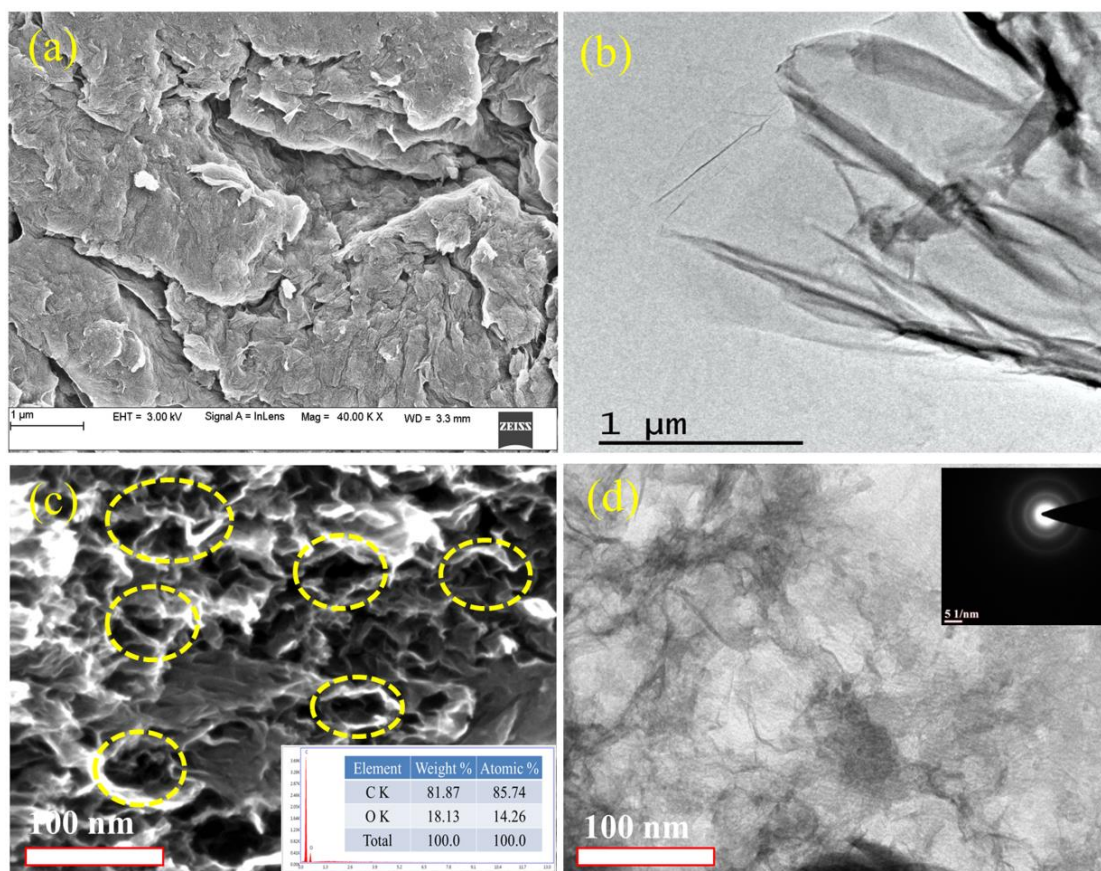


Figure 2.5 (a) FESEM and (b) TEM image of GO, (c) FESEM image (inset shows the EDX pattern and elemental composition of PG 28) and (d) TEM image of the PG sheet showing numerous pores on the sheet (inset shows the SAED pattern of PG).

AFM analysis was carried out in order to know the surface topography of the PG sample. The 3D image shown in Figure 2.6(a) shows some deep cavities, which corroborates the porous nature of the sample. The 2D topographic image shown in Figure 2.6(b) shows some voids/pits in the plane which confirms the porous nature of the material. The topographic image of one selected area and its corresponding measured height profile is represented in Figures 2.6(c) and 2.6(d). The topographic images confirm the successful synthesis of the PG.

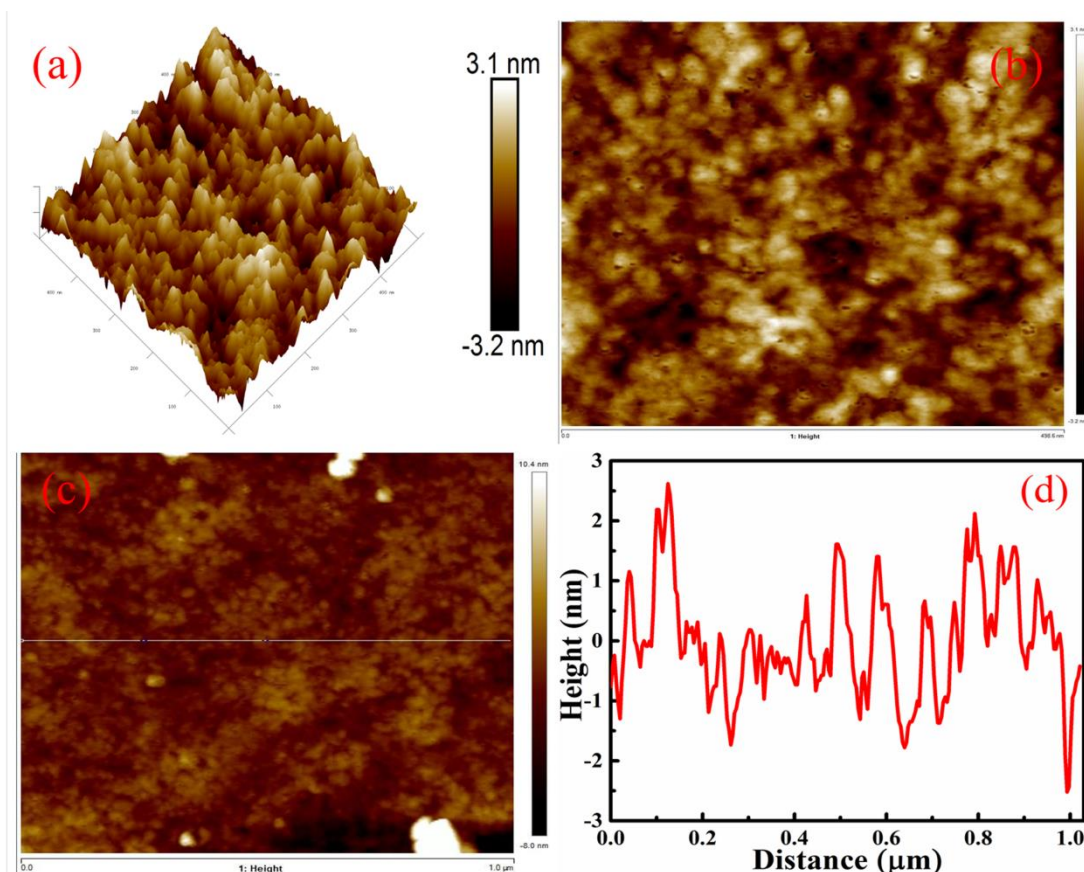


Figure 2.6 AFM image of PG 28 (a) 3D image, (b) 2D image showing the formation of pores, (c) Topographic image and (d) Height profile of the PG 28 corresponding to the white line drawn in (c). The value of R_a is 0.9 nm and R_q is 1.2 nm.

The surface area is an important parameter for PG. All the prepared samples were analyzed for their surface area. Figure 2.7(a) shows the N_2 adsorption-desorption isotherm of the PG samples, which conform to the characteristic type-IV isotherm with hysteresis loop in the P/P_0 range of 0.4-1.0. These results suggest the presence of mesopores in the samples. The calculated surface area of the samples by using the BET method were found to be 126, 185, 269, 420 and 338 $m^2 g^{-1}$ for PG 16, PG 20, PG 24, PG 28 and PG 32, respectively.

Among the tested samples, PG 28 exhibited the highest surface area as well as good restoration of graphitic moiety as indicated by the G band intensity in the Raman spectrum. These features contribute to high charge storage and transportation

characteristics. In view of this, the PG 28 sample has been selected as the best sample for electrochemical characterizations. The pore size analysis of the PG 28 sample has also been done and is shown in Figure 2.7(b). As can be seen from the plot, the sample possesses a porous structure with pores of microporous (1.7 nm) and mesoporous (3.5 and 9.8 nm) nature. The creation of the mesoporous structure at high temperatures is in accordance with the literature (Illán-Gómez et al., 1996). Such hierarchical porous structure and high surface area of the sample helped for high charge storage and thereby increases the capacitance value (Sevilla et al., 2011). The obtained surface area of the PG 28 sample is quite impressive and surpasses some of the previously reported literatures such as rGO ($111 \text{ m}^2 \text{ g}^{-1}$), 3D holey graphene through hydrothermal method ($41.5 \text{ m}^2 \text{ g}^{-1}$), graphene nanoplatelets ($48 \text{ m}^2 \text{ g}^{-1}$), PG network through hydrothermal method ($108 \text{ m}^2 \text{ g}^{-1}$), 3D graphene aerogel with bimodal pore structure ($49 \text{ m}^2 \text{ g}^{-1}$), RGO ($207 \text{ m}^2 \text{ g}^{-1}$), 3D PG film ($84 \text{ m}^2 \text{ g}^{-1}$) (Ahmed et al., 2017; Chai et al., 2019; Dimiev et al., 2015; Hwang et al. 2020; Riaz et al., 2018; Singh et al., 2017; Xue et al., 2020).

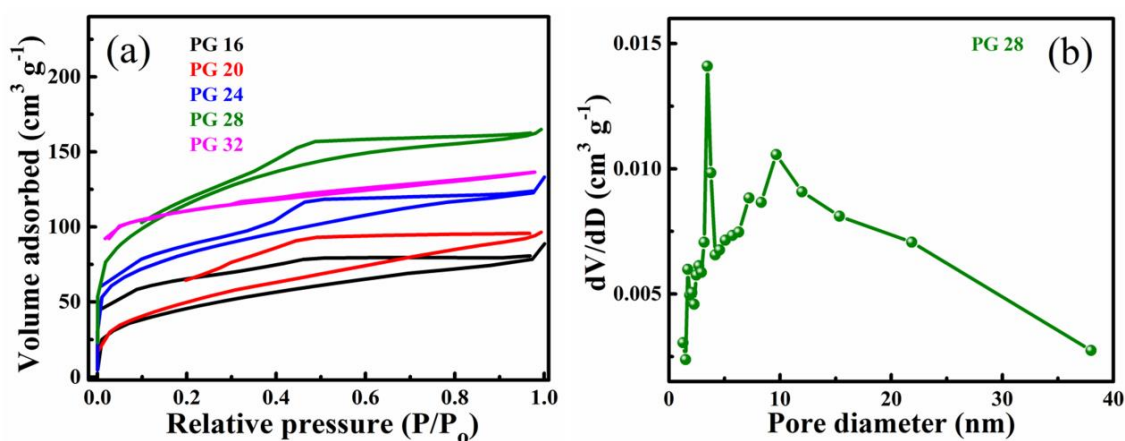


Figure 2.7 (a) BET surface area and (b) Pore size distribution of PG 28.

2.3.2 Role of Solvent Mixture on the Reduction of GO to PG

It is known that solvothermal reduction of GO proceeds in two stages: (1) Partial reduction that depends on the solvent polarity and (2) Further reduction to fully restore sp^2 structure of graphene. This second stage is strongly depending on solvent surface energy which controls the agglomeration of partially reduced GO. The solvent which can keep the GO well dispersed is believed to facilitate efficient reduction and thus the reduction of GO is highly susceptible to surface energy of solvents (Lin et al., 2014). It has been derived through appropriate theoretical considerations that for maintaining such good dispersal of GO, surface energy of the solvent should be in the range of 70-80 $mJ m^{-2}$ or slightly higher (Hernandez et al., 2008).

In the present study ethylene glycol-water binary mixture was used for the reduction of GO by solvothermal approach. The surface tension of water and ethylene glycol were calculated using equations 2.10 and 2.11, respectively.

$$\gamma = B \left(\frac{T_c - T}{T_c} \right)^\mu \left[1 + b \left(\frac{T_c - T}{T_c} \right) \right] \quad (2.10)$$

$$\gamma = \gamma_0 \left(1 - \frac{T}{T_c} \right)^n \quad (2.11)$$

Where $B = 235.8 \times 10^{-3} N m^{-1}$, $b = -0.625$, $\mu = 1.256$, T is the temperature of the solvent, T_c is the critical temperature, n is an empirical factor which is equal to 11/9 for organic liquids and γ_0 is a constant for each liquid which is given in equation 2.12.

$$\gamma_0 = \frac{kT_c}{V^{2/3}} \quad (2.12)$$

Where k is a universal constant (2.1×10^{-7}), V is the molar volume of the liquid and T_c is the critical temperature of the liquid. For ethylene glycol the value of γ_0 was found to be $1.5135 J m^{-2}$. The calculated surface tension values for water and ethylene glycol at our solvothermal condition of 433 K are $46.5 mJ m^{-2}$ and $21.6 mJ m^{-2}$, respectively. For a solution of an organic compound (here ethylene glycol) and water,

the surface tension can be expressed as in equation 2.13 (Connors et al., 1989; Khossravi et al., 1993).

$$\gamma_{mixing} = x \cdot \gamma_{ethylene\ glycol} + y \cdot \gamma_{water} \quad (2.13)$$

Where x and y represent the mole fractions of ethylene glycol and water, respectively. In the present used mixed solvent system, the calculated surface tension of binary mixture (equal volumes of ethylene glycol and water) was found to be 40.4 mJ m⁻² at 433 K. The surface energy can be calculated from surface tension values and the same for pure water, pure ethylene glycol and binary mixture are 89.8, 65.0 and 79.4 mJ m⁻², respectively. Hence, it is evident that the surface energy of water is on the higher side and that of ethylene glycol is on the lower side of required range for an efficient reduction process, whereas the surface energy of the solvent mixture used in the present study falls in the required range. Thus, the binary solvent mixture that was used in this study supposed to facilitate efficient reduction of GO under the employed solvothermal condition.

Further, under the prevailing conditions, the oxygen containing groups such as carboxylic, carbonyl and hydroxyl groups are believed to decompose into CO or CO₂ which can be entrapped into the hydrogel leading to the formation of the pores. Also, the overlapping and coalescence of graphene sheets can lead to the formation of pores in the resulting reduced graphene sheets, as reported previously (Hu et al., 2016; Mungse et al., 2014).

2.3.3 Electronic Structure Analysis by DFT

First-principles DFT electronic structure calculations were carried out to study the effect of pore formation in graphene sheets and its suitability as a material for supercapacitor application. For graphene based supercapacitors, the total capacitance is the resultant of double layer capacitance and quantum capacitance as though they were combined in series (Chen et al., 2017). Graphene has a large surface area due to which it can accommodate electrolyte ions and in turn increase the double layer

capacitance. Hence, the limiting factor is the finite quantum capacitance which is dependent on the electronic structure (Khosdel et al., 2015; Song et al., 2018). The optimized structure of pristine graphene is a 2D sheet with carbon atom forming hexagonal rings with C-C bond length of 1.42 Å consistent with the previous reports (Chen et al., 2017; Song et al., 2018). The electronic structure of pristine graphene reveals a zero band gap at K point (Dirac point) with valence band (VB) and conduction band (CB) touching each other with no states visible near the Fermi level in the DOS plot indicative of the vanishing gap (Figure 2.8a). As the quantum capacitance is directly proportional to the DOS near the Fermi level, the material exhibits lower capacitance as a direct consequence of lack of states near the Fermi level despite possessing considerable double layer capacitance. This becomes a major drawback for use of pristine graphene in supercapacitor application (Khosdel et al., 2015; Song et al., 2018).

When defect is introduced in graphene sheet in the form of a missing carbon atom a pore is formed. To simulate various defect concentration $10 \times 10 \times 1$ supercell with a single pore arising out of missing carbon atom; $5 \times 5 \times 1$ supercells with one and two pores were considered. The carbon atoms closer to the vacancy appear strained with C-C bond distance of 1.39 Å while the carbon atoms further away from the pore do not exhibit any such strain (C-C bond distance remains ~ 1.42 Å). Figure 2.8(b) reveals the appearance of a defect band, lying 0.035 eV above the valence band maximum (VBM) at K point and 0.084 eV below the conduction band minimum (CBM). The density of states shows a prominent sharp peak exactly at the Fermi level due to the flat defect band. The partial DOS (pDOS) reveal that the carbon atoms in close vicinity of the point defect is responsible for the increase in DOS near the Fermi level as the electronic structure becomes more localized in the area near the defect. The states formed have major contribution from the 'p' orbitals and minor contribution from 's' orbitals (Figure 2.9). It is believed that flatter bands and creation of higher density of states near the Fermi level leads to greater amount of accumulation of electrical charges there by increasing the supercapacitance of the

material as quantum capacitance is directly proportional to the DOS around the Fermi level (Chen et al., 2017; Song et al., 2018).

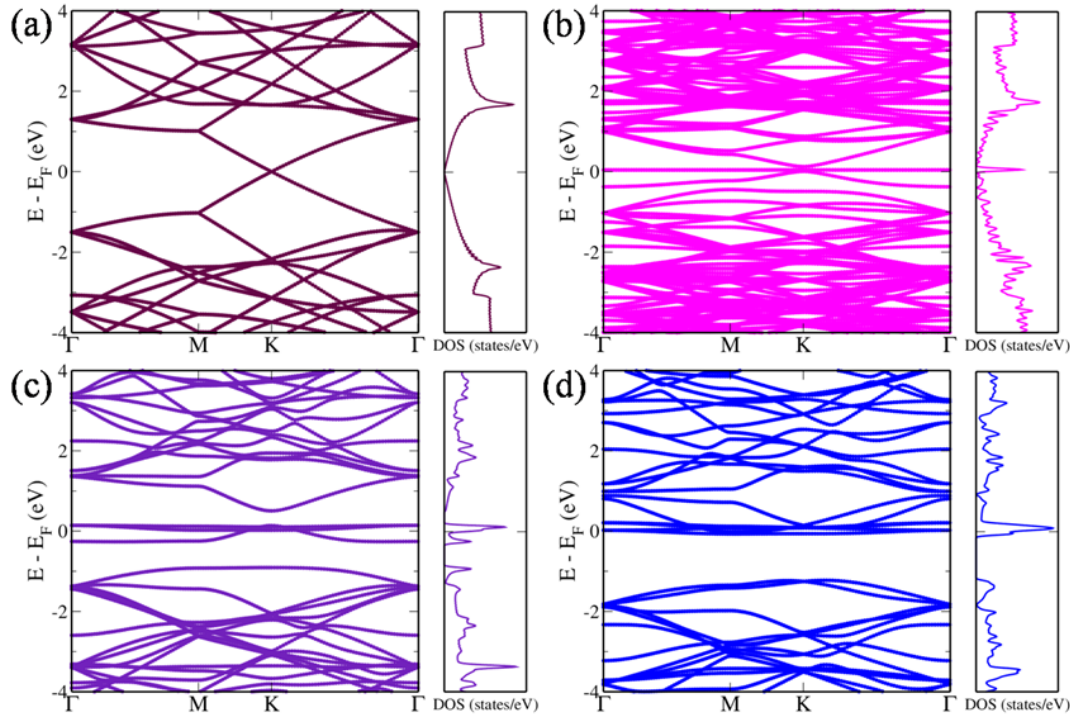


Figure 2.8 Electronic structure and DOS of (a) Pristine graphene, (b) $10 \times 10 \times 1$ supercell of porous graphene with a single pore, (c) $5 \times 5 \times 1$ supercell of porous graphene with a single pore and (d) $5 \times 5 \times 1$ supercell of porous graphene with double pores. The energies are shifted with respect to Fermi level which is set to zero.

The electronic structure of a $5 \times 5 \times 1$ supercell with a single pore reveals opening of the band gap with the mid gap defect level with a width of 0.399 eV, appearing 0.644 eV ($K \rightarrow M-\delta'$) above the VBM and 0.369 eV below the CBM (at K point). This appears as an asymmetric peak in the DOS plot (Figure 2.8c). When the number of pores is further increased to 2 per sheet, the mid gap defect level disappears and the bands introduced by the carbon atoms closer to the missing carbon atom appears just beneath the CBM overlapping with it (Figure 2.8d). An indirect band gap ($K+\delta \rightarrow M$) of 1.156 eV is observed. The abundant states near the Fermi

level and widened band gap increases the capacitance of the PG sheet improving its supercapacitor performance.

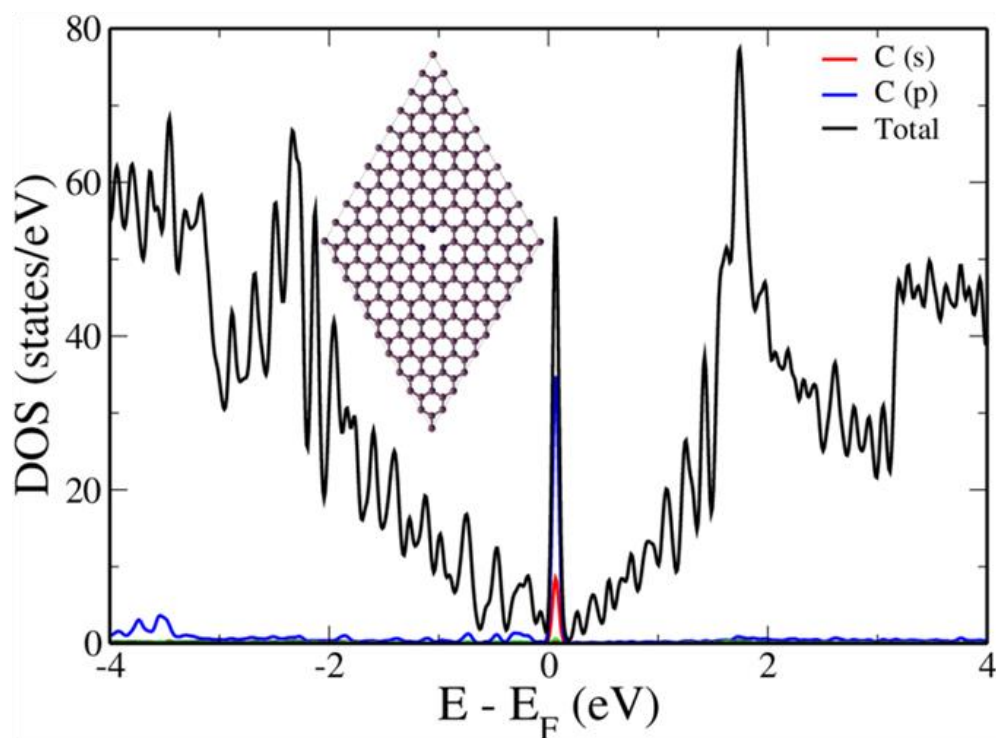


Figure 2.9 DOS of $10 \times 10 \times 1$ porous graphene sheet with a single pore. The contributions projected are from the three carbon atoms in the close vicinity of missing carbon atom (shown in darker color in crystal structure). The vacant spot depicts the missing carbon atom creating the pore.

To study the effect of pore size, the electronic structure and DOS of pristine graphene (structure I), PG with single carbon atom vacancy (structure II) and PG with two carbon atom vacancies (structure III) were compared (Figure 2.10 and 2.11). The electronic structure of PG reveals that VB and CB edges which were touching each other in the case of pristine graphene now move apart creating a gap (Figure 2.10). The carbon atoms surrounding the pore form a defect level in between the VB and CB (Figure 2.11). The prominent peak appearing at the Fermi level is contributed by the nearest C atoms (shown in blue) surrounding the vacancy defect with major contributions from C ‘p’ orbitals and minor contributions from ‘s’ orbitals (Figure

2.12). The smaller peak arises due to the contributions from states of C atom shown in grey. Larger DOS near the Fermi level amounts to higher electrical charge accumulation which in turn increases the capacitance value.

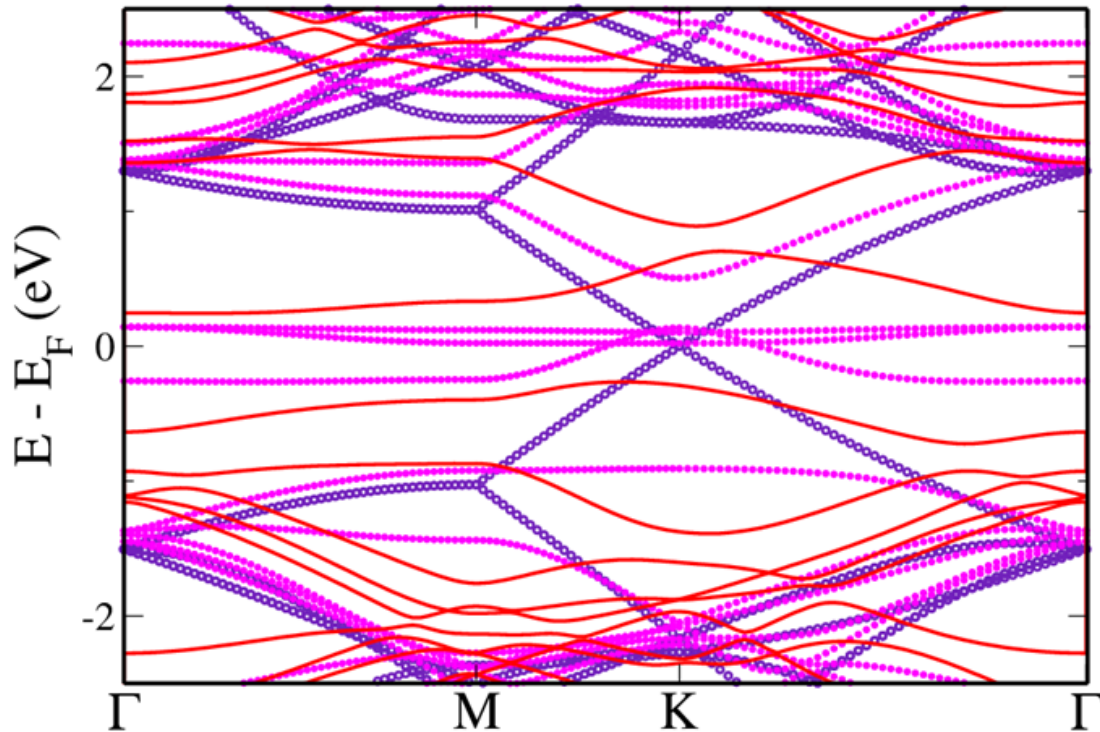


Figure 2.10 Electronic structure of defect free graphene (violet), porous graphene with single C vacancy (magenta), PG with two C vacancies (red).

When the pore size is increased by removing two nearby carbon atoms (structure: III) it was seen the appearance of humps on either side of Fermi level due to two defect level arising on either side. The electronic structure shows a dip formation near the K point by the topmost VB states while the bottommost CB moves further up effectively increasing the band gap (Figure 2.10). The formation of pore increases the surface area of the graphene sheets and facilitates better adsorption and migration of charges and thereby further enhancing the double layer capacitance. In addition to this, the tuning of electronic structure with increase in DOS near Fermi level brings about an increase in the quantum capacitance thus improving the overall supercapacitance performance.

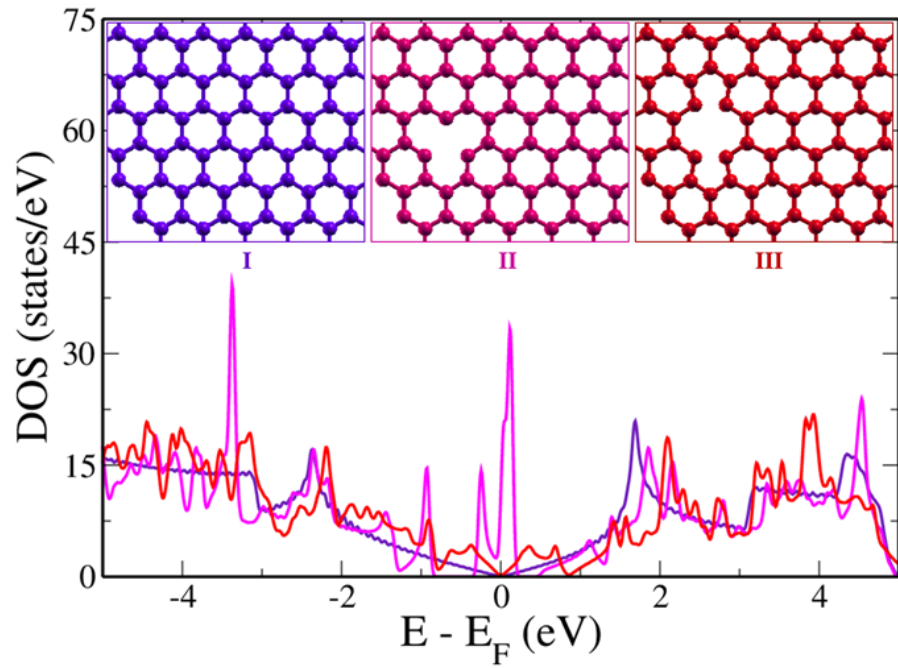


Figure 2.11 DOS plot of defect free graphene (I), porous graphene with single C vacancy (II) and two C vacancies (III). The graph is color coded.

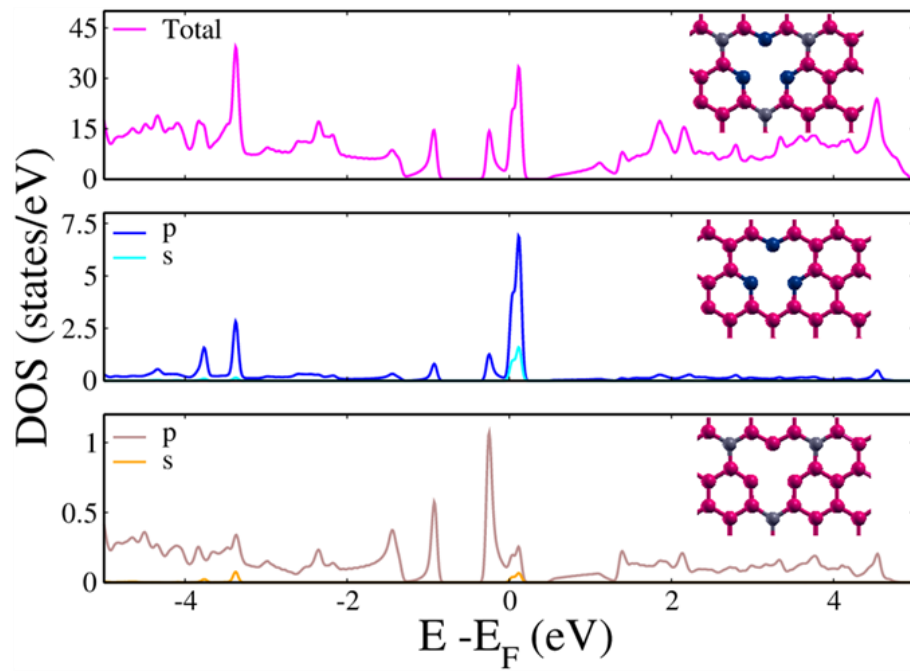


Figure 2.12 DOS plot of porous graphene with single C vacancy. Contributions from single C atom surrounding the pore is shown with color coding.

2.3.4 Electrochemical Study of PG as an Electrode

The electrochemical performance of the PG 28 sample was studied by a conventional 3 electrode method by using 2 M KOH as electrolyte employing CV, GCD and EIS. The electrochemical characterization was done in both negative and positive potential range. Figure 2.13(a) shows the CV curves at scan rates ranging from 5 to 200 mV s⁻¹ in the potential range -0.6 V to 0.2 V. The obtained CV curves are nearly rectangular in shape suggesting the EDLC behavior of the sample. The calculated specific capacitance values following equation (2.1, for n = 1) are 484, 473, 412, 356, 267, 156 and 85 F g⁻¹ for the scan rates 5, 10, 20, 30, 50, 100 and 200 mV s⁻¹, respectively.

The GCD curves at different current densities ranging from 1-6 A g⁻¹ are shown in Figure 2.13(b). The symmetrical nature of charge-discharge curves is suggestive of the good electrochemical trait of the material. The calculated specific capacitance values from the GCD data as per equation (2.2, for n = 1) are 437, 380, 326, 250, 232, 220, 158 and 128 F g⁻¹ for the current densities of 1, 1.5, 2, 2.5, 3, 4, 5 and 6 A g⁻¹, respectively. The calculated coulombic efficiency η (%) from the current densities of 1-6 A g⁻¹ is more than 95% suggesting the good charge-discharge profile of the electrode material.

The Nyquist plot of the PG 28 sample is displayed in Figure 2.13(c). The high frequency region is shown as an inset displaying the lower arc part of the plot. The very small semicircle at high frequency region and flat tail parallel to the Y-axis in the low frequency region are characteristic of good capacitive property of the material. The obtained Nyquist plot is best fitted by using Randle's circuit through ZSimpWin 3.21 computer controlled software and the fitted data with the corresponding equivalent circuit is presented in inset of Figure 2.13(c). In the fitted equivalent circuit, the double layer capacitance (C_{dl}) along with the charge-transfer resistance (R_{ct}) is in series connection with the solution resistance (R_s). The line making a 45° angle in the low frequency region is known as the Warburg impedance (W). The W is connected in series with the R_{ct} . The vertical line in the low frequency which is nearly

parallel to the imaginary axis (Z'' axis) deviates from its ideal capacitive nature due to the parallel connection of leakage current (R_L) with the constant phase element (Q_L) (Barzegar et al., 2016b).

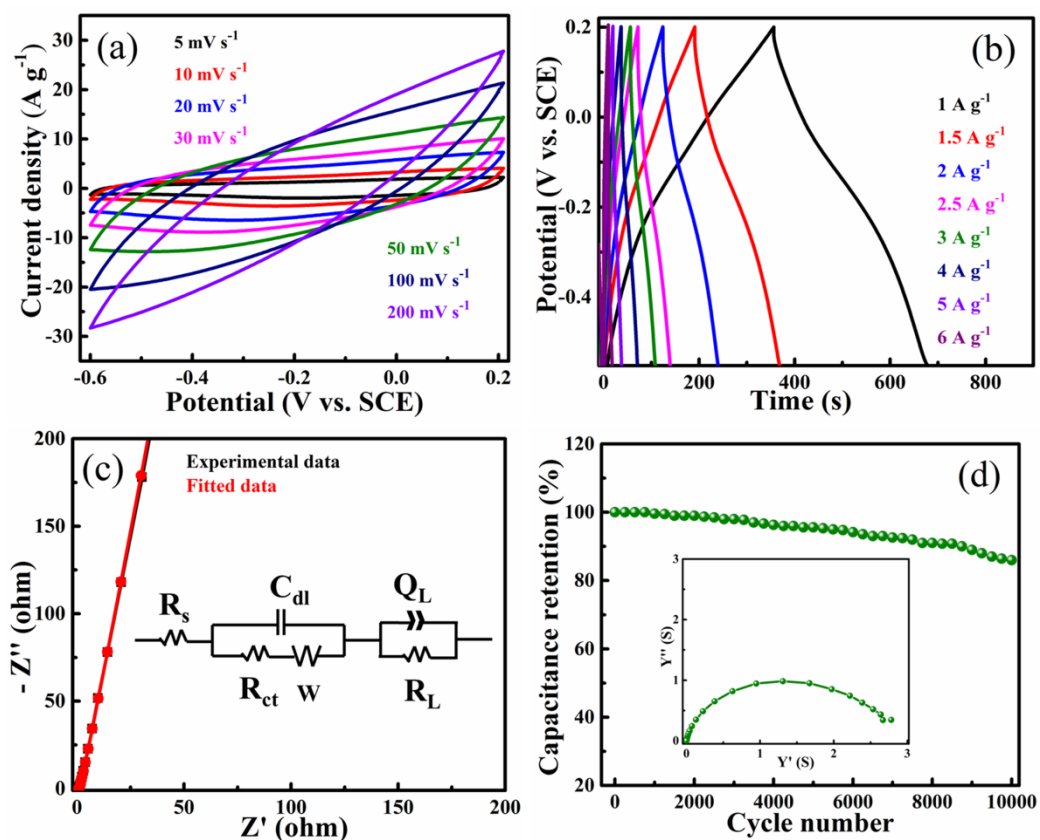


Figure 2.13 Electrochemical results of PG 28 in the negative potential range. (a) CV curves at various scan rates, (b) GCD curves at various current densities, (c) Nyquist plot: high frequency region and fitted equivalent circuit as insets and (d) Cyclic stability test at a scan rate of 100 mV s^{-1} for 10000 cycles.

The admittance plot for PG 28 is shown in the inset of Figure 2.13(d). From the admittance plots, the time constant (τ_o) value can be obtained using equation (2.14) by knowing the knee frequency values (f_o).

$$\tau_o = f_o^{-1} \quad (2.14)$$

From the knee frequency value, the relaxation time constant can be obtained. Above the knee frequency, the capacitor would be resistive in nature. Hence, the capacitor would be more useful below this knee frequency. The calculated knee frequency for the present material is 25.1 kHz and the corresponding time constant value is 39.8 μs . The result indicates that the material would be an efficient capacitor for a good range of frequency. The cyclic stability study is an important parameter for practical application of the supercapacitor. Hence, it was done for 10000 cycles at a constant scan rate of 100 mV s^{-1} in Figure 2.13(d). The test showed retention of 87% of the initial capacitance value even after 10000 cycles, suggesting the good stability of the material. The good performance executed by the material was mainly attributed to the porous nature of the sample. Further, the material exhibited a maximum energy density of 34.2 Wh kg^{-1} and a maximum power density of 2400.0 W kg^{-1} in the studied range of current density and is displayed in Table 2.3.

The electrochemical analysis of PG 28 sample in the positive potential range of 0 V - 0.5 V is shown in Figure 2.14. The CV curves at various scan rates ranging from 5 to 50 mV s^{-1} is displayed in Figure 2.14(a). It is evident from the nature of the CV curves that they show pseudocapacitive trait in the positive potential. The pair of redox peaks observed here is due to the presence of oxygen functionalities present in the PG sample as it is not completely reduced. They show redox reactivity in the positive potential range. Such results have also been reported in the literature (Deng et al., 2018; Oyedotun et al., 2017). Oyedotun et al., 2017 reported such kind of CV pattern for carbon nanorods in the positive potential range of 0 to 0.4 V. The calculated specific capacitance values for the PG 28 material are 666, 581, 556, 542 and 457 F g^{-1} at the scan rates of 5, 10, 20, 30 and 50 mV s^{-1} , respectively.

The GCD curves at different current densities ranging from 2 to 12 A g^{-1} are presented in Figure 2.14(b). The charge-discharge curves are also showing pseudocapacitive characteristics like that in the CV curves. The calculated specific capacitance values from the GCD data are 567, 501, 480, 427, 232, 392 and 373 F g^{-1} for the current densities of 2, 3, 4, 6, 8 and 12 A g^{-1} , respectively. The obtained coulombic efficiency η (%) value is more than 95% for the applied current density

range from 2-12 A g⁻¹ which is corroborating the good charge-discharge profile of the electrode material. The calculated maximum energy density and maximum power density of the material from this GCD data in the studied range of current density are 15.9 Wh kg⁻¹ and 2569.2 W kg⁻¹, respectively and is presented in Table 2.4.

Table 2.3 Energy density, power density and specific capacity values of PG 28 in a 3-electrode system in negative potential (-0.6 V to 0.2 V).

Current density (A g ⁻¹)	Energy density (Wh kg ⁻¹)	Power density (W kg ⁻¹)	Q _s (C g ⁻¹)
1	34.2	375.4	349.6
1.5	29.7	574.6	303.9
2	25.4	750.2	260.8
2.5	19.5	937.5	200.0
3	18.2	1125.0	185.4
4	17.2	1546.9	176.0
5	12.3	1932.0	126.4
6	10.0	2400.0	102.4

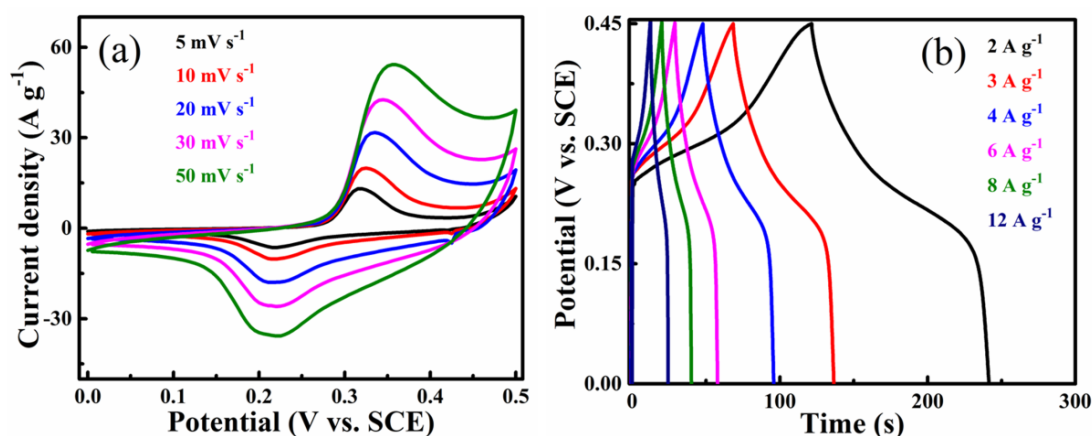


Figure 2.14 Electrochemical results of PG 28 in positive potential range (0 to 0.5 V). (a) CV curves at various scan rates and (b) GCD curves at various current densities.

Table 2.4 Energy density, power density and specific capacity values in positive potential (0 V to 0.5 V) window at various current density.

Current density (A g⁻¹)	Energy density (Wh kg⁻¹)	Power density (W kg⁻¹)	Q_s (C g⁻¹)
2	15.9	463.0	283.5
3	14.1	714.4	255.9
4	13.5	972.0	240.0
6	12.0	1441.1	213.5
8	11.0	1748.5	196.0
12	10.5	2569.2	186.0

Further, to evaluate the contribution of the blank electrode to the specific capacitance value of the material in both negative and positive potential windows, CV analysis for blank electrode and the blank electrode coated with the active material is carried out (Figure 2.15). The results very clearly demonstrate that the contribution from the blank electrode in both the potential windows is negligible.

To find the C_{EDL} and C_P in the PG 28 sample, equation 2.8 is used. It is known that the total capacitance is the sum of the double layer capacitance contribution (which occurs due to physisorption of electrolyte ions on to the surface of the electrode) and pseudocapacitance contribution (which is due to faradaic reactions/diffusion of electrolyte ions inside bulk of the material), respectively. It is well known that, when the scan rate tends to infinity ($v^{-1/2} \rightarrow 0$) the specific capacitance is due to the contribution from double layer capacitance and at low scan rates the contribution from the bulk dominates. The specific capacitance varies linearly with respect to $v^{-1/2}$ at lower scan rates and at higher scan rates the linearity is deviated due to the improper utilization of electroactive sites. Further, to obtain the capacitance contribution graphical method was employed and the cumulated capacitance graphs are sketched by considering the specific capacitance values in the y-axis and inverse square root of the scan rate in the x-axis as shown in the Figure 2.18.

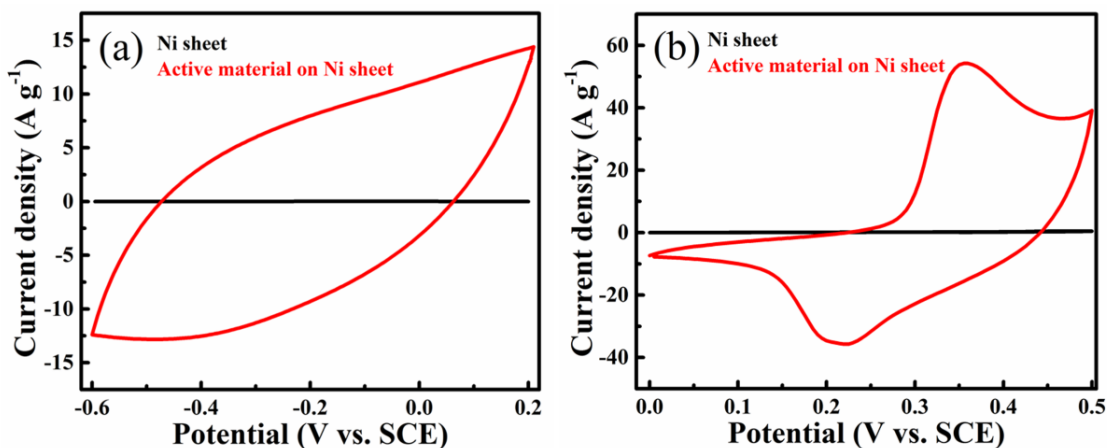


Figure 2.15 CVs of bare Ni sheet and PG 28 coated Ni sheet in (a) Negative and (b) Positive potential windows at a constant scan rate of 50 mV s^{-1} .

It is known that, as the scan rate tends to infinity, the C_{EDL} contribution dominates and the C_{P} contribution dominates at lower scan rates. In order to find out the C_{EDL} and C_{P} contributions the lower scan rate points are considered and linearly fitted and higher scan rate points are excluded owing to the deviation from the linearity (may be due to the nonexistence of electroactive sites for electrochemical reaction). The intercept was obtained by extrapolating the fitted curve towards the y-axis, which provides the C_{EDL} contribution and subtracting this C_{EDL} contribution from the total contribution $C_{\text{S}}(T)$ gives the C_{P} . The calculated C_{EDL} and C_{P} contribution of PG 28 sample in the negative potential range is 88.8% and 11.2%, respectively and in the positive potential range is 69.1% and 30.9%, respectively.

2.3.5 Electrochemical Study of Fabricated Supercapacitor Using PG Electrodes

The electrochemical performance of the fabricated symmetrical supercapacitor employing PG 28 electrodes is presented in Figure 2.16. The CV curves at various scan rates ranging from 5 to 200 mV s^{-1} are displayed in Figure 2.16(a). The obtained CV curves are nearly rectangular in shape suggesting the EDLC behavior of the sample. The calculated specific capacitance values by using equation 2.1 (for $n = 2$) are 297, 259, 207, 179, 145, 122 and 73 F g^{-1} for the scan rates 5, 10, 20, 30, 50, 100 and 200 mV s^{-1} , respectively. In order to check the effect of carbon paper on the

capacitance performance, the CV curves of carbon paper and supercapacitor device at a constant scan rate of 100 mV s^{-1} are compared (Figure 2.17). It is evident that the current collecting ability of the carbon paper is very poor as compared to the device.

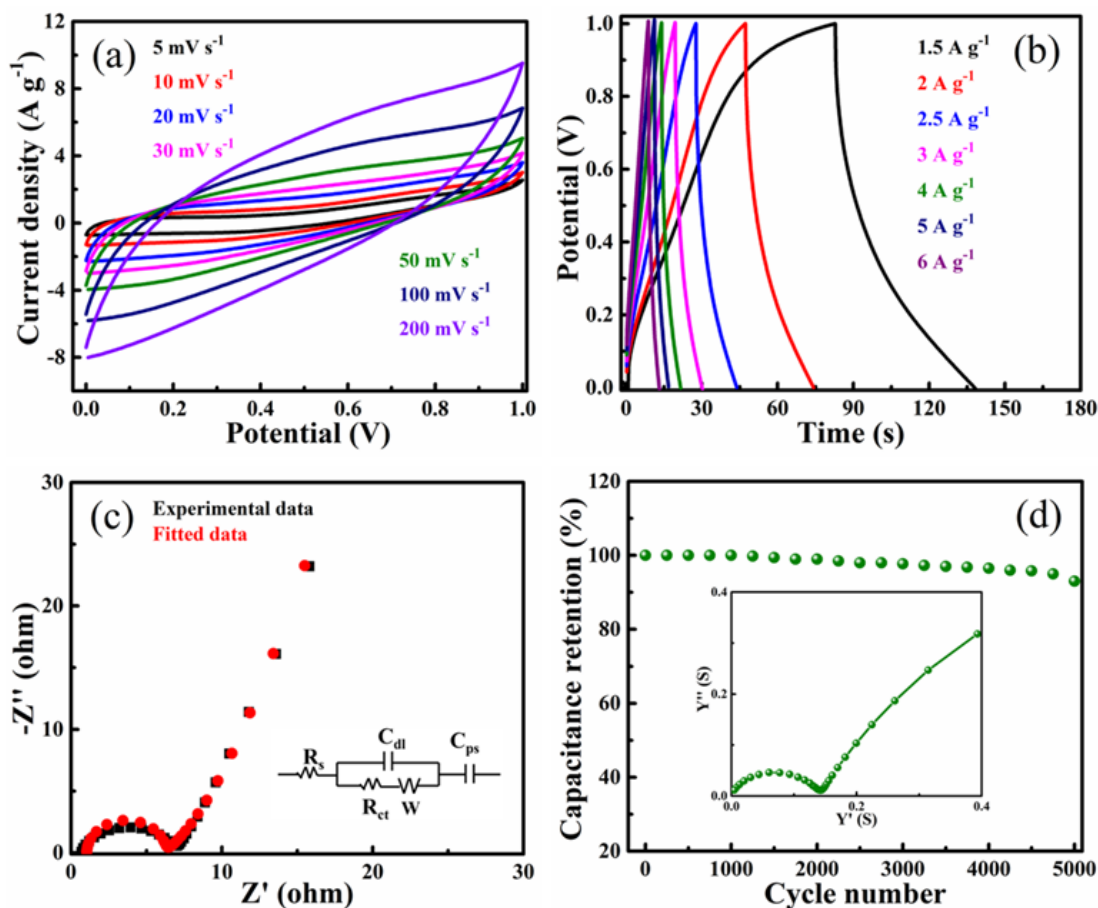


Figure 2.16 Electrochemical results of symmetrical supercapacitor fabricated from PG 28 electrodes. (a) CV curves at various scan rates, (b) GCD curves at various current densities, (c) Nyquist plot inset: equivalent circuit and (d) Cyclic stability test at a scan rate of 100 mV s^{-1} for 5000 cycles.

GCD curves at different current densities ranging from 1.5 to 6 A g^{-1} is shown in Figure 2.16(b). The near symmetrical charge-discharge curves are an indication of good electrochemical performance of the material. The calculated specific capacitance values employing equation 2.2 (for $n = 2$) are 189, 121, 110, 80, 77, 70 and 61 F g^{-1} for the current densities of 1.5, 2, 2.5, 3, 4, 5 and 6 A g^{-1} , respectively. The computed

coulombic efficiency η (%) for the charge-discharge curves at various current densities (1.5-6 A g⁻¹) were found more than 95% for the utilized current density.

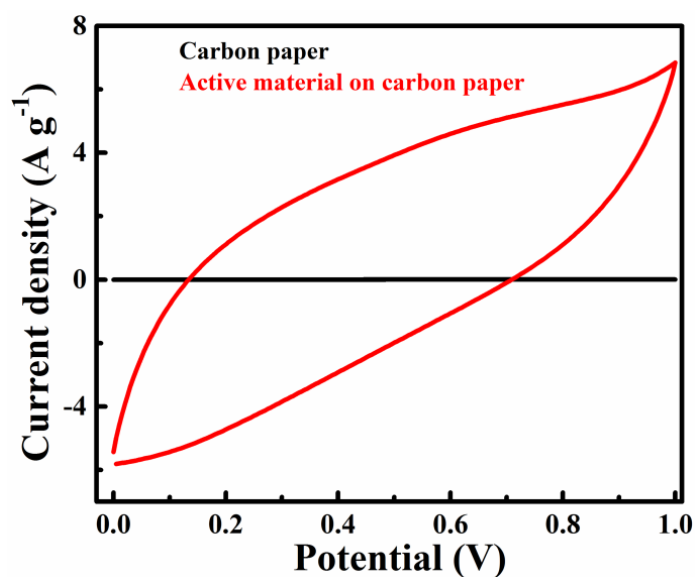


Figure 2.17 CV curves of carbon paper and PG 28 coated carbon paper at a scan rate of 100 mV s⁻¹.

Table 2.5 Energy density, power density and specific capacity values of the fabricated symmetrical supercapacitor.

Current density (A g ⁻¹)	Energy density (Wh kg ⁻¹)	Power density (W kg ⁻¹)	Q _s (C g ⁻¹)
1.5	26.3	1502.8	189
2	16.8	2016.7	121
2.5	15.3	2503.6	110
3	11.1	3078.0	80
4	10.7	3850.0	77
5	9.7	5000.0	70
6	8.5	6120.0	61

The calculated maximum energy density and maximum power density of the material from this GCD data in the studied range of current density are 26.3 Wh kg^{-1} and 6120.0 W kg^{-1} , respectively (Table 2.5). The obtained Nyquist plot with fitted data is presented in Figure 2.16(c). The high frequency region shows a semicircle and an inclined line in the low frequency region. The lower radius of the semicircle depicts the low resistance and high capacitive nature of the PG 28 active material. The inset in Figure 2.16(c) shows the fitted equivalent circuit determined according to the Randles equivalent circuit fitting method (Sahoo et al., 2017). The intercept at the real part (Z') on x-axis refers to the R_s of 0.5 ohm which mainly consists of resistance of the electrolyte solution, the contact resistance between active materials and current collectors. The diameter of the semicircle in the real part (Z') on x-axis depicts the R_{ct} of 6.9 ohm and the smaller diameter of the semicircle indicates the lesser resistance value of PG 28 sample, consistent with the CV and GCD results. The R_{ct} and C_{dl} of the supercapacitor is shown by the arc in the high frequency region. W is generated owing to the diffusion/transport of OH^- ions into the electroactive material.

The fabricated supercapacitor is tested for its stability by cycling tests at a scan rate of 100 mV s^{-1} and is presented in Figure 2.16(d). It is evident from the figure that the supercapacitor has retained 93% of the initial capacitance value even after 5000 cycles, indicating a fairly high stability of the material. The good performance executed by the material is mainly attributed to the porous nature of the sample. The specific capacitance values of PG 28 material was compared with those of the recently reported literatures and are presented in Table 2.6. It was seen from the table that our material exhibits highest capacitance amongst all other materials and it also has a merit of being synthesized using an eco-friendly and facile method. The calculated time constant plot from the admittance plot was found to be $3980 \mu\text{s}$. The specific capacity values for the symmetrical supercapacitor device were calculated by following equation 2.6 and are presented in Table 2.5. Further, the calculated C_{EDL} and C_P contribution of PG 28 sample in fabricated device is found to be 57.4% and 42.6 %, respectively (Figure 2.19).

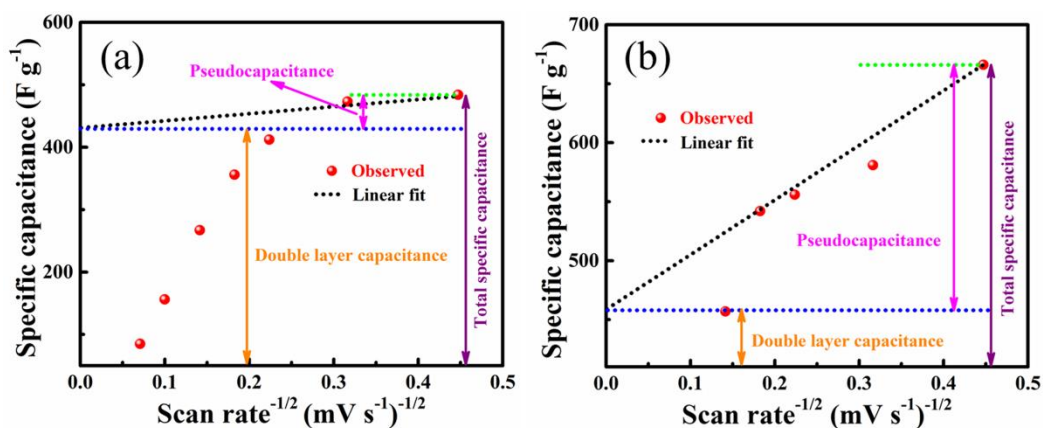


Figure 2.18 Determination of the C_{EDL} and C_P contribution of PG 28 in (a) Negative and (b) Positive potential window.

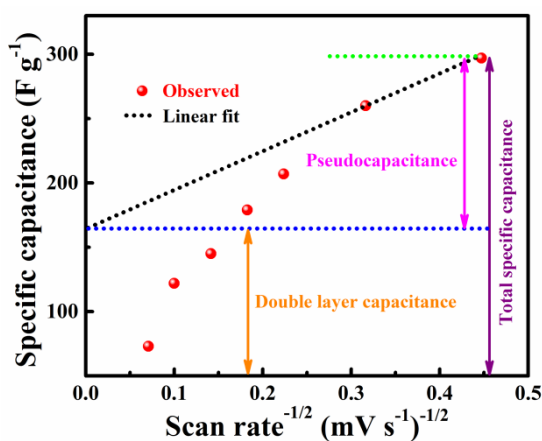


Figure 2.19 Determination of the C_{EDL} and C_P contribution of PG 28 in a symmetrical supercapacitor device.

Table 2.6 Comparison of capacitance values of PG 28 from earlier reports and present work.

Electrode material	C_s ($F g^{-1}$)	Electrolyte	Cyclic stability	References
Holey graphene aerogel through hydrothermal method	316 @ 1 A g^{-1}	6 M KOH	98% after 1000 cycles @ 20 $mV s^{-1}$	Bai et al. (2019)

3D holey graphene through hydrothermal method	141 @ 0.5 A g ⁻¹	1 M Na ₂ SO ₄	---	Chai et al. (2019)
3D RGH/Carbon dot composites by hydrothermal method	264 @ 1 A g ⁻¹	1 M H ₂ SO ₄ -PVA	91% after 5000 cycles @ 5 A g ⁻¹	Feng et al. (2018)
3D graphene aerogel through hydrothermal method	111 @ 1 A g ⁻¹	6 M KOH	---	Ghosh et al. (2018a)
Winged graphene nanofibres through microwave approach	60 @ 2 mV s ⁻¹	1 M Na ₂ SO ₄	---	Gong et al. (2014)
Graphene like foam through glucose blowing approach	147 @ 1 A g ⁻¹	6 M KOH	---	He et al. (2020)
PG network through hydrothermal method	338 @ 1 A g ⁻¹	1 M H ₂ SO ₄	100% after 10000 cycles @ 1 A g ⁻¹	Hwang et al. (2020)
PG through microwave method	133 @ 1 A g ⁻¹	6 M KOH	---	Kang et al. (2019)
3D graphene hydrogel through hydrothermal method	246 @ 1 A g ⁻¹	1 M H ₂ SO ₄	94% after 20000 cycles @ 2 A g ⁻¹	Liu et al. (2018)
3D graphene hydrogel through hydrothermal method	113 @ 0.5 A g ⁻¹	1 M Na ₂ SO ₄	83% after 1000 cycles @ 5 A g ⁻¹	Meng et al. (2018)
Flexible RGO foam by hydrazine reduction	110 @ 0.5 A g ⁻¹	1 M H ₂ SO ₄	---	Niu et al. (2012)
Graphene paper through	196 @ 1 mV s ⁻¹	1 M H ₂ SO ₄	93% after 10000 cycles	Sadak et al. (2018)

electrochemical exfoliation			@ 4 A g ⁻¹	
Activated carbon/MoS ₂ composite by hydrothermal method	251 @ 2 mV s ⁻¹	1 M Na ₂ SO ₄	88% after 5000 cycles @ 20 mV s ⁻¹	Sangeetha et al. (2018)
Flexible graphene paper pillared by carbon black by vacuum filtration method	138 @ 10 mV s ⁻¹	6 M KOH	96% after 2000 cycles @ 10 A g ⁻¹	Wang et al. (2012)
Holey graphene aerogel by solvothermal method	178 @ 0.2 A g ⁻¹	6 M KOH	---	Zang et al. (2016)
PG sheets by solvothermal method	666 (+ ve potential) 484 (- ve potential) @ 5 mV s ⁻¹	2 M KOH	87% after 10000 cycles @ 100 mV s ⁻¹	Present work

2.4 CONCLUSIONS

In summary, a greener approach for the synthesis of PG samples without addition of any toxic reducing agents and employing a 1:1 binary mixture of ethylene glycol and water as solvent in a solvothermal approach is reported. Morphological analysis revealed the formation of porous structure on the surface of the sheets. Among the synthesized PG samples, PG 28 showed a high surface area of 420 m² g⁻¹ with mesoporous structure and mean pore diameter of 3.4 nm according to BET analysis. The DFT calculations showed that the introduction of defects in the form of pores led to the increase in the DOS near the Fermi level due to introduction of 2p states of the carbon atoms in the close vicinity of the vacancy defects leading to the increase in the capacitance value. The PG 28 sample exhibited an impressive high

capacitance value of 666 F g^{-1} at a scan rate of 5 mV s^{-1} in the positive potential range of $0 - 0.5 \text{ V}$. The symmetrical supercapacitor fabricated using the PG 28 electrodes retained 93% of its initial capacitance value even after 5000 cycles of charge-discharge process and exhibited a maximum energy density of 26.3 Wh kg^{-1} and maximum power density of 6120.0 W kg^{-1} in the studied current density range. The impressive result shown by the material is mainly due to the high surface area of the sample with hierarchical porous structure which not only provided the open channels but also provided the conductive path for the efficient charge storage and transport of ions.



CHAPTER 3

***SOLVOTHERMAL SYNTHESIS OF NiO
NANOFLAKES FOR SUPERCAPACITOR
APPLICATION***

Chapter 3 describes the synthesis of NiO nanoflakes through a solvothermal approach and its thorough diffraction, microscopic, spectroscopic and surface area characterization. The electrochemical analysis of the NiO electrode material is studied and reported here in detail.

3.1 INTRODUCTION

Advancement in the field of science and technology has led to increase in the consumption of energy as well as increased quest for renewable sources of energy and materials for energy conversion and storage like thermoelectrics, fuel cells, batteries and supercapacitors (Bhat et al., 2020; Fang et al., 2020; Shenoy et al., 2020; Tian et al., 2020; Wu et al., 2020). The transition metal oxides are considered suitable electrode materials for supercapacitors owing to their high abundance, low cost, high electrical conductivity and resistance to corrosion. Oxides of Ni are particularly interesting due to the multiple oxidation states exhibited by Ni. In this context, NiO has gained considerable attention as an electrode material for supercapacitors due to high theoretical capacitance, low cost, thermal and chemical stability (Ahmed et al., 2019; Li et al., 2018; Lv et al., 2018; Mondal et al., 2018; Sannasi et al., 2020; Wang et al., 2019; Yang et al., 2014; Yus et al., 2019).

Various NiO nanostructures (nanoparticles, nanoplatelets, nanocubes and nanosheets) are synthesized by employing hydrothermal, sonochemical and precipitation method followed by calcination in air. The NiO nanomaterials previously reported have displayed capacitance values in the range from 47.6 to 720 F g⁻¹ (Ahmed et al., 2019; Li et al., 2018; Lv et al., 2018; Mondal et al., 2018; Sannasi et al., 2020; Wang et al., 2019; Yang et al., 2014; Yus et al., 2019). But the thorough literature survey points out that, very few reports are available for the synthesis of NiO nanoflakes and most of this use only water as a solvent. Mixture of solvents has not been reported so far for the synthesis of nanoflake. The synthesized nanoflakes by microwave, hydrothermal and co-precipitation method by using water as a solvent have depicted capacitance values in the range from 120–720 F g⁻¹ (Goel et al., 2018; Lv et al., 2018; Mondal et al., 2018; Sannasi et al., 2020). The observed high

capacitance value for the NiO nanoflakes was due to the use of high concentration (6 M) KOH as an electrolyte and Ni foam as a conducting substrate, respectively. Also in the reported literature the cyclic stability study is not so impressive and is studied at lower current densities which are not suitable for the commercial applications.

3.2 EXPERIMENTAL SECTION

The solvothermal method is an easy, low cost method, where the desired nanostructures can be synthesized by minimal energy consumption. For the synthesis of NiO nanoflakes, first 0.95 g of NiCl₂.6H₂O was added to a 50 mL of mixed solvent (1:1; ethylene glycol: water) system and stirred for 1 h. To this, 0.16 g of NaOH was added under stirring. After an hour, the whole reaction mixture was transferred to a teflon lined stainless steel autoclave of 100 mL capacity and heated at 160 °C for 16 h. After completion of the reaction, the autoclave was brought to room temperature and the green product was collected and washed with ethanol till the pH of the supernatant turned neutral. The green powder was dried at 80 °C overnight followed by calcination in air at 400 °C for 2 h to obtain the black NiO powder. The characterization and electrochemical studies were carried out as mentioned in chapter 2.

3.3 RESULTS AND DISCUSSION

3.3.1 Structural, Elemental and Morphological Analysis

XRD analysis was carried out to study the crystal structure and phase of the synthesized NiO nanoflakes. The XRD peaks appearing at 2θ positions of 37.2°, 43.2°, 62.8°, 75.2°, 79.4° were indexed to (111), (200), (220), (311) and (222) crystal planes of NiO respectively which is consistent with the standard JCPDS file number of 47-1049 in Figure 3.1(a) (Wang et al., 2019). The absence of impurity peaks indicated the successful formation of pure NiO. The broadening of the XRD peaks suggested the flakes could be of nano dimension. Hence, the average crystallite size was calculated by Scherer's formula ($D = 0.89\lambda/\beta \cos\theta$) and found to be 15 nm.

The Raman spectrum revealed bands at 396 cm^{-1} and 499 cm^{-1} corresponding to the first order transverse optical (TO) and longitudinal optical (LO) phonon modes of NiO (Figure 3.1b). Similarly, the peaks observed at 705 cm^{-1} and 1080 cm^{-1} corresponded to the combination of 2TO and 2LO phonon modes of NiO, respectively (Bose et al., 2016; Yang et al., 2013). The above results suggested the formation of NiO nanostructure.

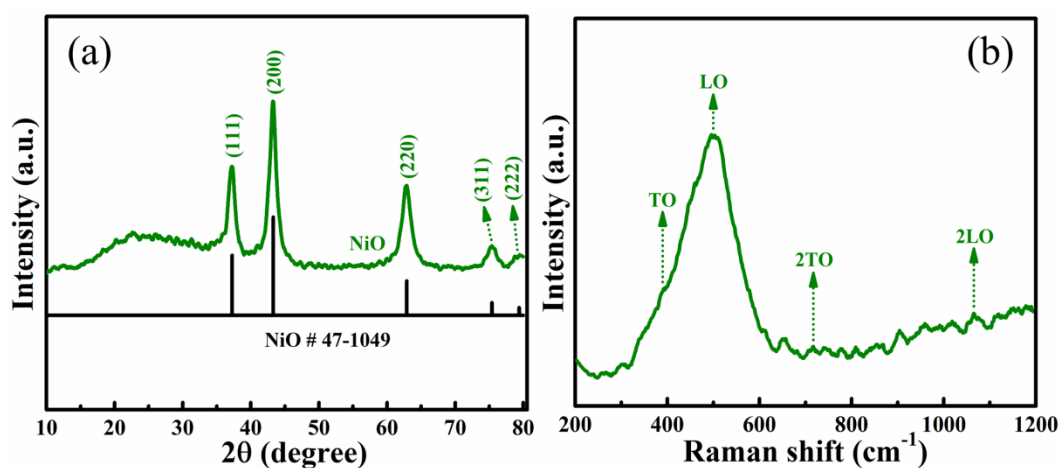


Figure 3.1 (a) XRD pattern of NiO with standard data and (b) Raman spectrum of NiO.

Figure 3.2(a) represents the FESEM image of the synthesized sample with flakes ranging in diameter from 35 to 75 nm. The EDX analysis indicates the presence of elements like Ni and O and a slight amount of C due to the carbon tape used during measurements (Figure 3.2b). The elemental mapping was carried out which showed presence of Ni and O uniformly distributed (Figure 3.2c-e). The low magnification TEM image clearly reveals the flake like structure of NiO nanoparticles (Figure 3.3a). The high resolution transmission electron microscopy (HRTEM) image showed two distinct set of planes viz. (111) and (200) with interplanar distances matching with those of XRD results (Figure 3.3b). The SAED pattern of the NiO presented as an inset of Figure 3.3(b) shows several concentric rings indicating the polycrystalline nature of the NiO sample. The indexing of the rings matches those with the XRD results.

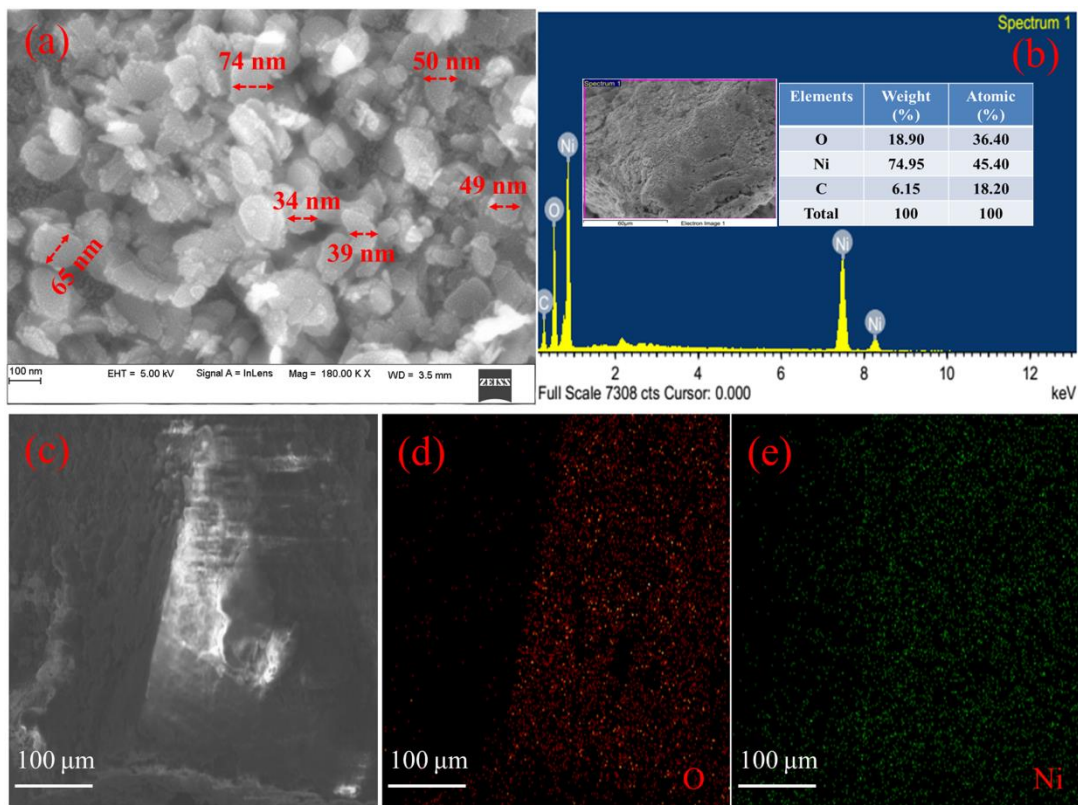


Figure 3.2 (a) FESEM image of NiO nanoflakes, (b) EDX pattern with elemental distribution profile, (c) Region of elemental mapping; elemental mapping profile of (d) O and (e) Ni.

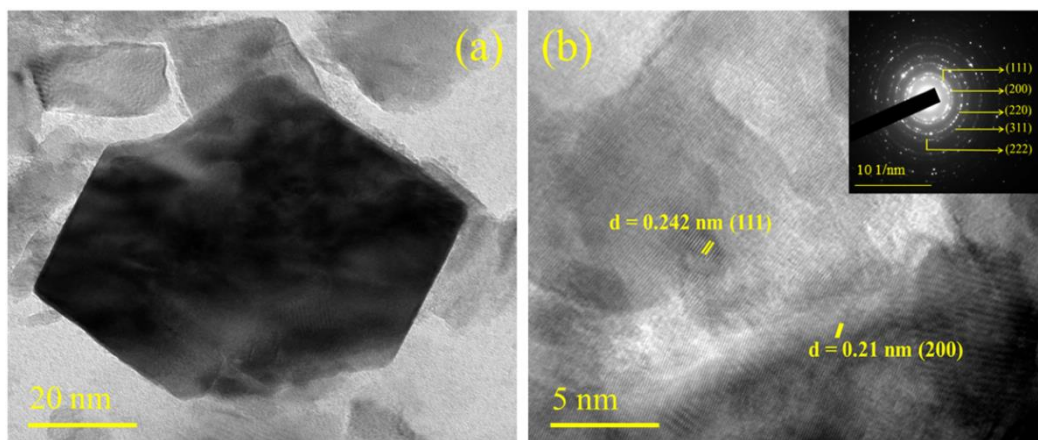


Figure 3.3 (a) TEM image of NiO nanoflake and (b) HRTEM image (SAED pattern as an inset).

The BET surface area plot of NiO nanoflakes can be categorized as type-IV isotherm with H3 hysteresis according to the IUPAC classification, as shown in Figure 3.4. The nanoflakes possessed a surface area of $35 \text{ m}^2 \text{ g}^{-1}$. The pore size distribution of the materials analysed by BJH method revealed a total pore volume of $0.086 \text{ cm}^3 \text{ g}^{-1}$ with an average pore diameter of 3.64 nm. The high surface area and mesoporous structure is believed to enhance the electrochemical properties by facilitating easier migration of ions during charging and discharging. The observed values of BET surface area of the NiO nanoflakes is higher or comparable to that obtained for NiO nanoplates ($18 \text{ m}^2 \text{ g}^{-1}$), NiO nanosheets ($12 \text{ m}^2 \text{ g}^{-1}$), NiO nanowires ($31.18 \text{ m}^2 \text{ g}^{-1}$), NiO nanostructure ($31.4 \text{ m}^2 \text{ g}^{-1}$), Co_3O_4 -NiO fish thorn like nanostructure ($5.17 \text{ m}^2 \text{ g}^{-1}$), NiO nanoplates ($28.7 \text{ m}^2 \text{ g}^{-1}$), NiO nanoparticles ($34.6 \text{ m}^2 \text{ g}^{-1}$), hexagon like NiO ($39.1 \text{ m}^2 \text{ g}^{-1}$) (Cuong et al., 2019; Hoa et al., 2018; Nguyen et al., 2018; Sancheti et al., 2018; Sekhar et al., 2018; Su et al., 2019; Voskanyan et al., 2018; Yu et al., 2019) as reported previously.

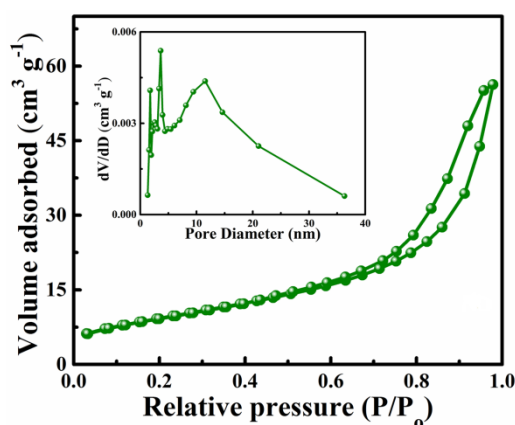


Figure 3.4 BET surface area of NiO (pore size distribution plot as an inset).

3.3.2 Electrochemical Study of NiO as an Electrode

The electrochemical performance of NiO electrode was studied by using CV, GCD and EIS analysis in a 3-electrode method by using 2 M KOH as an electrolyte. The CV curves of the NiO electrode in the potential range of 0-0.5 V at scan rates from 5-50 mV s^{-1} shows a pair of redox peaks indicating the faradic nature of the

material (Figure 3.5a). The calculated specific capacitance values were 305, 230, 163, 151 and 111 F g⁻¹ for the scan rates from 5 to 50 mV s⁻¹. The GCD curves for NiO electrode material measured at variable current densities in the range of 1-12 A g⁻¹ at a fixed potential window of 0-0.45 V depicted nearly symmetrical GCD curves with faradic nature (Figure 3.5b). The measured capacitance values were 190, 173, 147, 138, 126, 120 and 112 F g⁻¹ for the current densities ranging from 1-12 A g⁻¹.

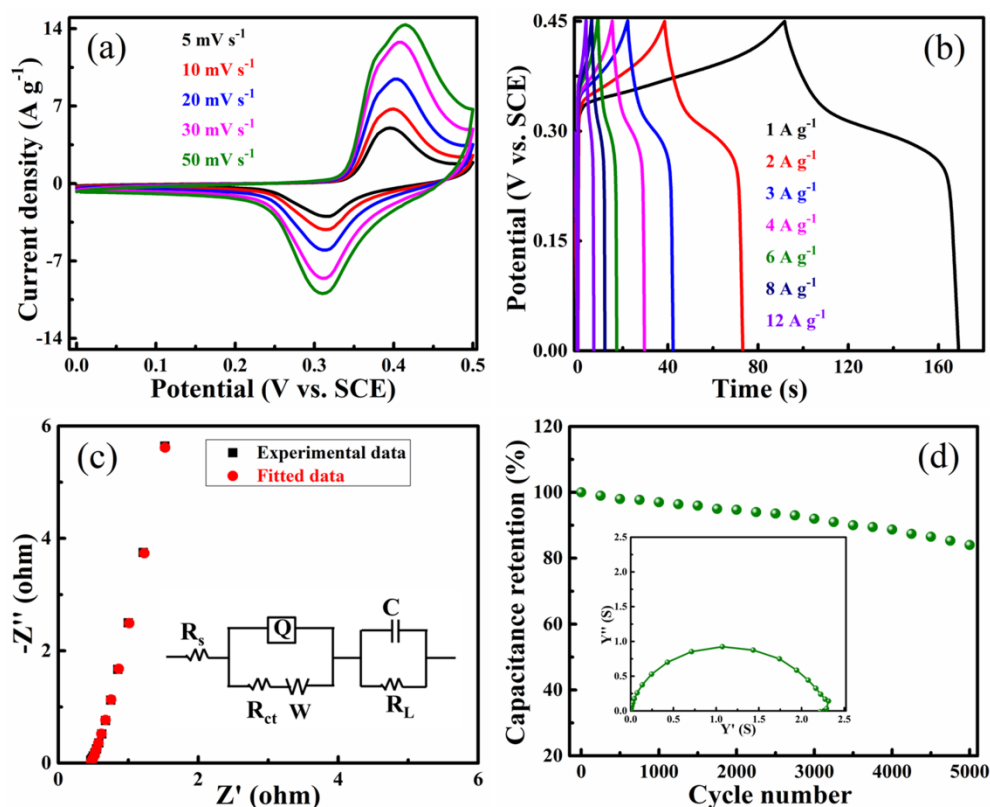


Figure 3.5 Electrochemical analysis of NiO in a 3-electrode system. (a) CV curves, (b) GCD curves, (c) Nyquist plot (fitted equivalent circuit as an inset) and (d) Cyclic stability data of NiO for 5000 cycles at a current density of 8 A g⁻¹ (inset shows the admittance plot of NiO electrode).

The comparison of the obtained capacitance values of NiO electrode with other reported NiO materials given in Table 3.1 reveals the success of the utilized synthetic technique in enhancing the performance of NiO which can be attributed to the mesoporous structure of the material which facilitates the ion transport and

reasonable occupation of the DOS near the Fermi level as indicated by the DFT calculations leading to increased quantum capacitance (Sethi et al., 2019b).

It can be seen from the CV and GCD study, as the scan rate/current density increases the capacitance value decreases. This phenomenon can be explained based on the equilibration time, as the scan rate increases there is very less time for the electrode material to store charge as the electrolyte interacts only on the surface of the electrode material whereas at low scan rate/current density the electrolyte ions can percolate inside the porous electrode due to longer duration available leading to the increase in the capacitance value (Dupont et al., 2016). The measured coulombic efficiency η (%) is more than 95% for the charge-discharge curves of NiO electrode material, which suggests good stability. The measured energy density, power density and specific capacity values for the electrode material are presented in Table 3.2.

Table 3.1 Comparison of electrochemical performance of NiO electrode with previously reported literatures.

Electrode material	C_s from CV ($F g^{-1}$)	C_s from GCD ($F g^{-1}$)	Electrolyte and substrate	Cyclic stability	References
NiO nanoparticles	47 @ 10 $mV s^{-1}$	---	3 M KOH ---	---	Ahmad et al. (2019)
NiO nanoparticles	---	112 $C g^{-1}$ @ 1 $A g^{-1}$	2 M KOH Ni foam	> 95% after 10000 cycles @ 3 $A g^{-1}$	Edison et al. (2018)
NiO nanoflakes	308 @ 5 $mV s^{-1}$	307 @ 0.5 $mV s^{-1}$	6 M KOH graphite plate	96% after 3000 cycles @ 2 $A g^{-1}$	Goel et al. (2018)
NiO thin film	674 @ 5 $mV s^{-1}$	672 @ 0.5 $mA cm^{-2}$	2 M KOH Thin film	72% after 2000 cycles	Gund et al. (2018)

				@ 100 mV s ⁻¹	
NiO nanopyramids	305 @ 2 mV s ⁻¹	325 @ 0.4 mA cm ⁻²	1 M KOH Stainless steel	91% after 1000 cycles @ 1 mA cm ⁻²	Kumar et al. (2017)
NiO nanosheets	---	385 @ 1 A g ⁻¹	6 M KOH Ni foam	82% after 4000 cycles @ 3 A g ⁻¹	Li et al. (2018)
NiO nanoflakes	---	720 @ 1 A g ⁻¹	2 M KOH Ni foam	> 80% after 5000 cycles @ 1 A g ⁻¹	Lv et al. (2018)
NiO nanoflakes	406 @ 2 mV s ⁻¹	224 @ 0.1 A g ⁻¹	1 M KOH Ni foam	---	Mondal et al. (2018)
NiO nanoplates	---	297 @ 2 A g ⁻¹	2 M KOH Graphite sheet	70% after 2000 cycles @ 20 A g ⁻¹	Qiu et al. (2018)
NiO nanoflakes	---	120 @ 1 A g ⁻¹	3 M HCl Ni foam	---	Sannasi et al. (2020)
NiO nanocubes	---	1012 mF cm ⁻² @ 1 mA cm ⁻²	6 M KOH Ni foam	70% after 6000 cycles @ 10 mA cm ⁻²	Sun et al. (2019)
NiO nanoplates	144 @ 2 mV s ⁻¹	250 @ 2 A g ⁻¹	1 M KOH Ni foam	---	Yus et al. (2019)
Hollow NiO nanostructures	---	580 @ 1 A g ⁻¹	6 M KOH ---	56% after 2000 cycles @ 2 A g ⁻¹	Wang et al. (2019)

Table 3.2 Energy density, power density and specific capacity values for the electrode.

Current density (A g⁻¹)	Energy density (Wh kg⁻¹)	Power density (W kg⁻¹)	Q_s (C g⁻¹)
1	5.3	225.0	85.5
2	4.8	449.8	77.8
3	4.1	674.3	66.2
4	3.9	901.1	62.1
6	3.5	1348.6	56.7
8	3.3	1773.1	54.0
12	3.1	2657.2	50.4

The Nyquist plot does not show semicircle in the high frequency region due to low R_s and R_{ct} in the electrode. The nearly flat tail parallel to the imaginary axis (Z'') in the medium low frequency region indicates the ideal capacitive behavior and faster kinetics of the electrode material (Sethi et al., 2020c). The good impedance values observed may be attributed to the mesoporous structure of NiO nanoflakes. The fitted equivalent circuit in the inset of Figure 3.5(c) represents the series connection of R_s , R_{ct} , W and Q . The vertical line in the medium low frequency which is nearly parallel to the imaginary axis is slightly deviated from the ideal capacitive nature due to the parallel connection of R_L with capacitive element (C). The obtained value of R_s is 0.48 ohm.

The stability of the electrode material was tested for 5000 cycles at a high current density of 8 A g⁻¹. The electrode was able to retain 100% capacity upto 200 cycles, after which a slight decrease in the value was observed due to the agglomeration of the nanostructures after repeated discharge cycles which restricted the passage of electrolyte ions into the porous electrode. After 5000 discharge cycles, the electrode was still able to maintain 84% of its initial value, which is higher than the reported values by various NiO nanostructures (Table 3.1). The admittance plot of NiO electrode is presented in the inset of Figure 3.5(d). The obtained knee frequency

is 3.98 kHz with a time constant (τ_o) value of 251 μ s. The obtained good capacitance value for NiO electrode is in accordance with the low time constant value (Sethi et al., 2020a; Sethi et al., 2019b).

3.3.3 Electrochemical Study of Fabricated Supercapacitor Using NiO Electrodes

The CV curves of the NiO electrodes in the potential range of 0-1 V at scan rates from 5-200 mV s^{-1} indicates that as the scan rate increases the current collecting ability of the device increases as shown in Figure 3.6(a). The calculated specific capacitance values were found to be 30.2, 22.8, 17.2, 14.9, 10.6, 8.5, 7.4 and 5.3 F g^{-1} for the scan rates of 5-200 mV s^{-1} , respectively. The GCD curves of the device at a variable current density from 3-8 A g^{-1} at a fixed potential window of 1 V shows nearly symmetric nature, as shown in Figure 3.6(b). The capacitance values calculated for the device from GCD plots were 8.8, 6.2, 4.6, 3.5 and 3.2 F g^{-1} for the current densities ranging from 3-8 A g^{-1} . The corresponding energy density, power density and specific capacity values for the device are presented in Table 3.3.

The Nyquist plot of the supercapacitor device in the high frequency region showed a large semicircle corresponding to the large R_{ct} value (Figure 3.6c). The observed large semicircle points towards low conductivity of the device resulting in lower capacitance value. The observed value of R_s was 0.49 ohm whereas R_{ct} was 109.5 ohm.

The fitted equivalent circuit presented as an inset in Figure 3.6(c) shows R_s , R_{ct} and W is in series connection while the real capacitance (Q_1) is in parallel connection with W . The deviation of the supercapacitor behavior from an ideal capacitive trait is believed to be due to the parallel connection of R_L with mass capacitance (Q_2) (Rantho et al., 2020; Zhou et al., 2014). The admittance plot of the supercapacitor device yields a knee frequency value of 2.51 Hz with the corresponding time constant value of 0.398 s (398000 μ s). The observed lower capacitance value is in agreement with the higher time constant value.

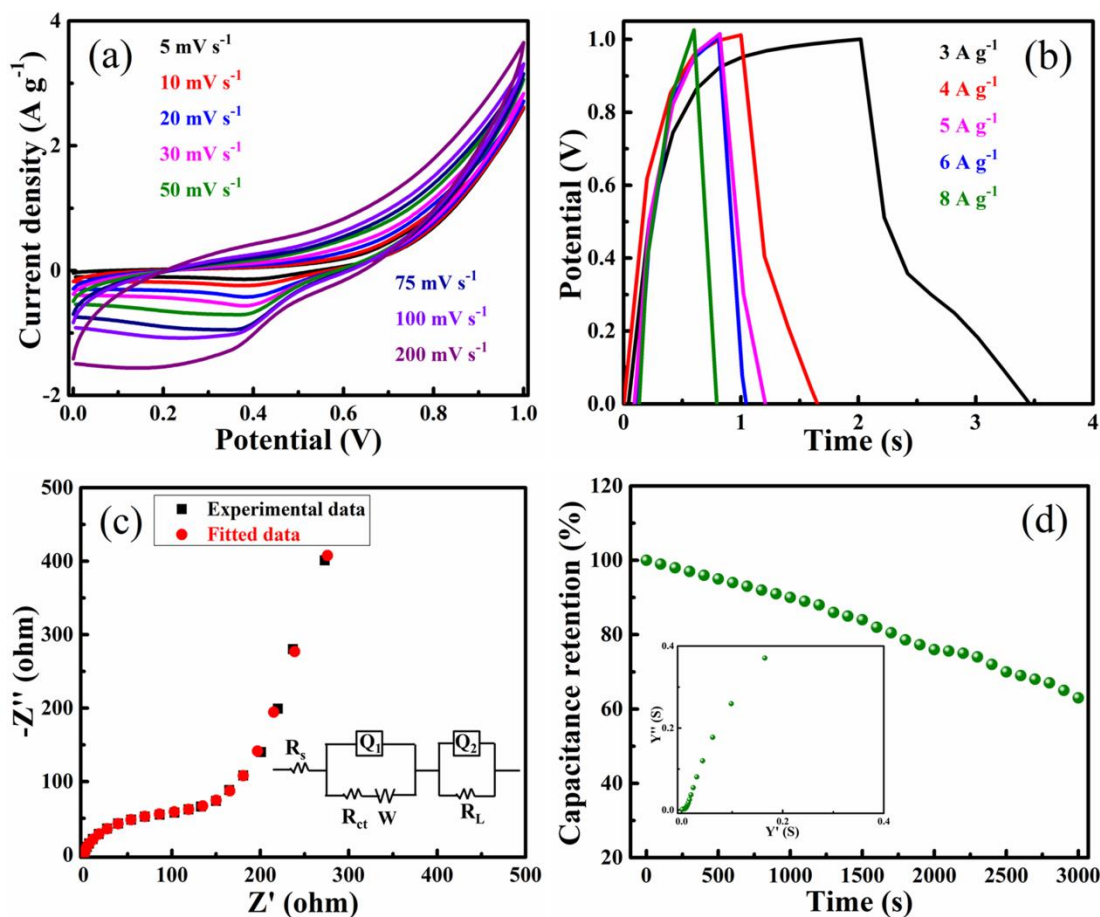


Figure 3.6 Electrochemical analysis of fabricated supercapacitor device by using NiO electrodes. (a) CV curves, (b) GCD curves, (c) Nyquist plot (fitted equivalent circuit as an inset) and (d) Cyclic stability data of NiO for 3000 cycles at a current density of 8 A g⁻¹ (inset shows the admittance plot of NiO device).

To figure out why the material showed good capacitance values in a 3-electrode system but exhibited mediocre performance in device, surface reactive sites were determined. The participation of surface reactive sites (Z) in the course of the redox process of NiO can be computed by using equation (3.1) (Umeshbabu et al., 2018).

$$Z = \frac{M\Delta VC_S}{F} \quad (3.1)$$

Where, M is the molecular mass of NiO ($74.6928 \text{ g mol}^{-1}$), ΔV (V) is the potential window, C_s (F g^{-1}) is the specific capacitance (obtained from CV curve) and F is the faraday constant ($96,485 \text{ C mol}^{-1}$). The Z value indicates the number of electroactive sites participating in the electrochemical redox reaction and it will be equal to 1 if all the electrochemical active sites are participating. The obtained value of Z for the NiO electrode is 0.12 and that for supercapacitor device is 0.02. The obtained result shows that around 12% of the active sites are involved in the 3-electrode method and only 2% active sites are involved in the redox reaction for the device. The obtained capacitance values are in agreement with the Z values.

Table 3.3 Energy density, power density and specific capacity values for the device.

Current density (A g^{-1})	Energy density (Wh kg^{-1})	Power density (W kg^{-1})	Q_s (C g^{-1})
3	1.20	3013.7	8.8
4	0.86	4000.0	6.2
5	0.64	5000.0	4.6
6	0.48	6034.5	3.5
8	0.44	8000.0	3.2

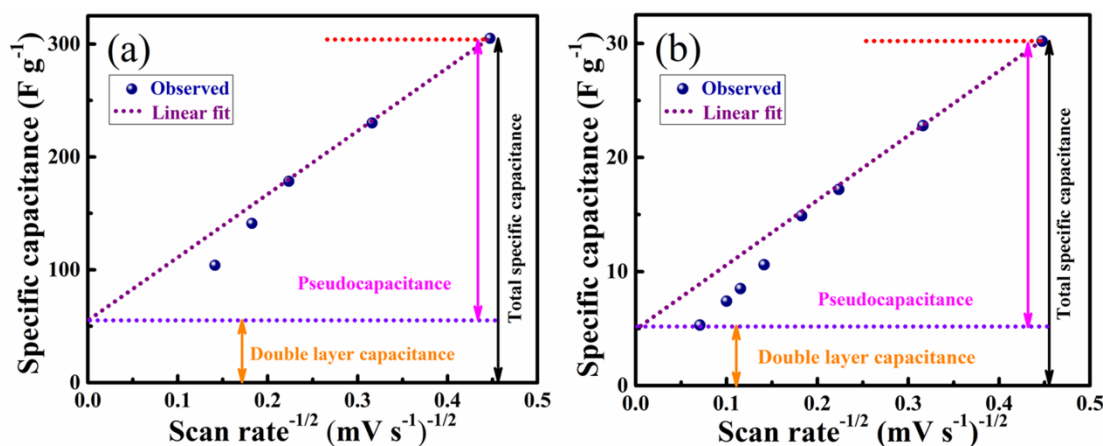


Figure 3.7 Determination of the C_{EDL} and C_P contribution of NiO in (a) 3-electrode and (b) Fabricated supercapacitor device.

The contribution of C_{EDL} and C_P to the total capacitance was determined by graphical method (Figure 3.7). The estimated C_P contribution for the 3-electrode and supercapacitor device is 82.2% and 81.5%, respectively. These results displayed that NiO is C_P dominant. These results indicate that compositing NiO with layered material would lead to even high performance.

3.4 CONCLUSIONS

NiO nanoflakes with a mesoporous structure of good crystallinity and surface area have been prepared employing a solvothermal approach. The material, when studied as an electrode, displayed a high capacitance value of 305 F g^{-1} at a scan rate of 5 mV s^{-1} apart from good rate capability and an appreciable coulombic efficiency of 95%. Along with high capacitance value, the electrode material has also retained 84% of its initial capacitance after 5000 cycles at a higher current density of 8 A g^{-1} . The fabricated symmetrical supercapacitor device also displayed high power density of 8000 W kg^{-1} at a higher applied current density of 8 A g^{-1} . The promising results displayed by the NiO nanoflakes was believed to be due to the high surface area of the mesoporous structure which acted as an ion-buffering reservoir for the diffusion of electrolyte ions within the porous network which ultimately imparted good electrochemical properties. These results indicate that the employed low cost technique can very well be utilized for the synthesis of other oxide materials for supercapacitor applications.



CHAPTER 4

***SIMPLE SOLVOTHERMAL SYNTHESIS OF
POROUS GRAPHENE-NiO NANOCOMPOSITES
WITH HIGH CYCLIC STABILITY FOR
SUPERCAPACITOR APPLICATION***

Chapter 4 presents PGNiO nanocomposite synthesis employing a mixed solvent system under a facile solvothermal method. The electrochemical performance of PGNiO composite is studied both as an electrode and a supercapacitor device.

4.1 INTRODUCTION

Supercapacitors store large amount of energy and deliver it very quickly and hence are used in a plethora of applications. Nowadays, hybrid supercapacitors, which are the combination of EDLC and pseudocapacitive materials, are in demand. In these supercapacitors, the electrochemical properties such as specific capacitance, cyclic stability, energy/power density have lot of scope for improvement (Liu et al., 2019; Sethi et al., 2020a; Sudhakar et al., 2018). Many authors have reported the synthesis of hybrid composites of NiO with different graphenic forms such as 3D N-doped carbon, reduced graphene oxide, porous carbon, graphene foam, mesoporous carbon sphere and graphene sheets with capacitance values in the range from 79.4 F g⁻¹ to 1161 F g⁻¹ (Banerjee et al., 2018; Chen et al., 2018; Huang et al., 2020; Li et al., 2020; Liu et al., 2019; Razali et al., 2018; Wang et al., 2018; Wu et al., 2019; Yus et al., 2019) at beneficial current densities. However, the obtained high specific capacitance values are mainly due to the utilization of 6 M KOH electrolyte or Ni foam as current collector. Although the use of Ni foam along with the concentrated KOH electrolyte increases the specific capacitance value due to the presence of interlinked pores in the Ni foam, the high cost and tedious procedure of its usage have limited its utility. Many previous studies have reported good or moderate capacitance values but the cyclic stability performance of the composites was not satisfactory even after the use of Ni foam current collector, due to the use of concentrated KOH electrolyte (4 M - 6 M) which triggers the delamination of electroactive material leading to the hampering of long term cyclic stability at higher current densities (Banerjee et al., 2018; Chen et al., 2018; Huang et al., 2020; Li et al., 2020; Liu et al., 2019; Razali et al., 2018; Wang et al., 2018; Wu et al., 2019; Yus et al., 2019).

4.2 EXPERIMENTAL SECTION

For the synthesis of x-PGNiO (x = 5, 10, 15, 20, 25 and 30 wt% GO loading) composite, a calculated quantity of GO (16 mg, 34.4 mg, 54 mg, 77.5 mg, 103 mg, 130 mg for 5, 10, 15, 20, 25 and 30 PGNiO, respectively) was dispersed in 1:1 mixture of water and ethylene glycol and sonicated in a bath sonicator for 2 h in order to achieve complete dispersion. Then, calculated amount of NiCl₂.6H₂O (0.2 M) was added to the mixed solvent of 10 mL (1:1, water + ethylene glycol mixture, 5 mL + 5 mL) which was then added to the GO dispersion dropwise and it was stirred continuously for 1 h. After 1 h stirring, 0.1 g NaOH (10 mL, 1:1, water + ethylene glycol mixture, 5 mL + 5 mL) was added dropwise and again stirred for 30 min. Then, the reaction mixture was transferred into a stainless steel autoclave of 100 mL capacity and heated at 160 °C for 16 h. Afterward, the oven was cooled to room temperature and the collected products were washed with deionized water several times followed by 1:1; water: ethanol mixture till the pH of the solution becomes neutral and dried at 70 °C overnight. Later, the products were calcined at 400 °C for 2 h in air to obtain PGNiO composite and named as 5 PGNiO - 30 PGNiO, respectively depending on the amount of GO loading. The characterization and electrochemical studies were carried out as mentioned in chapter 2.

4.3 RESULTS AND DISCUSSION

4.3.1 Structural, Elemental and Morphological Analysis

The XRD patterns of NiO and 10 PGNiO composite reveals peaks at 37.2°, 43.2°, 62.8°, 75.2°, 79.4° which could be readily indexed to (111), (200), (220), (311) and (222) crystal planes. The pattern corresponding to cubic NiO is consistent with the standard JCPDS file number of 47-1049 (Figure 4.1a) (Lu et al., 2018; Sun et al., 2018). The average crystallite size of pure NiO and 10 PGNiO are 15 nm and 12 nm as calculated by Scherer's formula ($D = 0.89\lambda/\beta\cos\theta$) and is supported by the broadened diffraction peaks indicating the nano domain of NiO structures. The

absence of other diffraction peaks in the XRD pattern suggests the purity of the prepared samples.

The Raman spectra for GO, PG and 10 PGNiO shown in Figure 4.1(b) reveals the presence of characteristic Raman signature for carbon materials viz. the D band and the G band in all the 3 samples. In GO, the D band intensity is low indicating lower amount of defects in the sample while PG reveals high degree of defects consistent with higher intensity of D band (Bantawal et al., 2019; Sadiq et al., 2017c; Sethi et al., 2019b). The intensity ratio of D to G band (I_D/I_G) indicates the degree of defect induced in the prepared sample. The calculated I_D/I_G ratio values are 0.76, 1.07 and 0.96 for GO, PG and 10 PGNiO composite, respectively. The successful formation of PG from GO is indicated by the increased I_D/I_G ratio. Further, this ratio is lower than that of PG in case of 10 PGNiO due to anchoring of NiO flakes on PG sheets.

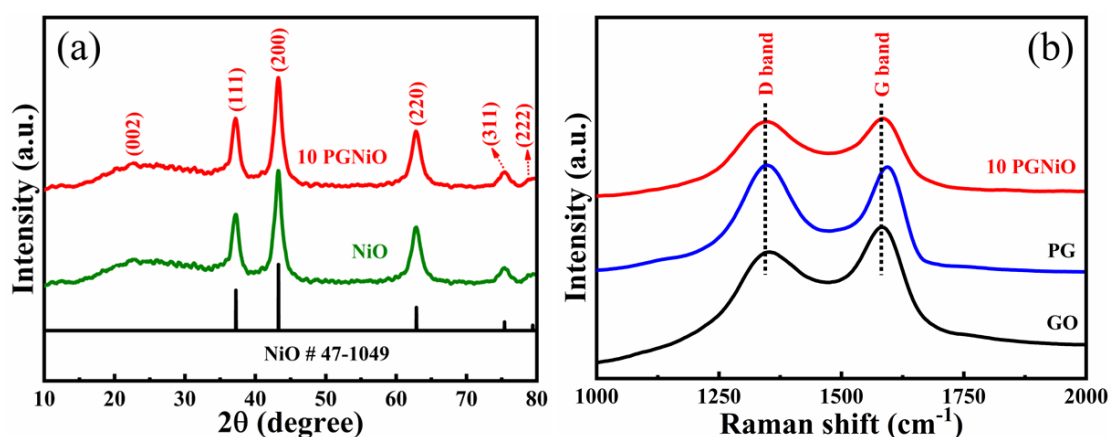


Figure 4.1 (a) XRD pattern of NiO, 10 PGNiO and (b) Raman spectra of GO, PG and 10 PGNiO composite.

The XPS survey spectrum in Figure 4.2(a) shows the existence of the C, O and Ni confirming the presence of the elements. The high resolution C 1s spectrum in Figure 4.2(b) is deconvoluted into three peaks of binding energies of 284.8 eV, 286.9 eV and 288.9 eV assigned to C-C/C=C, C-OH and C=O, respectively (Sethi et al., 2019b). The high resolution O 1s spectra in Figure 4.2(c) is also deconvoluted into

three peaks of binding energies of 530.0 eV, 531.9 eV, 534.3 eV corresponding to the M-O-M, O-C=O and C=O bonds, respectively (Sadiq et al., 2017d). The high resolution Ni 2p spectra in Figure 4.2(d) is deconvoluted into two spin doublets of $2p_{3/2}$ and $2p_{1/2}$ with their corresponding satellite peaks at binding energies of 855.4 eV ($2p_{3/2}$), 861.8 eV (Sat.), 873.5 eV ($2p_{1/2}$) and 880.1 eV (Sat.), respectively (Sadiq et al., 2017d).

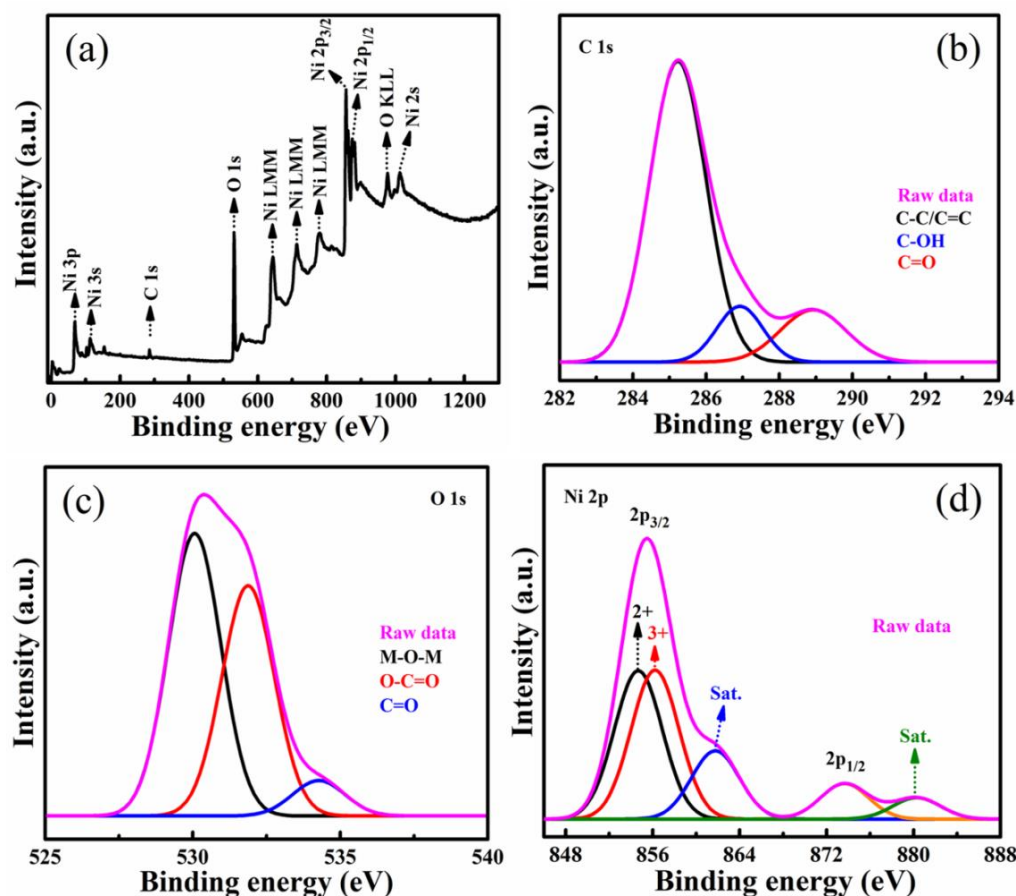


Figure 4.2 (a) XPS survey spectrum of 10 PGNiO; high resolution spectrum of (b) C 1s, (c) O 1s and (d) Ni 2p.

The FTIR spectrum of NiO shows a prominent peak at 588 cm^{-1} , which could be ascribed to the stretching modes of Ni-O in the sample. The FTIR spectrum of 10 PGNiO reveals the presence of peaks at 1630 cm^{-1} corresponding to the skeletal vibration from PG; apart from this, a sharp peak appeared at 590 cm^{-1} , which could be

ascribed to the Ni-O/Ni-O-Ni stretching vibration, indicating the incorporation of NiO into the PG (Figure 4.3) (Chime et al., 2020; Liu et al., 2019).

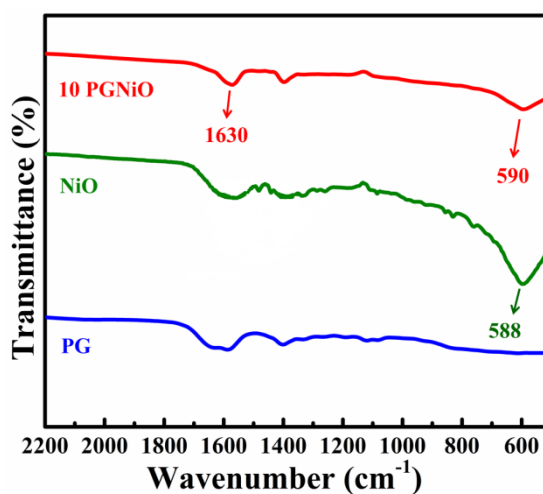


Figure 4.3 FTIR spectra of PG, NiO and 10 PGNiO.

The use of solvothermal method with mixed solvent system is believed to give rise to unique porous morphology with high surface area (Sethi et al., 2019a). The TEM image of the 10 PGNiO reveals NiO flakes distributed on PG sheets in various orientations as shown in Figure 4.4(a). The EDX spectra reveals Ni, O and C as the only detectable elements indicating the purity of the product obtained (Figure 4.4b). The elemental mapping profile of 10 PGNiO composite studied from the highlighted image in Figure 4.5 also supports the results from EDX. The HRTEM image displays planes corresponding to (200) of NiO with interplanar distances matching that from XRD results (Figure 4.4c). The concentric rings observed in the SAED pattern suggest good crystallinity of 10 PGNiO (Figure 4.4d).

The observed porous structure of 10 PGNiO composite from the morphological study led to probing into the surface area of the synthesized material. The BET curves obtained for 10 PGNiO indicated type IV isotherm of IUPAC classification (Figure 4.6). The anchoring of NiO flakes on PG decreased the surface area of PG from 126 m² g⁻¹ to 87 m² g⁻¹ in 10 PGNiO with a total pore volume of 0.265 cm³ g⁻¹ with an average pore diameter of 3.52 nm. In spite of possessing lower

surface area than PG, 10 PGNiO has higher surface area than NiO, contributing to the improvement of electrochemical performance.

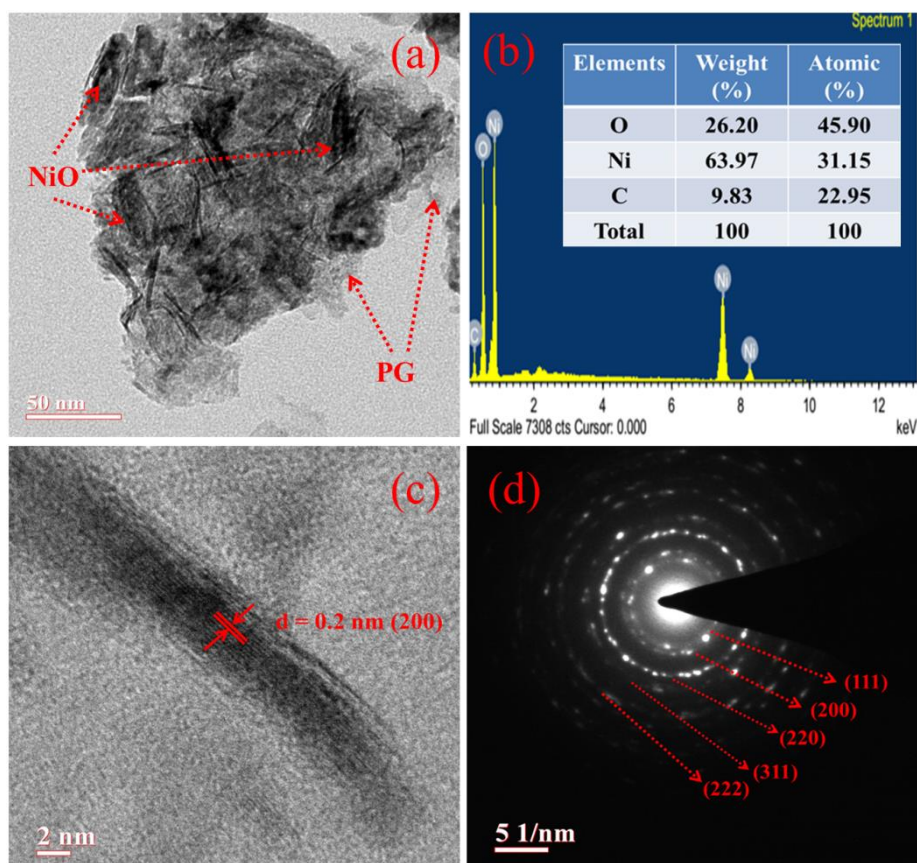


Figure 4.4 (a) TEM image, (b) EDX spectra, (c) HRTEM image and (d) SAED pattern of 10 PGNiO.

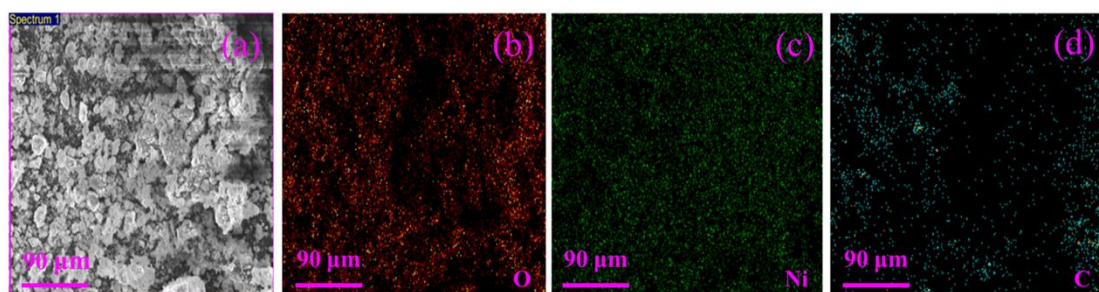


Figure 4.5 (a) Highlighted image from where the EDS mapping is done, elemental mapping of (b) O, (c) Ni and (d) C.

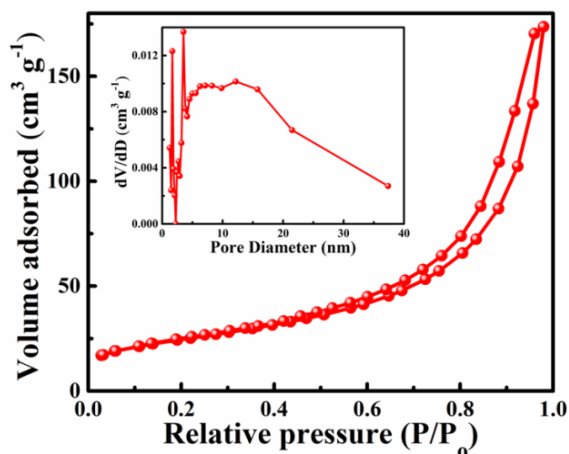


Figure 4.6 BET surface area plot of 10 PGNiO (pore size distribution plot of 10 PGNiO is shown in inset).

4.3.2 Electrochemical Study of PGNiO Composite Electrodes

The electrochemical performance of the PGNiO composites was analyzed by using CV, GCD and EIS in a 3-electrode method by using 2 M KOH as an electrolyte. The CV curves of the PGNiO composite materials in the potential range of 0-0.5 V at a constant scan rate of 5 mV s^{-1} reveals a pair of redox peaks indicating the faradaic nature of the material (Figure 4.7a). The 10 PGNiO composite occupied more area in CV plot as compared to the other electrode materials hinting towards higher capacitance value. The calculated specific capacitance values of 356, 511, 287, 239, 187 and 140 F g^{-1} for 5, 10, 15, 20, 25 and 30 PGNiO composites, respectively confirmed the previous statement. Here it is observed that after the incorporation of PG with NiO the capacitance values increased till the optimum loading. There after the capacitance values decreased owing to the agglomeration of PG sheets at higher concentration leading to decreased conductance.

Similar to CV, the GCD curves for all PGNiO composite materials measured at a constant current density of 1 A g^{-1} at a fixed potential window of 0-0.45 V showed faradaic type behavior of the composites (Figure 4.7b). The measured capacitance values for the composites (5-30 PGNiO) were 276, 477, 212, 151, 115

and 102 F g^{-1} , respectively. The measured coulombic efficiency η (%) of more than 90% for the electrode materials indicates the good charge-discharge feature of the electrode materials. The 10 PGNiO displayed more discharging time as compared to other materials and exhibited higher capacitance value. The estimated specific capacity values from the GCD curves were 124.2, 214.7, 93.2, 67.9, 51.8 and 45.9 C g^{-1} for the 5-30 PGNiO composites, respectively.

The EIS spectrum in the form of Nyquist plot of all the materials is shown in Figure 4.7(c). The Nyquist plots revealed the presence of a very small semicircle in the high frequency region, which suggested the low resistance value offered by the material and nearly a straight line towards the Y-axis, in the medium to low frequency region. This is suggestive of good capacitive trait of the materials. The obtained resistance and conductance values for the electrode materials are given in Table 4.1 below. These values follow the same trend shown by the capacitance values estimated by the CV and GCD datas. The knee frequency values obtained from the admittance plot (Figure 4.7d) and the corresponding time constant values tabulated clearly indicate that 10 PGNiO composite shows less resistance and more admittance value, therefore has less time constant value, strongly agreeing with the high capacitance value offered by it (Table 4.1) (Sethi et al., 2020b).

Table 4.1 Resistance, conductance, knee frequency and time constant values of electrode materials.

Electrode material	Resistance (Ω)	Conductance (S)	Knee frequency (kHz)	Time constant (μs)
5 PGNiO	0.28	3.6	15.90	62.9
10 PGNiO	0.24	4.1	25.10	39.8
15 PGNiO	0.31	3.2	10.00	100.0
20 PGNiO	0.52	1.92	2.51	398.4
25 PGNiO	0.63	1.58	1.59	628.9
30 PGNiO	0.65	1.53	1.00	1000.0

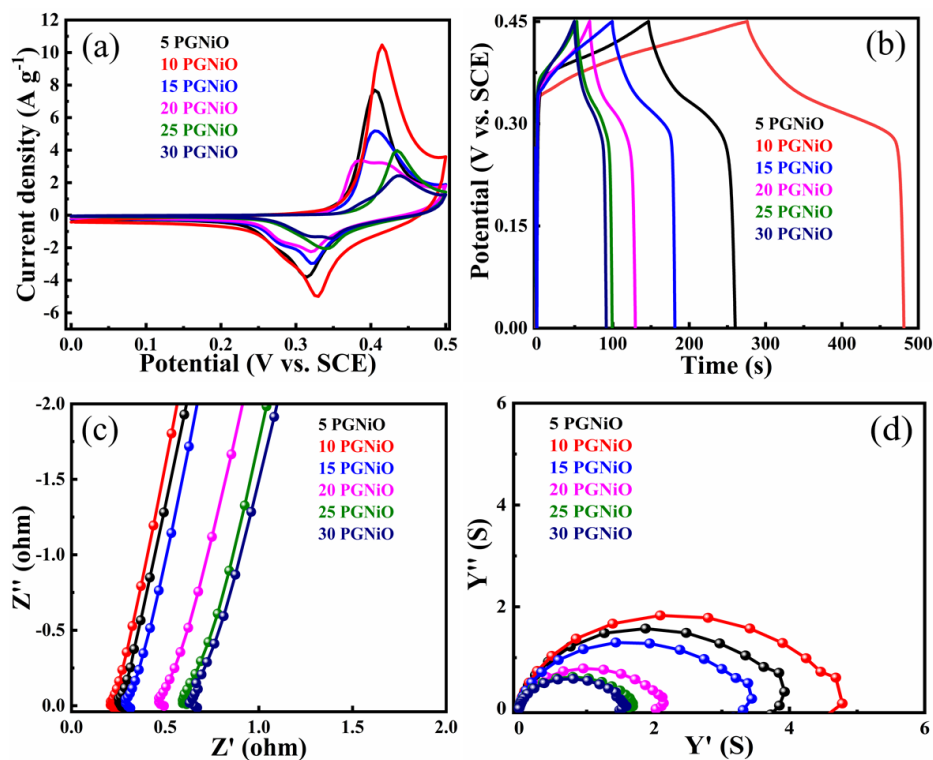


Figure 4.7 Electrochemical analysis of PGNiO composite electrodes. (a) CV plots at a constant scan rate of 5 mV s^{-1} , (b) GCD plots at a constant current density of 1 A g^{-1} , (c) EIS plots in the high frequency region and (d) Admittance plots.

4.3.3 Electrochemical Study of 10 PGNiO Composite Electrode

Among the composites, it is found that the 10 PGNiO composite delivered good electrochemical performance and hence it was further studied as an electrode material. The CV curves of 10 PGNiO at various scan rates ranging from $5\text{-}300 \text{ mV s}^{-1}$ are shown in Figure 4.8(a). The graphs exhibit redox peaks for the anodic and cathodic sweeps demonstrating the faradaic type trait of the material. As the scan rate increase from 5 mV s^{-1} to 300 mV s^{-1} , the CV curves show the same trend without any significant deviation suggesting the good stability of the composite material. The computed capacitance values are 511, 405, 333, 259, 207, 172, 112, 91 and 78 F g^{-1} for the scan rates of $5\text{-}300 \text{ mV s}^{-1}$, respectively. A capacitance value of 78 F g^{-1} is

obtained even with 60 fold increase in the scan rate, suggesting the good rate capability of the material.

The GCD study of 10 PGNiO at different current densities ranging from 1-12 A g⁻¹ is shown in Figure 4.8(b). The nearly symmetrical GCD curves lead to specific capacitance values of 477, 413, 394, 240, 163, 137 and 133 F g⁻¹ for the current density of 1, 2, 3, 4, 6, 8 and 12 A g⁻¹, respectively. The computed energy density, power density and specific capacity values for the current densities ranging from 1-12 A g⁻¹ is given in Table 4.2. The calculated coulombic efficiency of > 90% from the GCD curves suggested good charge-discharge profile of the material.

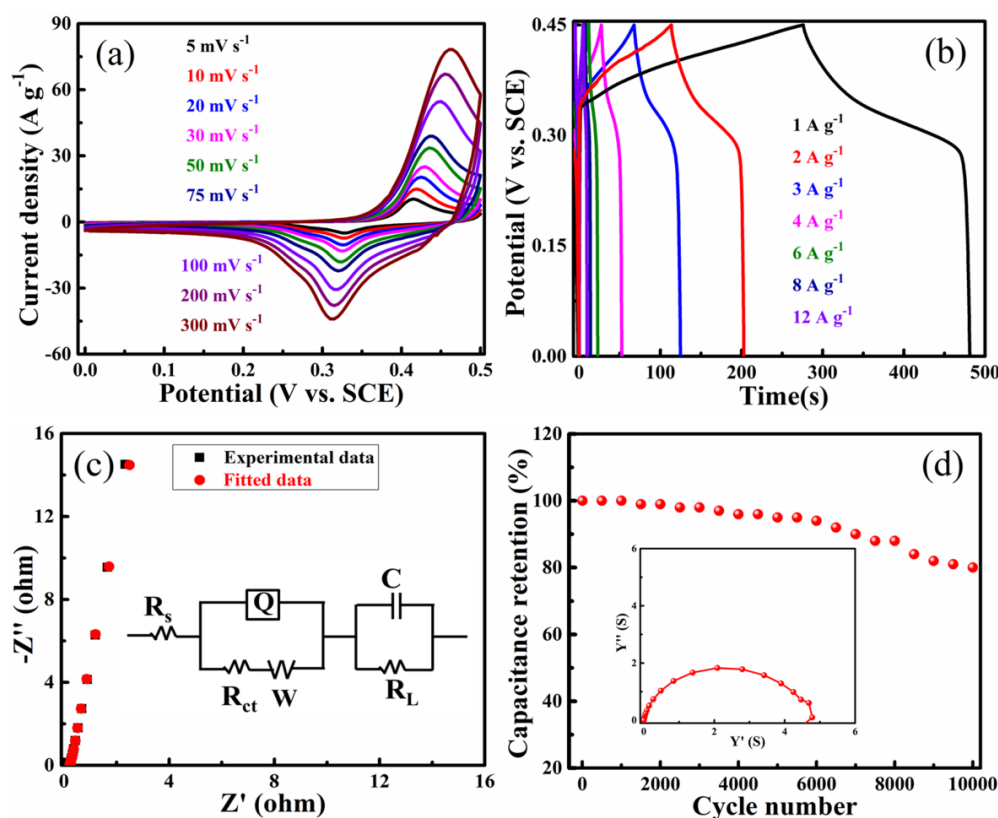


Figure 4.8 Electrochemical analysis of 10 PGNiO composite electrodes. (a) CV curves at various scan rates, (b) GCD curves at different current densities, (c) Fitted Nyquist plot (inset represents the fitted equivalent circuit) and (d) Cyclic stability plot at a current density of 8 A g⁻¹ for 10000 charge-discharge cycles (inset shows the admittance plot of 10 PGNiO composite electrode).

Table 4.2 Energy density, power density and specific capacity values of 10 PGNiO composite electrode.

Current density (A g ⁻¹)	Energy density (Wh kg ⁻¹)	Power density (W kg ⁻¹)	Q _s (C g ⁻¹)
1	13.4	225.0	214.7
2	11.6	450.1	185.9
3	11.1	676.1	177.3
4	6.7	893.3	108.0
6	4.6	1358.0	73.4
8	3.9	1823.4	61.7
12	3.7	2748.2	59.9

The Nyquist plot of 10 PGNiO composite in Figure 4.8(c) showed a straight line without any deviation in the low frequency region and absence of semicircle in the high frequency region indicating low R_s and R_{ct} value. A nearly flat tail parallel to the Z'' -axis (imaginary axis) in the low frequency region again suggests the faster kinetics and ideal capacitive nature of the material. This is attributed to the high surface area with large pore volume of the composite material. This type of impedance behavior is highly suitable for supercapacitor utility and the obtained high specific capacitance values are in strong agreement with the impedance results. The obtained Nyquist plot is best fitted by using Randle's circuit and the fitted data with the corresponding equivalent circuit is presented in inset of Figure 4.8(c) (Barzegar et al., 2016a; Sethi et al., 2020c).

10000 cycles were run to test the cyclic stability of 10 PGNiO electrode at a constant current density of 8 A g⁻¹ (Figure 4.8d). It was found that after 10000 cycles; almost 80% of the initial capacitance was still retained. The admittance plot of 10 PGNiO composite is displayed as an inset in Figure 4.8(d).

The CV curves of all the composites (5-30 PGNiO) at different scan rates ranging from 5–50 mV s^{-1} are given in Figure 4.9. The specific capacitance values for all the composites are presented in Table 4.3. The estimated C_{EDL} and C_{P} contributions for PGNiO composites determined via graphical method and tabulated indicates that the C_{EDL} contribution increased with the increase in the PG content and led to decrease in C_{P} contribution (Table 4.4; Figure 4.10).

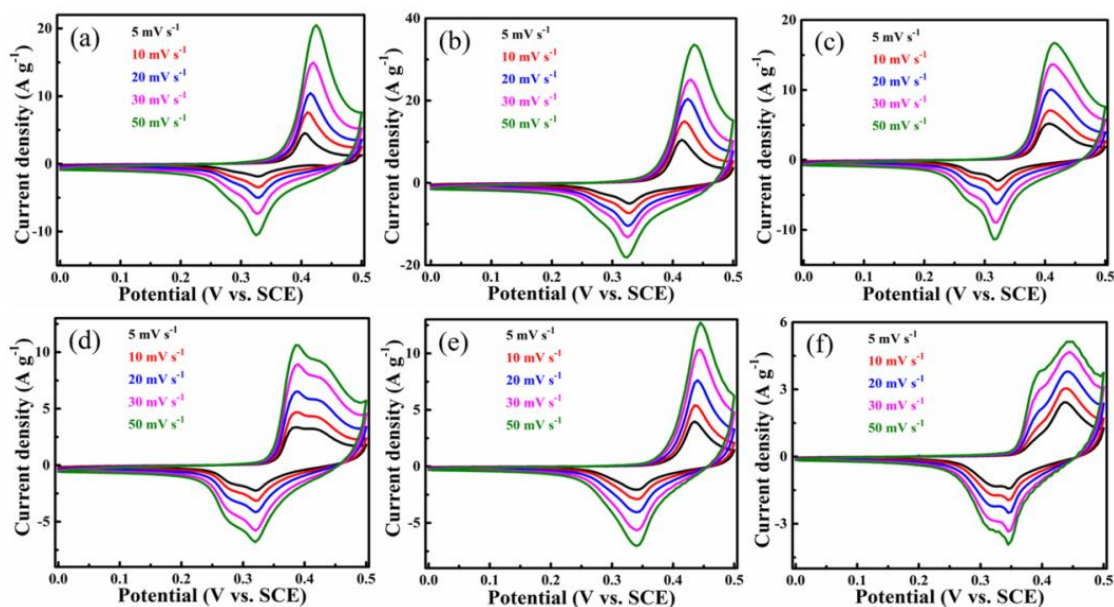


Figure 4.9 CV curves for (a) 5 PGNiO, (b) 10 PGNiO, (c) 15 PGNiO, (d) 20 PGNiO, (e) 25 PGNiO and (f) 30 PGNiO composite electrodes.

Table 4.3 Specific capacitance values of all PGNiO composites in different scan rates.

Composite	Scan rate (mV s^{-1})	C_{S} (F g^{-1})
5 PGNiO	5	356
	10	274
	20	217
	30	154
	50	113

10 PGNiO	5	511
	10	405
	20	333
	30	259
	50	207
15 PGNiO	5	287
	10	228
	20	189
	30	138
	50	101
20 PGNiO	5	239
	10	192
	20	158
	30	113
	50	82
25 PGNiO	5	187
	10	150
	20	125
	30	77
	50	53
30 PGNiO	5	140
	10	114
	20	95
	30	58
	50	39

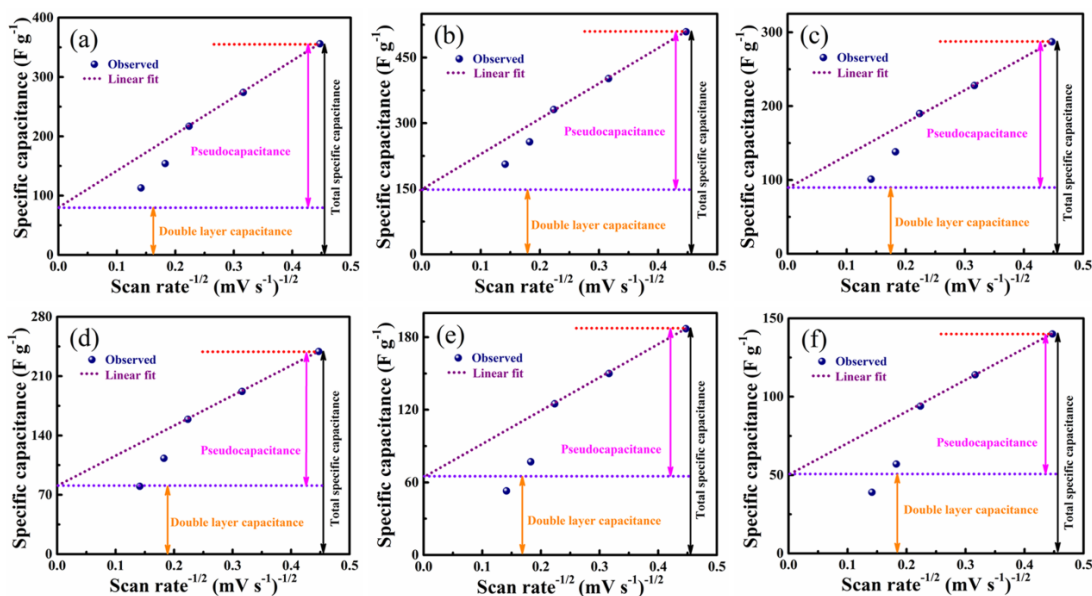


Figure 4.10 Determination of the C_{EDL} and C_P contribution of (a) 5 PGNiO, (b) 10 PGNiO, (c) 15 PGNiO, (d) 20 PGNiO, (e) 25 PGNiO and (f) 30 PGNiO composite electrodes.

Table 4.4 C_{EDL} and C_P contribution of electrode materials.

Composite	C_{EDL} (%)	C_P (%)
5 PGNiO	22.8	77.2
10 PGNiO	29.0	71.0
15 PGNiO	32.7	67.3
20 PGNiO	34.7	65.3
25 PGNiO	35.8	64.2
30 PGNiO	36.3	63.7

4.3.4 Electrochemical Study of Fabricated Supercapacitor Using 10 PGNiO Composite Electrodes

The 10 PGNiO nanocomposite is used as both cathode and anode for the fabrication of symmetrical supercapacitor in aqueous 2 M KOH electrolyte. The rectangular CV curves for supercapacitor device at varied scan rates ranging from 5-

700 mV s^{-1} depicts good electrochemical feature of the material, as shown in Figure 4.11(a). The calculated capacitance values from the CV curves are 86, 68, 55, 41, 29, 19, 16, 10, 8, 7, 6, 5 and 4 F g^{-1} for the scan rates ranging from 5-700 mV s^{-1} , respectively.

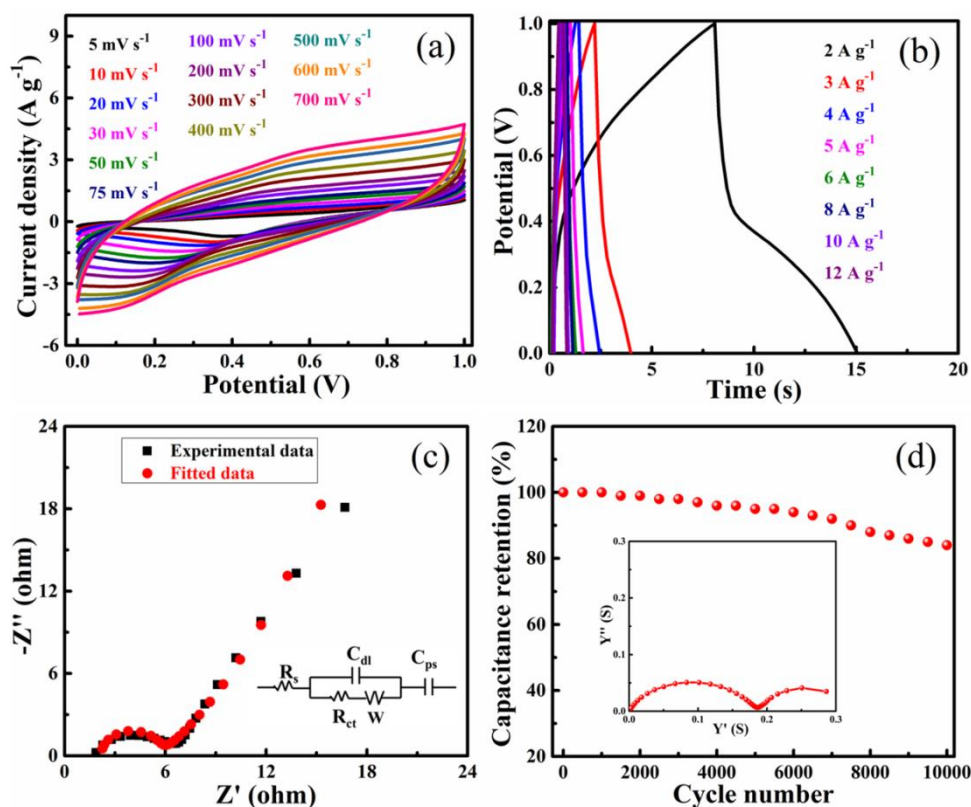


Figure 4.11 Electrochemical analysis of symmetric supercapacitor fabricated from 10 PGNiO nanocomposite electrodes. (a) CV Graphs at various scan rates, (b) GCD graphs at various current densities, (c) Fitted Nyquist plot with the equivalent circuit as an inset and (d) Cyclic stability study at a current density of 8 A g^{-1} with admittance plot in the inset.

The GCD curves for the current densities varying from 2-12 A g^{-1} are shown in Figure 4.11(b) and the calculated capacitance values are 43.0, 24.0, 14.5, 13.8, 12.0, 11.0, 9.8 and 8.4 F g^{-1} for the current densities varying from 2-12 A g^{-1} . The calculated coulombic efficiency of $> 90\%$ from the GCD curves suggested good charge-discharge profile of the material. The calculated energy density, power density

and specific capacity values from the GCD curves (Table 4.5) for the varying current densities of 2-12 A g⁻¹ tabulated indicates promising values ascribed to the good synergistic effect of the constituents in the PGNiO composite.

Table 4.5 Energy density, power density and specific capacity values of the fabricated symmetrical supercapacitor.

Current density (A g ⁻¹)	Energy density (Wh kg ⁻¹)	Power density (W kg ⁻¹)	Q _s (C g ⁻¹)
2	5.9	2000.0	43.0
3	3.3	3000.0	24.0
4	2.1	4200.0	14.5
5	1.9	5000.0	13.8
6	1.7	6120.0	12.0
8	1.5	8088.2	11.0
10	1.3	10000.0	9.8
12	1.1	12000.0	8.4

The Nyquist plot depicts a very small semicircle in the high frequency region and an inclined line in the low frequency region (Figure 4.11c). The plot is best fitted by using Randle's equivalent circuit shown in Figure 4.11(c) as an inset. Here, the obtained low value of R_s is 2.0 ohm and R_{ct} of 4.1 ohm, consistent with the CV and GCD results.

The cycle life of the fabricated supercapacitor is tested for 10000 cycles at an applied current density of 8 A g⁻¹. Until 1500 cycles, the capacitance retention is 100%. Then there is a slight decrease in the retention value and after 10000 cycles, around 84% of initial capacitance value is retained for the fabricated supercapacitor demonstrating its good retention capability (Figure 4.11d). The obtained knee frequency value of 251 Hz with a time constant value of 3980 μs from the admittance plot indicates the promising nature of the nanocomposite (Figure 4.11d inset). The C_{EDL} and C_P contribution for the fabricated supercapacitor device are 29.6% and

70.4%, respectively (Figure 4.12). The comparison of electrochemical performance of PGNiO electrodes with other reported literatures presented in Table 4.6 indicates that the current synthetic technique is able to produce superior electrochemical material and can be extended in the synthesis of other materials as well.

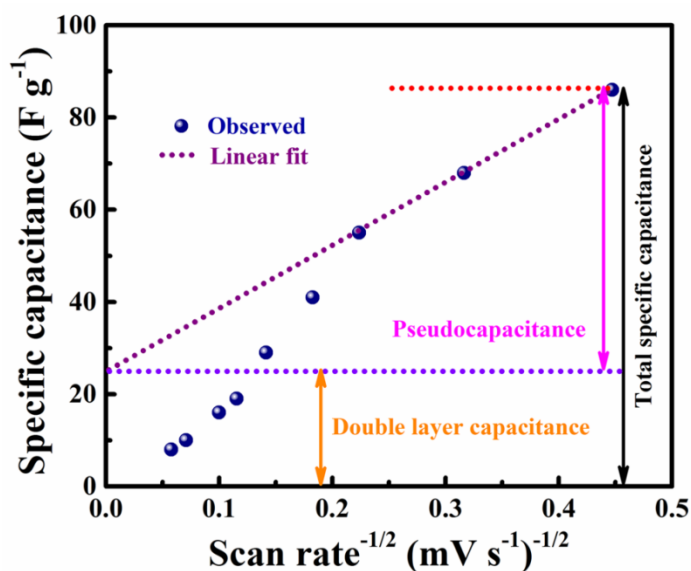


Figure 4.12 Determination of the C_{EDL} and C_P contribution of 10 PGNiO supercapacitor device.

Table 4.6 Comparison of 10 PGNiO electrodes with other reported literatures.

Electrode material	C_S ($F g^{-1}$)	Electrolyte	Cyclic stability	References
Amorphous carbon-NiO nanoflowers composite	79 @ 0.2 A g^{-1}	1 M Na_2SO_4	---	Banerjee et al. (2018)
Core shell carbon sphere-NiO composite	555 @ 1 A g^{-1}	6 M KOH	95% after 1000 cycles @ 10 A g^{-1}	Chen et al. (2018)
RGO-NiO nanocrystals composite	422 @ 1 A g^{-1}	2 M KOH	137% after 2000 cycles @ 4 A g^{-1}	Gui et al. (2017)

NiO/sulphonated graphene composite	520 @ 1 A g ⁻¹	6 M KOH	79% after 5000 cycles @ 10 A g ⁻¹	Huang et al. (2020)
NiO-RGO composite	590 @ 1 A g ⁻¹	1 M KOH	100% after 1000 cycles @ 1 A g ⁻¹	Kahimbi et al. (2017)
NiO/graphene composite	385 @ 1 A g ⁻¹	6 M KOH	82% after 4000 cycles @ 3 A g ⁻¹	Li et al. (2018)
3D NC/Ni@NiO composite	390 @ 1 A g ⁻¹	6 M KOH	70% after 5000 cycles @ 2 A g ⁻¹	Li et al. (2020)
NiO nanoparticles/mesoporous carbon nanospheres	406 @ 1 A g ⁻¹	6 M KOH	91% after 10000 cycles @ 3 A g ⁻¹	Liu et al. (2017)
Hierarchical shell-core structure, NiO nano spines @ C composite	1161 @ 2 A g ⁻¹	6 M KOH	92% after 3000 cycles @ 2 A g ⁻¹	Liu et al. (2019)
NiO nanodots on graphene composite	1020 @ 1 A g ⁻¹	2 M KOH	78% after 2000 cycles @ 5 A g ⁻¹	Lu et al. (2018)
Etched Carbon cloth-NiO-PANI composite	192 @ 0.5 A g ⁻¹	0.5 M H ₂ SO ₄	---	Razali et al. (2018)
RGO-NiO composite	880 @ 1 A g ⁻¹	6 M KOH	93% after 5000 cycles @ 5 A g ⁻¹	Sun et al. (2018)
N-Doped porous carbon/NiO nanosheet composite	404 @ 1 A g ⁻¹	6 M KOH	84% after 5000 cycles @ 5 A g ⁻¹	Wang et al. (2018)
NiO @ graphite carbon nano composite	317 @ 1 A g ⁻¹	6 M KOH	71% after 1500 cycles @ 2 A g ⁻¹	Wu et al. (2019)

RGO-NiO nanoplates hybrid structure	484 @ 1 A g ⁻¹	1 M KOH	---	Yus et al. (2019)
PGNiO electrode	511 @ 5 mV s ⁻¹ 477 @ 1 A g ⁻¹	2 M KOH	80% after 10000 cycles @ 8 A g ⁻¹	Present work

4.4 CONCLUSIONS

Superior quality PGNiO composite can be synthesized following an ecofriendly solvent mediated solvothermal method. Appropriate loading of the PG content on to the NiO nano flakes results in a robust composite structure which helps to prevent the volumetric shrinkage during electrochemical cyclings. The material displayed an impressive specific capacitance value of 511 F g⁻¹ at a scan rate of 5 mV s⁻¹ for the single electrode and an appreciable power density and long term electrochemical stability as a supercapacitor. The superior electrochemical performance of this composite is mainly due to the synergistic effect of the constituent materials, which provided effective ion reservoir and mechanical strength facilitating smooth diffusion of electrolyte ions throughout the electroactive material when the material is subjected to charge-discharge processes. Overall, the study portrays the PGNiO nanocomposite as a promising candidate for energy storage applications.



CHAPTER 5

***SOLVOTHERMAL SYNTHESIS OF NiFe_2O_4
NANOPARTICLES FOR HIGH-PERFORMANCE
SUPERCAPACITOR APPLICATIONS***

Chapter 5 deals with the synthesis and detailed characterization of NF nanoparticles prepared through a solvothermal route. The synthesized material was studied for its utility as supercapacitors.

5.1 INTRODUCTION

Recently mixed metal oxides/spinels are considered as superior electrode materials for supercapacitors as compared to the single oxides owing to the mixture of two metal domains, various oxidation states, easy synthesis and high electrochemical response. Among the spinels, NC has exhibited good electrochemical activity due to its high electrical conductivity (Sethi et al., 2019a; Pan et al., 2019). But the other spinels such as ZnCo_2O_4 , MnCo_2O_4 , CoFe_2O_4 and NF are less studied owing to their inadequate electrical conductivity (Aparna et al., 2018; Gao et al., 2019). It is known that the cubic spinel structure of NF possesses stronger bonds between oxygen and metal ions, which makes them more attractive for use in electrochemical energy storage devices (Javed et al., 2016; Sethi et al., 2020b). In NF, both Ni and Fe atoms with more than 2 oxidation states facilitate higher electrical conductivity and superior energy storage properties.

There are many studies on the synthesis of NF nanostructures by mainly hydrothermal and wet chemical methods and a few by sol-gel method (Anwar et al., 2011; Aparna et al., 2018; Bandgar et al., 2018; Bhojane et al., 2017; Gao et al., 2019; Hua et al., 2018; Kumar et al., 2013; Zhang et al., 2018). But the electrochemical study of thus synthesized NF reported very less specific capacitance value ranging from 95 to 350 F g^{-1} (Anwar et al., 2011; Bhojane et al., 2017). Wherever high values were reported ranging from 435 to 677 F g^{-1} , it was due to the usage of Ni foam or high concentration of KOH (6 M), which are not desirable for a low cost and facile experimentation (Bandgar et al., 2018). In some cases, where the capacitance values were of the order of 342-562 F g^{-1} , the capacitance retention ability was very low even for 1000 cycles making it unsuitable for commercialization (Bhojane et al., 2017; Hua et al., 2018). Hence, there is a requisite to synthesize NF by solvothermal method

such that it exhibits high value of supercapacitance without using Ni foam or high concentration of KOH and systematically study its electrochemical activities.

5.2 EXPERIMENTAL SECTION

NF was synthesized by solvothermal method using mixed solvents. First, $\text{Ni}(\text{NO}_3)_2 \cdot 6\text{H}_2\text{O}$ and $\text{Fe}(\text{NO}_3)_3 \cdot 9\text{H}_2\text{O}$ (1:2 mmol) are dissolved in 50 mL (1:1 mixture, deionized water + ethylene glycol) and it is sonicated in a bath sonicator for 30 min to ensure complete dissolution. Urea (9 mmol) is added to the mixture while stirring and the solution is kept stirred continuously for one hour to obtain homogeneity, which was then added to a teflon lined stainless steel autoclave and heated for 18 h at a temperature of 160 °C. Then, the autoclave is brought to room temperature gradually. The obtained brown color product is washed several times with deionized water followed by ethanol till neutral pH, after which it is dried at 70 °C. Later it is calcined at 400 °C for 2 h in air to get pure NF nanoparticles. The characterization and electrochemical studies were carried out as mentioned in chapter 2.

5.3 RESULTS AND DISCUSSION

5.3.1 Structural, Elemental and Morphological Analysis

The phase and crystallinity of the as synthesized NF are analyzed by XRD. Figure 5.1(a) shows the XRD pattern of NF with standard data (JCPDS card number # 074-2081). The XRD peaks show the crystalline nature of the material with broadened base suggesting the nano dimension of the synthesized NF. The absence of any other kind of peaks in the XRD pattern suggests the formation and high purity of the sample. The average crystal size is determined from the highest intensity peak from (311) crystal plane by using Debye-Scherrer's equation and the crystallite size is found to be around 17 nm.

Raman spectra of NF nanoparticles (Figure 5.1b) showed five Raman active modes i.e. $A_{1g} + E_g + 3 T_{2g}$ modes according to the group theory calculations (Kumar et al., 2013; Sadiq et al., 2017c; Sadiq et al., 2017d; Zhao et al., 2017). The T_{2g} mode

possesses three Raman bands including 206, 483 and 562 cm^{-1} . The bands at 321 and 692 cm^{-1} are assigned to E_g and A_{1g} modes, respectively. Raman signal of cubic NF at 692 cm^{-1} is attributed to the A_{1g} symmetry of oxygen in tetrahedral group, while the other modes describe the octahedral sites. Raman spectrum shows three different kinds of vibrational modes in the lattice. The A_{1g} mode arises due to the symmetric stretching of O atoms with Ni-O and Fe-O bonds in a tetrahedral structure. The three T_{2g} modes are generated due to the asymmetric stretching of Ni/Fe/O and asymmetric bending of O relative to the metal ion. The E_g mode is symmetric bending of O atom relative to the metal ion.

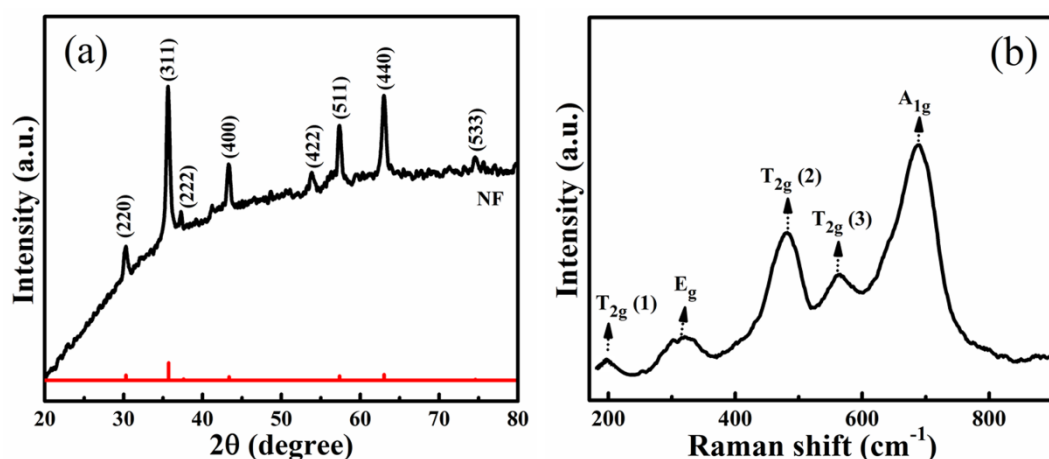


Figure 5.1 (a) XRD pattern of NF with the standard data and (b) Raman spectrum of NF nanoparticles.

The mixed solvent solvothermal approach led to the formation of uniformly distributed spherical nanoparticles as revealed by FESEM image of the size from 13 nm to 17 nm (Figure 5.2a). The EDX shows the presence of Ni, Fe and O as elemental constituents (Figure 5.2b). The presence of C peak is due to the carbon tape used during analysis. The observed atomic ratio of elements Ni, Fe and O in the sample is found to be approximately 1: 2: 4, supporting the formation of NF. The pores within NF nanoparticles are seen in the TEM images (Figure 5.2c and 5.2d). The measured interplanar distance in HRTEM image (Figure 5.2e) matches with (311) and (422) crystal planes of NF. The SAED patterns show well formed concentric rings,

depicting the polycrystalline nature of the NF (Figure 5.2f). The concentric rings correlate well with the XRD pattern of the NF nanoparticles, which further supports the formation of NF.

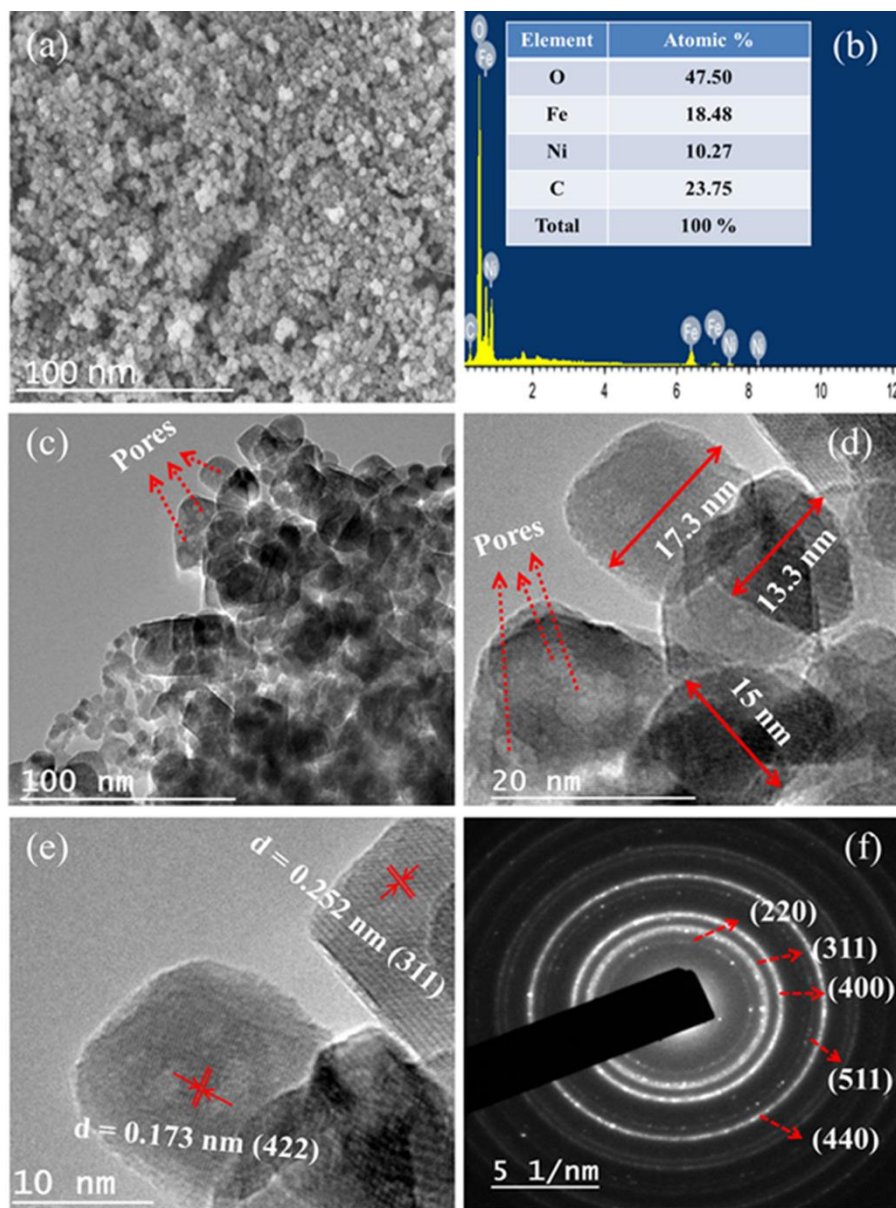


Figure 5.2 (a) FESEM image, (b) EDX data (inset shows the elemental composition), (c) Low magnification TEM image, (d) High magnification TEM image, (e) HRTEM image with measured interplanar distance matching with the (422) and (311) crystal planes and (f) SAED pattern of NF nanoparticles.

The BET surface area analysis is a prominent measurement tool to obtain information about the specific surface area value along with the pore volume and pore diameter. The BET plot determined is shown in Figure 5.3 and it belongs to type-IV class of isotherms. This kind of isotherm with H3 hysteresis loop is in general suggestive of porous nature of the material. The measured BET surface area of the NF nanoparticles is $80 \text{ m}^2 \text{ g}^{-1}$, seeming to be higher or comparable than previously reported values of NF nanomaterials ($0.968 \text{ m}^2 \text{ g}^{-1}$), NF nano flower ($25 \text{ m}^2 \text{ g}^{-1}$) and nano feather ($11 \text{ m}^2 \text{ g}^{-1}$), NF nanoarchitectures ($73 \text{ m}^2 \text{ g}^{-1}$), NF nanoparticles ($77 \text{ m}^2 \text{ g}^{-1}$), NF nanocrystals ($39 \text{ m}^2 \text{ g}^{-1}$), NF nanoparticles ($76 \text{ m}^2 \text{ g}^{-1}$) and NF/RGO composite ($57 \text{ m}^2 \text{ g}^{-1}$) (Anwar et al., 2011; Bandgar et al., 2018; Cao et al., 2015; Gao et al., 2019; Liu et al., 2014; Peng et al., 2012; Wu et al., 2016). Also, the BJH plot analysis revealed a large pore volume of $0.54 \text{ cm}^3 \text{ g}^{-1}$ and mesoporous nature of the material.

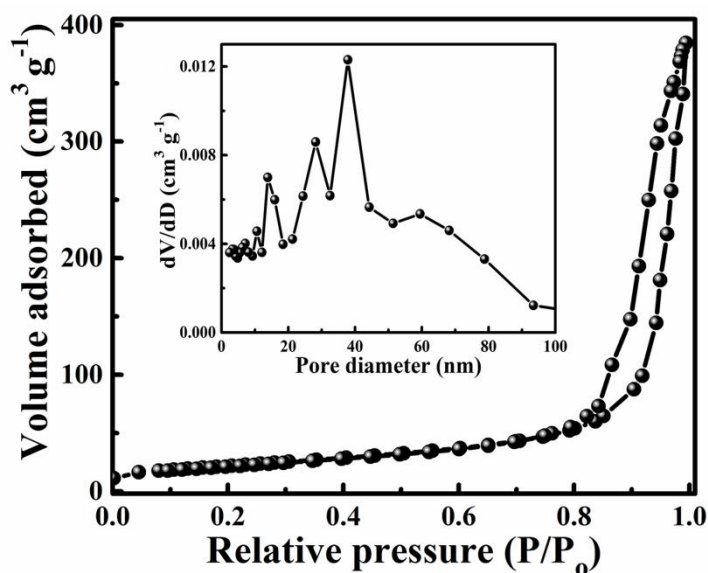


Figure 5.3 BET surface area plot of NF (inset shows BJH plot).

5.3.2 Electrochemical Study of NF as an Electrode

The electrochemical analyses of the NF electrodes are carried out using a 3-electrode method with 2 M KOH as electrolyte. The Figure 5.4(a) shows CV curves

of NF at varying scan rates ranging from 5-100 mV s^{-1} , which are typically of pseudocapacitive nature, showing a redox peak pair in the anodic and cathodic sweeps. The anodic part of the CV curve is asymmetric in nature. It is well known that the peaks are representative of reversible charge transfer reactions taking place on the material surface and obviously, in NF sample, faradic charge storage mechanism dominates over electrostatic charge storage mechanism. Thus, the major contribution to the capacitance of the sample is from pseudocapacitance due to reversible electrochemical reactions associated with $[\text{Ni/Fe}]\text{-O}/[\text{Ni/Fe}]\text{-O-OH}$ (Kumar et al., 2018). The observed asymmetric trait in the anodic peak of the CV curve is attributed to these processes. The calculated specific capacitance values are 478, 409, 289, 263, 203, 188 and 176 F g^{-1} for the scan rates of 5, 10, 20, 30, 50, 75 and 100 mV s^{-1} , respectively.

The GCD curves of NF at different current densities in the range from 1 to 16 A g^{-1} are displayed in Figure 5.4(b). The pseudocapacitive GCD curves with symmetrical loops are of high significance in the supercapacitor application. The high discharging time of the electrode material resulted in high specific capacitance values (Foo et al., 2016). The calculated specific capacitance values are 368, 360, 338, 320, 293 and 266 F g^{-1} for the current densities of 1, 2, 4, 8, 12 and 16 A g^{-1} , respectively. The calculated coulombic efficiency value is more than 95% for the GCD curves, which suggests the good charge-discharge profile of the electrode material. The computed specific capacity values are 165.6, 162.0, 152.1, 144.0, 131.8 and 119.7 C g^{-1} for the current densities of 1-16 A g^{-1} . A high power density of 3375.0 W kg^{-1} was obtained for the material while maintaining an energy density of 7.5 Wh kg^{-1} at a current density of 16 A g^{-1} . The energy density and power density values are tabulated in Table 5.1.

The reported specific capacitance values in 2 M KOH electrolyte, from the CV and GCD curves, are high as compared to previous reported literature, and are summarized in Table 5.2

Figure 5.4(c) shows the electrochemical impedance spectra in the form of Nyquist plot of NF along with a fitted equivalent circuit, in 2 M KOH electrolyte in the frequency range of 10^5 Hz - 0.01 Hz. From this Figure, it is evident that the material has good electrochemical characteristics such as high capacitance and conductivity. As can be seen from the inset of Figure 5.4(c), there is no semicircle in the high frequency region indicating the low R_s and R_{ct} values. The obtained value of R_s is 0.76 ohm with the conductance value of 1.28 S. An almost flat tail nearly parallel to the Z'' -axis (imaginary axis) in the low frequency region suggests the faster kinetics and ideal capacitive nature of the material. These features may be attributed to the nanoparticle structure with high surface area and large pore volume.

Table 5.1 Energy density and power density values of the NF electrode.

Current density (A g⁻¹)	Energy density (Wh kg⁻¹)	Power density (W kg⁻¹)
1	10.4	225.8
2	10.1	450.0
4	9.5	900.6
8	9.0	1800.0
12	8.2	2696.9
16	7.5	3375.0

The superior electrochemical performance is again tested for cyclic stability for continuous 10000 cycles at a high current density of 8 A g⁻¹. The structure of NF is such that it is able to sustain a rapid electron insertion/de-insertion process and in addition to that the high pore volume allowed the electrolyte ions to move freely across the bulk into the interior of the particles. The cyclic stability test (Figure 5.4d), clearly indicates that the electrode maintains its initial value upto 1500 cycles, thereafter the values slightly decrease. After large number of cycles, the particle aggregation may create hindrance to the transport of the ions inside the pores, which ultimately decreases the capacitance retention ability. At an applied current density of 8 A g⁻¹, 88% initial capacitance value is retained even after 10000 cycles for the NF

electrode material, which is higher than the reported NF and graphene/NF electrode material (Anwar et al., 2011; Aparna et al., 2018; Askari et al., 2020; Bandgar et al., 2018; Bhojane et al., 2017; Gao et al., 2019; Hua et al., 2018; Zhang et al., 2019). The capacitance retention values are compared in Table 5.2. The admittance plot for the single electrode is displayed in inset of Figure 5.4(d). The calculated time constant (τ_0) value for the single electrode is 398 μ s. The obtained high capacitance values are supported by low time constant values.

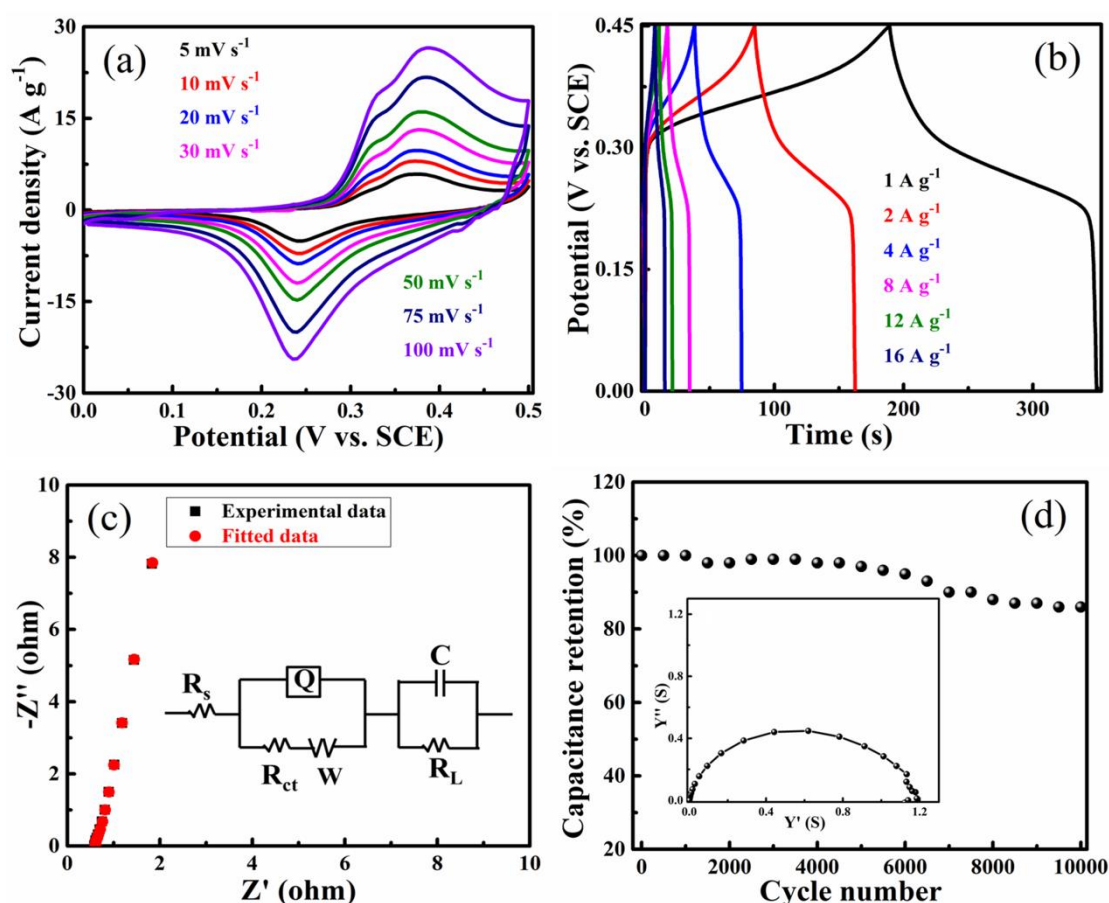


Figure 5.4 Electrochemical analysis of NF in a 3-electrode system: (a) CV curves, (b) GCD curves, (c) Nyquist plot (inset shows the fitted equivalent circuit) and (d) Cyclic stability data of NF for 10000 discharge cycles at a constant current density of 8 A g⁻¹ (inset shows the admittance plot of NF).

Table 5.2 Comparison of electrochemical performance of NF nanoparticles from this work with other reported NF nanostructures in a 3-electrode set up.

Electrode material	C _s from CV (F g ⁻¹)	C _s from GCD (F g ⁻¹)	Electrolyte	Cyclic stability	References
NF nanoparticles	97 @ 2 mV s ⁻¹	---	0.1 M NaCl	100% after 100 cycles @ 5 mV s ⁻¹	Anwar et al. (2011)
NF nanoassemblies	109 @ 2 mV s ⁻¹	---	3 M KOH	> 90% after 1000 cycles @ 10 mV s ⁻¹	Aparna et al. (2018)
NF nanoparticles	229 @ 10 mV s ⁻¹	183 @ 0.5 mA cm ⁻²	1 M KOH	88% after 2000 cycles @ 10 mV s ⁻¹	Askari et al. (2020)
NF nanoflowers	---	435 @ 5 mA cm ⁻²	6 M KOH	80% after 7000 cycles	Bandgar et al. (2018)
NF nanoparticles	---	174 @ 1 A g ⁻¹	1 M KOH	130% after 2000 cycles @ 1 A g ⁻¹	Gao et al. (2019)
NF nanocrystals	---	562 F g ⁻¹	2 M KOH	84% after 1000	Hua et al. (2018)

				cycles @ 4 A g ⁻¹	
NF nanocubes	---	325 @ 3 A g ⁻¹	1 M KNO ₃	79% after 10000 cycles @ 3 A g ⁻¹	Zhang et al. (2019)
NF nanoparticles	478 @ 5 mV s ⁻¹	368 @ 1 A g ⁻¹	2 M KOH	88% after 10000 cycles @ 8 A g ⁻¹	Present work

5.3.3 Electrochemical Study of Fabricated Supercapacitor Using NF Electrodes

The electrochemical performance of the fabricated supercapacitor is displayed in Figure 5.5. The CV curves at the scan rates ranging from 2-100 mV s⁻¹ are rectangular in shape indicating a signature of good electrochemical performance of the material and are suitable for supercapacitor application (Figure 5.5a) (Sethi et al., 2019b). The calculated specific capacitance values are 89, 77, 71, 64, 58 and 45 F g⁻¹ for the scan rates ranging from 2-100 mV s⁻¹. The GCD studies for the current densities ranging from 0.5-8 A g⁻¹ are displayed in Figure 5.5(b) and the symmetrical nature is an indication of good capacitive property. The calculated specific capacitance values are 64.0, 58.4, 52.0, 45.7, 39.0 and 23.6 F g⁻¹ for the current densities ranging from 0.5-8 A g⁻¹.

The Nyquist plot of the fabricated supercapacitor along with equivalent circuit displayed in Figure 5.5(c) shows a semicircle in the high frequency region and a large arc related to the resistance offered by the symmetrical cell. Here, the obtained low value of R_s is 1.25 ohm and R_{ct} value of 35.6 ohm.

The cyclic stability study for the symmetrical supercapacitor is performed for 10000 cycles at a higher applied current density of 8 A g⁻¹ (Figure 5.5d). After the 10000th cycle the cell was able to retain 81% of its initial capacitance. The decrease in

the retention value may be due to the particle agglomeration, drying of electrolyte owing to which the electrolyte ions cannot pass through the inner pores and interact only at the surface. The admittance plot for the supercapacitor device is displayed in inset of Figure 5.5(d). The calculated time constant (τ_0) value for the supercapacitor device is 10000 μs . The obtained low capacitance values are supported by high time constant values. The calculated energy density and power density values from the GCD curves are tabulated in Table 5.3. Also, the obtained capacitance value for the supercapacitor cell is compared with the recently reported literature (Table 5.4).

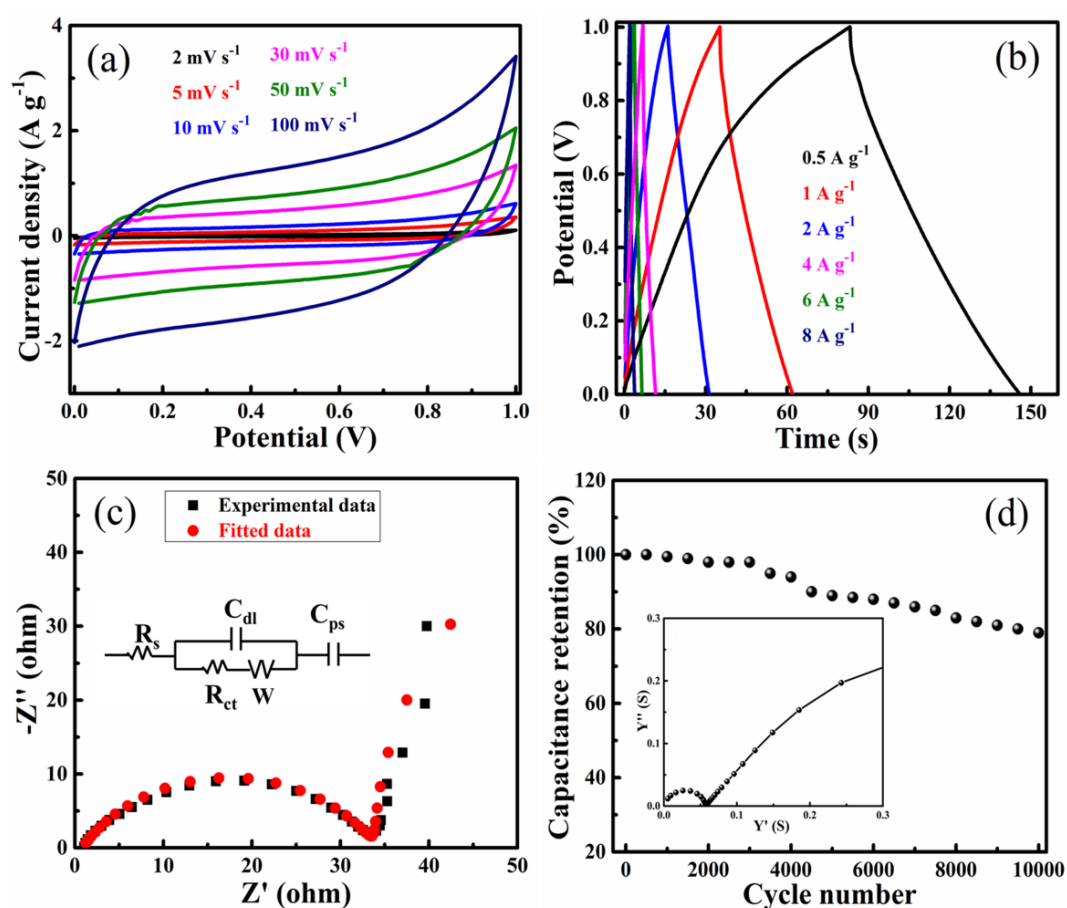


Figure 5.5 Electrochemical analysis of the fabricated supercapacitor device: (a) CV curves, (b) GCD curves, (c) Nyquist plot and (d) Cyclic stability study for 10000 discharge cycles at a constant current density of 8 A g⁻¹ in 2 M KOH electrolyte (inset shows the admittance plot).

Table 5.3 Energy density and power density values of the symmetrical supercapacitor.

Current density (A g⁻¹)	Energy density (Wh kg⁻¹)	Power density (W kg⁻¹)
1	9.0	506.3
2	8.1	1017.4
4	7.2	2031.3
8	6.3	4053.6
12	5.4	6000.0
16	3.2	8027.2

The Z values for the single electrode is estimated to be 0.50 and that for supercapacitor device is 0.22. The obtained values show that nearly 50% and 22% of the active sites are involved in the redox reaction for the electrode and supercapacitor device, respectively indicating the effect of the nano scale morphology along with porous nature of the material.

Table 5.4 Comparison of electrochemical properties of NF supercapacitor device of the present work with that reported in the literature.

Electrode material	C_s (F g⁻¹)	Electrolyte	Cyclic stability	References
NF nanosheet symmetric supercapacitor device	236 @ 2 mA cm ⁻²	PVA-KOH	98% after 7000 cycles (---)	Bandgar et al. (2018)
NF@rGO hybrid supercapacitor device	211 @ 0.5 A g ⁻¹	1 M Na ₂ SO ₄	94% after 5000 cycles @ 10 A g ⁻¹	Cai et al. (2019a)

1D NF/Graphene composite symmetric device	138 @ 0.1 A g ⁻¹	6 M KOH	40% after 10000 cycles @ 1 A g ⁻¹	Fu et al. (2018)
NF@NF//AC asymmetric device	---	2 M KOH	95% after 3000 cycles @ 10 mA cm ⁻²	Zhang et al. (2018)
NF@rGO symmetric supercapacitor device	139 @ 0.5 A g ⁻¹	1 M KNO ₃	93% after 6000 cycles @ 3 A g ⁻¹	Zhang et al. (2019)
NF nanoparticles symmetric supercapacitor device	89 @ 2 mV s ⁻¹ 64 @ 0.5 A g ⁻¹	2 M KOH	81% after 10000 cycles @ 8 A g ⁻¹	Present work

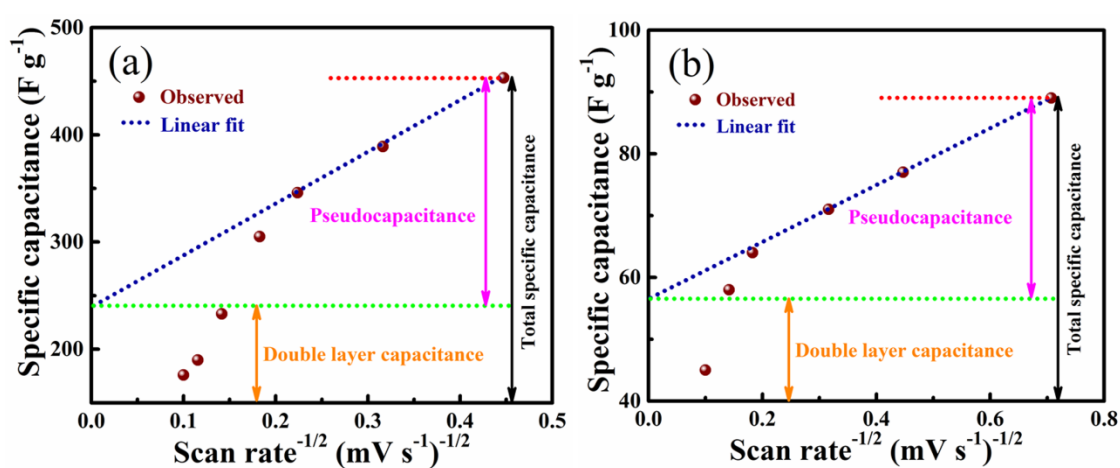


Figure 5.6 Determination of C_{EDL} and C_P contribution of NF in (a) 3-electrode system and (b) The fabricated supercapacitor device.

The graphically estimated value of C_P is 50.3% and C_{EDL} is 49.7% for the NF electrode material (Figure 5.6). Similarly, the C_{EDL} and C_P of the NF in a supercapacitor device are 67.9% and 32.1%, respectively.

5.4 CONCLUSIONS

A solvothermal method is applied for the synthesis of NF nanoparticles possessing high surface area. The NF nanoparticles when tested in a 3-electrode method showed a high capacitance value of 478 F g^{-1} from the CV study at a scan rate of 5 mV s^{-1} and 368 F g^{-1} at a current density of 1 A g^{-1} . The electrode material also depicted high energy density value of 10.4 Wh kg^{-1} and high power density value of 225.8 W kg^{-1} at the applied current density of 1 A g^{-1} . The life span of the material is tested for 10000 cycles and 88% of the initial capacitance value is retained after the charge-discharge cycles at a high current density of 8 A g^{-1} . The superior electrochemical performance of the nanoparticles is mainly ascribed to the nanoscale morphology with high surface area and high porosity providing substantial electroactive sites for the electrolyte ions insertion/de-insertion apart from sustaining its mechanical stability during the electrochemical process.



CHAPTER 6

***A POROUS GRAPHENE-NiFe₂O₄
NANOCOMPOSITE WITH HIGH
ELECTROCHEMICAL PERFORMANCE AND
HIGH CYCLING STABILITY FOR ENERGY
STORAGE APPLICATIONS***

Chapter 6 presents the synthesis and characterization of PGNF nanocomposites prepared through a solvothermal method. The morphological and structural features are thoroughly studied by sophisticated analytical tools. The synthesized material is studied for its utility in supercapacitors.

6.1 INTRODUCTION

The search for the novel multifunctional materials has attracted great interest among the scientific community owing to their peculiar traits. PG, a wonder material is one among such kinds, which exhibits excellent physical, chemical and electrical properties. Although the presence of pores increases the surface area, it suffers from the disadvantage of restacking of the sheets due to the π - π interaction. In order to solve this issue, researchers have tried to incorporate oxides of metals/spinel inside the sheets so as to keep the sheets apart by adding the foreign molecules as spacers (Ghosh et al., 2018; Meng et al., 2018; Sethi et al., 2020a). In this scenario, spinels are of much interest, as they provide high electrical conductivity owing to their abundance, presence of two metal domains and their environmentally benign nature (An et al., 2019). Thus, composite of PG and spinels are expected to provide superior electrochemical properties compared to single oxides due to their high mechanical strength, stability, high electrical conductivity and enhanced physico-chemical properties (Sethi et al., 2020a).

Many spinels of Ni, such as NiO, NiMoO₄ and NiMn₂O₄ with their graphene composites have been utilized as attractive electrode materials for supercapacitors. However, not much is explored with regard to the spinel NF and its graphene composites (Bashir et al., 2019; Fu et al., 2018; Wang et al., 2013). NF nanostructures and its composites with materials such as graphene, polyaniline, carbon nanofibers, poly(3,4-ethylenedioxythiophene) (PEDOT), carbon nano tube (CNT), MoS₂ etc., have been prepared and studied for their electrochemical performance (Bashir et al., 2019; Fu et al., 2018; Ge et al., 2016; Ghosh et al., 2018; Hareesh et al., 2016; Kumar et al., 2018; Wang et al., 2013; Zhang et al., 2019; Zhao et al., 2017). The reports reveal the versatile utility of the NF composites, but when checked for the

supercapacitive performance it is found that their performance is not appreciable either in terms of capacitance value, cyclic stability or rate capability values.

6.2 EXPERIMENTAL SECTION

For the synthesis of x-PGNF (x = 5, 10, 15, 20, 25 and 30 wt% GO loading) composites, a calculated quantity of GO (30 mg, 60 mg, 102 mg, 145 mg, 193 mg, 248 mg for 5, 10, 15, 20, 25 and 30 PGNF, respectively) was dissolved in a 1:1 mixture of water and ethylene glycol and sonicated in a bath sonicator for 2 h in order to achieve complete dispersion. Then, 1 mmol $\text{Ni}(\text{NO}_3)_2 \cdot 4\text{H}_2\text{O}$ and 2 mmol $\text{Fe}(\text{NO}_3)_3 \cdot 9\text{H}_2\text{O}$ were mixed separately in a 10 mL mixture of water and ethylene glycol (1:1) and were added to the dispersion and stirred continuously for 1 h. Then, 6 mmol of urea was added slowly and again stirred for 30 minutes. The whole reaction mixture was then transferred into a stainless steel autoclave of 100 mL capacity and was heated at 160 °C for 18 h. Afterward, the oven was cooled to room temperature and the products were collected and washed with deionized water several times followed by washing with a 1:1 water: ethanol mixture till the pH became neutral and dried at 70 °C overnight. The products were calcined at 400 °C for 2 h in a muffle furnace to obtain PGNF composites and were named 5 PGNF, 10 PGNF, 15 PGNF, 20 PGNF, 25 PGNF and 30 PGNF, respectively depending on the % of GO loading. The characterization and electrochemical studies were carried out as mentioned in chapter 2.

6.3 RESULTS AND DISCUSSION

6.3.1 Structural, Elemental and Morphological Analysis

The powder XRD patterns of NF and 10 PGNF at angles 18.4°, 30.29°, 35.67°, 37.6°, 43.38°, 53.95°, 57.38°, 63.02°, 74.60° correspond to the (111), (220), (311), (222), (400), (422), (511), (440) and (533) crystal planes of the NF which match well with the standard JCPDS card number # 074-2081 (Bhosale et al., 2015; Sethi et al., 2020b) as shown in Figure 6.1(a).

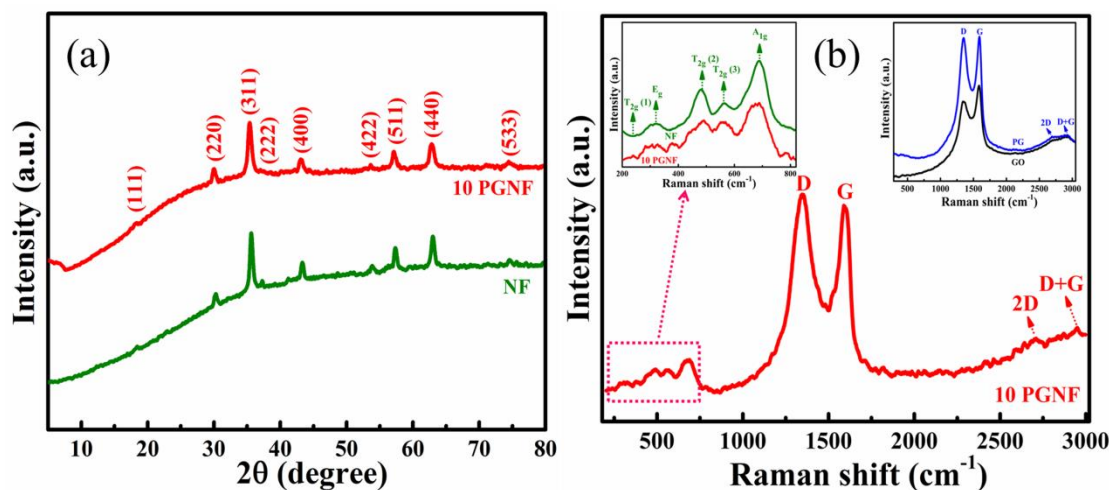


Figure 6.1 (a) XRD pattern of NF and 10 PGNF, (b) Raman spectra of 10 PGNF (inset shows the Raman spectra of NF, GO and PG).

The XRD peaks are sharp at the top and slightly broadened at the base, which suggests the crystalline nature and nano dimension of the synthesized NF and 10 PGNF material. In the 10 PGNF composite sample, widening of the XRD peaks is observed as compared to bare NF sample, this can be attributed to the introduction of PG in the NF phase. Also, no other diffraction planes are present in the XRD pattern, indicating the purity of the prepared material.

The Raman spectrum for GO, PG, NF and 10 PGNF is shown in Figure 6.1(b). The Raman spectra of GO and PG depicts the appearance of D, G, 2D and D+G bands which suggest the formation of oxide of graphite and PG (inset of Figure 6.1b) (Mohamed et al., 2017a; Sethi et al., 2019a). The Raman spectra of 10 PGNF composite shows the Raman signatures of D band at 1347.3 cm^{-1} , G band at 1597.8 cm^{-1} , 2D band at 2703.3 cm^{-1} and D+G band at 2949.8 cm^{-1} . The intensity of D band in 10 PGNF composite is somewhat higher as compared to the G band, suggesting that good amount of defect sites is introduced in the composite sample. Also, the appearance of D+G band in the composite strongly supports the presence of defects in the sample (Sethi et al., 2020a). The peaks in the range, $200\text{-}750\text{ cm}^{-1}$ correspond to the vibrational modes of NF (Sethi et al., 2020b). The magnified spectrum of NF is shown as an inset, where the assigned Raman peaks correspond to the spinel NF phase

(Sethi et al., 2020b; Zhao et al., 2018). The above result confirms the formation of PGNF composite under solvothermal method. The ratio of I_D/I_G is a measure of the formation of the defects in the carbon materials (Sadiq et al., 2018b). The calculated I_D/I_G values for GO, PG and 10 PGNF are 0.76, 1.01 and 1.06, respectively. The increase in the I_D/I_G value for 10 PGNF composite as compared to PG strongly supports the presence of defects in the sample which may offer many active sites for the storage of charge and can contribute to the enhancement of the specific capacitance values of the material (Zhang et al., 2019).

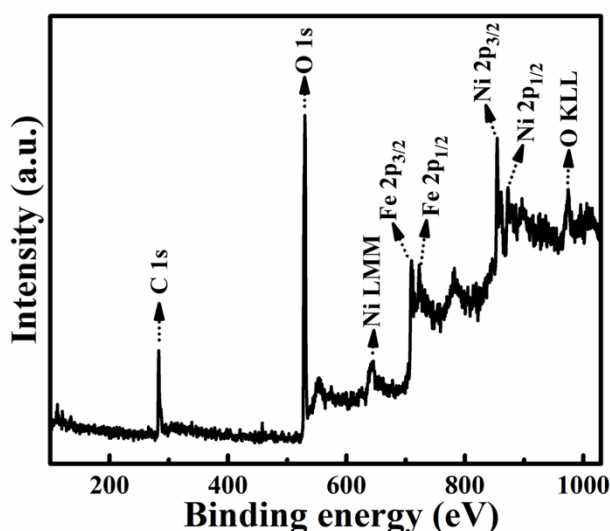


Figure 6.2 XPS survey spectrum of 10 PGNF composite.

The XPS survey spectrum of 10 PGNF composite is shown in Figure 6.2, displaying the presence of elements like C, O, Fe and Ni in the sample without any other elements, depicting the purity of the sample. From the XPS spectrum, the oxidation states of the metal with their corresponding binding energies and metal-oxygen binding energies can be determined. The high resolution deconvoluted XPS spectrum of C 1s is shown in Figure 6.3(a) and the binding energies at 284.2, 285.6, 286.2 and 288.1 eV corresponds to the C=C, C-O, C=O and O-C=O bonds, respectively (Mohamed et al., 2017a; Sadiq et al., 2017d). The high resolution O 1s spectrum is deconvoluted into 3 peaks in Figure 6.3(b) with binding energies of 529.4, 531.0 and 532.0 eV ascribed to the M-O-M, O-C=O and C=O bonds, respectively

(Sadiq et al., 2017d). The high resolution Ni 2p spectrum, in Figure 6.3(c) and Fe 2p spectrum in Figure 6.3(d) shows the presence of +2 and +3 oxidation states of Ni and Fe, respectively and are well consistent with the reported literatures (Subramanya et al., 2015c; Badrayyana et al., 2015d; Zhang et al., 2016; Zheng et al., 2018).

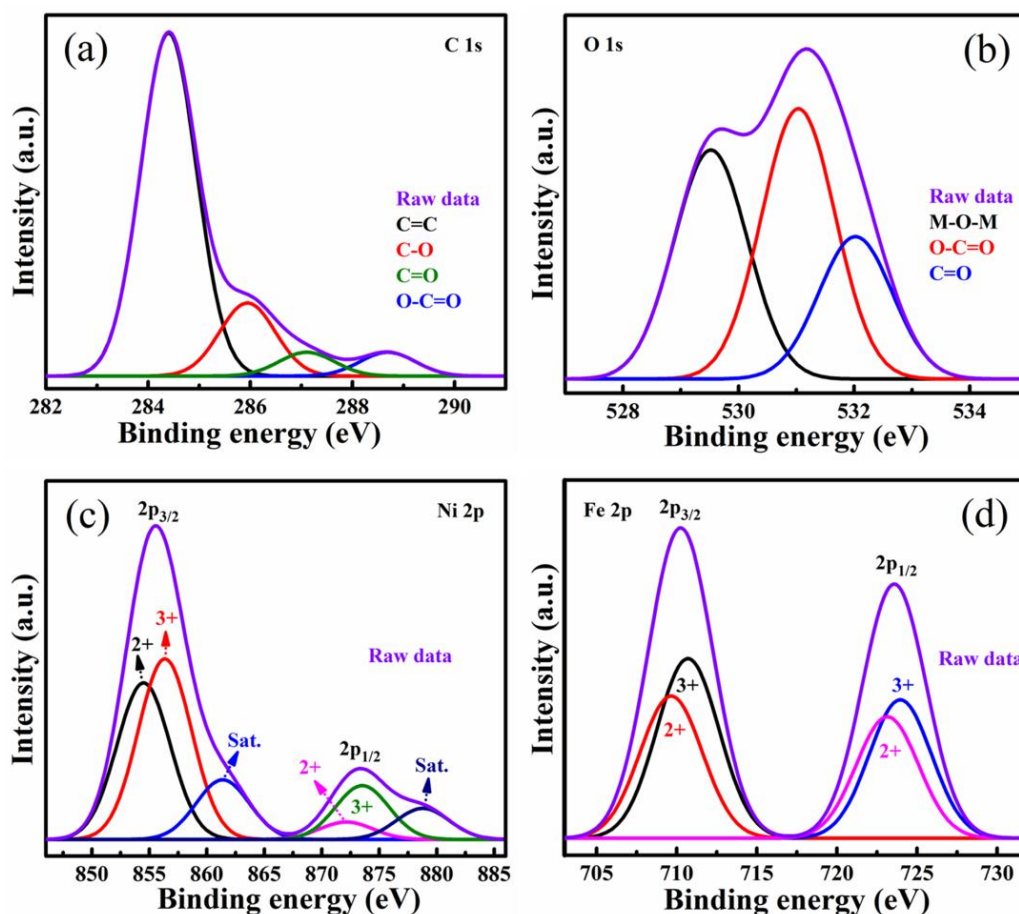


Figure 6.3 XPS deconvoluted spectra of (a) C 1s, (b) O 1s, (c) Ni 2p and (d) Fe 2p, of 10 PGNF composite.

The FTIR spectrum for 10 PGNF is presented in Figure 6.4 along with that of NF and PG for comparison. In the 10 PGNF sample the observed peak at 1568 cm^{-1} is due to the skeletal vibration from PG sample. The peak at 591 cm^{-1} corresponds to the metal-oxygen vibrational modes of NF (Bashir et al., 2019; Wang et al., 2013). The FTIR result is again corroborating the results from Raman analysis.

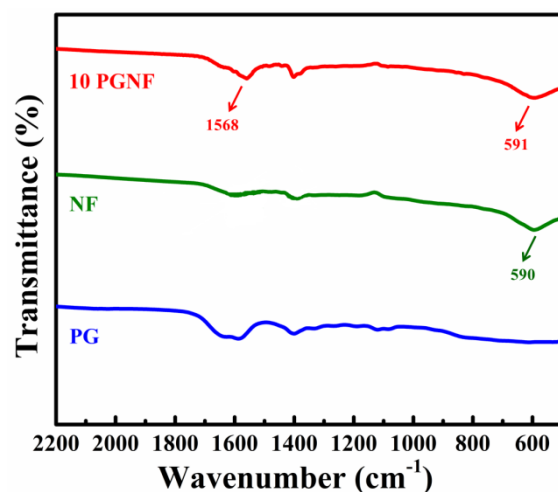


Figure 6.4 FTIR spectra of PG, NF and 10 PGNF.

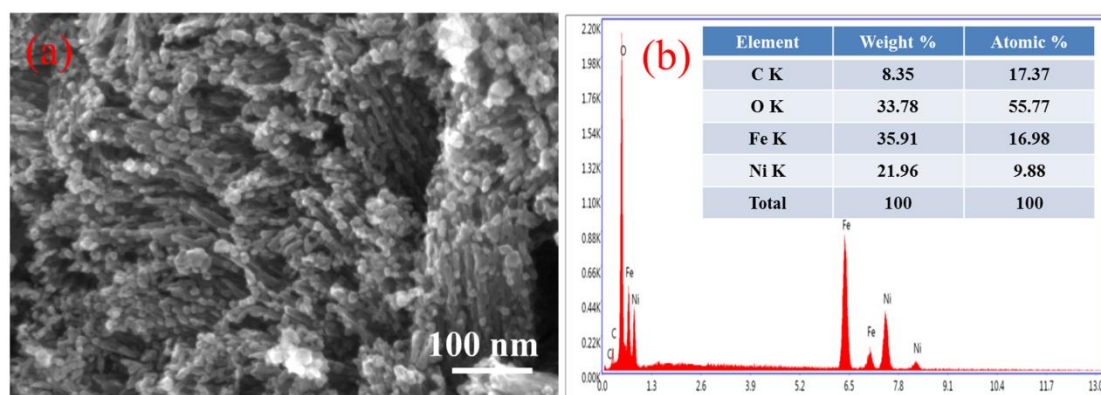


Figure 6.5 FESEM image of (a) 10 PGNF and (b) EDX profile of 10 PGNF.

The 10 PGNF composite shown in Figure 6.5(a) displays slightly aggregated distribution of NF nanoparticles over the PG surface, ensuring the anchoring of NF nanoparticles over PG surface. The EDX image in Figure 6.5(b) reveals the presence of C, O, Ni and Fe only and confirms the purity of the material formed. The TEM images of the composites are displayed in Figure 6.6. The low and high magnification image in Figure 6.6(a) and 6.6(b) shows the presence of NF nanostructures anchored on the PG surface. The HRTEM image is shown in Figure 6.6(c), where the measured lattice fringe corresponds to the (311) crystal plane of NF. The SAED pattern of NF in

Figure 6.6(d) confirms the polycrystalline nature of the material and the concentric patterns matches with the crystal plane details of NF nanoparticles.

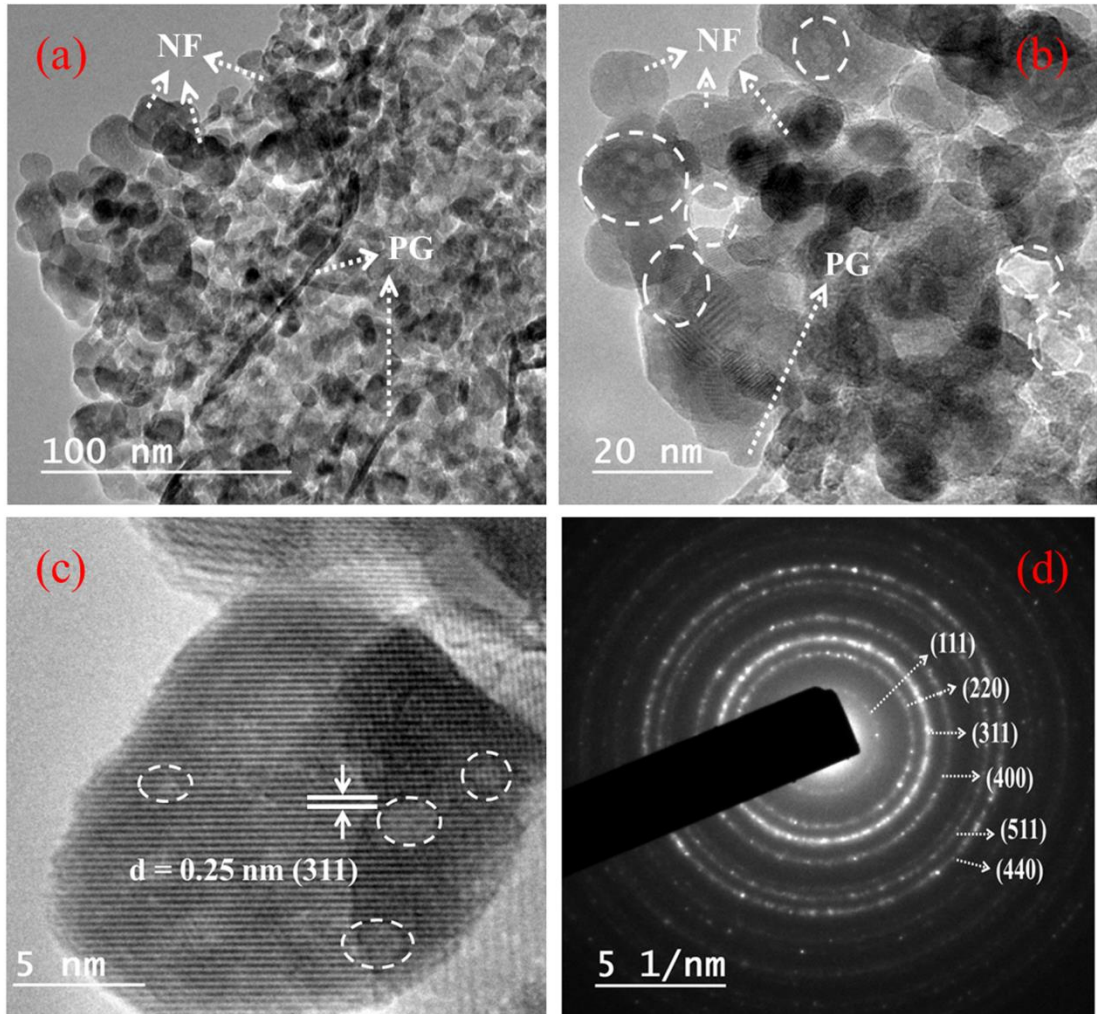


Figure 6.6 TEM (a) Low magnification image, (b) High magnification image (pores are marked with white circles), (c) HRTEM image and (d) SAED pattern of 10 PGNF.

The elemental profile determined from the highlighted portion of 10 PGNF composite (Figure 6.7a) for C, Ni, Fe and O are presented in the Figure 6.7(b), 6.7(c), 6.7(d) and 6.7(e), respectively showing uniform distribution of the elements verifying the formation of the PGNF composite.

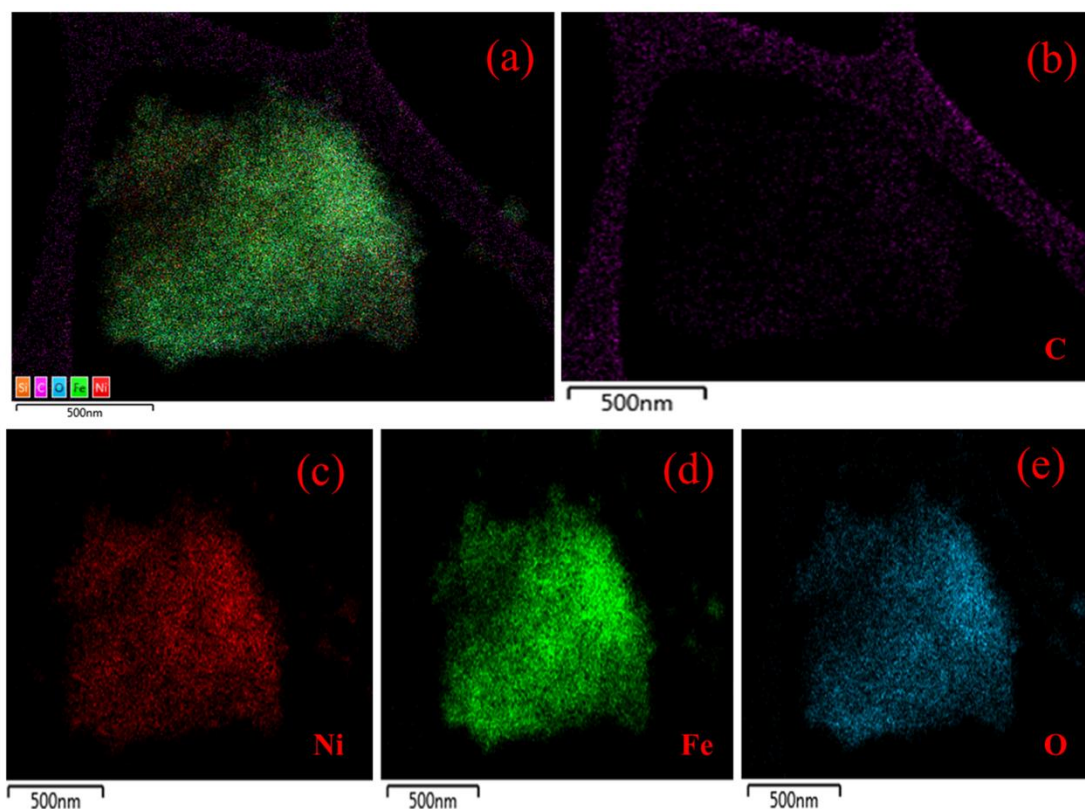


Figure 6.7 (a) Highlighted image from where the EDS mapping is done, elemental mapping of (b) C, (c) Ni, (d) Fe and (e) O.

The BET surface area for the 10 PGNF composite is found to be $107 \text{ m}^2 \text{ g}^{-1}$ as shown in Figure 6.8, which is quite less as compared to the PG sample ($269 \text{ m}^2 \text{ g}^{-1}$), due to the reduction in surface area as a result of the anchoring of bush like NF nanoparticles on to the PG surface (as shown in the FESEM and TEM images). However, the obtained surface area for our composite material is impressive and is surpassing some of the previously reported literatures such as NF/graphene nanosheets ($92.18 \text{ m}^2 \text{ g}^{-1}$), NF/graphene nanosheet composite ($47.6 \text{ m}^2 \text{ g}^{-1}$), NF/rGO composite ($78.4 \text{ m}^2 \text{ g}^{-1}$), NF/graphene capsule composite ($43.6 \text{ m}^2 \text{ g}^{-1}$), NF/RGO composite ($57.3 \text{ m}^2 \text{ g}^{-1}$), NF/MoS₂ composite ($45.8 \text{ m}^2 \text{ g}^{-1}$), NF/CNT composite ($70.7 \text{ m}^2 \text{ g}^{-1}$) (Chen et al., 2016; Gao et al., 2020; Li et al., 2017; Shaymaa et al., 2018; Wu et al., 2016; Zhao et al., 2017; Zou et al., 2020). The obtained pore volume and pore diameter for 10 PGNF composite is $0.2 \text{ cm}^3 \text{ g}^{-1}$ and 3.5 nm , respectively.

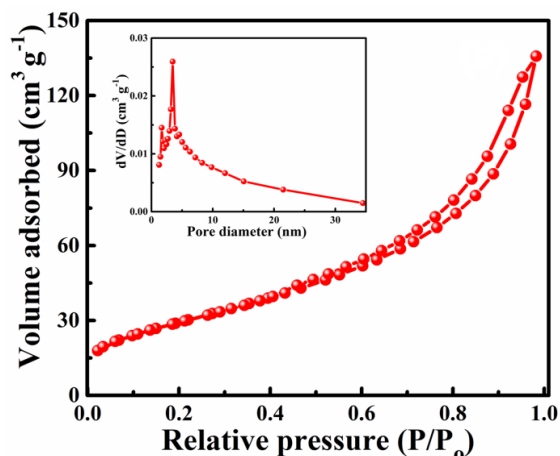


Figure 6.8 BET surface area of 10 PGNF (inset shows the pore size distribution plot).

6.3.2 Electrochemical Study of PGNF Composite Electrodes

The electrochemical performances of all the PGNF composites were analyzed by following a 3-electrode method in 2 M KOH electrolyte. The Figure 6.9(a) shows the CV curves of the PGNF composite electrodes in the potential range of 0-0.5 V at a constant scan rate of 5 mV s^{-1} , the pair of redox peaks appearing in the CV curves is an indication of Faradaic nature of the material. Among the composites, the 10 PGNF composite occupies more area as compared to the other PGNF composites. As capacitance is directly proportional to the area occupied, 10 PGNF can store more charge due to which it can deliver high capacitance value (1465 F g^{-1}). The calculated specific capacitance values for PGNF composite electrodes at a constant scan rate of 5 mV s^{-1} are 753, 1465, 1074, 944, 524 and 374 F g^{-1} for 5, 10, 15, 20, 25 and 30 PGNF composite, respectively.

The GCD curves of the electrodes measured at a constant current density of 1 A g^{-1} at a fixed potential window of 0-0.45 V are shown in Figure 6.9(b). As can be seen from the figure, the GCD curves reveal the battery type nature of the composites. Also, the nearly symmetrical GCD curves are signature of good coulombic efficiency. The calculated coulombic efficiencies are 91.0%, 95.8%, 96.4%, 91.2%, 89.3% and 88.0% for 5, 10, 15, 20, 25 and 30 PGNF composites, respectively. The calculated

specific capacitance values for PGNF composite electrodes at a constant current rate of 1 A g⁻¹ are 541, 1320, 991, 653, 303 and 237 F g⁻¹ for 5, 10, 15, 20, 25 and 30 PGNF composite, respectively. The 10 PGNF electrode material displayed more discharging time and has shown high capacitance value (1320 F g⁻¹) among all the composites.

The Nyquist plots of all the PGNF composite electrodes are shown in Figure 6.9(c). The plot reveals the absence of semicircle, suggesting the low resistance value offered by the material. The straight line in the low frequency region, nearly parallel to the Y-axis is suggestive of good capacitive nature of the electrode material (Balamurugan et al., 2018; Kumar et al., 2018). The resistance values of all PGNF electrodes are listed in Table 6.1.

Table 6.1 Resistance, conductance, knee frequency and time constant values of electrode materials.

Electrode material	Resistance (Ω)	Conductance (S)	Knee frequency (kHz)	Time constant (μs)
5 PGNF	0.60	1.66	10.00	100.0
10 PGNF	0.38	2.63	39.80	25.1
15 PGNF	0.44	2.27	25.10	39.8
20 PGNF	0.58	1.72	15.90	62.9
25 PGNF	0.68	1.47	6.31	158.4
30 PGNF	0.75	1.33	3.98	251.2

The 10 PGNF composite electrode displayed a very low resistance value of 0.38 ohm, which may be due to the high surface area and porous nature of the electrode material, through which the diffusion of electrolyte ions are easily facilitated leading to faster kinetics. As the PG content is increased beyond 10%, there is an increase in the resistance value, which may be due to the blockage of pores/agglomeration of composite electrode materials. The admittance plots are displayed in Figure 6.9(d). From the admittance plots the time constant values can be

obtained by knowing the knee frequency values. The knee frequency value for the PGNF composites and the corresponding time constant values are mentioned in Table 6.1.

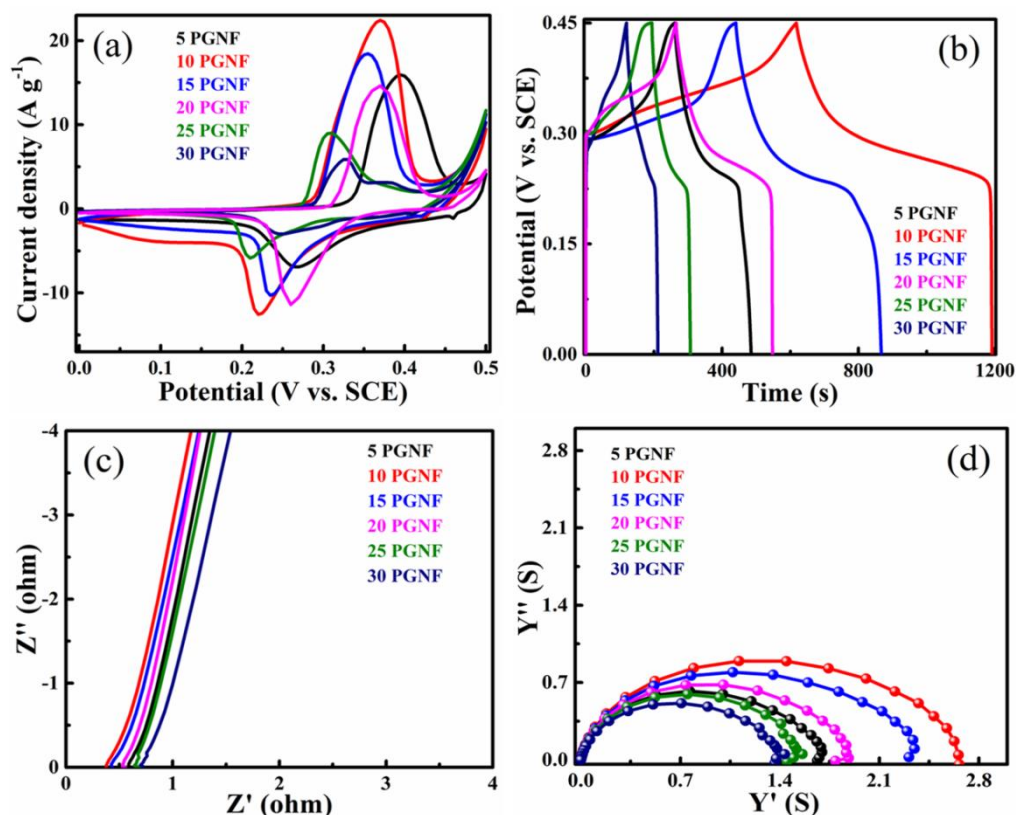


Figure 6.9 Electrochemical performance of PGNF composite electrodes measured in a 3–electrode system. (a) CV curves at a constant scan rate of 5 mV s⁻¹, (b) GCD curves at a constant current density of 1 A g⁻¹, (c) Nyquist plots and (d) Admittance plots.

From Table 6.1, it is obvious that the 10 PGNF composite is showing lower resistance value and higher admittance value, therefore the time constant value is low for 10 PGNF composite electrode, which is in accordance with the high capacitance value offered by the 10 PGNF composite electrode. The obtained higher electrochemical performance for 10 PGNF composite electrode is primarily due to the optimal loading of PG in the composite, after which there is a gradual decrease in the electrochemical performance as the PG loading is increased.

6.3.3 Electrochemical Study of 10 PGNF Composite Electrode

The higher electrochemical performance shown by the 10 PGNF composite electrode material led us to study its electrochemical properties in detail. The CV plot of 10 PGNF reveals Faradaic redox peaks at the anodic and cathodic sweeps demonstrating the pseudocapacitive trait of the material (Figure 6.10a). As the scan rate increases from 5 mV s^{-1} to 50 mV s^{-1} , the CV curves show nearly the same trend without any significant deviation, which suggests the good electrochemical stability of the 10 PGNF electrode material. The computed capacitance values from the CV curves are 1465, 1266, 1121, 876 and 563 F g^{-1} for the scan rates of 5, 10, 20, 30 and 50 mV s^{-1} , respectively. A high capacitance value of 563 F g^{-1} is still obtained with 10 fold increase in the scan rate, suggesting the good rate capability of the electrode material. The variation of specific capacitance values from the CV curves with scan rate for PGNF composites is presented in Table 6.2.

The GCD study of the 10 PGNF electrode material at different current densities ranging from of $1\text{-}20 \text{ A g}^{-1}$ in a fixed potential window of $0\text{-}0.45 \text{ V}$ is shown in Figure 6.10(b). The nearly symmetrical GCD plot shown by the electrode material is an indication of good capacitive property. The estimated specific capacitance values are 1320, 1227, 1129, 1107, 1084, 987, 889 and 800 F g^{-1} for the current densities of 1, 2, 4, 6, 8, 12, 16 and 20 A g^{-1} , respectively. For a 20 fold increase in the current density, the specific capacitance value still remains at 800 F g^{-1} , which is 60.6% of the initial value. This result demonstrates impressive rate capability and the high practical utility of 10 PGNF as a supercapacitor electrode material and further supports the results from CV studies. The estimated coulombic efficiency η (%) value is more than 95% for the GCD curves, which suggests the good charge-discharge profile of the electrode material. The computed specific capacitance and specific capacity values from the GCD curves of PGNF composites are presented in Table 6.3.

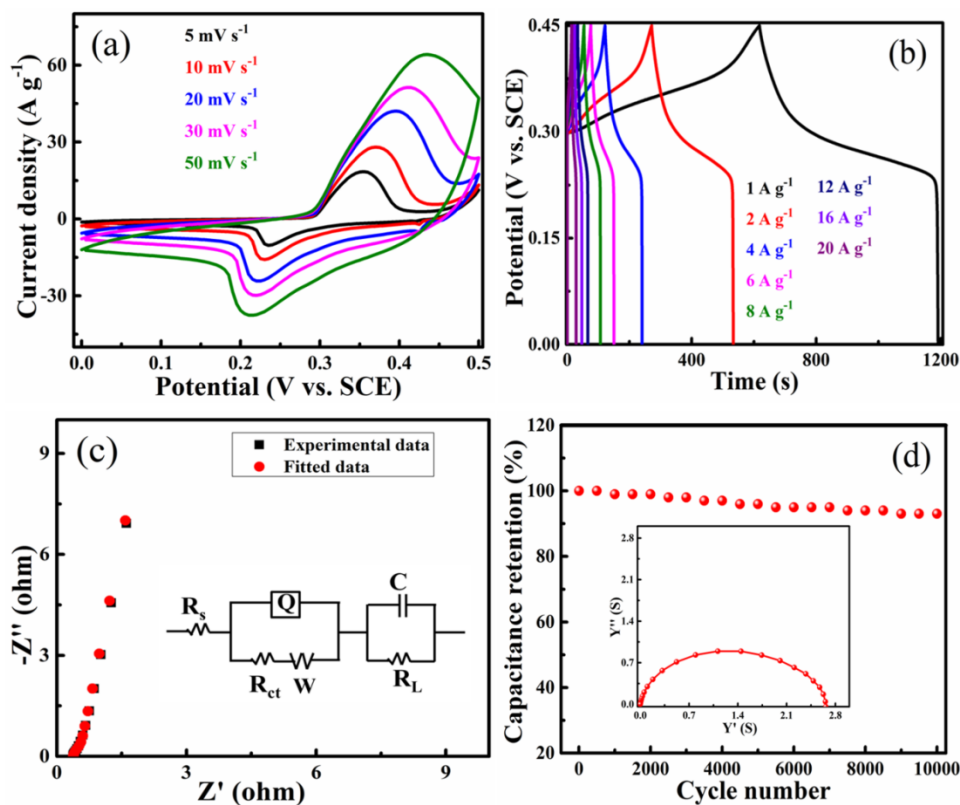


Figure 6.10 Electrochemical performance of 10 PGNF composite electrode. (a) CV curves at different scan rates, (b) GCD at different current densities, (c) Nyquist plot (inset shows the equivalent circuit) and (d) Cyclic stability data of 10 PGNF composite for 10000 discharge cycles at a constant current density of 8 A g^{-1} in 2 M KOH electrolyte (inset shows the admittance plot).

The Nyquist plot of the 10 PGNF composite electrode shown in Figure 6.10(c) reveals the absence of semicircle and a straight line without any deviation in the low frequency region, this type of impedance behavior is highly suitable for supercapacitor utility as they provide low resistance value with high capacitance. The obtained high specific capacitance values are in strong agreement with the impedance results. The cyclic life of the 10 PGNF electrode material is studied for up to 10000 cycles at a high current density of 8 A g^{-1} . It is observed that even after 10000 cycles, around 94% of the initial capacitance value is retained for the electrode material indicating good stability (Figure 6.10d). The admittance plot of 10 PGNF composite electrode is presented as an inset in Figure 6.10(d).

Table 6.2 Specific capacitance values of PGNF composite electrodes from CV.

Composite	Scan rate (mV s⁻¹)	C_s (F g⁻¹)
5 PGNF	5	753
	10	594
	20	481
	30	408
	50	335
10 PGNF	5	1465
	10	1266
	20	1121
	30	876
	50	563
15 PGNF	5	1074
	10	945
	20	847
	30	727
	50	490
20 PGNF	5	944
	10	836
	20	757
	30	562
	50	395
25 PGNF	5	524
	10	473
	20	440
	30	403
	50	315
30 PGNF	5	374
	10	343

	20	319
	30	282
	50	255

Table 6.3 Specific capacitance and capacity values calculated for PGNF composite electrodes from GCD.

Composite	Current density (A g⁻¹)	C_s (F g⁻¹)	Q_s (C g⁻¹)
5 PGNF	1	541	243.5
	2	526	236.7
	4	452	203.4
	6	364	163.8
	8	304	136.8
	12	299	134.6
	16	263	118.4
	20	208	93.6
10 PGNF	1	1320	594.0
	2	1227	552.2
	4	1129	508.1
	6	1107	498.2
	8	1084	487.8
	12	987	444.2
	16	889	400.1
	20	801	360.0
15 PGNF	1	991	446.0
	2	756	340.2
	4	552	248.4
	6	456	205.2
	8	402	181.0

	12	372	167.4
	16	320	144.0
	20	278	125.1
20 PGNF	1	653	293.9
	2	578	260.1
	4	487	219.2
	6	403	181.4
	8	369	166.1
	12	327	147.2
	16	302	135.9
	20	251	113.0
25 PGNF	1	303	136.4
	2	261	117.5
	4	236	106.2
	6	205	92.3
	8	183	82.4
	12	157	70.7
	16	141	63.5
	20	133	59.9
30 PGNF	1	237	106.7
	2	196	88.2
	4	156	70.2
	6	140	63.0
	8	129	58.1
	12	115	51.8
	16	107	48.2
	20	97	43.7

The energy density and power density of the electrode material at current densities ranging from 1-20 A g⁻¹ are displayed in Table 6.4. A high energy density value of 37.2 Wh kg⁻¹ is obtained while maintaining a power density of 225.5 W kg⁻¹

at a current density of 1 A g^{-1} and the electrode material still maintains a good energy density value of 22.5 Wh kg^{-1} with a power density value of 4500.0 W kg^{-1} at a higher current density of 20 A g^{-1} . This result reveals the superb stability of the electrode material. The comparison of electrochemical performance of 10 PGNF electrode with other reported literatures are presented in Table 6.5.

Table 6.4 Energy density and Power density values calculated from GCD graph for 10 PGNF electrode material.

Current density (A g^{-1})	Energy density (Wh kg^{-1})	Power density (W kg^{-1})
1	37.2	225.5
2	34.5	450.3
4	31.8	901.4
6	31.1	1350.4
8	30.4	1802.2
12	27.8	2704.8
16	25.0	3600.4
20	22.5	4500.0

The CV curves of all the composites (5-30 PGNF) at different scan rates ranging from $5\text{--}50 \text{ mV s}^{-1}$ are given in Figure 6.11. The specific capacitance values for all the composites are presented in Table 6.2. The calculated C_{EDL} contributions are 28.1%, 53.8%, 57.7%, 60.9%, 68.4% and 70.0% for 5, 10, 15, 20, 25 and 30 PGNF composite, respectively. As can be seen from the results, as the PG content increased, the extent of C_{EDL} contribution also increased and obviously the C_{P} value got reduced. The trend is in agreement with reported literature (Ruan et al., 2019).

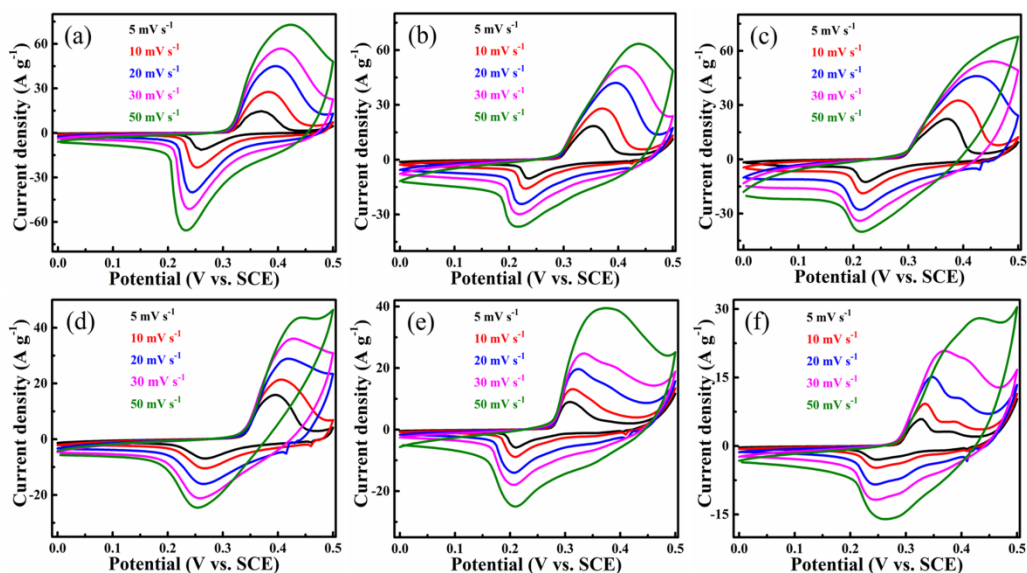


Figure 6.11 CV curves for (a) 5, (b) 10, (c) 15, (d) 20, (e) 25 and (f) 30 PGNF composite.

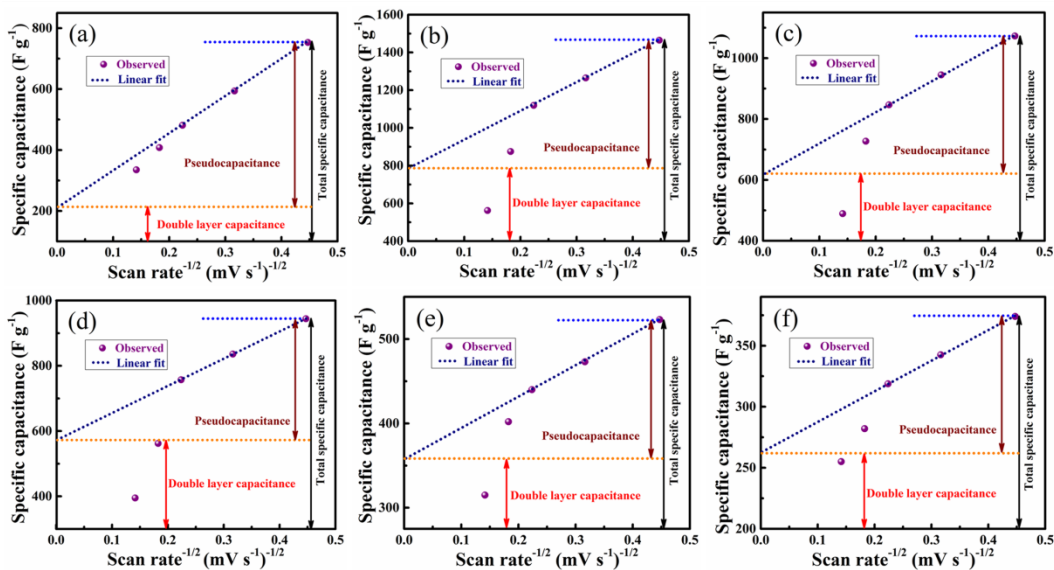


Figure 6.12 Determination of the C_{EDL} and C_P contribution. Specific capacitance vs. inverse square root of scan rate of (a) 5, (b) 10, (c) 15, (d) 20, (e) 25 and (f) 30 PGNF composite.

6.3.4 Electrochemical Study of Fabricated Supercapacitor Using 10 PGNF Composite Electrodes

The 10 PGNF composite electrode material displayed satisfactory results when it was tested as an electrode. This motivated us to study the electrode property in a symmetrical supercapacitor set up in aqueous 2 M KOH electrolyte. The CV curves of the fabricated supercapacitor with 10 PGNF composite electrode at various scan rates ranging from 5-400 mV s⁻¹ shows a rectangular nature, which further predicts the good electrochemical feature of the material (Figure 6.13a). The calculated specific capacitance values from the CV curves are 303, 267, 235, 219, 180, 134, 92, 70 and 54 F g⁻¹ for the scan rates ranging from 5-400 mV s⁻¹. The symmetrical GCD curves at varying current densities ranging from 4-14 A g⁻¹ reveal the good capacitive behavior of the material (Figure 6.13b). The calculated specific capacitance (specific capacity) values from the GCD curves are 160 F g⁻¹ (160 C g⁻¹), 153 F g⁻¹ (153 C g⁻¹), 149 F g⁻¹ (149 C g⁻¹), 138 F g⁻¹ (138 C g⁻¹), 128 F g⁻¹ (128 C g⁻¹), 122 F g⁻¹ (122 C g⁻¹) and 115 F g⁻¹ (115 C g⁻¹) for the current densities varying from 4-14 A g⁻¹ with coulombic efficiency more than 90%.

The Nyquist plot reveals a small semicircle in the high frequency region and flat tail in the low frequency region suggesting good electrochemical characteristics of the supercapacitor (Figure 6.13c). The best fitted equivalent circuit for the device is shown in inset of Figure 6.13(c). The cycle life of the symmetrical supercapacitor was tested for 10000 cycles at an applied current density of 8 A g⁻¹, after the completion of the cycles around 96% of the initial capacitance value is retained for the supercapacitor demonstrating its good cyclic stability (Figure 6.13d). The incorporation of spinel NF nanoparticles in between the PG sheets prevents its restacking due to π - π interaction and results in the formation of a robust hybrid structure. The material maintains its electroactive channels intact without collapsing during repeated cycling leading to enhanced stability of the electrode and fabricated supercapacitor device.

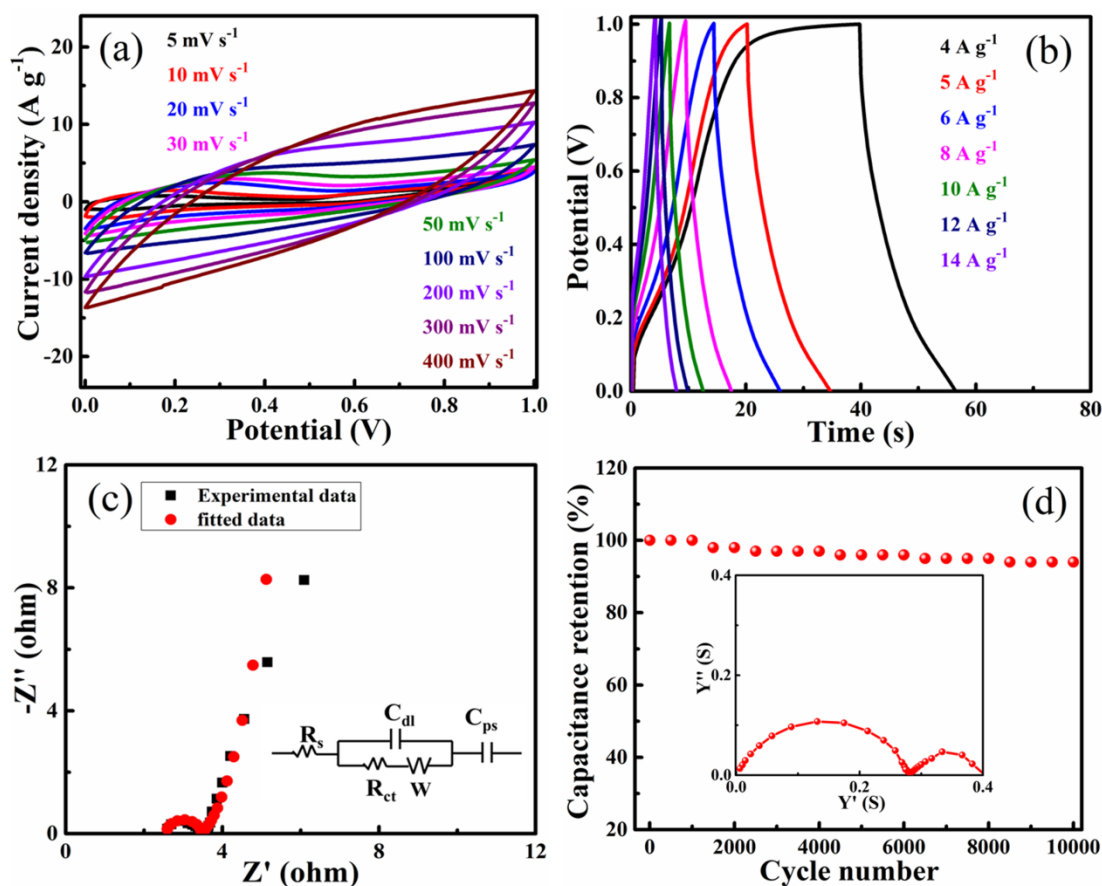


Figure 6.13 Electrochemical analysis of symmetrical supercapacitor device fabricated using 10 PGNF composite electrodes. (a) CV curves at various scan rates, (b) GCD curves at various current densities, (c) Nyquist plot (inset shows the equivalent circuit) and (d) Cyclic stability data for 10000 discharge cycles at a constant current density of 8 A g^{-1} in 2 M KOH electrolyte (inset shows the admittance plot).

The admittance plot of the supercapacitor is displayed in the inset of Figure 6.13(d). The obtained knee frequency for the plot is 398 Hz and the time constant value estimated from this knee frequency value is 0.00251 second ($2510 \mu\text{s}$). The lower time constant value suggests that the device can change from resistive trait to supercapacitor trait within very less time, which is an added quality for a good supercapacitor. The computed energy density and power density values from the GCD curves are displayed in Table 6.5. The obtained energy density and power density values at a current density of 4 A g^{-1} is 22.2 Wh kg^{-1} and 4000.0 W kg^{-1} , respectively

and at a current density of 14 A g^{-1} , they remain 16 Wh kg^{-1} and 14375 W kg^{-1} , respectively showing its stability and utility. The calculated C_{EDL} and C_{P} contribution by graphical method is 55.8% and 44.2%, respectively (Figure 6.14). Also, the obtained specific capacitance values for the electrode material and the fabricated supercapacitor are compared with the recent literature report, which shows an impressive performance of the current material (Table 6.6 and 6.7).

Table 6.5 Energy density and power density values of the 10 PGNF nanocomposite in a fabricated symmetrical supercapacitor device.

Current density (A g^{-1})	Energy density (Wh kg^{-1})	Power density (W kg^{-1})
4	22.2	4000.0
5	21.3	5006.5
6	20.8	6048.4
8	19.1	8023.3
10	17.9	10403.3
12	16.9	12200.0
14	16.0	14375.0

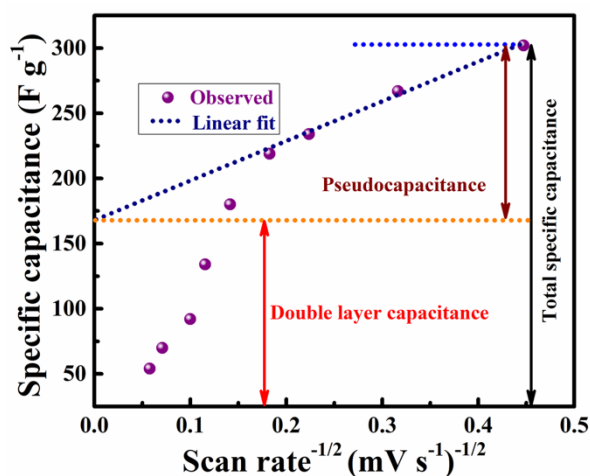


Figure 6.14 Determination of the C_{EDL} and C_{P} contribution of the fabricated symmetrical supercapacitor device.

Table 6.6 Comparison of electrochemical performance of 10 PGNF electrode with other reported literature.

Electrode material	C_s ($F g^{-1}$)	Electrolyte	Cyclic stability	References
Cu substituted NF @ Graphene sheet electrode	735 @ 1.47 $mA g^{-1}$	1 M KOH	85% after 1000 cycles @ 1.47 $mA g^{-1}$	Bashir et al. (2019)
NF@RGO electrode	215.7 @ 0.5 $A g^{-1}$	1 M Na_2SO_4	89% after 10000 cycles @ 10 $A g^{-1}$	Cai et al. (2019b)
NF@RGO electrode	488 @ 1 $A g^{-1}$	PVA- KNO_3 electrolyte	89% after 10000 cycles @ 3 $A g^{-1}$	Zhang et al. (2019)
PGNF electrode	1465 @ 5 mVs^{-1} 1320 @ 1 $A g^{-1}$	2 M KOH	94% after 10000 cycles @ 8 $A g^{-1}$	This work

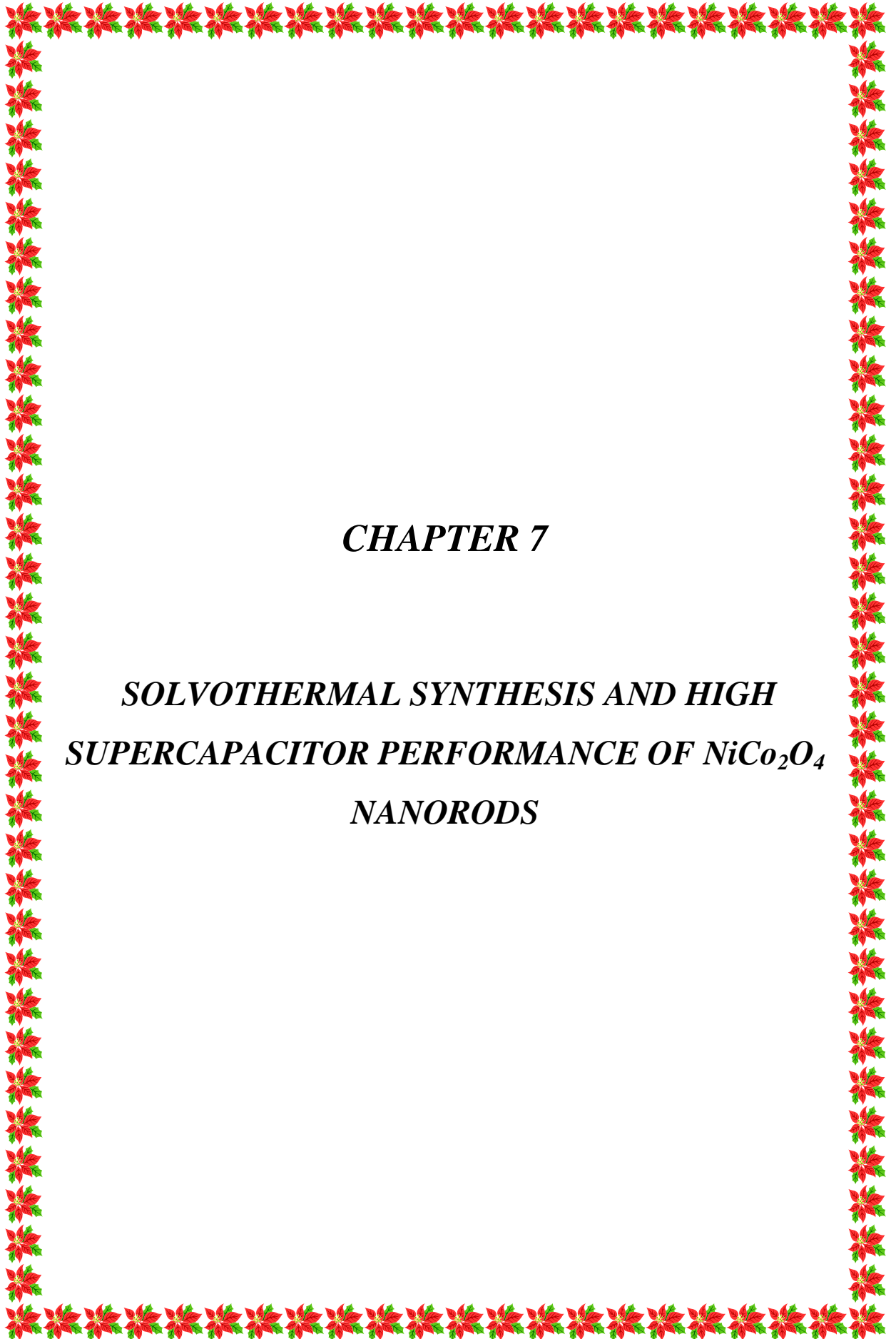
Table 6.7 Comparison of electrochemical properties of 10 PGNF supercapacitor device of the present work with that reported in the literature.

Electrode material	C_s ($F g^{-1}$)	Electrolyte	Cyclic stability	References
NF@Graphene symmetric supercapacitor device	481 @ 0.1 $A g^{-1}$	6 M KOH	99% after 10000 cycles @ 1 $A g^{-1}$	Fu et al. (2018)
NF@CNT asymmetric supercapacitor device	66 @ 5 $mV s^{-1}$	2 M KOH	79% after 2500 cycles @ 2 $A g^{-1}$	Kumar et al. (2018)
NF@Graphene symmetric supercapacitor device	3.1 @ 100 $mV s^{-1}$	1 M Na_2SO_4	---	Soam et al. (2020)

NF@RGO symmetric supercapacitor device	121 @ 0.5 A g ⁻¹	PVA-KNO ₃ electrolyte	93% after 6000 cycles @ 3 A g ⁻¹	Zhang et al. (2019)
PGNF symmetric supercapacitor device	303 @ 5 mV s ⁻¹ 160 @ 4 A g ⁻¹	2 M KOH	96% after 10000 cycles @ 8 A g ⁻¹	This work

6.4 CONCLUSIONS

The synthesis of the PGNF nanocomposite via a solvothermal method is reported in which the NF nanoparticles incorporated in PG has led to good electrochemical performance as a single electrode material and as a supercapacitor. The electrode material showed a high capacitance value of 1465 F g⁻¹ at a scan rate of 5 mV s⁻¹ and 94% initial capacitance retention value after 10000 cycles at a high current density of 8 A g⁻¹. The fabricated symmetrical supercapacitor device also showed an appreciable specific capacitance value of 303 F g⁻¹ at a scan rate of 5 mV s⁻¹ and retained 96% initial capacitance value after 10000 cycles at a high current density of 8 A g⁻¹. The energy density and power density values of the fabricated supercapacitor were 22.2 Wh kg⁻¹ and 4000.0 W kg⁻¹, respectively at the current density of 4 A g⁻¹ and 16 W h kg⁻¹ and 14375 W kg⁻¹, respectively at current density of 14 A g⁻¹. This superior electrochemical performance is mainly due to the synergic contribution from the component materials making it a promising electrode material for supercapacitor application.



CHAPTER 7

***SOLVOTHERMAL SYNTHESIS AND HIGH
SUPERCAPACITOR PERFORMANCE OF NiCo_2O_4
NANORODS***

Chapter 7 deals with the synthesis and characterization of NC nanorods prepared through a solvothermal method. The morphological and structural features are thoroughly studied by sophisticated analytical tools. The synthesized material was studied its utility for the application in supercapacitors.

7.1 INTRODUCTION

Rapid depletion of conventional energy sources has caused growing demand and concern for portable, affordable and environment-friendly power sources. Hence, research activities are now accelerated towards the development of alternative energy sources, i.e. energy storage and conversion devices (Arico et al., 2005; Gregory et al., 1972; Walsh et al., 2001; Winter et al., 2004). Current research is focused on developing robust, environmentally friendly, lightweight and economic electrochemical energy storage and conversion devices to mitigate the energy crisis. As the pseudocapacitive phenomena is dependent on the transfer of charge between electrode and electrolyte, a competent way to ameliorate the storage capacity is to synthesize the materials with specific morphology of nano dimensions and high surface area. In this context solvothermal route is an attractive method to produce the desired morphology with good selectivity which will be beneficial for the energy storage applications (Li et al., 2014; Umeshbabu et al., 2014).

The literature survey on solvothermal synthesis of NC nanostructures (hexagonal NC nanostructures, NC nanoneedles, NC nanoparticles and nanowires, NC nanoplates, NC nanoparticles, NC quantum dots, urchin and sheaf like NC nanostructures, NC crystals and NC nanowires) reveals that most of the synthetic work has been done using water or a mixture of water with either DMF (Dimethylformamide) or alcohol (Bhagwan et al., 2019; Cao et al., 2020; Chatterjee et al., 2020; Kim et al., 2016; Saravanakumar et al., 2017; Siwatch et al., 2020; Umeshbabu et al., 2014; Wu et al., 2011; Yuan et al., 2012). The aid of surfactants like CTAB has been taken. As per our knowledge, not many reports are there on the preparation of NC nanorods using 1:1 mixture of water and ethylene glycol. Since the removal of final traces of surfactant is difficult, the present work opted for a

surfactant free route using a low temperature solvothermal approach. Since dielectric constant and viscosity plays an important role in the morphology of the final product, in this study water-ethylene glycol mixture was used. Ethylene glycol is known to favor the formation of 1D structures and addition of it as a co-solvent decreases the dielectric constant of water and hence leads to homogenous precipitation due to creation of supersaturation in low dielectric medium solvents and faster kinetics (Hu et al., 2000; Yang et al., 2013). Also, surfactant free low temperature synthesis using this combination has not been reported yet. In addition, the solvent mixture used is green and environmentally friendly. Therefore, the present study is carried out through a solvothermal method without the addition of surfactants and with an aim to improve the electrochemical performance in terms of capacitance and cyclability at higher current densities. Also, in the earlier reports, the electrochemical analysis was done utilizing Ni foam as the current collector, which is costlier as compared to the Ni sheet. It is evident that there is much scope for further investigation of NC nanostructures.

7.2 EXPERIMENTAL SECTION

For the synthesis of NC nanorods, 2 mmol $\text{Co}(\text{Ac})_2 \cdot 4\text{H}_2\text{O}$ and 1 mmol $\text{Ni}(\text{Ac})_2 \cdot 4\text{H}_2\text{O}$ were mixed in deionized water and ethylene glycol mixture (1:1) with the aid of ultrasonication. Then, 3 mmol urea was dissolved in deionized water and ethylene glycol mixture and was added slowly to the above solution while stirring. After 1 h, the whole reaction mixture was placed into a teflon-lined stainless-steel autoclave and kept at 160 °C for 16 h in an electric oven. After cooling, the violet pink colored product was collected by repeated centrifugation and washed by deionized water followed by ethanol and kept for drying at 60 °C overnight. Then, the product was calcined at 400 °C for 2 h in air to obtain spinel NC nanorods.

7.3 RESULTS AND DISCUSSION

7.3.1 Structural, Elemental and Morphological Analysis

The XRD peaks (Figure 7.1a) at 31.09° , 36.61° , 38.48° , 44.54° , 55.28° , 59.16° and 64.86° corresponded to the (220), (311), (222), (400), (422), (511) and (440) crystal planes of cubic phase NC, which matches well with the standard JCPDS card no. 20-0781 (Mondal et al., 2015). The average crystallite size was found to be 11.23 nm. The obtained XRD traces exhibit sharp peaks, which confirm the highly crystalline nature of the prepared NC nanorods.

Raman analysis was done in order to confirm the composition and structure of the as synthesized sample, the spectra is presented in Figure 7.1(b). The peaks at 473, 527 and 620 cm^{-1} represents the E_g , F_{2g} and A_{1g} phonon modes of NC, respectively. There is no indication of the presence of OH group in the Raman spectra, which suggests the absence of hydroxides of Ni or Co and formation of pure NC phase after calcination in air. The peak at 473 cm^{-1} is attributed to the Raman active mode E_g corresponding to the stretching vibrations of Co-O and Ni-O bonds. The peaks at 527 cm^{-1} and 620 cm^{-1} can be indexed to the F_{2g} and A_{1g} Raman active phonon modes of Co-O stretching vibration of the NC sample (Siwatch et al., 2020), respectively.

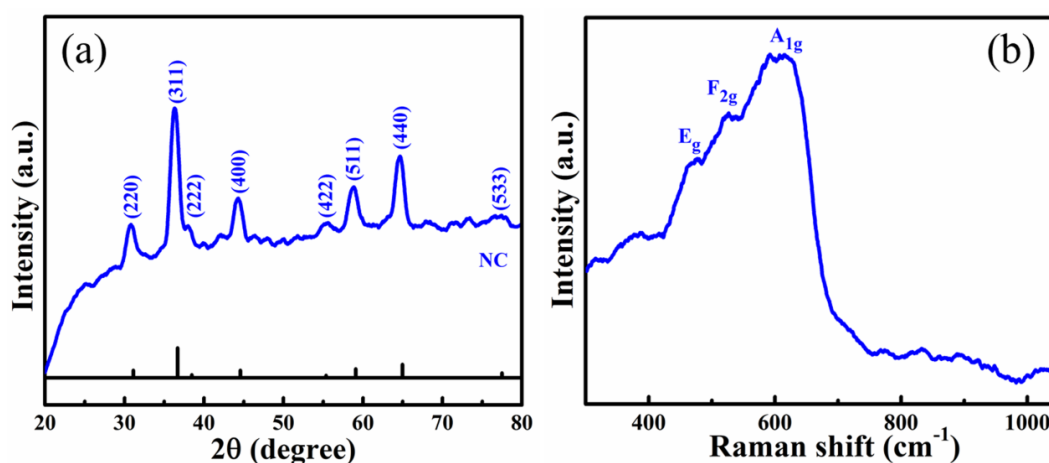


Figure 7.1 (a) XRD pattern with standard data and (b) Raman spectra of the NC nanorods.

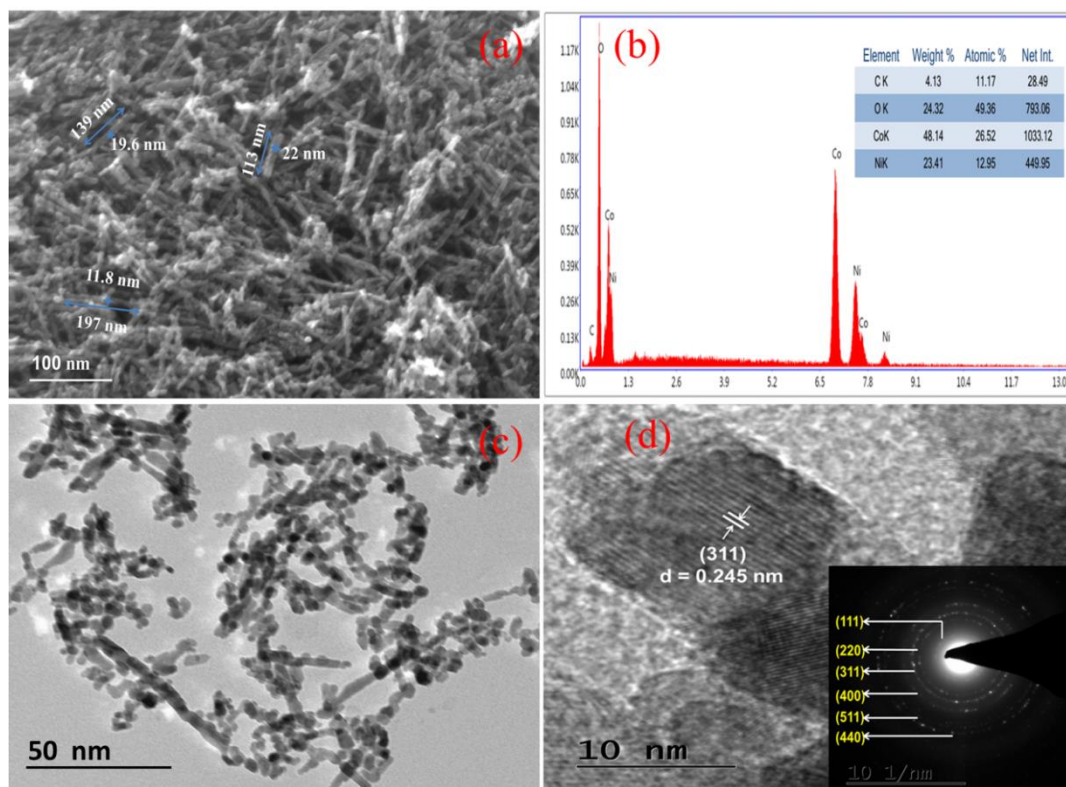


Figure 7.2 (a) FESEM image, (b) EDX profile with elemental composition data as an inset, (c) TEM image and (d) HRTEM image and the SAED pattern (inset) of the NC.

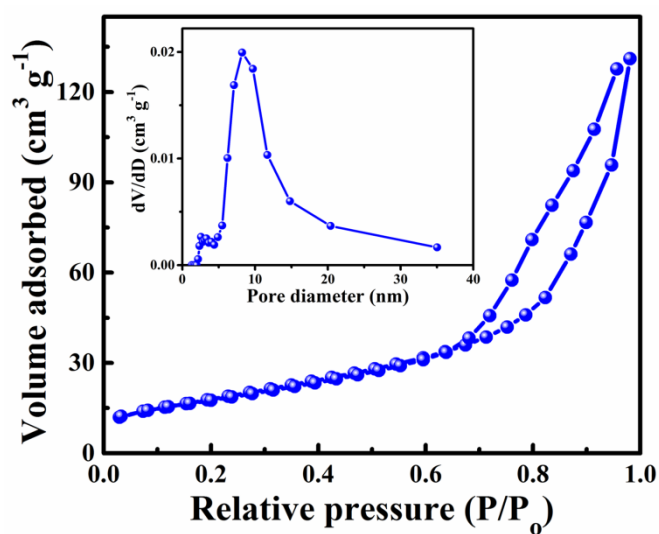


Figure 7.3 Nitrogen adsorption and desorption isotherm of the NC nanorods (inset shows the pore size distribution curve).

The FESEM image shown in Figure 7.2(a) reveals that uniform nanorods are formed. The measured length of the nanorods was in the range of 100-200 nm, whereas its diameter ranged from 15-25 nm. This kind of 1D morphology is quite ideal for the application of supercapacitor electrode material (Yang et al., 2013) and expected to show good capacitive behavior. The EDX profile is shown in Figure 7.2 (b), which distinctly demonstrates the presence of elements like Ni, Co and O suggesting the purity of the NC phase. The TEM image shows the formation of uniform nanorods (Figure 7.2c). In HRTEM image, the measured interplanar distance matches well with the high intense (311) crystal plane spacing (Figure 7.2d). The SAED pattern reveals concentric rings depicting the polycrystalline nature of the sample (Figure 7.2d inset). The nano size and high crystallinity of the prepared samples may offer more electroactive surface area for the ion diffusion and in turn will improve electrochemical performance at high rates and thus superior capacitive behavior can be expected from these NC nanorods.

Figure 7.3 shows the BET isotherm of the nanorods, which is classified as Type-IV isotherm in accordance with the IUPAC classification. A high surface area of $65.73 \text{ m}^2 \text{ g}^{-1}$, with a high pore volume of $0.2 \text{ cm}^3 \text{ g}^{-1}$ and the pore size distribution in the range between 2-10 nm along with average pore diameter of 8.23 nm was obtained for the prepared nanorods. Such a high surface area with large pore volume, pore diameter and mesoporous nature of the nanorods is expected to show the good transfer of electrolytes within the pores for better electrochemical redox reactions by enhancing the electrode-electrolyte contact area (Yuan et al., 2012).

7.3.2 Electrochemical Study of NC as an Electrode

The CV curves at scanning rates from $5\text{-}50 \text{ mV s}^{-1}$ are typically pseudocapacitive in nature depicting redox peaks in the anodic and cathodic scans (Figure 7.4a). As the scan rate increases from 5 to 50 mV s^{-1} , the anodic peak moves to higher potential and cathodic peak shifts to lower potential suggesting better electrochemical reversibility (Bhojane et al., 2016; Umeshbabu et al., 2014). The

calculated capacitance values are 440, 416, 375, 316 and 280 F g⁻¹ for 5, 10, 20, 30 and 50 mV s⁻¹, respectively.

The GCD curves of the material (Figure 7.4b) shows the charge-discharge curves at applied current densities ranging from 1 to 12 A g⁻¹. The GCD curves are highly symmetrical, suggesting the good capacitive property. The measured capacitance values from the GCD curves are 233, 186, 143, 121, 107 and 87 F g⁻¹ for current densities 1, 2, 4, 6, 8 and 12 A g⁻¹, respectively. The computed coulombic efficiency for the charge-discharge curves is more than 86%, which corroborates the good charge-discharge trait of the NC electrode material. From the electrochemical study, it is concluded that with the increase in scan rate/current density, the capacitive performance showed a decrease in the value. This could be owing to the fact that, at lower scan rate/current density, the electrolyte ions have sufficient time to move across the active sites of the electrode material contributing to high capacitance values. On the other hand, at higher scan rates the movement of ions is very fast and the interaction with the surface of the electroactive material is less and hence the capacitance value decreases (Shakir et al., 2010). The Nyquist diagram of the NC nanorods (Figure 7.4c) shows a low semicircle in the high frequency region and a nearly flat tail parallel to the Y-axis in the low frequency region, showcasing good electrochemical characteristics of the prepared material. The small semicircle at high frequency region is a signature of low charge transfer resistance and fast ion/electron transfer which led to superior electrochemical capacitance (Bhojane et al., 2016; Qian et al., 2013).

The cyclic stability plot of the nanorods at a high current density of 8 A g⁻¹ for 2000 charge-discharge cycles clearly demonstrates that the capacitance values remained constant up to 400 cycles, then there is a little decrease in the value, which then remains constant up to 1700 cycles and thereafter slightly decreases (Figure 7.4d). After 2000 cycles, only 6% decrease in the initial capacitance value was observed for the prepared nanorods. Such a high electrochemical performance of the NC material was mainly attributed to the nanostructure of the rods. The synthesized NC nanorods possess high surface area of 65.73 m² g⁻¹ with high pore volume of 0.2

$\text{cm}^3 \text{g}^{-1}$ and the structure is mesoporous in nature. Such nano architectures with highly porous nature can facilitate the easy transportation of OH^- ions inside the nanorods for the effective utilization of the electroactive material, and it can withstand the strain which was generated during the ion intercalation/de-intercalation action leading to the high capacitance and stability (Bhojane et al., 2016; Zhu et al., 2014). The admittance plot for the 3-electrode method is displayed in inset of Figure 7.4(d). The knee frequency (f_0) value is 1590 Hz and the calculated time constant (τ_0) value is 628.9 μs . Low time constant values support the obtained high capacitance values.

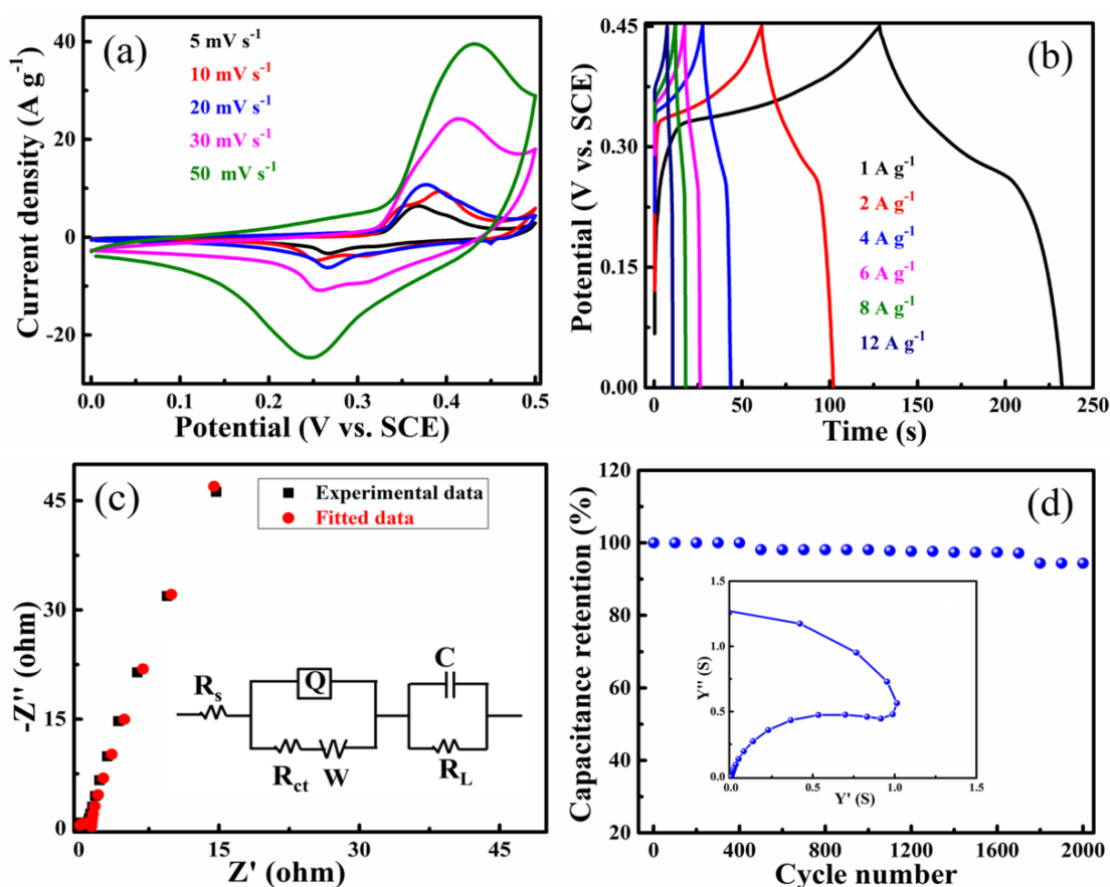


Figure 7.4 Electrochemical analysis for 3-electrode method. (a) CV curves, (b) GCD curves, (c) Nyquist plot (inset shows the fitted equivalent circuit) and (d) Cyclic stability plot (inset shows the admittance plot).

The calculated energy and power density for the 3-electrode method are shown in Table 7.1. A fairly good energy density of 2.5 Wh kg⁻¹ was obtained while maintaining a high power density of 2557.0 W kg⁻¹ at an applied current density of 12 A g⁻¹. The computed specific capacity values for the NC electrode at different current densities ranging from 1-12 A g⁻¹ are also presented in Table 7.1. The specific capacitance values offered by NC nanorods are high or comparable to other NC nanostructures (Table 7.3).

Table 7.1 Energy density, power density and Specific capacity data at different current densities for the 3-electrode method.

Current density (A g ⁻¹)	Energy density (Wh kg ⁻¹)	Power density (W kg ⁻¹)	Q _s (C g ⁻¹)
1	6.6	225	104.9
2	5.2	448	83.7
4	4.0	888	64.3
6	3.4	1302	54.4
8	3.0	1771	48.1
12	2.5	2557	39.2

7.3.3 Electrochemical Study of Fabricated Supercapacitor Using NC Electrodes

The NC nanostructures were also tested in a symmetrical 2-electrode method in order to check the practical applicability. The CV curves obtained from the 2-electrode cell is shown in Figure 7.5(a), at scan rates from 2-30 mV s⁻¹, the CV curves are quite rectangular with small redox peaks for cathodic and anodic sweeps confirming the pseudocapacitive nature of the material. The calculated specific capacitance values are 90, 82, 80, 75 and 72 F g⁻¹ for 2, 5, 10, 20 and 30 mV s⁻¹, respectively. Figure 7.5(b) shows the GCD curves of the nanorods at various current densities from 0.5 to 8 A g⁻¹. The symmetrical charge-discharge curves are also a signature of good capacitive behavior. The calculated capacitance values are 91, 73, 62, 53, 47 and 35 F g⁻¹ for 0.5, 1, 2, 4, 6 and 8 A g⁻¹, respectively. Also, the estimated

coulombic efficiency is more than 95% for the charge-discharge curves, which suggests the good charge-discharge profile of the supercapacitor device.

Figure 7.5(c) shows the Nyquist diagram of the prepared supercapacitor, where a large semicircle is noticed in the high frequency region and a nearly flat tail parallel to the Y-axis was observed at the low frequency region, demonstrating the good electrochemical performance of the symmetrical supercapacitor. The equivalent circuit is best fitted and is presented in the inset of Figure 7.5(c). The cyclic stability study for the symmetrical supercapacitor depicts that around 91% of the initial capacitance value was retained at a high current density of 8 A g⁻¹ after 2000 cycles (Figure 7.5d), which indicated its potential towards practical supercapacitor application. The admittance plot for the supercapacitor device is displayed in inset of Figure 7.5(d). The knee frequency (f_0) value is 10 Hz and the calculated time constant (τ_0) value for supercapacitor device is 10000 μ s. Low time constant values support the obtained high capacitance values. The energy and power density of the prepared supercapacitor calculated and is given in Table 7.2. A high energy density of 4.8 Wh kg⁻¹ and a high power density of 8028.0 W kg⁻¹ was obtained at a high current density of 8 A g⁻¹. Thus, the superior electrochemical performance of the NC electrode material makes it a better electroactive material for advanced supercapacitor application.

Table 7.2 Energy density, power density and specific capacity data at different current densities for the supercapacitor device.

Current density (A g⁻¹)	Energy density (Wh kg⁻¹)	Power density (W kg⁻¹)	Q_s (C g⁻¹)
0.5	12.6	506	91
1	10.1	997	73
2	8.6	2000	62
4	7.4	4003	53
6	6.5	6026	47

8	4.8	8028	35
---	-----	------	----

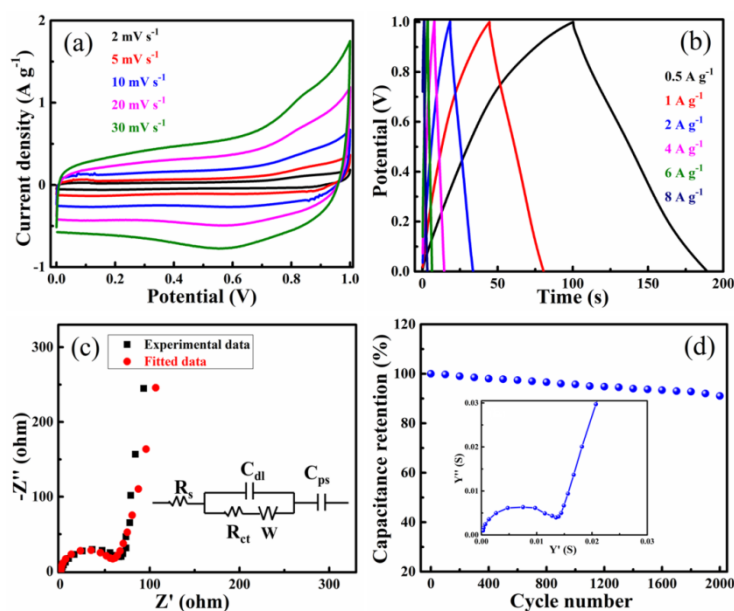


Figure 7.5 Electrochemical analysis for 2 electrode method. (a) CV curves, (b) GCD curves, (c) Nyquist plot and (d) Cyclic stability study of NC at a current density of 8 A g⁻¹ (inset shows the admittance plot).

Table 7.3 Comparison of electrochemical data of NC with the reported literature.

Electrode material	C _s (F g ⁻¹)	Electrolyte and substrate	Cyclic stability	References
Oxygen vacancy rich NC nanoneedles	1076 @ 0.5 A g ⁻¹	1 M KOH Ni foam	114% after 1000 cycles @ 10 A g ⁻¹	Cao et al. (2020)
NC nanourchins	412 @ 0.5 A g ⁻¹	1 M KOH Ni foam	86% after 1000 cycles @ 10 A g ⁻¹	Cao et al. (2020)
NC nanoplates	332 @ 5	2 M KOH	86% after 2000	Kim et al.

	mV s^{-1}	Ni foam	cycles @ 2.5 A g^{-1}	(2016)
NC nanosheets	560 @ 2 A g^{-1}	3 M KOH Ni foam	95% after 5000 cycles @ 10 A g^{-1}	Mondal et al. (2015)
NC nanoflakes	330 @ 20 mV s^{-1}	2 M KOH ITO substrate	97% after 900 cycles @ 20 mV s^{-1}	Salunkhe et al. (2011)
NC nanoparticles	354 @ 10 mV s^{-1}	2 M KOH Ni foam	---	Saravanakumar et al. (2017)
NC quantum dots	362 @ 0.5 A g^{-1}	1 M Na_2SO_4 FTO glass slide	---	Siwatch et al. (2020)
Urchin like NC nanoneedles	234 @ 1 A g^{-1}	3 M KOH Ni foam	---	Zhang et al. (2017)
Firework shaped NC microspheres	696 @ 1 A g^{-1}	2 M KOH Ni foam	86% after 10000 cycles @ 50 mV s^{-1}	Zhang et al. (2019)
NC nanowires	830 @ 2 A g^{-1}	3 M KOH Ni foam	80% after 20000 cycles @ 10 mA cm^{-2}	Zhao et al. (2018)
NC nanorods	565 @ 1 A g^{-1}	2 M KOH Ni foam	77% after 1000 cycles @ 2 A g^{-1}	Zhu et al. (2014)
NC nanorods	440 @ 5 mV s^{-1} 233 @ 1 A g^{-1}	2 M KOH Ni sheet	94% after 2000 cycles @ 8 A g^{-1}	Present work

The calculated Z values for the 3-electrode as well as for supercapacitor device are 0.5485 and 0.2244, respectively. Therefore, the obtained high capacitance values for the NC nanorods were mainly attributed to the participation of electroactive sites due to the nanorod structure for the better redox reaction.

The estimated C_P is 28.2%, whereas the C_{EDL} is 71.8% for the 3-electrode method (Figure 7.6a). Similarly, by following the same procedure, the C_{EDL} and C_P contribution of the NC in a supercapacitor device is of 75% and 25%, respectively (Figure 7.6b). From the experiment it is found that NC is C_{EDL} dominant, the obtained inverse order of capacitance contribution for the NC electrode material could be believed to the physicochemical properties of electrode (crystal structure, chemical composition, surface area and porosity), effect of aqueous electrolyte (smaller size of aqueous ions have better permeability into the porous network), grain boundary and microstructure effect as stated by (Dupont et al., 2016; Dupont et al., 2018; Toupin et al., 2002). This kind of similar observations is also found in many literatures where it was found that the C_{EDL} dominance for NC electrode as reported by (Chen et al., 2014; Umeshbabu et al., 2014).

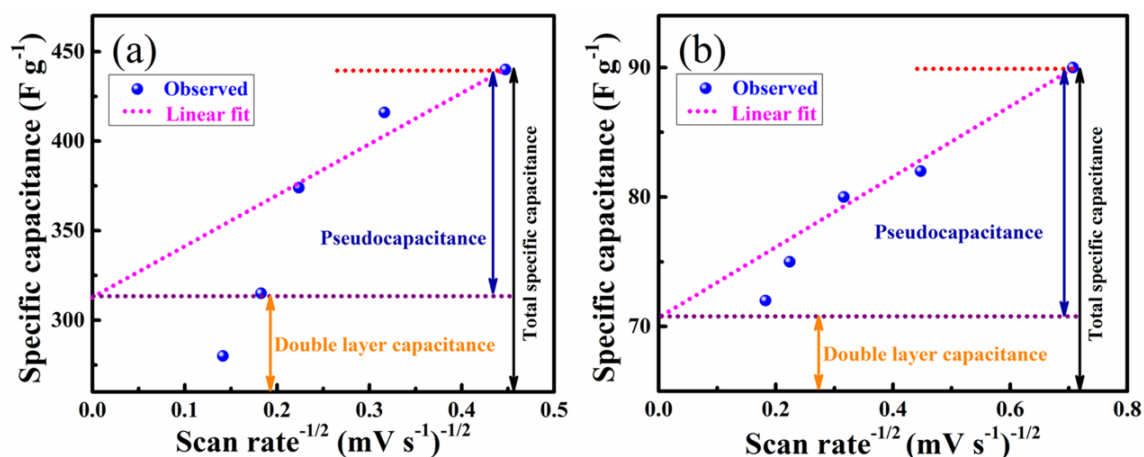


Figure 7.6 Determination of C_{EDL} and C_P contribution of NC in (a) 3-electrode system and (b) Fabricated supercapacitor device.

7.4 CONCLUSIONS

In conclusion, the present study reports the synthesis of NC nanorods employing a low temperature solvothermal approach. The structural and morphological analyses confirm the formation of NC nanorods. From the electrochemical study capacitance value of 440 F g^{-1} was obtained at a scan rate of 5 mV s^{-1} in a 3-electrode method. Apart from the high capacitance value, the electrode material exhibited an excellent cyclic performance of only 6% decrease in the initial capacitance rate after 2000 continuous cycles. A symmetric supercapacitor was also fabricated in order to study the practical applicability. The symmetric supercapacitor showed good capacitance value of 91 F g^{-1} at an applied discharge current of 0.5 A g^{-1} and 90 F g^{-1} at a scan rate of 2 mV s^{-1} . The electrode material depicted an energy density of 2.5 Wh kg^{-1} , power density of 2557.0 W kg^{-1} at a current density of 12 A g^{-1} in a 3-electrode method and 4.8 Wh kg^{-1} , 8028.0 W kg^{-1} at a current density of 8 A g^{-1} in a symmetrical supercapacitor device. Such a high electrochemical performance was mainly due to the nano-architecture of the NC, which can act as a buffering channel for fast ion/electron transport and maintains its mechanical strength after the continuous charge/discharge cycles imparted good rate capability. Thus, the prepared material can be utilized as an active electrode material for high performance supercapacitor application.



CHAPTER 8

***POROUS GRAPHENE-NiCo₂O₄ NANOROD
HYBRID COMPOSITE AS A HIGH
PERFORMANCE SUPERCAPACITOR ELECTRODE
MATERIAL***

Chapter 8 presents the synthesis and characterization of PGNC nanocomposites prepared through solvothermal method. The morphological and structural features are thoroughly studied by sophisticated analytical tools. The synthesized material was studied for its utility in supercapacitor applications.

8.1 INTRODUCTION

Among the pseudocapacitive materials, NC has recently emerged as a potential supercapacitor electrode material owing to its splendid electrochemical behavior in comparison with NiO and Co₃O₄ (Sethi et al., 2019a). This is due to the better redox properties and higher electrical conductivity, which can lead to 2 to 3 orders higher capacitance as compared to single metal oxides (Wei et al., 2018). Hybridization of NC with PG leads to the emergence of interesting properties and hence has been receiving increased attention by the research community lately (Low et al., 2019).

NC-carbon based hybrid composites have been prepared by using various techniques mainly involving hydrothermal approach usually followed by freeze-drying or electrodeposition followed by calcination in air (Al-Rubaye et al., 2017; Foo et al., 2016; Jiang et al., 2018; Mondal et al., 2017). The carbon-based component of the composite was in the form of PG oxide, rGO, graphene foam, activated carbon or carbon cloth. NC nanostructures, on the other hand, had various structures, such as sheets, spheres, needles or rods (Mondal et al., 2015; Xu et al. 2018; Zhang et al., 2017; Zhu et al., 2014). In the earlier reports, the electrochemical analysis of the composites was carried out by depositing the material on a Ni-foam current collector (Al-Rubaye et al., 2017; Foo et al., 2016; Jiang et al., 2018; Mondal et al., 2017). Although using Ni-foam current collectors leads to higher capacitance values owing to the presence of interconnected pores in the foam, it is not cost effective.

8.2 EXPERIMENTAL SECTION

For the synthesis of x-PGNC (where, x = 5, 10, 15, 20, 25 and 30 wt% GO, respectively) first, an appropriate amount of GO (50 mg, 100 mg, 160 mg, 192 mg, 320 mg and 400 mg for 5, 10, 15, 20, 25 and 30 PGNC, respectively) was dispersed uniformly in a 1:1 mixture of water (25 mL) and ethylene glycol (25 mL) solvent under sonication for 2 h. Then, 1 mmol of $\text{Ni}(\text{Ac})_2 \cdot 4\text{H}_2\text{O}$ and 2 mmol of $\text{Co}(\text{Ac})_2 \cdot 4\text{H}_2\text{O}$ were dissolved in a 1:1 mixture of water (10 mL) and ethylene glycol (10 mL) and were added to the GO dispersion under continuous stirring. After an hour, 6 mmol of urea was added slowly and stirred for 30 min. The whole reaction mixture was then poured into a stainless steel autoclave of 100 mL capacity and was heated at 160 °C for 16 h. Later, it was allowed to cool down naturally to room temperature and the products were collected and washed with deionized water several times followed by ethanol and dried at 70 °C overnight. The products were calcined at 400 °C for 2 h in order to obtain the PGNC composite. The characterization and electrochemical studies were carried out as mentioned in chapter 2.

8.3 RESULTS AND DISCUSSION

8.3.1 Structural, Elemental and Morphological Analysis

The powder XRD patterns of the cubic NC and 10 PGNC (Figure 8.1a) match well with the JCPDS card no # 20-0781 with peaks at 31.17°, 36.6°, 38.2°, 44.57°, 55.4°, 59.0°, 64.7° and 77.5° corresponding to the (220), (311), (222), (400), (422), (511), (440) and (533) crystal planes (Sethi et al., 2019a). The absence of other peaks indicates the purity of the sample. The average crystal size determined using Scherrer's equation applied to the (311) peak of 10 PGNC was found to be 9.5 nm.

The Raman spectra of GO, PG and 10 PGNC composites are shown in Figure 8.1(b). In GO, the D band at 1354.4 cm^{-1} arises due to the defects related to the breathing mode of k-point phonons of A_{1g} symmetry (Wu et al., 2018). The formation of the G band at 1580 cm^{-1} is due to the first order scattering of the E_{2g} phonons of sp^2

C atoms (Mohamed et al., 2017a; Mohamed et al., 2017b; Sadiq et al., 2017c). The lower intensity of the D band as compared to the G band is due to the low degree of defect present in the graphite sample. The relative intensity ratio (I_D/I_G) of the D and G bands is a measure of defects formed in the sample and is inversely proportional to the average size of the sp^2 domains (Sadiq et al., 2017d). The calculated I_D/I_G values for GO and PG samples are 0.76 and 1.06, respectively. In PG, the intensity of the D band increases in comparison to GO, owing to the formation of defects such as cracks and vacancies in the PG sheets (Sethi et al., 2019b). The shift in the position of the D band to 1349.2 cm^{-1} and the G band to 1592.4 cm^{-1} again confirms the better reduction of GO to PG (Bantawal et al., 2019; Sethi et al., 2019b). In 10 PGNC, the D band is located at 1348.1 cm^{-1} and the G band was located at 1587 cm^{-1} , along with the peaks at 716 cm^{-1} , 507 cm^{-1} and 481 cm^{-1} , which can be assigned to the A_{1g} , F_{2g} and E_g modes of the NC sample (Sethi et al., 2019a). The formation of the 2D peak along with the D + G band indicates the formation of defects in the composite. The decrease in the I_D/I_G value to 0.97 may be due to the anchoring of NC nanorods on the PG surface (Wu et al., 2018).

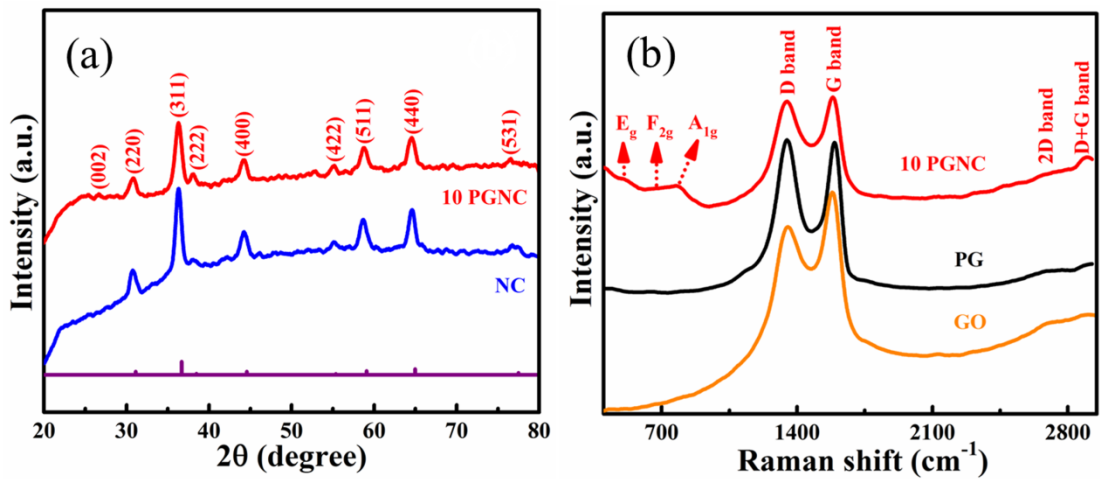


Figure 8.1 (a) XRD patterns of NC, 10 PGNC and (b) Raman spectra of GO, PG and 10 PGNC.

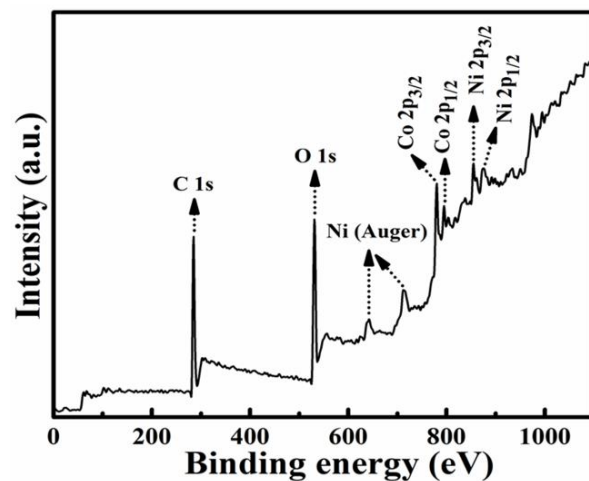


Figure 8.2 XPS survey spectrum of 10 PGNC.

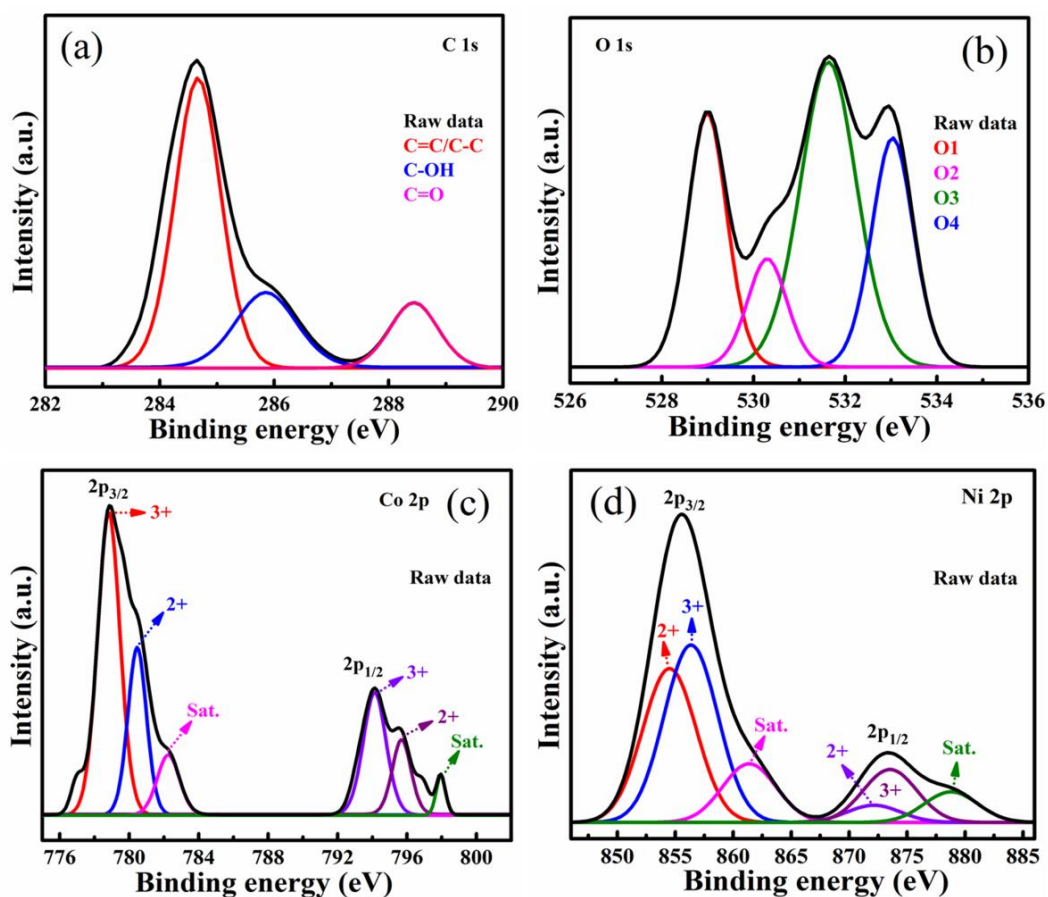


Figure 8.3 Deconvoluted XPS plot of 10 PGNC: (a) C 1s, (b) O 1s, (c) Co 2p and (d) Ni 2p.

The XPS survey spectrum of 10 PGNC confirms the presence of C, O, Ni and Co (Figure 8.2). The deconvoluted C 1s spectra show peaks at binding energies of 284.5, 285.9 and 288.3 eV corresponded to C=C/C–C, C–O and C=O functional groups (Figure 8.3a) (Mohamed et al., 2018a). The Peaks at 528.9 (O1), 530.6 (O2), 531.7 (O3) and 533 eV (O4) shown in the deconvoluted O 1s spectrum correspond to the oxygen bonded to the metal (Co/Ni), hydroxyl groups or the surface-adsorbed oxygen and chemisorbed water (Figure 8.3b) (Sadiq et al., 2017c; Subramanya et al., 2015a). Both the Co 2p (Figure 8.3c) and Ni 2p spectra (Figure 8.3d) with two spin-orbit doublets of Co²⁺, Co³⁺ and Ni²⁺, Ni³⁺ along with two shakeup satellites (denoted as “Sat.”) are in accordance with the reported literature (Ko et al., 2017; Subramanya et al., 2015c).

The FTIR spectra for PG, NC and 10 PGNC is presented in Figure 8.4. In the 10 PGNC sample, the observed peak at 1556 cm⁻¹ is due to the skeletal vibration from PG sample. The peaks appeared at 551 and 644 cm⁻¹ correspond to the metal-oxygen vibrational modes of NC (Siwatch et al., 2020). The FTIR result again corroborates the results from Raman analysis.

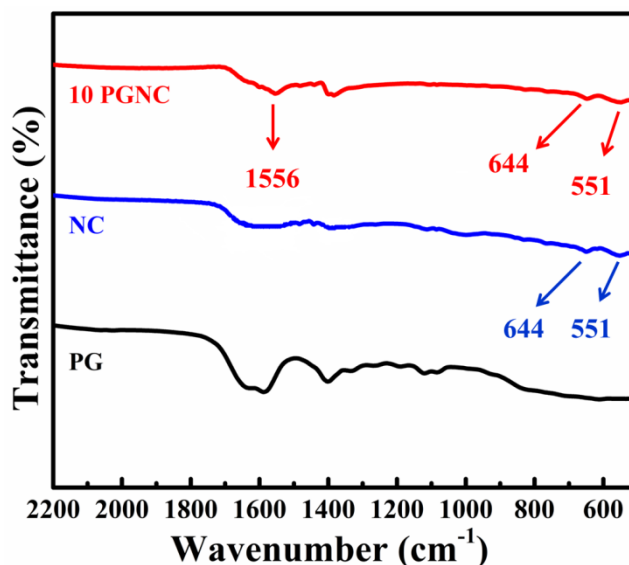


Figure 8.4 FTIR spectra of PG, NC and 10 PGNC.

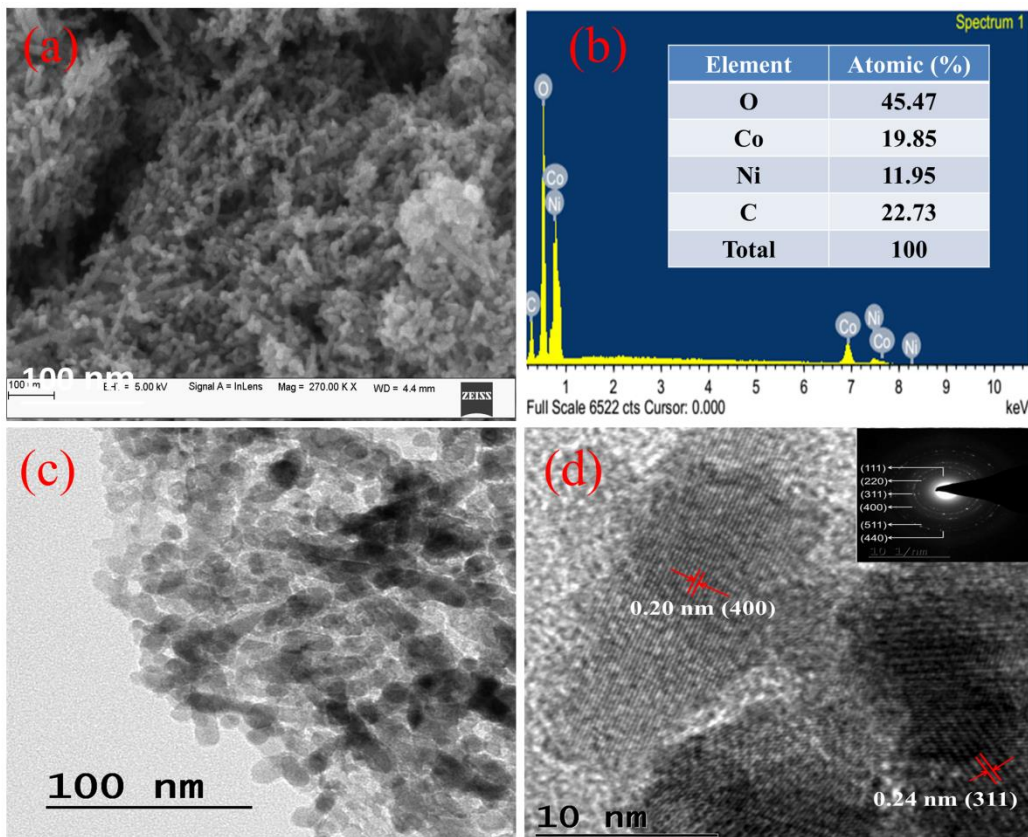


Figure 8.5 (a) FESEM image (b) EDX profile with elemental data as an inset, (c) TEM image and (d) HRTEM image of 10 PGNC (inset shows the SAED pattern revealing polycrystalline nature).

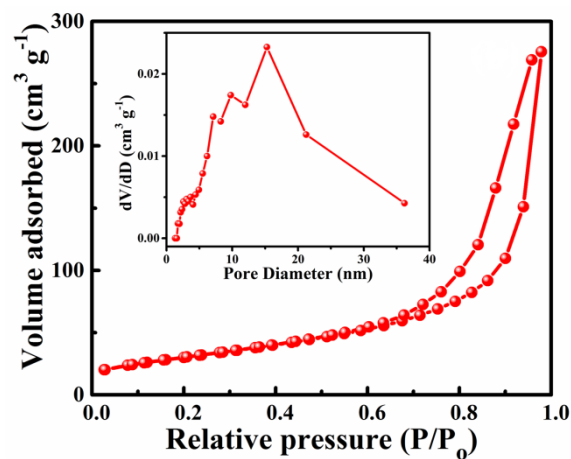


Figure 8.6 N₂ adsorption and desorption isotherms of 10 PGNC (inset shows the pore size distribution plot).

The morphology of the as synthesized materials is shown in Figure 8.5. The FESEM and TEM images of 10 PGNC (Figure 8.5a and 8.5c) reveal uniformly distributed NC nanorods over the PG surface. The EDX profile of 10 PGNC (Figure 8.5b inset) confirms the presence of elements such as C, O, Ni and Co with the Ni/Co atomic ratio of 1:2. Lattice fringes of the planes (311) with a d-spacing of 0.24 nm and (400) with a d-spacing of 0.20 nm are clearly visible in the HRTEM image (Figure 8.5d).

The N₂ adsorption and desorption isotherms of 10 PGNC were found to be of type-IV according to the IUPAC classification as shown in Figure 8.6. A high specific surface area of 109 m² g⁻¹ for the mesoporous 10 PGNC was obtained, which is higher than the reported literatures such as NC nanorods/3D porous ultrathin carbon networks (98 m² g⁻¹), three-dimensional hierarchical rGO/NC nanostructures (105 m² g⁻¹), rGO-NC hollow-spheres (21 m² g⁻¹) and mesoporous NC nanoneedle/carbon cloth arrays (44.8 m² g⁻¹) (Dong et al., 2019; Foo et al., 2016; Mondal et al., 2017; Zhang et al., 2014). The decrease in the surface area of the 10 PGNC composite may be due to the anchoring of NC nanorods on the PG surface. The pore size distribution of 10 PGNC (inset of Figure 8.6) clearly indicates the formation of the mesoporous structure with a total pore volume of 0.421 cm³ g⁻¹. Such porous structures with a high specific surface area are considered to be suitable for supercapacitor applications due to the unique structure that can easily facilitate the transfer of ions and electrons at the electrode/electrolyte interface (Sethi et al., 2019b; Subramanya et al., 2015a).

8.3.2 Electrochemical Study of PGNC Composite Electrodes

The electrochemical performances of the PGNC samples were studied by a conventional 3 electrode method by using 2 M KOH as electrolyte employing CV, GCD and EIS. The CV graphs of the PGNC composite samples in the potential range of 0-0.5 V show a pair of redox peaks during the anodic and cathodic sweeps depicting the pseudocapacitive nature of the materials (Figure 8.7a). The calculated capacitance values for the PGNC composites from the CV curves at a constant scan rate of 5 mV s⁻¹ were 735, 1533, 983, 942, 401 and 263 F g⁻¹ for the 5, 10, 15, 20, 25

and 30 PGNC composites, respectively. As can be seen from the plots, among the composites, the CV of 10 PGNC occupies more area, and shows more current collecting ability and a higher capacitance value as compared to the other composites in the series. The increase in the capacitance value from 5 to 10 PGNC is due to the synergistic beneficial effects of the two components. Later, with an increase in the PG content, there is a possibility of agglomeration of the PG sheets hindering the transport or wrapping of NC, inhibiting its redox properties.

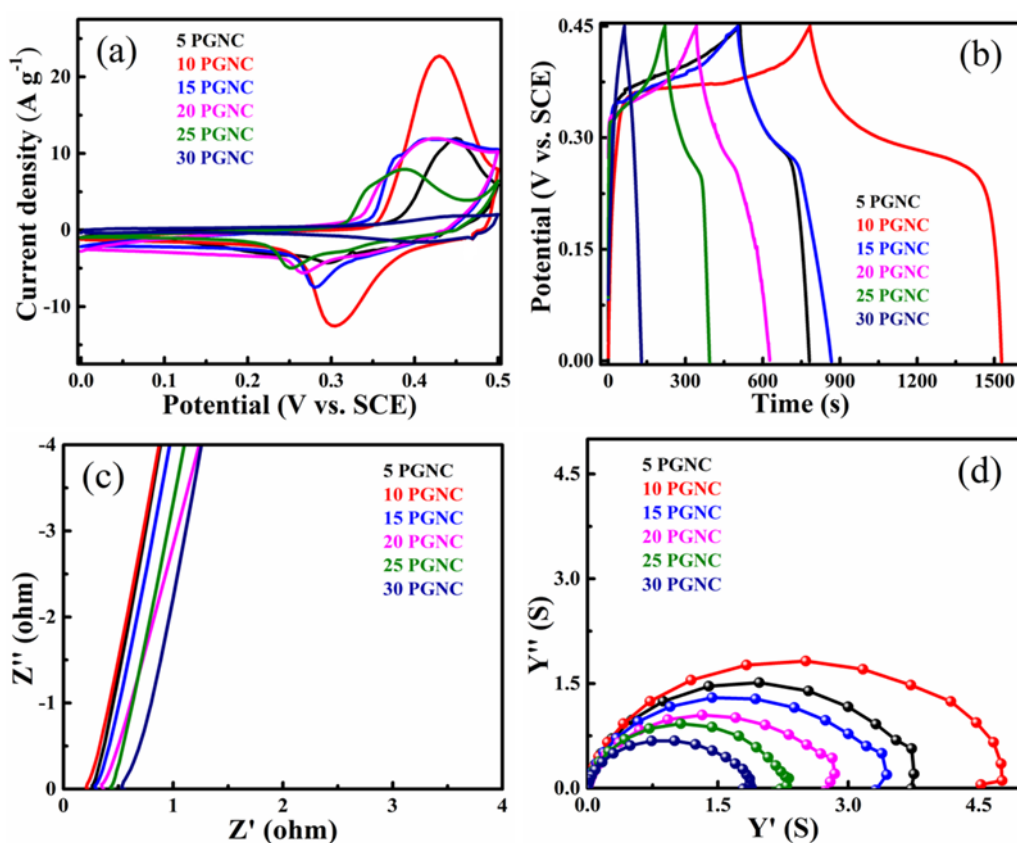


Figure 8.7 Electrochemical performance of PGNC composite electrodes: (a) CV curves at a constant scan rate of 5 mV s^{-1} , (b) GCD curves at a constant current density of 1 A g^{-1} , (c) Nyquist plots in the high frequency region and (d) Admittance plots.

The GCD graphs of the PGNC composites show a pseudocapacitive nature and are nearly symmetrical, which is a signature of good electrochemical behavior

(Figure 8.7b). The calculated specific capacitance (specific capacity) values for the PGNC composites at the fixed current density of 1 A g^{-1} for 5, 10, 15, 20, 25 and 30 PGNC composites are 612 (275.4), 1684 (757.8), 840 (378.0), 742 (333.9), 387 (174.1) and 157 F g^{-1} (70.7 C g^{-1}). Also, among the PGNC composites, 10 PGNC requires more time to discharge and hence possesses a higher capacitance (capacity) value (Subramanya et al., 2015a). The calculated coulombic efficiency are 68%, 96%, 79%, 82%, 88% and 94% for the composites of 5, 10, 15, 20, 25 and 30 PGNC, respectively. The composite 10 PGNC has displayed more coulombic efficiency as compared to other composites which suggested the good discharge profile of the 10 PGNC material.

The Nyquist plots of all the PGNC composite electrodes are shown in Figure 8.7(c). The plot reveals the absence of semicircle, suggesting the low resistance value offered by the material. The straight line in the low frequency region, nearly parallel to the Y-axis is suggestive of good capacitive nature of the electrode materials. The resistance and conductance values of all PGNC composites are presented in Table 8.1. The admittance plot of all composites is presented in Figure 8.7(d), by knowing the knee frequency values the estimated τ_o value is presented in Table 8.1. The observed high capacitance value of 10 PGNC is in accordance with the low time constant value.

Table 8.1 Resistance, conductance, knee frequency and time constant values of electrode materials.

Electrode material	Resistance (Ω)	Conductance (S)	Knee frequency (kHz)	Time constant (μs)
5 PGNC	0.26	3.84	15.9	62.9
10 PGNC	0.20	5.00	39.8	25.1
15 PGNC	0.31	3.22	25.1	39.8
20 PGNC	0.37	2.70	15.9	62.9
25 PGNC	0.43	2.32	10.0	100.0
30 PGNC	0.55	1.81	6.31	158.4

8.3.3 Electrochemical Study of 10 PGNC Composite Electrode

The higher capacitance value of 10 PGNC makes it a suitable candidate for further study. The CV curves of 10 PGNC reveal that as the scan rate increases, the current collecting ability of the material increases (Figure 8.8a). This may be ascribed to the better $\text{NiCo}_2\text{O}_4 \leftrightarrow \text{NiOOH} + 2\text{CoOOH}$ reaction kinetics (Mondal et al., 2017). From the CV study, high capacitance values of 1533, 1365, 1231, 925 and 710 F g^{-1} were obtained at scan rates of 5, 10, 20, 30 and 50 mV s^{-1} , respectively. These values are higher than many other graphene-based NC composites reported in the literature.

To investigate the discharging capability, a variable current charge-discharge study was carried out within a potential window of 0.45 V and the GCD curves were analyzed at different current densities ranging from 1 to 12 A g^{-1} (Figure 8.8b). The specific capacitance values obtained from the GCD curves at applied current densities of 1, 2, 4, 6, 8 and 12 A g^{-1} are 1684, 1559, 1004, 361, 277 and 230 F g^{-1} , respectively. The computed specific capacity (C g^{-1}) values from the charge-discharge curves are 757.8, 701.6, 451.8, 162.4, 124.7 and 103.5 C g^{-1} for the current densities ranging from 1-12 A g^{-1} . The computed coulombic efficiency η (%) from the GCD curves for 10 PGNC are more than 95%. The specific capacitance values of the other PGNC composite materials, from CV and GCD data at different scan rates and applied current densities, are tabulated in Table 8.2 and 8.3, respectively.

The Nyquist plot of 10 PGNC does not show the presence of an arc in the high frequency region and consists of a straight line in the low frequency tail, depicting the low diffusion resistance of the composite electrode material (Figure 8.8c). This may be attributed to the 3D structure of PGNC composites, which provides a high surface area and enough pores for the diffusion of electrolyte ions without any hindrance (Subramanya et al., 2015a; Subramanya et al., 2015b). The obtained value of R_s is 0.2 ohm.

The cyclic stability is also an important parameter for measuring the cycle life of a supercapacitor. The cyclic stability test carried out at a current density of 8 A g^{-1}

reveals that the electrode material shows 100% retention of initial capacitance up to 1300 cycles. A high initial capacitance retention value of 94% even after 10000 charge-discharge cycles was observed (Figure 8.8d), which is higher than that of the pristine NC and PG reported earlier (Sethi et al., 2019a; Sethi et al., 2019b). This kind of stability is achieved due to the synergistic effect of the porous structure of graphene and high electrochemical activity of NC, the combination of which increases the conductivity apart from facilitating the easy transportation of the electrons during cycling. The energy density and power density data calculated from the charge-discharge curves are tabulated in Table 8.4. The comparison of the electrochemical performance of the 10 PGNC electrodes with existing literature is given in Table 8.5.

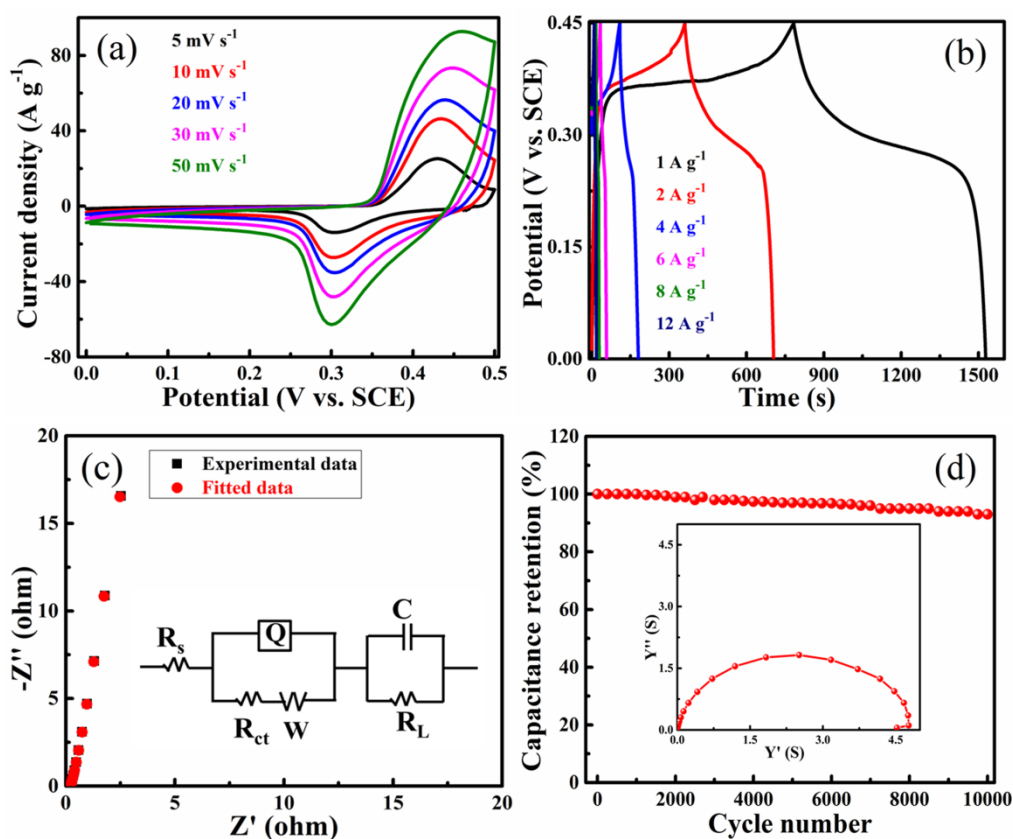


Figure 8.8 Electrochemical analysis of the 10 PGNC composite: (a) CV curves, (b) GCD curves, (c) Nyquist plot with an equivalent circuit as inset and (d) Cyclic stability test at a constant current density of 8 A g^{-1} for 10000 cycles (inset shows the admittance plot).

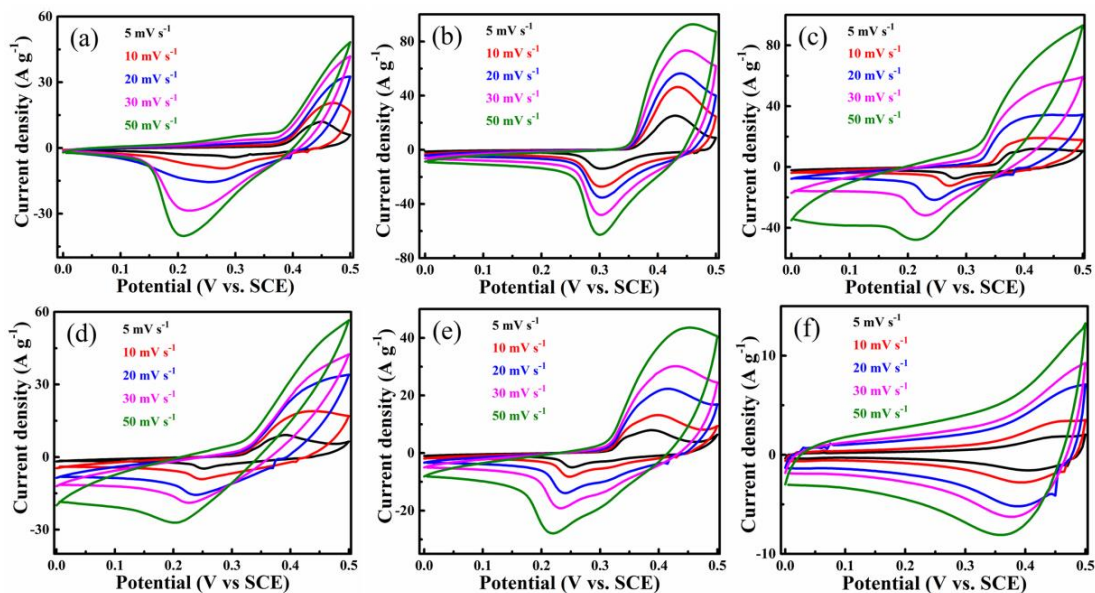


Figure 8.9 CV curves for (a) 5, (b) 10, (c) 15, (d) 20, (e) 25 and (f) 30 PGNC composite.

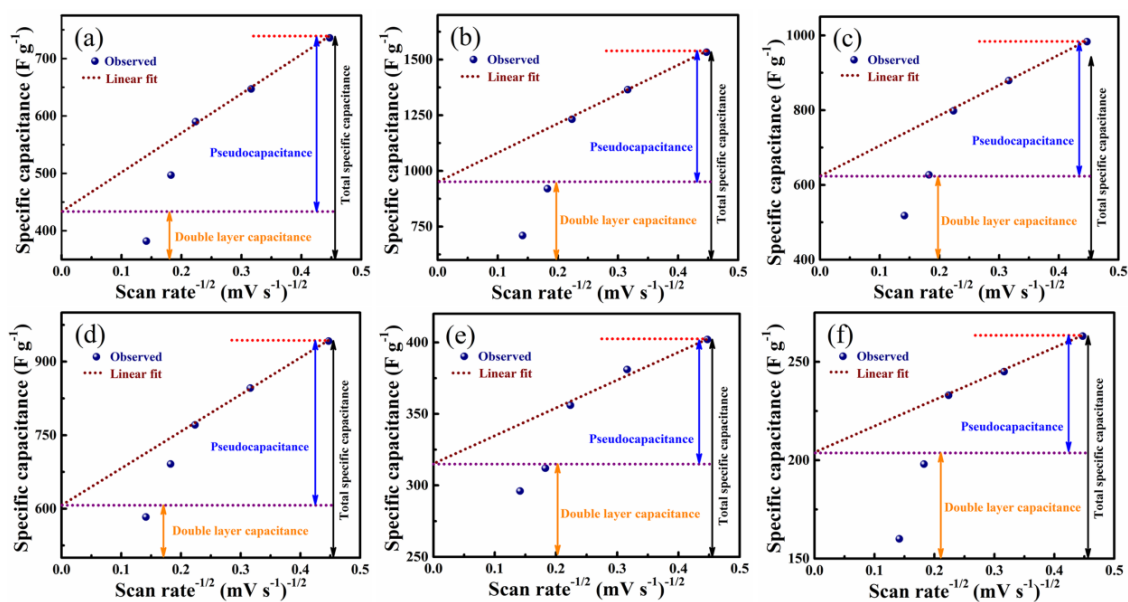


Figure 8.10 Determination of the C_{EDL} and C_P contribution. Specific capacitance vs. inverse square root of scan rate of (a) 5, (b) 10, (c) 15, (d) 20, (e) 25 and (f) 30 PGNC composite.

The CV curves of all the composites (5-30 PGNC) at different scan rates ranging from 5–50 mV s⁻¹ are given in Figure 8.9. The specific capacitance values for all the composites are presented in Table 8.2. The calculated C_{EDL} contributions are 57.8%, 62.0%, 63.5%, 64.2%, 77.4% and 79.0% for 5, 10, 15, 20, 25 and 30 PGNC composite, respectively. As can be seen from the results, as the PG content increased, the extent of C_{EDL} contribution also increased and obviously the C_P value got reduced. The trend is in agreement with reported literature (Ruan et al., 2019).

Table 8.2 Specific capacitance values of PGNC composites from CV.

Composite	Scan rate (mV s ⁻¹)	C _s (F g ⁻¹)
5 PGNC	5	735
	10	647
	20	589
	30	497
	50	382
10 PGNC	5	1533
	10	1365
	20	1231
	30	925
	50	710
15 PGNC	5	983
	10	874
	20	798
	30	627
	50	518
20 PGNC	5	942
	10	823
	20	736
	30	691
	50	593

25 PGNC	5	401
	10	382
	20	356
	30	312
	50	296
30 PGNC	5	264
	10	244
	20	233
	30	197
	50	159

Table 8.3 Specific capacitance and capacity values of PGNC composites from GCD data.

Composite	Current density ($A\ g^{-1}$)	C_s ($F\ g^{-1}$)	Q_s ($C\ g^{-1}$)
5 PGNC	1	612	275.4
	2	397	178.7
	4	267	120.2
	6	198	89.1
	8	153	68.9
	12	107	48.2
10 PGNC	1	1684	757.8
	2	1559	701.6
	4	1004	451.8
	6	361	162.4
	8	277	124.7
	12	230	103.5
15 PGNC	1	840	378.0
	2	485	218.3
	4	336	151.2

	6	267	120.2
	8	201	90.5
	12	145	65.3
20 PGNC	1	742	334.0
	2	683	307.4
	4	231	103.9
	6	187	84.2
	8	160	72.0
	12	157	70.7
25 PGNC	1	387	174.2
	2	290	130.5
	4	222	99.9
	6	186	83.7
	8	165	74.3
	12	141	63.5
30 PGNC	1	157	70.7
	2	141	63.5
	4	123	55.4
	6	110	49.5
	8	101	45.5
	12	90	40.5

Table 8.4 Energy density and power density of 10 PGNC electrode.

Current density (A g⁻¹)	Energy density (Wh kg⁻¹)	Power density (W kg⁻¹)
1	47.4	225.5
2	43.8	451.3
4	28.2	900.0
6	10.2	1353.8

8	7.8	1797.8
12	6.2	2704.2

Table 8.5 Comparison of electrochemical performance of 10 PGNC electrode with reported literature.

Electrode material	C_s (F g ⁻¹)	Electrolyte	Stability	References
rGO- porous NC composite	1185 @ 2 A g ⁻¹	2 M KOH	98% after 10000 cycles @ 2 A g ⁻¹	Al-Rubaye et al. (2017)
NC-N-doped graphene composites	563 @ 1 A g ⁻¹	6 M KOH	90% after 5000 cycles @ 3 A g ⁻¹	Chang et al. (2019)
NC-3D-porous carbon network	1297 @ 0.5A g ⁻¹	3 M KOH	---	Dong et al. (2019)
rGO-NC nanocomposites	613 @ 1 A g ⁻¹	2 M KOH	91% after 2000 cycles @ 1 A g ⁻¹	Foo et al. (2016)
NC-rGO hybrid nanostructures	932 @ 1 A g ⁻¹	3 M KOH	84% after 5000 cycles @ 2 A g ⁻¹	Jiang et al. (2018)
FeCoNi@Graphene nanoplatelets nanocomposites	538 @ 1 A g ⁻¹	1 M KOH	91% after 5000 cycles @ 10 A g ⁻¹	Li et al. (2019)
rHGO-NC@Carbon fibers	1178 @ 1 A g ⁻¹	3 M KOH	87% after 5000 cycles @ 5 A g ⁻¹	Li et al. (2019)
rGO-NC hollow spheres composite	971 @ 0.5 A g ⁻¹	3 M KOH	76% after 5000 cycles @ 10 A g ⁻¹	Mondal et al. (2017)

Carbonized channels wrapped by NC nanosheets	1541 @ 1 A g ⁻¹	3 M KOH	86% after 10000 cycles @ 10 A g ⁻¹	Qu et al. (2019)
GO-MWCNT-NC hybrid composite	707 @ 2.5 A g ⁻¹	6 M KOH	88% after 5000 cycles @ 2.5 A g ⁻¹	Ramesh et al. (2018)
SnO ₂ @NC-N-MWCNTs hybrid composite	728 @ 4 A g ⁻¹	6 M KOH	92% after 5000 cycles @ 4 A g ⁻¹	Ramesh et al. (2019)
N-doped porous carbon-NC hybrid electrode	948 @ 1 A g ⁻¹	1 M KOH	87% after 2000 cycles @ 10 A g ⁻¹	Tang et al. (2019)
NC decorated dopamine derived carbon nanocomposites	667 @ 5 A g ⁻¹	2 M KOH	95% after 2000 cycles @ 10 A g ⁻¹	Veeramani et al. (2016)
3D mesoporous NC@Graphene nanocomposites	778 @ 1 A g ⁻¹	2 M KOH	90% after 10000 cycles @ 10 A g ⁻¹	Wei et al. (2014)
NC-Carbon composite	920 @ 1 A g ⁻¹	6 M KOH	94% after 5000 cycles @ 1 A g ⁻¹	Xu et al. (2019)
NC-CNF composite	786 @ 1 A g ⁻¹	6 M KOH	87% after 5000 cycles @ 4 A g ⁻¹	Yang et al. (2018)
NC nanoneedle/carbon cloth arrays	660 @ 2 A g ⁻¹	2 M KOH	92% after 3000 cycles @ 2 A g ⁻¹	Zhang et al. (2014)
rGO-NC composite	1003 @ 1 A g ⁻¹	6 M KOH	57% after 10000 cycles	Zhang et al. (2019)

			@ 10 A g ⁻¹	
3D PG-NC hybrid film	708 @ 1 A g ⁻¹	1 M KOH	94% after 6000 cycles @ 10 A g ⁻¹	Zhou et al. (2020)
PGNC composite	1684 @ 1A g ⁻¹ 1533 @ 5 mV s ⁻¹	2 M KOH Ni sheet	94% after 10000 cycles @ 8 A g ⁻¹	Present work

8.3.4 Electrochemical Study of Fabricated Supercapacitor Using 10 PGNC Composite Electrodes

The practical application of the 10 PGNC composite was studied by fabricating a symmetrical supercapacitor in a potential window of 1.2 V. The 10 PGNC delivered specific capacitance values of 266, 238, 224, 200, 188 and 158 F g⁻¹ (Figure 8.11a), at the scan rates of 2, 5, 10, 30, 50 and 100 mV s⁻¹, respectively. A high value of 158 F g⁻¹ at the higher scan rate (100 mV s⁻¹) strongly supports the superior supercapacitor performance of the material. The calculated specific capacitance (specific capacity) values from GCD for 10 PGNC are 225 (270), 200 (240), 195 (234), 121 (145.2), 97 (116.4) and 75 (90) (Figure 8.11b) for the current densities of 1, 2, 4, 6, 8 and 12 A g⁻¹, respectively. The coulombic efficiency for PGNC device is > 90%, respectively. The NC showed a low specific capacitance value, which can be attributed to its lower electronic conductivity compared to 10 PGNC (Sethi et al. 2019a). From this, it is evident that although the supercapacitive performance of NC is poor, the compositing of PG with NC leads to a 3-4 fold increase in the capacitance value. Also, the capacitance values obtained from the CV and GCD curves for the symmetrical supercapacitor of 10 PGNC are very high as compared to the symmetric/asymmetric supercapacitor using porous materials reported in the literature (Table 8.6).

The energy density and power density values of 10 PGNC were computed using the charge-discharge curves and the values are shown in Table 8.7. Notably, at a current density of 1 A g⁻¹, a high power density of 1208.0 is obtained for 10 PGNC

while maintaining an energy density value of 45.3 Wh kg^{-1} while at a high current density of 12 A g^{-1} , the supercapacitor still showed an energy density of 11.48 Wh kg^{-1} with a high power density of $17843.5 \text{ W kg}^{-1}$. The obtained energy density and power density values of 10 PGNC are high as compared to the values reported for materials like NC/3D-OPC//3D-OPC (29.2 Wh kg^{-1} at 1550.0 W kg^{-1}), NC/GA//AC (25.4 Wh kg^{-1} at 658.0 W kg^{-1}), NC NSs@HMRA//AC (15.4 Wh kg^{-1} at 500.0 W kg^{-1}), NC@GQDs//AC (38.1 Wh kg^{-1} at 800.0 W kg^{-1}), 3D-NC/Ni//3D-NC/Ni (0.88 Wh kg^{-1} at 157.0 W kg^{-1}), NC@3D N,S RGO (33.6 Wh kg^{-1} at 1196.0 W kg^{-1}) and Co-Ni-OH/rGO/CC//Co-Ni-OH/rGO/CC (30.3 Wh kg^{-1} at 1500.0 W kg^{-1}) (Dong et al., 2019; Jiu et al., 2019; Lu et al., 2014; Luo et al., 2019; Ramadoss et al., 2016; Sivakumar et al., 2019; Wang et al., 2019).

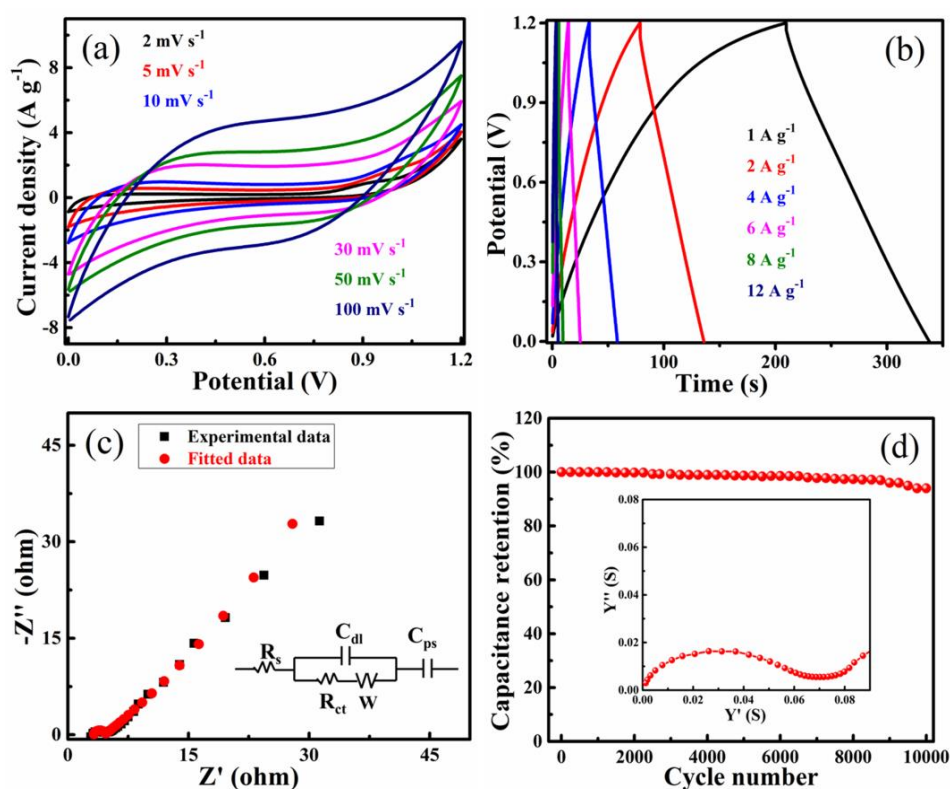


Figure 8.11 Electrochemical analysis of the fabricated supercapacitor using 10 PGNC: (a) CV curves, (b) GCD curves, (c) Nyquist plot with an equivalent circuit, and (d) Cyclic stability test at a constant current density of 8 A g^{-1} (inset shows the admittance plot).

The Nyquist plot of the supercapacitor fabricated with 10 PGNC shows a small semicircle in the high frequency region with a tail making an angle of 45° in the low frequency region, showing the Warburg resistance of the capacitor (Figure 8.11c). The smaller semi-circle implies the very low resistance of the capacitor and high capacitive nature of the material. The best fitted equivalent circuit for the 10 PGNC device is shown in inset of Figure 8.11(c).

The cyclic stability plot of 10 PGNC (Figure 8.11d) shows that up to 2000 cycles, the capacitance value remains unaltered, after which there is a slight decrease in the value with 96% retention of the initial capacitance value after 5000 cycles. This value is higher than that of the fabricated PG supercapacitor, which showed 93% retention for 5000 cycles (Sethi et al., 2019b). Around 93% of the initial capacitance value is retained even after 10000 cycles for 10 PGNC. This shows that 10 PGNC shows better cyclic stability than both NC and PG. This may be attributed to the combined action of the composite components, as stated earlier. The admittance plot shows a knee frequency value of 1595 Hz with a relaxation time constant value of 627 μ s for 10 PGNC (inset of Figure 8.11d).

Table 8.6 Comparison of electrochemical performance of 10 PGNC in a symmetrical/asymmetrical supercapacitor with reported literature.

Composites	C_s ($F g^{-1}$) in symmetrical supercapacitor cell	C_s ($F g^{-1}$) in asymmetrical supercapacitor cell	Stability	References
NC/3D-OPC//3D-OPC	---	82 @ 1 $A g^{-1}$	88%, 3000 cycles @ 1 $A g^{-1}$	Dong et al. (2019)
NC/GA//AC	---	87 @ 1 $A g^{-1}$	78%, 3000 cycles @ 1	Jiu et al. (2019)

			A g ⁻¹	
rHGO/NC/CF //AC	---	192 @ 1 A g ⁻¹	83%, 5000 cycles @ 2 A g ⁻¹	Li et al. (2019)
NC/GQDs//AC	---	107 @ 1 A g ⁻¹	72%, 3000 cycles @ 4 A g ⁻¹	Luo et al. (2019)
3D-NC/Ni//3D- NC/Ni	18 @ 0.1 mA	---	100%, 5000 cycles @ 0.8 mA	Ramadoss et al. (2016)
NC//3D N,S RGO	---	108 @ 2 A g ⁻¹	125%, 12000 cycles @ 10 A g ⁻¹	Sivakumar et al. (2019)
Co-Ni- OH/rGO/CC// Co-Ni- OH/rGO/CC	151 @ 2.5 A g ⁻¹	---	85%, 3000 cycles @ 5 A g ⁻¹	Wang et al. (2019)
PGNC composite	225 @ 1 A g ⁻¹	---	93%, 10000 cycles @ 8 A g ⁻¹	Present work

Table 8.7 Energy density and power density values of the fabricated supercapacitor.

Current density (A g ⁻¹)	Energy density (Wh kg ⁻¹)	Power density (W kg ⁻¹)
1	45.3	1208.0
2	40.0	2440.7
4	39.0	4808.2
6	24.2	7260.0
8	16.4	11576.5
12	11.4	17843.5

The calculated C_{EDL} contribution is 70% for 10 PGNC supercapacitor device (Figure 8.12). The increased capacitance in the 10 PGNC sample revealed the synergistic effect of the constituents of composites towards the overall capacitance (Gao et al., 2018).

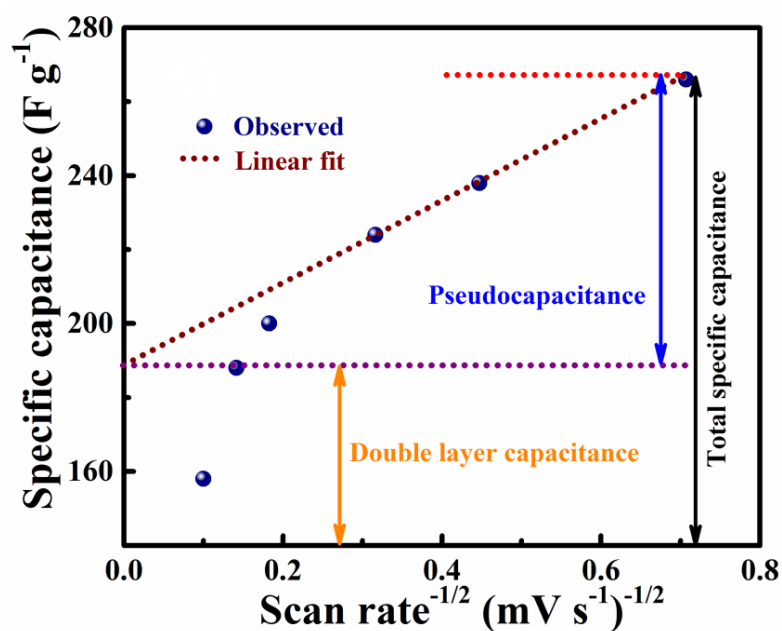
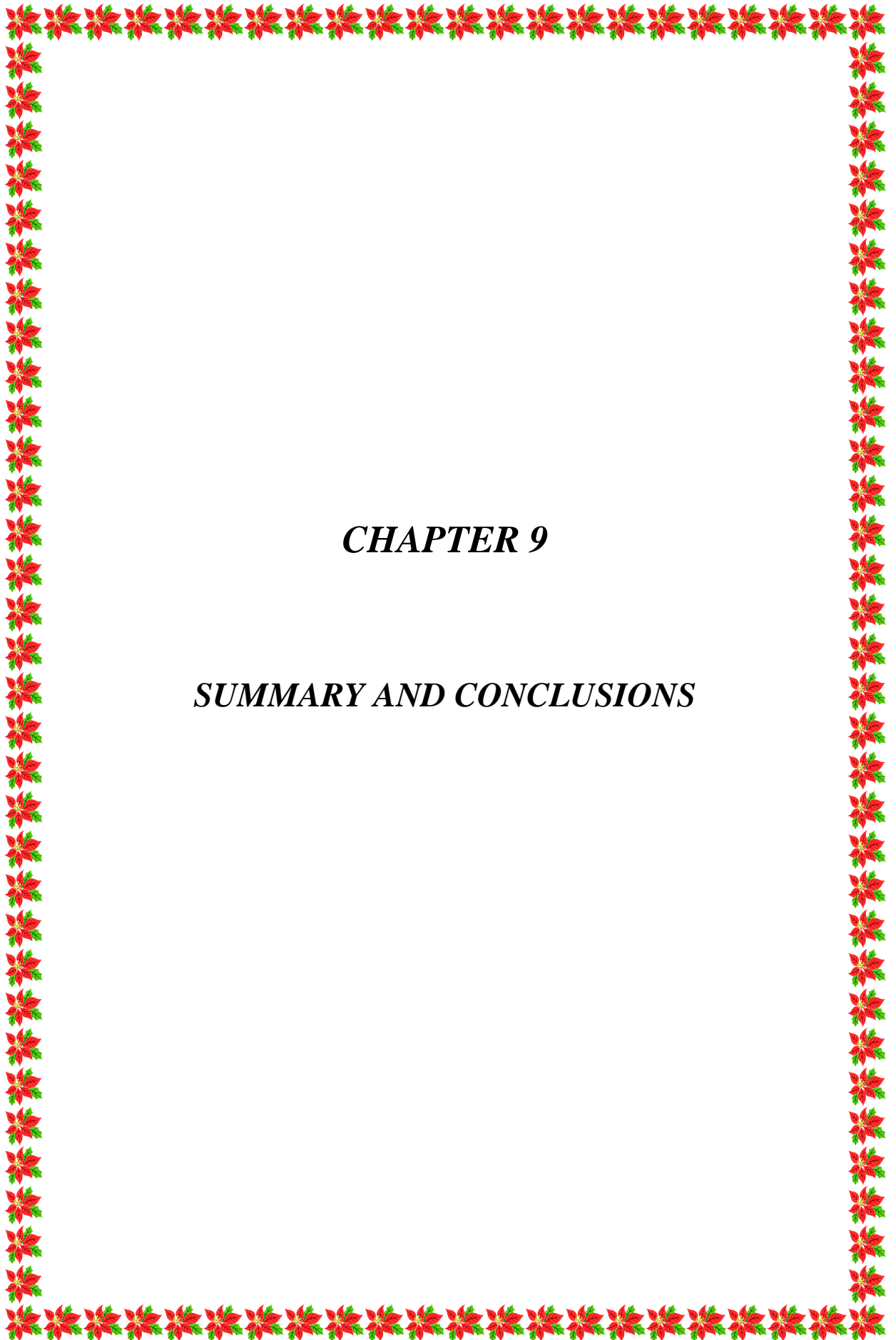


Figure 8.12 Determination of the C_{EDL} and C_P contribution of the 10 PGNC fabricated supercapacitor.

8.4 CONCLUSIONS

A one-pot solvothermal approach followed by calcination in air was employed for the synthesis of PGNC hybrid composites. The structural and morphological analysis revealed that the nanorods were uniformly distributed over the PG surface, making it a 3D hybrid structure. The prepared materials were tested as an active capacitive material for supercapacitor application in a 3-electrode setup. Apart from high capacitance values (1533 F g^{-1} at a scan rate of 5 mV s^{-1} and 1684 F g^{-1} at a current density of 1 A g^{-1}), the electrode material exhibited very high capacitance retention (94% of its initial value) after 10000 cycles at a current density of 8 A g^{-1} . The symmetrical supercapacitor fabricated employing these electrodes exhibits a high capacitance value of 266 F g^{-1} at a scan rate of 2 mV s^{-1} and 225 F g^{-1} at a current density of 1 A g^{-1} . The superior electrochemical behavior of this material in comparison with the NC is primarily attributed to the synergistic effect of the high surface area, electronic conductivity and high quantum capacitance of the PG. The high energy density (45.3 W h kg^{-1}), high power density ($17843.5 \text{ W kg}^{-1}$) and high cyclic stability (a retention of 93% of its initial capacitance even after 10000 charge-discharge cycles) of the fabricated supercapacitor make it a promising candidate for commercial applications.



CHAPTER 9

SUMMARY AND CONCLUSIONS

Chapter 9 outlines the summary of the work presented in the thesis along with the important conclusions drawn from the study. Scope for further research has also been included here.

9.1 SUMMARY

The thesis reports the successful synthesis of seven different kinds of novel electrode materials such as PG, NiO, PGNiO, NF, PGNF, NC and PGNC using a solvothermal method. All the synthesized electrode materials were carefully characterized for their structural, elemental, spectroscopic, morphological and surface area properties by employing appropriate techniques such as XRD, Raman, XPS, FTIR, FESEM, HRTEM and BET surface area analysis. The electrode materials were then investigated for the energy storage applications. The electrochemical characterizations such as CV, GCD, EIS and cyclic stability test were performed in an aqueous 2 M KOH electrolyte. A brief summary of the overall work presented in the thesis is given below.

Chapter 1 gives a brief introduction to the basic concepts of the study undertaken. It also gives a brief overview of the relevant works in the literature which focuses upon PG, NiO, NF, NC, PGNiO, PGNF and PGNC, their synthesis methods and their role in supercapacitor application. Scope and objectives of the present research work have been given at the end.

Chapter 2 presents and discusses an eco-friendly approach for the synthesis of PG and its energy storage application. In this chapter, the synthesis of PG with high surface area by a low-cost and eco-friendly method for mass production, employing an energy matching solvent system consisting of a mixture of 1:1 ethylene glycol and water (EG+H₂O) is discussed. The study of its supercapacitor performance in terms of specific capacitance and cyclability is also carried out. The superior electrochemical activity observed has been mainly attributed to the high surface area of PG sheets and its mesoporous structure, which is highly beneficial for the efficient storage of charges and transport of ions, which in turn enhances the supercapacitor performance.

In this chapter, the first principles DFT calculations were also performed to show the enhancement of charge bearing capacity of PG over graphene.

Chapter 3 deals with hassle-free solvothermal synthesis of NiO nanoflakes for supercapacitor application. This chapter reports the synthesis of NiO nanoflakes with high surface area using a mixed solvent solvothermal route, followed by calcination of the metal hydroxide in air. The as obtained nanoflakes when utilized as an electrode displayed a high capacitance value of 305 F g^{-1} at a scan rate of 5 mV s^{-1} with good rate capability and coulombic efficiency along with retention of 84% of the initial capacitance value after 5000 cycles at a current density of 8 A g^{-1} . The designed symmetrical supercapacitor by using the NiO electrodes also executed good electrochemical performance with good capacitance retention, along with high power density. The promising electrochemical features exhibited by the material has proved its suitability as a supercapacitor and can be further improvised by compositing it with carbon materials to improve the electrochemical performance.

Chapter 4 presents a simple solvothermal synthesis of PGNiO nanocomposites for supercapacitor application. This chapter reports the study of a hybrid composite of PG with nano flake structured NiO synthesized through an eco-friendly mixed solvent mediated solvothermal approach with an intent to improve the electrochemical performance in terms of capacitance, cyclic stability and power density. The synthesized 10 PGNiO composite electrode displayed a specific capacitance value of 511 F g^{-1} at a scan rate of 5 mV s^{-1} and 477 F g^{-1} at a current density of 1 A g^{-1} with 80% retention of initial capacitance value after 10000 discharge cycles at a current density of 8 A g^{-1} . The fabricated supercapacitor device exhibited a high power density of 12000 W kg^{-1} at a high current density of 12 A g^{-1} . The impressive electrochemical accomplishment is attributed to the presence of porous structure and good surface area of PGNiO composite, which not only acted as an ion-buffering reservoir but also maintained the mechanical strength during the continuous charge - discharge cycles.

Chapter 5 gives a descriptive report on solvothermal synthesis of NF nanoparticles for high performance supercapacitor applications. The study, describes the synthesis of NF nanoparticles using 1:1 water and ethylene glycol. The synthesis employing mixed solvent mediated route is a simple low temperature solvothermal approach to yields material with high capacitance value and high life cycle. The as prepared NF nanoparticles were studied for their electrochemical response for utilization as supercapacitor electrode material. When the electrode material is tested in aqueous 2 M KOH electrolyte, a high capacitance value of 478 F g^{-1} at a scan rate of 5 mV s^{-1} was obtained. The electrode material also exhibited good capacitance retention value of 88% after continuous 10000 cycles at a high current density of 8 A g^{-1} . The better electrochemical performance displayed by the electrode is primarily attributed to the nano dimension and good surface area along with mesoporous structure and large pore volume of NF. The easy synthetic route, high capacitance value in low concentration of KOH and absence of expensive current collectors like Ni foam makes the material potent to be used as electrode material in supercapacitors.

Chapter 6 deals with the synthesis, characterization and electrochemical performance of PGNF nanocomposite. In this chapter, PG of high surface area and NF of nano dimension, the combination of which led to PGNF composites was synthesized for the amelioration of the electrochemical performance. The prepared nanocomposites via a facile, low temperature solvothermal route depicted high electrochemical performance (1465 F g^{-1}) and cyclic stability (96% retention after 10000 cycles). The fabricated supercapacitor device also delivered impressive energy density and power density. This is primarily attributed to the synergic effect of the composite components and connotes their robust application in the field of supercapacitors.

Chapter 7 describes the synthesis, characterization and high supercapacitor performance of NC nanorods. This chapter describes the synthesis of NC nanorods by a low-temperature solvothermal route without the addition of templates and the study of their electrochemical properties by using an aqueous electrolyte. The

electrochemical study of this NC material revealed good performance and can be utilized for high performance supercapacitor application.

Chapter 8 provides details of template free low temperature solvothermal synthesis, characterization and energy storage applications of PGNC nanocomposites. This chapter presents the synthesis of 3D PGNC composites by a simple solvothermal method followed by calcination in air. The novelty of the work lies in the use of the mixed solvent for the synthesis of the composite to control the morphology of each constituent so as to improve the overall supercapacitance performance. The electrochemical results displayed from the CV, GCD and EIS studies proved the PGNC composite to be a potential material for high performance supercapacitor application.

Chapter 9 outlines the summary of the work presented in the thesis along with important conclusions drawn from the study. The results of the experimental investigation displayed in the thesis are presented in the tabular form and in Figure 9.1 (a) and (b). Scope for further research has also been included in this chapter.

References used have been listed at the end followed by the Bio-data.

9.2 CONCLUSIONS

- PG, oxides of Nickel (NiO, NF and NC) and its composites (PGNiO, PGNF and PGNC) can be easily synthesized by eco-friendly solvothermal method for supercapacitor applications with high performance.
- The synthesized electrode materials are economic, they exhibited high electrochemical performance and cyclic stability.
- Compositing of oxides of nickel with PG improved its electrochemical performance and stability due to the synergistic action of the components.
- Among the studied materials, PGNC exhibited highest capacitance value and cyclic stability as an electrode while PGNF had better performance as a fabricated device.

Table 9.1 Summarized results of the synthesized materials as an electrode.

Electrode material	C_S from CV (F g⁻¹)	C_S from GCD (F g⁻¹)	Energy density (Wh kg⁻¹)	Power density (W kg⁻¹)	Cyclic stability
PG	484 @ 5 mV s ⁻¹	437 @ 1 A g ⁻¹	34.2	375.4	87% after 10000 cycles
NiO	305 @ 5 mV s ⁻¹	190 @ 1 A g ⁻¹	5.3	225.0	84% after 5000 cycles
PGNiO	511 @ 5 mV s ⁻¹	477 @ 1 A g ⁻¹	13.4	225.0	80% after 10000 cycles
NF	478 @ 5 mV s ⁻¹	368 @ 1 A g ⁻¹	10.4	225.8	88% after 10000 cycles
PGNF	1465 @ 5 mV s ⁻¹	1320 @ 1 A g ⁻¹	37.2	225.5	94% after 10000 cycles
NC	440 @ 5 mV s ⁻¹	233 @ 1 A g ⁻¹	6.6	225.0	94% after 2000 cycles
PGNC	1533 @ 5 mV s ⁻¹	1684 @ 1 A g ⁻¹	47.4	225.5	94% after 10000 cycles

Table 9.2 Summarized results of the fabricated symmetrical supercapacitor device.

Electrode material	C_s from CV (F g⁻¹)	C_s from GCD (F g⁻¹)	Energy density (Wh kg⁻¹)	Power density (W kg⁻¹)	Cyclic stability
PG	297 @ 5 mV s ⁻¹	189 @ 1 A g ⁻¹	26.3	1502.8	93% after 5000 cycles
NiO	30.2 @ 5 mV s ⁻¹	8.8 @ 3 A g ⁻¹	1.2	3013.7	63% after 3000 cycles
PGNiO	86 @ 5 mV s ⁻¹	43 @ 2 A g ⁻¹	5.9	2000.0	84% after 10000 cycles
NF	77 @ 5 mV s ⁻¹	58.4 @ 1 A g ⁻¹	9.0	506.3	81% after 10000 cycles
PGNF	303 @ 5 mV s ⁻¹	160 @ 4 A g ⁻¹	22.2	4000.0	96% after 10000 cycles
NC	82 @ 5 mV s ⁻¹	73 @ 1 A g ⁻¹	12.6	506.0	91% after 2000 cycles
PGNC	266 @ 5 mV s ⁻¹	255 @ 1 A g ⁻¹	45.3	1208.0	93% after 10000 cycles

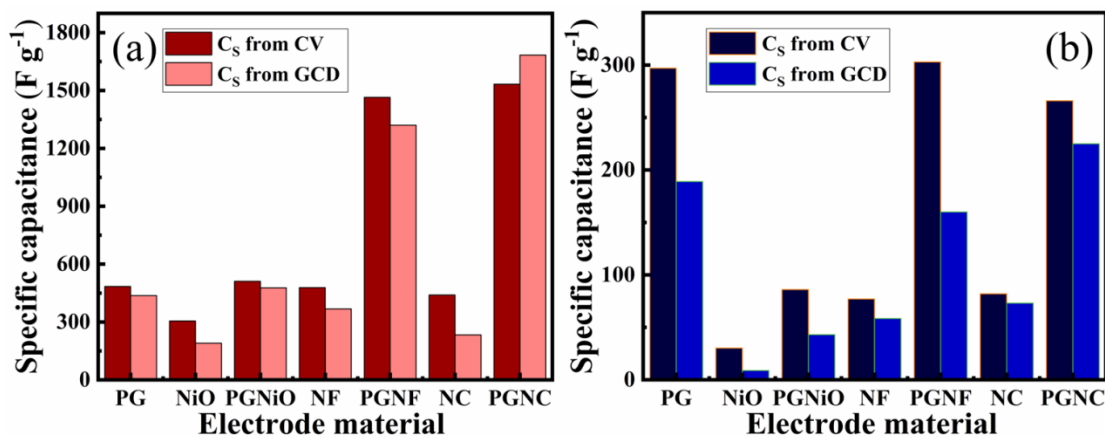
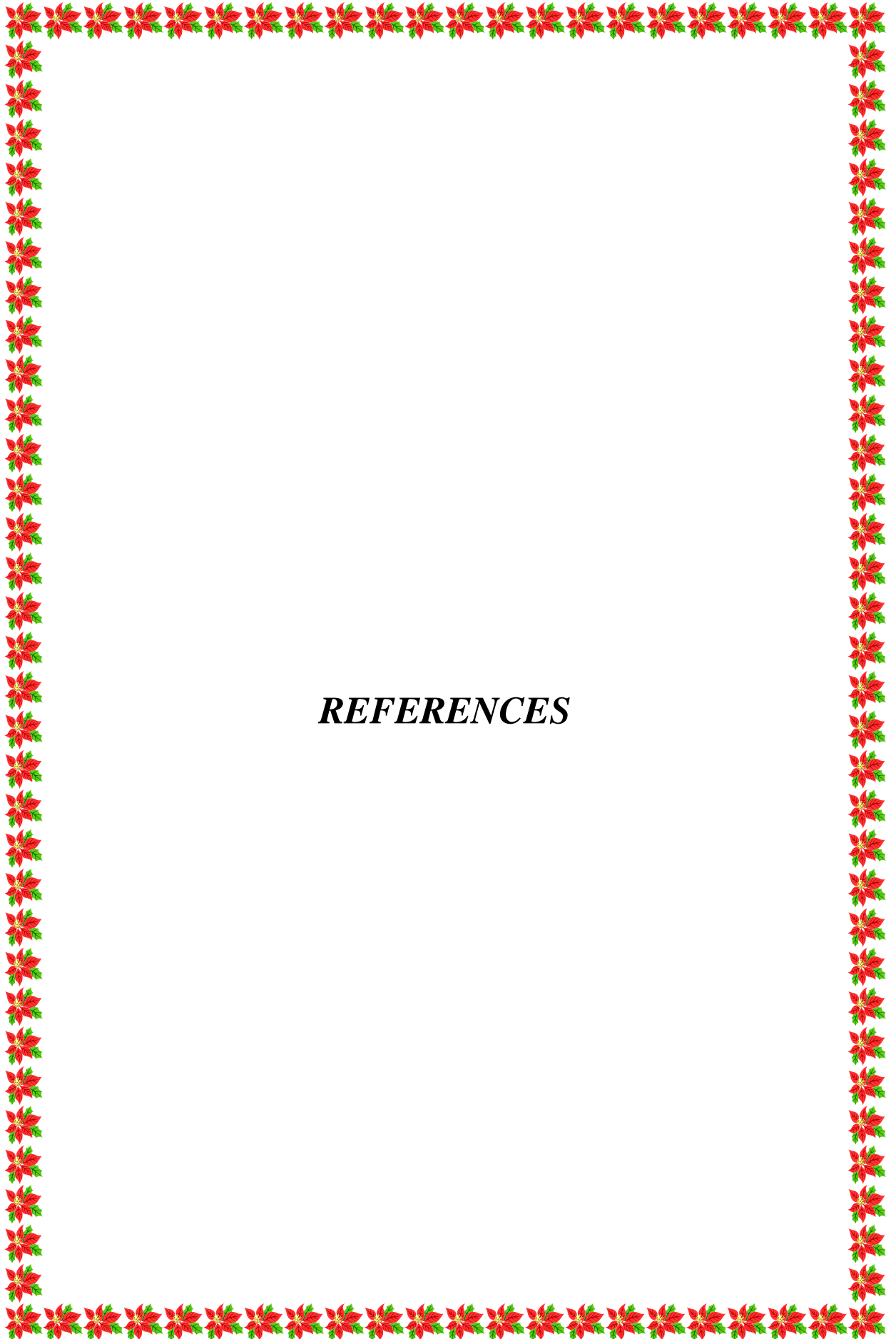


Figure 9.1 Comparison of specific capacitance values from CV and GCD data (a) for the electrode material and (b) for the supercapacitor device.

9.3 SCOPE FOR FUTURE WORK

- The electrochemical performance of the synthesized materials could be further improved by suitable doping of the oxides.
- The synthesized materials could be studied for hydrogen evolution reaction and photocatalysis.
- Various other oxides of nickel and their composites with PG can be synthesized and studied for their electrochemical performance.



REFERENCES

Ahmed, A., Ahmed, S., Johari, R., Parvaz, M. and Rafat, M. (2019). "Dual-energy application of NiO: Electrochemical and photovoltaic properties." *Optik*, 179, 485–491.

Ahmed, M.S. and Kim, Y.B. (2017). "Amide-functionalized graphene with 1, 4-diaminobutane as efficient metal-free and porous electrocatalyst for oxygen reduction." *Carbon*, 111, 577–586.

Al-Rubaye, S., Rajagopalan, R., Dou, S.X. and Cheng, Z. (2017). "Facile synthesis of a reduced graphene oxide wrapped porous NiCo₂O₄ composite with superior performance as an electrode material for supercapacitors." *J. Mater. Chem. A*, 5, 18989–8997.

An, C., Zhang, Y., Guo, H. and Wang, Y. (2019). "Metal oxide-based supercapacitors: progress and perspectives." *Nanoscale Adv.*, 1, 4644–4658.

Anwar, S., Muthu, K.S., Ganesh, V. and Lakshminarasimhan, N. (2011). "A comparative study of electrochemical capacitive behavior of NiFe₂O₄ synthesized by different routes." *J. Electrochem. Soc.*, 158, A976–A981.

Aparna, M.L., Grace, A.N., Sathyanarayanan, P. and Sahu, N.K. (2018). "A comparative study on the supercapacitive behaviour of solvothermally prepared metal ferrite (MFe₂O₄, M= Fe, Co, Ni, Mn, Cu, Zn) nanoassemblies." *J. Alloys Compd.*, 745, 385–395.

Arico, A. S., Bruce, P., Scrosati, B., Tarascon, J. M. and Van, S. W. (2005). "Nanostructured materials for advanced energy conversion and storage devices." *Nat. Mater.*, 4, 366–377.

Askari, M.B. and Salarizadeh, P. (2020). "Binary nickel ferrite oxide (NiFe₂O₄) nanoparticles coated on reduced graphene oxide as stable and high-performance asymmetric supercapacitor electrode material." *Int. J. Hydrogen Energy*. <https://doi.org/10.1016/j.ijhydene.2020.07.063>.

Badrayyana, S., Bhat, D.K., Shenoy, S., Ullal, Y. and Hegde, A.C. (2015d). “Novel Fe–Ni-Graphene composite electrode for hydrogen production.” *Int. J. Hydrogen Energy*, 40, 10453–10462.

Bai, Y., Yan, Z., Kang, L. and Liu, Z.H. (2019). “Preparation and capacitance of V₂O₅/holey graphene hybrid aerogel electrode with high performance.” *J. Alloys Compd.*, 780, 792–799.

Bai, Y., Yang, X., He, Y., Zhang, J., Kang, L., Xu, H., Shi, F., Lei, Z. and Liu, Z.H. (2016). “Formation process of holey graphene and its assembled binder-free film electrode with high volumetric capacitance.” *Electrochim. Acta*, 187, 543–551.

Balamurugan, S., Devi, M.D., Prakash, I. and Devaraj, S. (2018). “Lithium-ion doped NiFe₂O₄/SiO₂ nanocomposite aerogel for advanced energy storage devices.” *Appl. Surf. Sci.*, 449, 542–550.

Bandgar, S.B., Vadiyar, M.M., Ling, Y.C., Chang, J.Y., Han, S.H., Ghule, A.V. and Kolekar, S.S. (2018). “Metal precursor dependent synthesis of NiFe₂O₄ thin films for high-performance flexible symmetric supercapacitor.” *ACS Appl. Energy Mater.*, 1, 638–648.

Banerjee, D., Ghorai, U.K., Das, N.S., Das, B., Thakur, S. and Chattopadhyay, K.K. (2018). “Amorphous Carbon Nanotubes–Nickel Oxide Nanoflower Hybrids: A Low Cost Energy Storage Material.” *ACS Omega*, 3, 6311–6320.

Bantawal, H., Sethi, M., Shenoy, U.S. and Bhat, D.K. (2019). “Porous Graphene Wrapped SrTiO₃ Nanocomposite: Sr–C Bond as an Effective Coadjutant for High Performance Photocatalytic Degradation of Methylene Blue.” *ACS Appl. Nano Mater.*, 2, 6629–6636.

Barzegar, F., Bello, A., Momodu, D., Madito, M.J., Dangbegnon, J. and Manyala, N. (2016a). “Preparation and characterization of porous carbon from expanded graphite

for high energy density supercapacitor in aqueous electrolyte.” *J. Power Sources*, 309, 245–253.

Barzegar, F., Khaleed, A.A., Ugbo, F.U., Oyeniran, K.O., Momodu, D.Y., Bello, A., Dangbegnon, J.K. and Manyala, N. (2016b). “Cycling and floating performance of symmetric supercapacitor derived from coconut shell biomass.” *AIP Adv.*, 6, 115306.

Bashir, B., Rahman, A., Sabeeh, H., Khan, M.A., Aboud, M.F.A., Warsi, M.F., Shakir, I., Agboola, P.O. and Shahid, M. (2019). “Copper substituted nickel ferrite nanoparticles anchored onto the graphene sheets as electrode materials for supercapacitors fabrication.” *Ceram. Int.*, 45, 6759–6766.

Bhagwan, J., Nagaraju, G., Ramulu, B., Sekhar, S.C. and Yu, J.S. (2019). “Rapid synthesis of hexagonal NiCo_2O_4 nanostructures for high-performance asymmetric supercapacitors.” *Electrochim. Acta*, 299, 509–517.

Bhat, D.K. and Shenoy, U.S. (2020b). “SnTe Thermoelectrics: Dual step approach for enhanced performance.” *J. Alloys Compd.*, 834, 155181.

Bhojane, P., Sen, S. and Shirage, P.M. (2016). “Enhanced electrochemical performance of mesoporous NiCo_2O_4 as an excellent supercapacitive alternative energy storage material.” *Appl. Surf. Sci.*, 377, 376–384.

Bhojane, P., Sharma, A., Pusty, M., Kumar, Y., Sen, S. and Shirage, P. (2017). “Synthesis of ammonia-assisted porous nickel ferrite (NiFe_2O_4) nanostructures as an electrode material for supercapacitors.” *J. Nanosci. Nanotech.*, 17, 1387–1392.

Bhosale, S.V., Suryawanshi, S.R., Bhoraskar, S.V., More, M.A., Joag, D.S. and Mathe, V.L. (2015). “Influence of morphology and crystallinity on field emission properties of NiFe_2O_4 nanoparticles grown by high-temperature vapor phase condensation route.” *Mater. Res. Exp.*, 2, 095001.

Biswas, S., Sharma, V., Mandal, D., Chowdhury, A., Chakravarty, M., Priya, S., Gowda, C.C., De, P., Singh, I. and Chandra, A. (2020). “Hollow nanostructures of metal oxides as emerging electrode materials for high performance supercapacitors.” *Cryst. Eng. Commun.*, 22, 1633–1644.

Bose, P., Ghosh, S., Basak, S. and Naskar, M.K. (2016). “A facile synthesis of mesoporous NiO nanosheets and their application in CO oxidation.” *J. Asian Ceram. Soc.*, 4, 1–5.

Brousse, T., Bélanger, D. and Long, J.W. (2015). “To be or not to be pseudocapacitive?” *J. Electrochem. Soc.*, 162, A5185–A5189.

Cai, Y.Z., Cao, W.Q., He, P., Zhang, Y.L. and Cao, M.S. (2019b). “NiFe₂O₄ nanoparticles on reduced graphene oxide for supercapacitor electrodes with improved capacitance.” *Mater. Res. Exp.*, 6, 105535.

Cai, Y.Z., Cao, W.Q., Zhang, Y.L., He, P., Shu, J.C. and Cao, M.S. (2019a). “Tailoring rGO-NiFe₂O₄ hybrids to tune transport of electrons and ions for supercapacitor electrodes.” *J. Alloys Compd.*, 811, 152011.

Cao, N., Zou, X., Huang, Y. and Zhao, Y. (2015). “Preparation of NiFe₂O₄ architectures for affinity separation of histidine-tagged proteins.” *Mater. Lett.*, 144, 161–164.

Cao, Z., Liu, C., Huang, Y., Gao, Y., Wang, Y., Li, Z., Yan, Y. and Zhang, M. (2020). “Oxygen-vacancy-rich NiCo₂O₄ nanoneedles electrode with poor crystallinity for high energy density all-solid-state symmetric supercapacitors.” *J. Power Sources*, 449, 227571. <https://doi.org/10.1016/j.jpowsour.2019.227571>

Chai, Y. Li, Z., Wang, J., Mo, Z. and Yang, S. (2019). “Construction of hierarchical holey graphene/MnO₂ composites as potential electrode materials for supercapacitors.” *J. Alloys Compd.*, 775, 1206–1212.

Chang, X., Li, W., Liu, Y., He, M., Zheng, X., Lv, X. and Ren, Z. (2019). "Synthesis and characterization of NiCo₂O₄ nanospheres/nitrogen-doped graphene composites with enhanced electrochemical performance." *J. Alloys Compd.*, 784, 293–300.

Chatterjee, M., Saha, S., Das, S. and Pradhan, S.K. (2020). "Advanced asymmetric supercapacitor with NiCo₂O₄ nanoparticles and nanowires electrodes: A comparative morphological hierarchy." *J. Alloys Compd.*, 821, 153503.

Chen, C., Chen, C., Huang, P., Duan, F., Zhao, S., Li, P., Fan, J., Song, W. and Qin, Y. (2014). "NiO/nanoporous graphene composites with excellent supercapacitive performance produced by atomic layer deposition." *Nanotechnology*, 25, 504001.

Chen, G., Guan, H., Dong, C. and Wang, Y. (2018). "Synthesis of core-shell carbon sphere@ nickel oxide composites and their application for supercapacitors." *Ionics*, 24, 513–521.

Chen, H., Jiang, J., Zhang, L., Qi, T., Xia, D. and Wan, H. (2014). "Facilely synthesized porous NiCo₂O₄ flowerlike nanostructure for high-rate supercapacitors." *J. Power Sources*, 248, 28–36.

Chen, L., Li, X., Ma, C., Wang, M., Zhou, J. (2017). "Interaction and quantum capacitance of nitrogen/sulfur co-doped graphene: A theoretical calculation." *J. Phys. Chem. C*, 121, 18344–18350.

Chen, X., Huang, Y., Zhang, K., Feng, X. and Li, S. (2016). "Self-assembled flower-like NiFe₂O₄ decorated on 2D graphene nanosheets composite and their excellent electrochemical performance as anode materials for LIBs." *J. Alloys Compd.*, 686, 905–913.

Chime, U.K., Nkele, A.C., Ezugwu, S., Nwanya, A.C., Shinde, N.M., Kabede, M., Ejikeme, P.M., Maaza, M. and Ezema, F.I. (2020). "Recent progress in nickel oxide-based electrodes for high-performance supercapacitors." *Curr. Opin. Electrochem.*, 21, 175–181.

Connors, K.A. and Wright, J.L. (1989). “Dependence of surface tension on composition of binary aqueous-organic solutions.” *Anal. Chem.*, 61, 194–198.

Cuong, N.D., Van Thi, T.T. and Van Hieu, N. (2019). “Konjac glucomannan-templated synthesis of three-dimensional NiO nanostructures assembled from porous NiO nanoplates for gas sensors.” *RSC Adv.*, 9, 9584–9593.

Deng, T., Zhang, W., Arcelus, O., Wang, D., Shi, X., Zhang, X., Carrasco, J., Rojo, T. and Zheng, W. (2018). “Vertically co-oriented two dimensional metal-organic frameworks for packaging enhanced supercapacitive performance.” *Commun. Chem.* 1, 1–9.

Dimiev, A.M., Ceriotti, G., Metzger, A., Kim, N.D. and Tour, J.M. (2016). “Chemical mass production of graphene nanoplatelets in ~ 100 % yield.” *ACS Nano*, 10, 274–279.

Dong, K., Wang, Z., Sun, M., Wang, D., Luo, S. and Liu, Y. (2019). “Construction of NiCo₂O₄ nanorods into 3D porous ultrathin carbon networks for high-performance asymmetric supercapacitors.” *J. Alloys Compd.*, 783, 1–9.

Dupont, M.F. and Donne, S.W. (2016). “Charge storage mechanisms in electrochemical capacitors: Effects of electrode properties on performance.” *J. Power Sources*, 326, 613–623.

Dupont, M.F., Forghani, M., Cameron, A.P. and Donne, S.W. (2018). “Effect of electrolyte cation on the charge storage mechanism of manganese dioxide for electrochemical capacitors.” *Electrochim. Acta*, 271, 337–350.

Edison, T.N.J.I., Atchudan, R. and Lee, Y.R. (2018). “Binder-free electro-synthesis of highly ordered nickel oxide nanoparticles and its electrochemical performance.” *Electrochim. Acta*, 283, 1609–1617.

Eftekhari, A. (2018). “The mechanism of ultrafast supercapacitors.” *J. Mater. Chem. A*, 6, 2866–2876.

Fan, Z., Zhao, Q., Li, T., Yan, J., Ren, Y., Feng, J. and Wei, T. (2012). “Easy synthesis of porous graphene nanosheets and their use in supercapacitors.” *Carbon*, 50, 1699–1712.

Fang, J., Liu, Q., Yang, S., Zhang, X., Wei, C., Tan, M. and Wen, S. (2018). “Design and synthesis of N-doped mesoporous carbon@NiCo₂O₄ nanocomposites with various morphologies for high electrochemical performance applied in supercapacitors.” *Mater. Res. Bulletin*, 105, 312–317.

Fang, S., Bresser, D. And Passerini, S. (2020) “Transition metal oxide anodes for electrochemical energy storage in lithium-and sodium-ion batteries.” *Adv. Energy Mater.*, 10, 1902485.

Feng, H., Xie, P., Xue, S., Li, L., Hou, X., Liu, Z., Wu, D., Wang, L. and Chu, P.K. (2018). “Synthesis of three-dimensional porous reduced graphene oxide hydrogel/carbon dots for high-performance supercapacitor.” *J. Electroanal. Chem.*, 808, 321–328.

Foo, C.Y., Lim, H.N., Mahdi, M.A.B., Chong, K.F. and Huang, N.M. (2016). “High-performance supercapacitor based on three-dimensional hierarchical rGO/nickel cobaltite nanostructures as electrode materials.” *J. Phys, Chem. C*, 120, 21202–21210.

Fu, M., Chen, W., Zhu, X. and Liu, Q. (2018). “One-step preparation of one dimensional nickel ferrites/graphene composites for supercapacitor electrode with excellent cycling stability.” *J. Power Sources*, 396, 41–48.

Gao X., Wang, W., Bi, J., Chen, Y., Hao, X., Sun, X. And Zhang, J. (2019) “Morphology-controllable preparation of NiFe₂O₄ as high performance electrode material for supercapacitor.” *Electrochim. Acta*, 296, 181–189.

Gao, H., Wang, X., Wang, G., Hao, C., Huang, C. and Jiang, C. (2019). “Facile construction of a $\text{MgCo}_2\text{O}_4@ \text{NiMoO}_4/\text{NF}$ core-shell nanocomposite for high-performance asymmetric supercapacitors.” *J. Mater. Chem. C*, 7, 13267–13278.

Gao, J.S., Liu, Z., Lin, Y., Tang, Y., Lian, T. and He, Y. (2020). “ NiCo_2O_4 nanofeathers derived from prussian blue analogues with enhanced electrochemical performance for supercapacitor.” *Chem. Eng. J.*, 388, 124368. <https://doi.org/10.1016/j.cej.2020.124368>.

Gao, X., Bi, J., Wang, W., Liu, H., Chen, Y., Hao, X., Sun, X. and Liu, R. (2020). “Morphology-controllable synthesis of NiFe_2O_4 growing on graphene nanosheets as advanced electrode material for high performance supercapacitors.” *J. Alloys Compd.*, 826, 154088.

Gao, X., Wang, W., Bi, J., Chen, Y., Hao, X., Sun, X. and Zhang, J. (2019). “Morphology-controllable preparation of NiFe_2O_4 as high performance electrode material for supercapacitor.” *Electrochim. Acta*, 296, 181–189.

Gao, Z., Zhang, L., Chang, J., Wang, Z., Wu, D., Xu, F., Guo, Y. and Jiang, K. (2018). “ ZnCo_2O_4 -reduced graphene oxide composite with balanced capacitive performance in asymmetric supercapacitors.” *Appl. Surf. Sci.*, 442, 138–147.

Ge, J., Fan, G., Si, Y., He, J., Kim, H.Y., Ding, B., Al-Deyab, S.S., El-Newehy, M. and Yu, J. (2016). “Elastic and hierarchical porous carbon nanofibrous membranes incorporated with NiFe_2O_4 nanocrystals for highly efficient capacitive energy storage.” *Nanoscale*, 8, 2195–2204.

Ghosh, K., Yue, C.Y., Sk, M.M., Jena, R.K. and Bi, S. (2018a). “Development of a 3D graphene aerogel and 3D porous graphene/ $\text{MnO}_2@$ polyaniline hybrid film for all-solid-state flexible asymmetric supercapacitors.” *Sustain. Energy Fuels*, 2, 280–293.

Ghosh, K. and Yue, C.Y. (2018b). “Development of 3D MoO_3 /graphene aerogel and sandwich-type polyaniline decorated porous MnO_2 -graphene hybrid film based high

performance all-solid-state asymmetric supercapacitors.” *Electrochim. Acta*, 276, 47–63.

Giannozzi, P., Baroni, S., Bonini, N., Calandra, M., Car, R., Cavazzoni, C., Ceresoli, D., Chiarotti, G.L., Cococcioni, M., Dabo, I. et al. (2009). “Quantum ESPRESSO: A modular and open-source software project for quantum simulations of materials.” *J. Phys.: Condens. Matter.*, 21, 395502.

Goel, S., Tomar, A.K., Sharma, R.K. and Singh, G. (2018). “Highly pseudocapacitive NiO nanoflakes through surfactant-free facile microwave-assisted route.” *ACS Appl. Energy Mater.*, 1, 1540–1548.

Gong, C., He, Y., Zhou, J., Chen, W., Han, W., Zhang, Z., Zhang, P., Pan, X., Wang, Z. and Xie, E. (2014). “Synthesis on winged graphene nanofibers and their electrochemical capacitive performance.” *ACS Appl. Mater. Interfaces*, 6, 14844–14850.

Gregory, D.P., Ng, D.Y.C., Long, G.M., and Bockris, J.O.M. (1972) “Electrochemistry of cleaner environments.” Plenum Press, New York.

Gui, J., Zhang, J., Liu, T., Peng, Y. and Chang, J. (2017). “Two-step controllable preparation of NiO nanocrystal anchored reduced graphene oxide sheets and their electrochemical performance as supercapacitors.” *New J. Chem.*, 41, 10695–10702.

Gund, G.S., Lokhande, C.D. and Park, H.S. (2018). “Controlled synthesis of hierarchical nanoflake structure of NiO thin film for supercapacitor application.” *J. Alloys Compd.*, 741, 549–556.

Han, X., Funk, M.R., Shen, F., Chen, Y.C., Li, Y., Campbell, C.J., Dai, J., Yang, X., Kim, J.W., Liao, Y. and Connell, J.W. (2014). “Scalable holey graphene synthesis and dense electrode fabrication toward high-performance ultracapacitors.” *ACS Nano*, 8, 8255–8265.

Hareesh, K., Shateesh, B., Joshi, R.P., Dahiwal, S.S., Bhoraskar, V.N., Haram, S.K. and Dhole, S.D. (2016). "PEDOT: PSS wrapped NiFe₂O₄/rGO tertiary nanocomposite for the super-capacitor applications." *Electrochim. Acta*, 201, 106–116.

He, C., Jiang, Y., Zhang, X., Cui, X. and Yang, Y. (2019). "A Simple Glucose-Blowing Approach to Graphene-Like Foam/NiO Composites for Asymmetric Supercapacitors." *Energy Technol.*, 1900923.

Hernandez, Y., Nicolosi, V., Lotya, M., Blighe, F.M., Sun, Z., De, S., McGovern, I.T., Holland, B., Byrne, M., Gun'Ko, Y.K., Boland, J.J., Niraj, P., Duesberg, G., Krishnamurthy, S., Goodhue, R., Hutchison, J., Scardaci, V., Ferrari, A.C. and Coleman, J.N. (2008). "High-yield production of graphene by liquid-phase exfoliation of graphite." *Nat. Nanotech.*, 3, 563–568.

Hoa, N.D., Hung, C.M., Van Duy, N. and Van Hieu, N. (2018). "Nanoporous and crystal evolution in nickel oxide nanosheets for enhanced gas-sensing performance." *Sens. Actuators B Chem.*, 273, 784–793.

Hu, K., Xie, X., Szkopek, T. and Cerruti, M., (2016). "Understanding hydrothermally reduced graphene oxide hydrogels: from reaction products to hydrogel properties." *Chem. Mater.*, 28, 1756–1768.

Hu, M.Z.C., Payzant, E.A., Byers, C.H. (2000). "Sol-gel and ultrafine particle formation via dielectric tuning of inorganic salt-alcohol-water solutions." *J. Colloid Interface Sci.*, 222, 20–36.

Hua, M., Xu, L., Cui, F., Lian, J., Huang, Y., Bao, J., Qiu, J., Xu, Y., Xu, H., Zhao, Y. and Li, H. (2018). "Hexamethylenetetramine-assisted hydrothermal synthesis of octahedral nickel ferrite oxide nanocrystallines with excellent supercapacitive performance." *J. Mater. Sci.*, 53, 7621–7636.

Huang, C., Hao, C., Zheng, W., Zhou, S., Yang, L., Wang, X., Jiang, C. and Zhu, L. (2020). "Synthesis of polyaniline/nickel oxide/sulfonated graphene ternary composite for all-solid-state asymmetric supercapacitor." *Appl. Surf. Sci.*, 505, 144589.

Hwang, J., Ha, S.J., Ramadoss, A., Yoon, K.Y. and Jang, J.H. (2020). "Stacking-free porous graphene network for high capacitive performance." *ACS Appl. Energy Mater.*, 3, 4348–4355.

Illán-Gómez, M.J., Garcia-Garcia, A., Salinas-Martinez de Lecea, C. and Linares-Solano, A. (1996) "Activated carbons from Spanish coals. 2. Chemical activation." *Energy Fuels*, 10, 1108–1114.

Javed, M.S., Zhang, C., Chen, L., Xi, Y. and Hu, C. (2016). "Hierarchical mesoporous NiFe₂O₄ nanocone forest directly growing on carbon textile for high performance flexible supercapacitors." *J. Mater. Chem. A*, 4, 8851–8859.

Jiang, H., Yang, K., Ye, P., Huang, Q., Wang, L. and Li, S. (2018). "Optimized NiCo₂O₄/rGO hybrid nanostructures on carbon fiber as an electrode for asymmetric supercapacitors." *RSC Adv.*, 8, 37550–37556.

Jiang, Y., Chen, D., Song, J., Jiao, Z., Ma, Q., Zhang, H., Cheng, L., Zhao, B. and Chu, Y. (2013). "A facile hydrothermal synthesis of graphene porous NiO nanocomposite and its application in electrochemical capacitors." *Electrochim. Acta*, 91, 173–178.

Jiu, H., Jiang, L., Gao, Y., Zhang, Q. and Zhang, L. (2019). "Synthesis of three-dimensional graphene aerogel-supported NiCo₂O₄ nanowires for supercapacitor application." *Ionics*, 25, 4325–4331.

Kahimbi, H., Hong, S.B., Yang, M. and Choi, B.G. (2017). "Simultaneous synthesis of NiO/reduced graphene oxide composites by ball milling using bulk Ni and graphite oxide for supercapacitor applications." *J. Electroanal. Chem.*, 786, 14–19.

Kang, H.G., Jeong, J.M., Hong, S.B., Lee, G.Y., Kim, J.W. and Choi, B.G. (2019). “Scalable exfoliation and activation of graphite into porous graphene using microwaves for high-performance supercapacitors.” *J. Alloys Compd.*, 770, 458–465.

Khoshdel, M.M., Targholi, E., Momeni, M.J. (2015). “A first principle calculation of quantum capacitance of co-doped graphenes as supercapacitor electrodes.” *J. Phys. Chem. C*, 119, 26290–26295.

Khosrabi, D. and Connors, K.A. (1993). “Solvent effects on chemical processes. 3. Surface tension of binary aqueous organic solvents.” *J. Sol. Chem.*, 22, 321–330.

Kim, H.K., Bak, S.M., Lee, S.W., Kim, M.S., Park, B., Lee, S.C., Choi, Y.J., Jun, S.C., Han, J.T., Nam, K.W. and Chung, K.Y. (2016). “Scalable fabrication of micron-scale graphene nanomeshes for high-performance supercapacitor applications.” *Energy Environ. Sci.*, 9, 1270–1281.

Kim, T., Ramadoss, A., Saravanakumar, B., Veerasubramani, G.K. and Kim, S.J. (2016). “Synthesis and characterization of NiCo₂O₄ nanoplates as efficient electrode materials for electrochemical supercapacitors.” *Appl. Surf. Sci.*, 370, 452–458.

Kitchamsetti, N., Chikate, P.R., Patil, R.A., Ma, Y.R., Shirage, P.M. and Devan, R.S. (2019). “Perforated mesoporous NiO nanostructures for an enhanced pseudocapacitive performance with ultra-high rate capability and high energy density.” *Cryst. Eng. Comm.*, 21, 7130–7140.

Ko, T.H., Radhakrishnan, S., Seo, M.K., Khil, M.S., Kim, H.Y. and Kim, B.S. (2017). “A green and scalable dry synthesis of NiCo₂O₄/graphene nanohybrids for high-performance supercapacitor and enzymeless glucose biosensor applications.” *J. Alloys Compd.*, 696, 193–200.

Kolathodi, M.S., Palei, M. and Natarajan, T.S. (2015). “Electrospun NiO nanofibers as cathode materials for high performance asymmetric supercapacitors.” *J. Mater. Chem. A*, 3, 7513–7522.

Kumar, A., Sanger, A., Kumar, A. and Chandra, R. (2017). “Single-step growth of pyramidally textured NiO nanostructures with improved supercapacitive properties.” *Int. J. Hydrogen Energy*, 42, 6080–6087.

Kumar, D.R., Prakasha, K.R., Prakash, A.S. and Shim, J.J. (2020). “Direct growth of honeycomb-like NiCo₂O₄@ Ni foam electrode for pouch-type high-performance asymmetric supercapacitor.” *J. Alloys Compd.*, 155370. <https://doi.org/10.1016/j.jallcom.2020.155370>.

Kumar, N., Kumar, A., Huang, G.M., Wu, W.W. and Tseng, T.Y. (2018). “Facile synthesis of mesoporous NiFe₂O₄/CNTs nanocomposite cathode material for high performance asymmetric pseudocapacitors.” *Appl. Surf. Sci.*, 433, 1100–1112.

Kumar, P.R. and Mitra, S. (2013). “Nickel ferrite as a stable, high capacity and high rate anode for Li-ion battery applications.” *RSC Adv.*, 3, 25058–25064.

Lamiel, C. and Shim, J.J. (2016). “Mesoporous 3D graphene@NiCo₂O₄ arrays on nickel foam as electrodes for high-performance supercapacitors.” *Mater. Lett.*, 170, 105–109.

Li, C., Wang, X., Li, S., Li, Q., Xu, J., Liu, X., Liu, C., Xu, Y., Liu, J., Li, H. and Guo, P. (2017). “Optimization of NiFe₂O₄/rGO composite electrode for lithium-ion batteries.” *Appl. Surf. Sci.*, 416, 308–317.

Li, L., Zhang, Y.Q., Liu, X.Y., Shi, S.J., Zhao, X.Y., Zhang, H., Ge, X., Cai, G.F., Gu, C.D., Wang, X.L. and Tu, J.P. (2014) “One-dimension MnCo₂O₄ nanowire arrays for electrochemical energy storage.” *Electrochim. Acta*, 116, 467–474.

Li, S., Yang, K., Ye, P., Jiang, H., Zhang, Z., Huang, Q. and Wang, L. (2019). “Hierarchical interpenetrating rHGO-decorated NiCo₂O₄ nanowires architectures for high-performance supercapacitors.” *Appl. Surf. Sci.*, 473, 326–333.

Li, Y., Hou, X., Zhang, Z., Hai, Z., Xu, H., Cui, D., Zhuiykov, S. and Xue, C. (2018). “NiCo₂O₄ particles with diamond-shaped hexahedron structure for high-performance supercapacitors.” *Appl. Surf. Sci.*, 436, 242–251.

Li, Y., Wei, Q., Wang, R., Zhao, J., Quan, Z., Zhan, T., Li, D., Xu, J., Teng, H. and Hou, W. (2020). “3D hierarchical porous nitrogen-doped carbon/Ni@NiO nanocomposites self-templated by cross-linked polyacrylamide gel for high performance supercapacitor electrode.” *J. Colloid Interface Sci.*, 570, 286–299.

Li, Y., Zhai, J., Zhao, L., Chen, J., Shang, X., Song, C., Chen, J., Liu, S. and Meng, F. (2019). “FeCoNi alloy-encapsulated graphene nanoplatelets with excellent magnetic properties, thermal stability and electrochemical performances.” *J. Solid State Chem.*, 276, 19–29.

Li, Z., Zhang, W., Liu, Y., Guo, J. and Yang, B. (2018). “2D nickel oxide nanosheets with highly porous structure for high performance capacitive energy storage.” *J. Phys. D Appl. Phys.*, 51, 045302.

Lin, L., Zheng, X., Zhang, S. and Allwood, D.A., (2014). “Surface energy engineering in the solvothermal deoxidation of graphene oxide” *Adv. Mater. Interfaces*, 1, 1300078.

Liu, G., Shao, J., Gao, Y., Chen, Z. and Qu, Q. (2017). “One-pot syntheses of spinel AB₂O₄ (A= Ni or Co, B= Mn or Fe) microspheres with different hollow interiors for supercapacitors application.” *Chin. J. Chem.*, 35, 67–72.

Liu, L., Sun, L., Liu, J., Xiao, X., Hu, Z., Cao, X., Wang, B. and Liu, X. (2014). “Enhancing the electrochemical properties of NiFe₂O₄ anode for lithium ion battery through a simple hydrogenation modification.” *Int. J. Hydrogen Energy*, 39, 11258–11266.

- Liu, M., Wang, X., Zhu, D., Li, L., Duan, H., Xu, Z., Wang, Z. and Gan, L. (2017). “Encapsulation of NiO nanoparticles in mesoporous carbon nanospheres for advanced energy storage.” *Chem. Eng. J.*, 308, 240–247.
- Liu, P., Yang, M., Zhou, S., Huang, Y. and Zhu, Y. (2019). “Hierarchical shell-core structures of concave spherical NiO nanospines@carbon for high performance supercapacitor electrodes.” *Electrochim. Acta*, 294, 383–390.
- Liu, X., Zou, S., Liu, K., Lv, C., Wu, Z., Yin, Y., Liang, T. and Xie, Z. (2018). “Highly compressible three-dimensional graphene hydrogel for foldable all-solid-state supercapacitor.” *J. Power Sources*, 384, 214–222.
- Liu, Y., Gao, C., Li, Q. and Pang, H. (2019). “Nickel oxide/graphene composites: synthesis and applications.” *Chem. Eur. J.*, 25(9), 2141–2160.
- Low, W.H., Khiew, P.S., Lim, S.S., Siong, C.W. and Ezeigwe, E.R. (2019). “Recent development of mixed transition metal oxide and graphene/mixed transition metal oxide based hybrid nanostructures for advanced supercapacitors.” *J. Alloys Compd.*, 775, 1324–1356.
- Lu, X.F., Wu, D.J., Li, R.Z., Li, Q., Ye, S.H., Tong, Y.X. and Li, G.R. (2014). “Hierarchical NiCo₂O₄ nanosheets@hollow microrod arrays for high-performance asymmetric supercapacitors.” *J. Mater. Chem. A*, 2(13), 4706–4713.
- Lu, Y., Su, L., Qi, J., Lei, S., Liu, B., Zang, Q., Shi, S. and Yan, X. (2018). “A combined DFT and experimental study on the nucleation mechanism of NiO nanodots on graphene.” *J. Mater. Chem. A*, 6, 13717–13724.
- Luo, J., Wang, J., Liu, S., Wu, W., Jia, T., Yang, Z., Mu, S. and Huang, Y. (2019). “Graphene quantum dots encapsulated tremella-like NiCo₂O₄ for advanced asymmetric supercapacitors.” *Carbon*, 146, 1–8.

Lv, J., Wang, Z. and Miura, H. (2018). “Facile synthesis of mesoporous NiO nanoflakes on graphene foam and its electrochemical properties for supercapacitor application.” *Solid State Commun.*, 269, 45–49.

Marcano, D.C., Kosynkin, D.V., Berlin, J.M., Sinitskii, A., Sun, Z., Slesarev, A., Alemany, L.B., Lu, W. and Tour, M. (2010). “Improved synthesis of graphene oxide.” *ACS Nano*, 4, 4806–4814.

Meng, X., Lu, L. and Sun, C. (2018). “Green synthesis of three-dimensional MnO₂/graphene hydrogel composites as a high-performance electrode material for supercapacitors.” *ACS Appl. Mater. Interfaces*, 10, 16474–16481.

Mishra, A.K., Ramaprabhu, S. (2011). “Functionalized graphene-based nanocomposites for supercapacitor application.” *J. Phys. Chem. C*, 115, 14006–14013.

Mohamed, M.J.S. and Bhat, D.K. (2017b). “A facile microwave approach to synthesize RGO-BaWO₄ composites for high performance visible light induced photocatalytic degradation of dyes.” *AIMS Mater. Sci.*, 4, 487.

Mohamed, M.J.S., Shenoy, S. and Bhat, D.K. (2018a). “Novel NRGO-CoWO₄-Fe₂O₃ nanocomposite as an efficient catalyst for dye degradation and reduction of 4-nitrophenol.” *Mat. Chem. Phys.*, 208, 112–122.

Mohamed, M.J.S., Shenoy, U.S. and Bhat, D.K. (2017a). “High Performance Dual Catalytic Activity of Novel Zinc Tungstate-Reduced Graphene Oxide Nanocomposites.” *Adv. Sci., Eng. Med.*, 9, 115–121.

Mondal, A., Maiti, S., Mahanty, S. and Panda, A.B. (2017). “Large-scale synthesis of porous NiCo₂O₄ and rGO-NiCo₂O₄ hollow-spheres with superior electrochemical performance as a faradaic electrode.” *J. Mater. Chem. A*, 5, 16854–16864.

Mondal, A.K., Su, D., Chen, S., Kretschmer, K., Xie, X., Ahn, H.J. and Wang, G. (2015). "A Microwave Synthesis of Mesoporous NiCo₂O₄ Nanosheets as Electrode Materials for Lithium-Ion Batteries and Supercapacitors." *Chem. Phys. Chem.*, 16, 169–175.

Mondal, M., Das, B., Howli, P., Das, N.S. and Chattopadhyay, K.K. (2018). "Porosity-tuned NiO nanoflakes: Effect of calcination temperature for high performing supercapacitor application." *J. Electroanal. Chem.*, 813, 116–126.

Mousavi-Khoshdel, M., Targholi, E. and Momeni, M.J. (2015). "First-principles calculation of quantum capacitance of codoped graphenes as supercapacitor electrodes." *J. Phys. Chem. C*, 119, 26290–26295.

Mungse, H.P., Sharma, O.P., Sugimura, H., Khatri, O.P. (2014). "Hydrothermal deoxygenation of graphene oxide in sub-and supercritical water." *RSC Adv.*, 4, 22589–22595.

Nguyen, K., Hoa, N.D., Hung, C.M., Le, D.T.T., Van Duy, N. and Van Hieu, N. (2018). "A comparative study on the electrochemical properties of nanoporous nickel oxide nanowires and nanosheets prepared by a hydrothermal method." *RSC Adv.*, 8, 19449–19455.

Niu, Z., Chen, J., Hng, H.H., Ma, J. and Chen, X. (2012). "A leavening strategy to prepare reduced graphene oxide foams." *Adv. Mater.*, 24, 4144–4150.

Oyedotun, K.O., Madito, M.J., Bello, A., Momodu, D.Y., Mirghni, A.A. and Manyala, N. (2017). "Investigation of graphene oxide nanogel and carbon nanorods as electrode for electrochemical supercapacitor." *Electrochim. Acta*, 245, 268–278.

Pan, C., Liu, Z., Li, W., Zhuang, Y., Wang, Q. and Chen, S. (2019). "NiCo₂O₄@ Polyaniline Nanotubes Heterostructure Anchored on Carbon Textiles with Enhanced Electrochemical Performance for Supercapacitor Application." *J. Phys. Chem. C*, 123, 25549–25558.

Peng, T., Zhang, X., Lv, H. and Zan, L. (2012). "Preparation of NiFe₂O₄ nanoparticles and its visible-light-driven photoactivity for hydrogen production." *Catal. Commun.*, 28, 116–119.

Perdew, J.P. Burke, K. and Ernzerhof, M. (1996) "Generalized Gradient Approximation Made Simple." *Phys. Rev Lett.*, 77, 3865–3868.

Qian, L., Gu, L., Yang, L., Yuan, H. and Xiao, D. (2013). "Direct growth of NiCo₂O₄ nanostructures on conductive substrates with enhanced electrocatalytic activity and stability for methanol oxidation." *Nanoscale*, 5, 7388–7396.

Qiu, D., Ma, X., Zhang, J., Lin, Z. and Zhao, B. (2018). "In situ synthesis of mesoporous NiO nanoplates embedded in a flexible graphene matrix for supercapacitor electrodes." *Mater. Lett.*, 232, 163–166.

Qiu, L., Li, D. And Cheng, H.M. (2018). "Structural control of graphene based materials for unprecedented performance." *ACS Nano*, 12, 5085–5092.

Qu, Z., Shi, M., Wu, H., Liu, Y., Jiang, J. and Yan, C. (2019). "An efficient binder-free electrode with multiple carbonized channels wrapped by NiCo₂O₄ nanosheets for high-performance capacitive energy storage." *J. Power Sources*, 410, 179–187.

Ramadoss, A., Kang, K.N., Ahn, H.J., Kim, S.I., Ryu, S.T. and Jang, J.H. (2016). "Realization of high performance flexible wire supercapacitors based on 3-dimensional NiCo₂O₄/Ni fibers." *J. Mater. Chem. A*, 4(13), 4718–4727.

Ramesh, S., Vikraman, D., Karuppasamy, K., Yadav, H.M., Sivasamy, A., Kim, H.S., Kim, J.H. and Kim, H.S. (2019). "Controlled synthesis of SnO₂@NiCo₂O₄/nitrogen doped multiwalled carbon nanotube hybrids as an active electrode material for supercapacitors." *J. Alloys Compd.*, 794, 186–194.

Ramesh, S., Vikraman, D., Kim, H.S., Kim, H.S. and Kim, J.H. (2018). "Electrochemical performance of MWCNT/GO/NiCo₂O₄ decorated hybrid

nanocomposite for supercapacitor electrode materials.” *J. Alloys Compd.*, 765, 369–379.

Rantho, M.N., Madito, M.J. and Manyala, N. (2020). “High-performance symmetric supercapacitor device based on carbonized iron-polyaniline/nickel graphene foam.” *J. Alloys Compd.*, 819, 152993.

Razali, S.A. and Majid, S.R. (2018). “Electrochemical performance of binder-free NiO-PANI on etched carbon cloth as active electrode material for supercapacitor.” *Mater. Design*, 153, 24–35.

Riaz, M.A., Hadi, P., Abidi, I.H., Tyagi, A., Ou, X., Luo, Z. (2017). “Recyclable 3D graphene aerogel with bimodal pore structure for ultrafast and selective oil sorption from water.” *RSC Adv.*, 7, 29722–29731.

Ruan, S., Ma, C., Wang, J., Qiao, W. and Ling, L. (2019). “Facile synthesis of graphene-wrapped porous MnCO₃ microspheres with enhanced surface capacitive effects for superior lithium storage.” *Chem. Eng. J.*, 367, 64–75.

Russo, P., Hu, A. and Compagnini, G. (2013). “Synthesis, properties and potential applications of porous graphene: A Review.” *Nano Micro Lett.*, 5, 260–273.

Sadak, O., Sundramoorthy, A.K. and Gunasekaran, S. (2018). “Facile and green synthesis of highly conductive graphene paper.” *Carbon*, 138, 108–117.

Sadiq, M.M.J., Mutyala, S., Mathiyarasu, J. Bhat, D.K. (2017e). “RGO/ZnWO₄/Fe₃O₄ nanocomposite as an efficient electrocatalyst for oxygen reduction reaction.” *J. Electroanal. Chem.*, 799, 102–110.

Sadiq, M.M.J., Shenoy, U.S. and Bhat, D.K. (2016). “Novel RGO–ZnWO₄–Fe₃O₄ nanocomposite as high performance visible light photocatalyst.” *RSC Adv.*, 6, 61821–61829.

Sadiq, M.M.J., Shenoy, U.S. and Bhat, D.K. (2017c). “Enhanced photocatalytic performance of N-doped RGO-FeWO₄/Fe₃O₄ ternary nanocomposite in environmental applications.” *Mater. Today Chem.*, 4, 133–141.

Sadiq, M.M.J., Shenoy, U.S. and Bhat, D.K. (2017d). “NiWO₄-ZnO-NRGO ternary nanocomposite as an efficient photocatalyst for degradation of methylene blue and reduction of 4-nitro phenol.” *J. Phys. Chem. Solids*, 109, 124–133.

Sadiq, M.M.J., Shenoy, U.S. and Bhat, D.K. (2018b). “Synthesis of BaWO₄/NRGO-gC₃N₄ nanocomposites with excellent multifunctional catalytic performance via microwave approach.” *Front. Mater. Sci.*, 12, 247–263.

Sahoo, M.K., Gogoi, P., Rajeshkhanna, G., Chilukuri, S.V. and Rao, G.R. (2017). “Significance of optimal N-doping in mesoporous carbon framework to achieve high specific capacitance.” *Appl. Surf. Sci.*, 418, 40–48.

Salunkhe, R.R., Jang, K., Yu, H., Yu, S., Ganesh, T., Han, S.H. and Ahn, H. (2011). “Chemical synthesis and electrochemical analysis of nickel cobaltite nanostructures for supercapacitor applications.” *J. Alloys Compd.*, 509, 6677–6682.

Sancheti, S.V., Saini, C., Ambati, R. and Gogate, P.R. (2018). “Synthesis of ultrasound assisted nanostructured photocatalyst (NiO supported over CeO₂) and its application for photocatalytic as well as sonocatalytic dye degradation.” *Catal. Today*, 300, 50–57.

Sangeetha, D.N. and Selvakumar, M. (2018). “Active-defective activated carbon/MoS₂ composites for supercapacitor and hydrogen evolution reactions.” *Appl. Surf. Sci.*, 453, 132–140.

Sannasi, V., Maheswari, K.U., Karthikeyan, C. and Karuppuchamy, S. (2020). “H₂O₂-assisted microwave synthesis of NiO/CNT nanocomposite material for supercapacitor applications.” *Ionics*, 26, 4067–4079.

Saravanakumar, B., Priyadharshini, T., Ravi, G., Ganesh, V., Sakunthala, A. and Yuvakkumar, R. (2017). "Hydrothermal synthesis of spherical NiCo₂O₄ nanoparticles as a positive electrode for pseudocapacitor applications." *J. Sol-Gel Sci. Tech.*, 84, 297–305.

Sekhar, S.C., Nagaraju, G. and Yu, J.S. (2018). "High-performance pouch-type hybrid supercapacitor based on hierarchical NiO-Co₃O₄-NiO composite nanoarchitectures as an advanced electrode material." *Nano Energy*, 48, 81–92.

Sethi, M. and Bhat, D.K. (2019a). "Facile solvothermal synthesis and high supercapacitor performance of NiCo₂O₄ nanorods." *J. Alloys Compd.*, 781, 1013–1020.

Sethi, M., Bantawal, H., Shenoy, U.S. and Bhat, D.K. (2019b). "Eco-friendly synthesis of porous graphene and its utilization as high performance supercapacitor electrode material." *J. Alloys Compd.*, 799, 256–266.

Sethi, M., Shenoy, S. and Bhat, D.K. (2020c). "Porous graphene-NiFe₂O₄ nanocomposite with high electrochemical performance and high cyclic stability for energy storage application." *Nanoscale Adv.*, 2, 4229–4241.

Sethi, M., Shenoy, U.S. and Bhat, D.K. (2020a). "Porous graphene–NiCo₂O₄ nanorod hybrid composite as a high performance supercapacitor electrode material." *New J. Chem.*, 44(10), 4033–4041.

Sethi, M., Shenoy, U.S., Muthu, S. and Bhat, D.K. (2020b). "Facile solvothermal synthesis of NiFe₂O₄ nanoparticles for high-performance supercapacitor applications." *Front. Mater. Sci.*, 14, 120–132.

Sevilla, M., Mokaya, R. and Fuertes, A.B. (2011). "Ultrahigh surface area polypyrrole-based carbons with superior performance for hydrogen storage." *Energy Environ. Sci.*, 4, 2930–2936.

Shakir, I., Shahid, M., Yang, H.W. and Kang, D.J. (2010). “Structural and electrochemical characterization of α -MoO₃ nanorod-based electrochemical energy storage devices.” *Electrochim. Acta*, 56, 376–380.

Sharma, V., Sudipta, B., Baranidharan, S., Prasenjit, H., Brajesh, D. and Amreesh C. (2019). “Electrode materials with highest surface area and specific capacitance cannot be the only deciding factor for applicability in energy storage devices: inference of combined life cycle assessment and electrochemical studies.” *ACS Sustain. Chem. Eng.*, 7, 5385–5392.

Shaymaa, A.R., Rajagopalan, R., Subramaniam, C., Tai, Z., Xian, J., Wang, X., Dou, S.X. and Cheng, Z. (2018). “NiFe₂O₄ nanoparticles coated on 3D graphene capsule as electrode for advanced energy storage applications.” *Dalton Trans.*, 47, 14052–14059.

Shenoy, U.S. and Bhat, D.K. (2020). “Bi and Zn co-doped SnTe Thermoelectrics: interplay of resonance levels and heavy hole band dominance leading to enhanced performance and a record high room temperature ZT.” *J. Mater. Chem. C*, 8, 2036–2042.

Singh, S.K., Dhavale, V.M., Boukherroub, R., Kurungot, S. and Szunerits, S. (2017). “N-doped porous reduced graphene oxide as an efficient electrode material for high performance flexible solid-state supercapacitor.” *Appl. Mater. Today*, 8, 141–149.

Sivakumar, P., Jana, M., Kota, M., Lee, H.S. and Park, H.S. (2019). “Porous interconnected NiCo₂O₄ nanosheets and nitrogen-and sulfur-codoped reduced graphene oxides for high-performance hybrid supercapacitors.” *J. Alloys Compd.*, 781, 515–523.

Siwatch, P., Sharma, K. and Tripathi, S.K. (2020). “Facile synthesis of NiCo₂O₄ quantum dots for asymmetric supercapacitor.” *Electrochim. Acta*, 329, 135084. <https://doi.org/10.1016/j.electacta.2019.135084>.

Soam, A., Kumar, R., Thatoi, D. and Singh, M., (2020). “Electrochemical performance and working voltage optimization of nickel ferrite/graphene composite based supercapacitor.” *J. Inorg. Organomet. Polym. Mater.*, 30, 3325–3331.

Song, C., Wang, J., Meng, Z., Hu, F. and Jian, X. (2018). “Density functional theory calculation for quantum capacitance of graphene oxide as supercapacitor electrode.” *Chem. Phys. Chem.*, 19, 1579–1583.

Srivastava, M., Uddin, M.E., Singh, J., Kim, N.H. and Lee, J.H. (2014). “Preparation and characterization of self-assembled layer by layer NiCo₂O₄-reduced graphene oxide nanocomposite with improved Electrocatalytic properties.” *J. Alloys Compd.*, 590, 266–276.

Su, C., Zhang, L., Han, Y., Ren, C., Chen, X., Hu, J., Zeng, M., Hu, N., Su, Y., Zhou, Z. and Yang, Z. (2019). “Controllable synthesis of crescent-shaped porous NiO nanoplates for conductometric ethanol gas sensors.” *Sens. Actuators B Chem.*, 296, 126642.

Subramanya, B. and Bhat, D.K. (2015b). “Novel eco-friendly synthesis of graphene directly from graphite using 2,2,6,6-tetramethylpiperidine 1-oxyl and study of its electrochemical properties.” *J. Power Sources*, 275, 90–98.

Subramanya, B. and Bhat, D.K. (2015a). “Novel one-pot green synthesis of graphene in aqueous medium under microwave irradiation using a regenerative catalyst and the study of its electrochemical properties.” *New J. Chem.*, 2015, 39, 420–430.

Subramanya, B., Ullal, Y., Shenoy, S.U., Bhat, D.K. and Hegde, A.C. (2015c). “Novel Co–Ni–graphene composite electrodes for hydrogen production.” *RSC Adv.*, 5, 47398–47407.

Sudhakar, Y.N., Selvakumar M. and Bhat, D.K. (2018) “Biopolymer Electrolytes: Fundamentals and Applications in Energy Storage.” *Elsevier, Oxford, UK.*

Sun, M., Wang, J., Xu, M., Fang, Z., Jiang, L., Han, Q., Liu, J., Yan, M., Wang, Q. and Bi, H. (2019). “Hybrid Supercapacitors Based on Interwoven CoO-NiO-ZnO Nanowires and Porous Graphene Hydrogel Electrodes with Safe Aqueous Electrolyte for High Supercapacitance.” *Adv. Electron. Mater.*, 5, 1900397.

Sun, S., Wang, S., Li, S., Li, Y., Zhang, Y., Chen, J., Zhang, Z., Fang, S. and Wang, P. (2016). “Asymmetric supercapacitors based on a NiCo₂O₄/three dimensional graphene composite and three dimensional graphene with high energy density.” *J. Mater. Chem. A*, 4, 18646–18653.

Sun, W., Xiao, L. and Wu, X. (2019). “Facile synthesis of NiO nanocubes for photocatalysts and supercapacitor electrodes.” *J. Alloys Compd.*, 772, 465–471.

Sun, X., Lu, H., Liu, P., Rufford, T.E., Gaddam, R.R., Fan, X. and Zhao, X.S. (2018). “A reduced graphene oxide–NiO composite electrode with a high and stable capacitance.” *Sustain. Energy Fuels*, 2, 673–678.

Tan, Y., Li, Y., Kong, L., Kang, L. and Ran, F. (2018). “Synthesis of ultra-small gold nanoparticles decorated onto NiO nanobelts and their high electrochemical performance.” *Dalton Trans.*, 47, 8078–8086.

Tang, Q., Zhou, Y., Ma, L. and Gan, M. (2019). “Hemispherical flower-like N-doped porous carbon/NiCo₂O₄ hybrid electrode for supercapacitors.” *J. Solid State Chem.*, 269, 175–183.

Tian, Y., Yu, Z., Cao, L., Zhang, X.L., Sun, C. and Wang, D.W. (2020). “Graphene oxide: An emerging electromaterial for energy storage and conversion.” *J. Energy Chem.*, 55, 323–344.

Toupin, M., Brousse, T. and Bélanger, D. (2002). “Influence of microstructure on the charge storage properties of chemically synthesized manganese dioxide.” *Chem. Mater.*, 14, 3946–3952.

Trung, N.B., Van Tam, T., Dang, D.K., Babu, K.F., Kim, E.J., Kim, J. and Choi, W.M. (2015). “Facile synthesis of three-dimensional graphene/nickel oxide nanoparticles composites for high performance supercapacitor electrodes.” *Chem. Eng. J.*, 264, 603–609.

Umeshbabu, E., Justin, P. and Rao, G.R. (2018). “Tuning the surface morphology and pseudocapacitance of MnO₂ by a facile green method employing organic reducing sugars.” *ACS Appl. Energy Mater.*, 1, 3654–3664.

Umeshbabu, E., Rajeshkhanna, G. and Rao, G.R. (2014). “Urchin and sheaf-like NiCo₂O₄ nanostructures: synthesis and electrochemical energy storage application.” *Int. J. Hydrogen Energy*, 39, 15627–15638.

Veeramani, V., Madhu, R., Chen, S.M. and Sivakumar, M. (2016). “Flower-like nickel–cobalt oxide decorated dopamine-derived carbon nanocomposite for high performance supercapacitor applications.” *ACS Sustain. Chem. Eng.*, 4(9), 5013–5020.

Vickraman, P. and Reddy, B.J. (2018). “Synthesis and characterization of high porous carbon sphere@nickel oxide core-shell nanocomposite for supercapacitor applications.” *J. Electroanal. Chem.*, 823, 342–349.

Voskanyan, A.A. and Chan, K.Y. (2018). “Scalable synthesis of three-dimensional meso/macroporous NiO with uniform ultralarge randomly packed mesopores and high catalytic activity for soot oxidation.” *ACS Appl. Nano Mater.*, 1, 556–563.

Walsh, F.C. (2001). “Electrochemical technology for environmental treatment and clean energy conversion.” *Pure Appl. Chem.*, 73, 1819–1837.

Wang, D., Wei, A., Tian, L., Mensah, A., Li, D., Xu, Y. and Wei, Q. (2019). “Nickel-cobalt layered double hydroxide nanosheets with reduced graphene oxide grown on carbon cloth for symmetric supercapacitor.” *Appl. Surf. Sci.*, 483, 593–600.

Wang, G., Sun, X., Lu, F., Sun, H., Yu, M., Jiang, W., Liu, C. and Lian, J. (2012). “Flexible pillared graphene-paper electrodes for high-performance electrochemical supercapacitors.” *Small*, 8, 452–459.

Wang, L., Tan, H., Chen, J., Zhang, H., Li, Z. and Qiu, H. (2019). “Porous graphene synthesized by partial combustion for high-performance supercapacitors.” *Mater. Lett.*, 252, 345–348.

Wang, X., Chen, L., Li, F., Zhang, S., Chen, X. and Yin, J. (2019). “Synthesis of hollow NiO nanostructures and their application for supercapacitor electrode.” *Ionics*, 25, 697–705.

Wang, X., Fang, Y., Shi, B., Huang, F., Rong, F. and Que, R. (2018). “Three-dimensional NiCo₂O₄@NiCo₂O₄ core-shell nanocones arrays for high-performance supercapacitors.” *Chem. Eng. J.*, 344, 311–319.

Wang, X., Li, Q., Zhang, Y., Yang, Y., Cao, Z. and Xiong, S. (2018). “Synthesis and capacitance properties of N-doped porous carbon/NiO nanosheet composites using coal-based polyaniline as carbon and nitrogen source.” *Appl. Surf. Sci.*, 442, 565–574.

Wang, Z., Zhang, X., Li, Y., Liu, Z. and Hao, Z. (2013). “Synthesis of graphene–NiFe₂O₄ nanocomposites and their electrochemical capacitive behavior.” *J. Mater. Chem. A*, 1, 6393–6399.

Wei, H., Hu, H., Feng, J., Zhang, M. and Hua, T. (2018). “Yarn-form electrodes with high capacitance and cycling stability based on hierarchical nanostructured nickel-cobalt mixed oxides for weavable fiber-shaped supercapacitors.” *J. Power Sources*, 400, 157–166.

Wei, Y., Chen, S., Su, D., Sun, B., Zhu, J. and Wang, G. (2014). “3D mesoporous hybrid NiCo₂O₄@graphene nanoarchitectures as electrode materials for supercapacitors with enhanced performances.” *J. Mater. Chem. A*, 2(21), 8103–8109.

Winter, M. and Brodd, R.J. (2004). “What are batteries, fuel cells, and supercapacitors?” *Chem. Rev.*, 104, 4245–4270.

Wu, F., Wang, X., Li, M. and Xu, H. (2016). “A high capacity NiFe₂O₄/RGO nanocomposites as superior anode materials for sodium-ion batteries.” *Ceram. Int.*, 42, 16666–16670.

Wu, J.B., Lin, M.L., Cong, X., Liu, H.N. and Tan, P.H. (2018). “Raman spectroscopy of graphene-based materials and its applications in related devices.” *Chem. Soc. Rev.*, 47, 1822–1873.

Wu, M., Liao, J., Yu, L., Lv, R., Li, P., Sun, W., Tan, R., Duan, X., Zhang, L., Li, F. and Kim, J. (2020). “Roadmap on carbon materials for energy storage and conversion.” *Chem. Asian J.*, 15, 995–1013.

Wu, S.R., Liu, J.B., Wang, H. and Yan, H. (2019). “NiO@graphite carbon nanocomposites derived from Ni-MOFs as supercapacitor electrodes.” *Ionics*, 25, 1–8.

Wu, Y.Q., Chen, X.Y., Ji, P.T., and Zhou, Q.Q. (2011). “Sol–gel approach for controllable synthesis and electrochemical properties of NiCo₂O₄ crystals as electrode materials for application in supercapacitors.” *Electrochim. Acta*, 56, 7517–7522.

Xu, K., Yang, J. and Hu, J. (2018). “Synthesis of hollow NiCo₂O₄ nanospheres with large specific surface area for asymmetric supercapacitors.” *J. Colloid Interface Sci.*, 511, 456–462.

Xu, Y., Lin, Z., Zhong, X., Huang, X., Weiss, N.O., Huang, Y. and Duan, X. (2014). “Holey graphene frameworks for highly efficient capacitive energy storage.” *Nat. Commun.*, 5, 1–8.

Xu, Z., Yang, L., Jin, Q. and Hu, Z. (2019). “Improved capacitance of NiCo₂O₄/carbon composite resulted from carbon matrix with multilayered graphene.” *Electrochim. Acta*, 295, 376–383.

Xue, J., Gao, Z., Xiao, L., Zuo, T., Gao, J., Li, D. and Qu, L. (2020). “An ultrafast supercapacitor based on 3D ordered porous graphene film with AC line filtering performance.” *ACS Appl. Energy Mater.*, 3, 5182–5189.

Yan, D., Wang, W., Luo, X., Chen, C., Zeng, Y. and Zhu, Z. (2018). “NiCo₂O₄ with oxygen vacancies as better performance electrode material for supercapacitor.” *Chem. Eng. J.*, 334, 864–872.

Yang, W., Gao, Z., Ma, J., Wang, J., Wang, B. and Liu, L. (2013). “Effects of solvent on the morphology of nanostructured Co₃O₄ and its application for high-performance supercapacitors.” *Electrochim. Acta*, 112, 378–385.

Yang, Y., Zeng, D., Gu, L., Liu, B., Guo, F., Ren, Y. and Hao, S. (2018). “Support-induced morphology and content tailored NiCo₂O₄ nanostructures on temperature-dependent carbon nanofibers with enhanced pseudocapacitive performance.” *Electrochim. Acta*, 286, 1–13.

Yang, Z., Xu, F., Zhang, W., Mei, Z., Pei, B. and Zhu, X. (2014). “Controllable preparation of multishelled NiO hollow nanospheres via layer-by-layer self-assembly for supercapacitor application.” *J. Power Sources*, 246, 24–31.

Yang, Z.K., Teng, Y., Xia, J. and Du, P. (2013). “Nickel oxide nanoflowers: formation, structure, magnetic property and adsorptive performance towards organic dyes and heavy metal ions.” *J. Mater. Chem. A*, 1, 8731–8736.

Yao, M., Wang, N., Yin, J. and Hu, W. (2017). “Mesoporous three dimension NiCo₂O₄/graphene composites fabricated by self-generated sacrificial template method for a greatly enhanced specific capacity.” *J. Mater. Sci.: Mater. Electronics*, 28, 11119–11124.

Yu, K., Hu, J., Li, X., Zhang, L. and Lv, Y. (2019). “Camellia-like NiO: A novel cataluminescence sensing material for H₂S.” *Sens. Actuators B Chem.*, 288, 243–250.

Yuan, C., Li, J., Hou, L., Yang, L., Shen, L. and Zhang, X. (2012). “Facile template-free synthesis of ultralayered mesoporous nickel cobaltite nanowires towards high-performance electrochemical capacitors.” *J. Mater. Chem.*, 22, 16084–16090.

Yus, J., Bravo, Y., Sanchez-Herencia, A.J., Ferrari, B. and Gonzalez, Z. (2019). “Electrophoretic deposition of RGO-NiO core-shell nanostructures driven by heterocoagulation method with high electrochemical performance.” *Electrochim. Acta*, 308, 363–372.

Zang, P., Gao, S., Dang, L., Liu, Z. and Lei, Z. (2016). “Green synthesis of holey graphene sheets and their assembly into aerogel with improved ion transport property.” *Electrochim. Acta*, 212, 171–178.

Zdravkov, B.D., Cermak, J.J., Sefara, M. and Jank, J. (2007). “Pore classification in the characterization of porous materials: a perspective.” *Cent. Eur. J. Chem.*, 5, 385–395.

Zhang, D., Yan, H., Lu, Y., Qiu, K., Wang, C., Tang, C., Zhang, Y., Cheng, C. and Luo, Y. (2014). “Hierarchical mesoporous nickel cobaltite nanoneedle/carbon cloth arrays as superior flexible electrodes for supercapacitors.” *Nanoscale Res. Lett.*, 9, 1–9.

Zhang, G., Li, Y., Zhou, Y. and Yang, F. (2016). “NiFe Layered-Double-Hydroxide-Derived NiO- NiFe₂O₄/Reduced Graphene Oxide Architectures for Enhanced Electrocatalysis of Alkaline Water Splitting.” *ChemElectroChem*, 3, 1927–1936.

Zhang, N., Li, Y., Xu, J., Li, J., Wei, B., Ding, Y., Amorim, I., Thomas, R., Thalluri, S.M., Liu, Y. and Yu, G. (2019). “High-performance flexible solid-state asymmetric supercapacitors based on bimetallic transition metal phosphide nanocrystals.” *ACS Nano*, 13, 10612–10621.

Zhang, S., Gao, H., Zhou, J., Jiang, F. and Zhang, Z. (2019). “Hydrothermal synthesis of reduced graphene oxide-modified NiCo₂O₄ nanowire arrays with enhanced reactivity for supercapacitors.” *J. Alloys Compd.*, 792, 474–480.

Zhang, W., Xin, W., Hu, T., Gong, Q., Gao, T. and Zhou, G. (2019). “One-step synthesis of NiCo₂O₄ nanorods and firework-shaped microspheres formed with necklace-like structure for supercapacitor materials.” *Ceram. Int.*, 45, 8406–8413.

Zhang, X., Zhang, Z., Sun, S., Wu, Y., Sun, Q. and Liu, X. (2018). “A facile one-step hydrothermal approach to synthesize hierarchical core-shell NiFe₂O₄@NiFe₂O₄ nanosheet arrays on Ni foam with large specific capacitance for supercapacitors.” *RSC Adv.*, 8, 15222–15228.

Zhang, X., Zhu, M., Ouyang, T., Chen, Y., Yan, J., Zhu, K., Ye, K., Wang, G., Cheng, K. and Cao, D. (2019). “NiFe₂O₄ nanocubes anchored on reduced graphene oxide cryogel to achieve a 1.8 V flexible solid-state symmetric supercapacitor.” *Chem. Eng. J.*, 360, 171–179.

Zhang, Y., Wang, J., Wei, H., Hao, J., Mu, J., Cao, P., Wang, J. and Zhao, S. (2016). “Hydrothermal synthesis of hierarchical mesoporous NiO nanourchins and their supercapacitor application.” *Mater. Lett.*, 162, 67–70.

Zhang, Y., Zhang, Y., Zhang, D. and Sun, L. (2017). “Urchin-like NiCo₂O₄ nanoneedles grown on mesocarbon microbeads with synergistic electrochemical properties as electrodes for symmetric supercapacitors.” *Dalton Trans.*, 46, 9457–9465.

Zhao, D., Hu, F., Umar, A. and Wu, X. (2018). “NiCo₂O₄ nanowire based flexible electrode materials for asymmetric supercapacitors.” *New J. Chem.*, 42, 7399–7406.

Zhao, Y., Hao, M., Wang, Y., Sha, Y. and Su, L. (2016). “Effect of electrolyte concentration on the capacitive properties of NiO electrode for supercapacitors.” *J. Solid State Electrochem.*, 20, 81–85.

Zhao, Y., Xu, L., Yan, J., Yan, W., Wu, C., Lian, J., Huang, Y., Bao, J., Qiu, J., Xu, L. and Xu, Y. (2017). “Facile preparation of NiFe₂O₄/MoS₂ composite material with synergistic effect for high performance supercapacitor.” *J. Alloys Compd.*, 726, 608–617.

Zhao, Y., Yuan, M., Chen, Y., Yan, J., Xu, L., Huang, Y., Lian, J., Bao, J., Qiu, J., Xu, L. and Xu, Y. (2018). “Construction of molybdenum dioxide nanosheets coated on the surface of nickel ferrite nanocrystals with ultrahigh specific capacity for hybrid supercapacitor.” *Electrochim. Acta*, 260, 439–448.

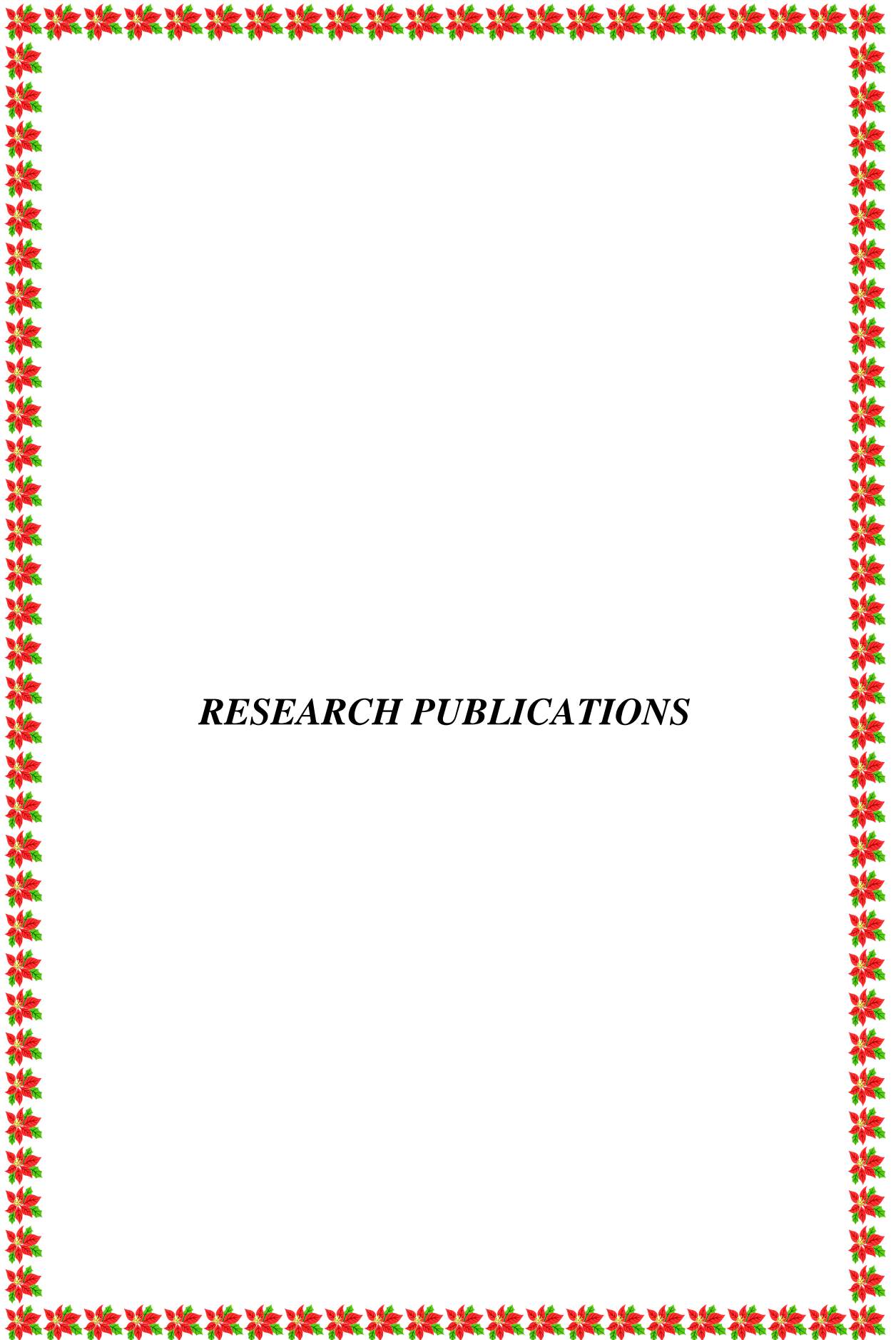
Zheng, L., Guan, L., Yang, G., Chen, S. and Zheng, H. (2018). “One-pot synthesis of CoFe₂O₄/rGO hybrid hydrogels with 3D networks for high capacity electrochemical energy storage devices.” *RSC Adv.*, 8, 8607–8614.

Zhou, Y., Huang, Z., Liao, H., Li, J., Wang, H. and Wang, Y. (2020). “3D porous graphene/NiCo₂O₄ hybrid film as an advanced electrode for supercapacitors.” *Appl. Surf. Sci.*, 147598. <https://doi.org/10.1016/j.apsusc.2020.147598>.

Zhou, Y., Xu, H., Lachman, N., Ghaffari, M., Wu, S., Liu, Y., Ugur, A., Gleason, K.K., Wardle, B.L. and Zhang, Q.M. (2014). “Advanced asymmetric supercapacitor based on conducting polymer and aligned carbon nanotubes with controlled nanomorphology.” *Nano Energy*, 9, 176–185.

Zhu, Y., Pu, X., Song, W., Wu, Z., Zhou, Z., He, X., Lu, F., Jing, M., Tang, B. and Ji, X. (2014). “High capacity NiCo₂O₄ nanorods as electrode materials for supercapacitor.” *J. Alloys Compd.*, 617, 988–993.

Zou, Y., Li, Z., Liu, Y., Duan, J. and Long, B. (2020). “Coaxial structure of NiFe₂O₄/CNTs composites as anodes for enhanced lithium ion batteries.” *J. Alloys Compd.*, 820, 153085.



RESEARCH PUBLICATIONS

Research Papers Published in International Journals

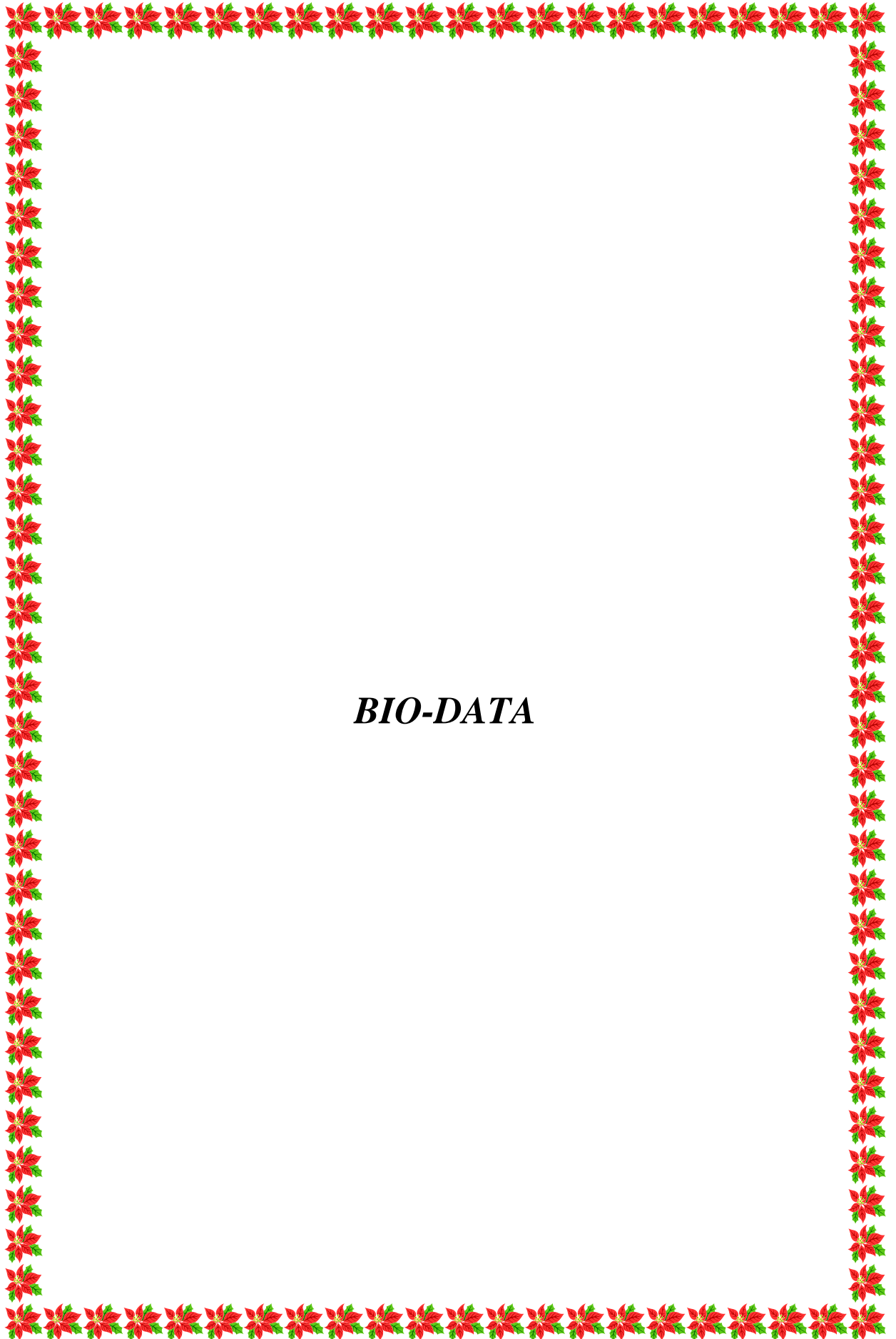
- ✚ **Sethi, M.** and Bhat, D. K. (2019). “Facile solvothermal synthesis and high supercapacitor performance of NiCo₂O₄ nanorods.” *J. Alloys Compd.*, 781, 1013–1020.
- ✚ **Sethi, M.**, Bantawal, H., Shenoy, S. U. and Bhat, D. K. (2019). “Ecofriendly synthesis of porous graphene and its utilization as high performance supercapacitor electrode material.” *J. Alloys Compd.*, 799, 256–266.
- ✚ **Sethi, M.**, Shenoy, S. U. and Bhat, D. K. (2020). “Porous graphene–NiCo₂O₄ nanorod hybrid composites as a high performance supercapacitor electrode material.” *New J. Chem.*, 44, 4033–4041.
- ✚ **Sethi, M.**, Shenoy, S. U., Selvakumar M. and Bhat, D. K. (2020). “Facile solvothermal synthesis of NiFe₂O₄ nanoparticles for high performance supercapacitor applications.” *Front. Mater. Sci.*, 14, 120–132.
- ✚ **Sethi, M.**, Shenoy, S. U. and Bhat, D. K. (2020). “A Porous graphene-NiFe₂O₄ nanocomposite with high electrochemical performance and high cycling stability for energy storage applications.” *Nanoscale Adv.*, 2, 4229–4241.
- ✚ **Sethi, M.**, Shenoy, S. U. and Bhat, D. K. (2021). “Simple solvothermal synthesis of porous graphene-NiO nanocomposites with high cyclic stability for supercapacitor application.” *J. Alloys Compd.*, 854, 157190.
- ✚ **Sethi, M.**, Shenoy, S. U. and Bhat, D. K. (2021). “Hassle-free solvothermal synthesis of NiO nanoflakes for supercapacitor application.” *Phys B Condens. Matter*, 611, 412959.

Research Papers Presented in Conferences

- ✚ **Sethi, M.** and Bhat, D.K. (2017). “High-performance symmetrical supercapacitor based on graphene–NiCo₂O₄ nanocomposites.” CRSI-NSC and CRSI-ACS Symposium in Chemistry, 13th - 16th July, ICT-Hyderabad, India.
- ✚ **Sethi, M.** and Bhat, D.K. (2017). “Graphene-nickel cobaltite nanocomposite as high performance supercapacitor electrode material.” International Conference on

Crystal Ball Vision on Science & Engineering for Societal Upliftment, 7th - 8th August, CSIR-NIO, Goa, India.

- ✚ **Sethi, M.** and Bhat, D.K. (2017). “Electrochemical study of graphene-NiCo₂O₄ nanocomposites for high performance supercapacitor applications.” ICAM-I2CAM Energy School, 25th November - 02nd December, JNCASR, Bangalore, India.
- ✚ **Sethi, M.** and Bhat, D.K. (2018). “Green preparation of graphene-NiFe₂O₄ nanocomposite through solvothermal approach: utility of material for high performance supercapacitor application.” 37th Annual conference of ICC’12th - 14th December, NITK Surathkal, Mangalore, India.
- ✚ **Sethi, M.** and Bhat, D.K. (2019). “Novel porous graphene synthesized through solvothermal approach as high performance electrode material for supercapacitors.” International Conference on Physics of Materials and Nanotechnology (ICPN-2019), 19th - 21st September, Mangalore University, Mangalore, India.
- ✚ **Sethi, M.,** Shenoy, S. U. and Bhat, D. K. (2019). “Porous graphene–NiCo₂O₄ nanorod hybrid composite as high performance supercapacitor electrode material.” Second International Conference on Nanoscience and Nanotechnology (ICNAN’19), 29th November -1st December, VIT, Vellore, India.



BIO-DATA

BIODATA

Name: Meenaketan Sethi

Date of Birth: 24 April 1991

Place of Birth: Rourkela

Nationality: Indian

Sex: Male

Present address: Research Scholar, Department of Chemistry,
NITK Surathkal, Mangalore- 575025, India.

Permanent address: JE-121, Bhakta Nagar, Jhirpani,
Rourkela-769042, Odisha, India.

Mobile: +91-8861909361

E-mail: meenaketan.nitrk112@gmail.com, meenaketansth32@gmail.com

LinkedIn: <https://www.linkedin.com/in/meenaketan-sethi-b608b9b2/>

Google Scholar: <https://scholar.google.co.in/citations?user=pmAH0lQAAAAJ&hl=en>


Research Gate: https://www.researchgate.net/profile/Meenaketan_Sethi3

ORCID iD: 0000-0002-7566-2469

Academic Qualifications:

- Ph.D. (July 2015 onwards), NITK Surathkal, Chemistry, CGPA 8.67
- M.Sc. (2014), NIT Rourkela, Chemistry, 1st Class
- B.Sc. (2012), Sambalpur University, Chemistry (Honours with distinction), 1st Class
- Class XII (2008), CHSE, Odia, English, Physics, Chemistry, Mathematics, Biology, 2nd Class
- Class X (2006), BSE, Odia, English, Sanskrit, Science, Mathematics, Social Science, 1st Class

Awards/Certificates:

-  People's Choice Nanoartography 2019 award to the image "NiO nanourchins." "Prize award: USD 500." The Nanoartography competition was organized by A. J. Drexel Nanomaterials Institute, Drexel University, Philadelphia, USA.

- ✚ Institute research fellowship award from NITK Surathkal, Mangalore to pursue Ph.D. in the Year 2015.
- ✚ CIA merit scholarship in the year 2010.
- ✚ Dharitri IT scholarship TDSQT in the year 2008.

Academic Projects:

Project	Topic	Institute	Period
Ph.D.	Studies on porous graphene, oxides of nickel and their nanocomposites for supercapacitor application	National Institute of Technology Karnataka (NITK), Surathkal.	July 2015 onwards
Project Asst. II	Study of carbon dynamics in estuaries and near shore waters of Dhamra and Mahanadi	CSIR - Institute of Minerals and Materials Technology (IMMT), Bhubaneswar.	February 2015 to June 2015
M.Sc. Research Project	Magnesium oxide nanostructures: synthesis, characterization and environmental application.	National Institute of Technology, Rourkela.	Year 2013
M.Sc. Summer Internship	Sol-Gel synthesis and characterization of ZnO-based nanocomposites.	Centre for Green Energy Technology (CGET), Pondicherry Central University.	May 2013 to July 2013

Aim:

- To be a scientist or academician to continue research in energy storage and conversion devices, corrosion science, dye adsorption and photocatalysis.
- Research from lab scale to industrial scale.
- Search new applications of porous graphene in membrane technology and waste water treatment.

Experimental Skills:

- ✚ Multistep reaction synthesis (Preparation, purification and characterization).
- ✚ Green synthesis.
- ✚ Experience in smooth operation of microwave reactor, hydrothermal autoclave, probe sonicator, muffle furnace, electrochemical workstations, UV-Visible spectrophotometer, Differential scanning calorimetry (DSC), FTIR and homogenizer.
- ✚ Experience on fabrication of electrodes and devices for supercapacitor application, dye degradation application.

Computer skills:

Operating system: Windows

Image analysis: ImageJ

Graphing: Origin

Crystallography: X'Pert HighScore Plus

Text processor: MS Word

Others: IVIUMstat, ZSimpWin 3.21

Languages:

Odia: Mother tongue

English: Fluent

Hindi: Fluent

Sanskrit: Fluent

Journal Publications:

- ✚ **Sethi, M.,** Shenoy, S. U. and Bhat, D. K. (2021). "Simple solvothermal synthesis of porous graphene-NiO nanocomposites with high cyclic stability for supercapacitor application." *J. Alloys Compd.*, 854, 157190. **(Impact Factor: 4.65) DOI: 10.1016/j.jallcom.2020.157190.**
- ✚ **Sethi, M.,** Shenoy, S. U. and Bhat, D. K. (2021). "Hassle-free solvothermal synthesis of NiO nanoflakes for supercapacitor application." *Phys. B Condens. Matter*, 611, 412959. **(Impact Factor: 1.9) DOI: 10.1016/j.physb.2021.412959.**

- ✚ **Sethi, M.,** Shenoy, S. U. and Bhat, D. K. (2020). “A Porous graphene-NiFe₂O₄ nanocomposite with high electrochemical performance and high cycling stability for energy storage applications.” *Nanoscale Adv.*, 2, 4229–4241. **DOI: 10.1039/D0NA00440E.**
- ✚ **Sethi, M.,** Shenoy, S. U., Selvakumar M. and Bhat, D. K. (2020). “Facile solvothermal synthesis of NiFe₂O₄ nanoparticles for high performance supercapacitor applications.” *Front. Mater. Sci.*, 14, 120–132. **(Impact Factor: 1.747). DOI: 10.1007/s11706-020-0499-3.**
- ✚ **Sethi, M.,** Shenoy, S. U. and Bhat, D. K. (2020). “Porous graphene–NiCo₂O₄ nanorod hybrid composites as a high performance supercapacitor electrode material.” *New J. Chem.*, 44, 4033–4041. **(Impact Factor: 3.288). DOI: 10.1039/C9NJ05725K.**
- ✚ Bantawal, H. **Sethi, M.,** Shenoy, U.S. and Bhat, D.K. (2019) “Porous graphene wrapped-SrTiO₃ nanocomposite: Sr-C bond as an effective coadjutant for high performance photocatalytic degradation of Methylene Blue.” *ACS Appl. Nano Mater.*, 10, 6629–6636. **DOI: 10.1021/acsnm.9b01513.**
- ✚ **Sethi, M.,** Bantawal, H., Shenoy, S. U. and Bhat, D. K. (2019). “Eco-friendly synthesis of porous graphene and its utilization as high performance supercapacitor electrode material.” *J. Alloys Compd.*, 799, 256–266. **(Impact Factor: 4.65). DOI: 10.1016/j.jallcom.2019.05.302.**
- ✚ **Sethi, M.,** and Bhat, D. K. (2019). “Facile solvothermal synthesis and high supercapacitor performance of NiCo₂O₄ nanorods.” *J. Alloys Compd.*, 781, 1013–1020. **(Impact Factor: 4.65). DOI: 10.1016/j.jallcom.2018.12.143.**
- ✚ Dhal, J. P., **Sethi, M.,** Mishra B. G., and Hota. G. (2015). “MgO nanomaterials with different morphologies and their sorption capacity for removal of toxic dyes.” *Mater. Lett.*, 141, 267–271. **(Impact Factor: 3.2). DOI: 10.1016/j.matlet.2014.10.055.**

Conference Proceedings:

- ✚ **Sethi, M. and Bhat, D.K.** (2020). “Engineered porous nanopillars of Co_3O_4 : Hydrothermal synthesis and energy storage application.” *AIP Conf. Proceedings*, 2247, 040014. **DOI: 10.1063/5.0004416**
- ✚ **Sethi, M. and Bhat, D.K.** (2020). “Novel porous graphene synthesized through solvothermal approach as high performance electrode material for supercapacitors.” *AIP Conf. Proceedings*, 2244 (1), 040002. **DOI: 10.1063/5.0009234**
- ✚ **Sethi, M. and Bhat, D.K.** (2020). “NiO nanoplates for energy storage application: Role of electrolyte concentration on the energy storage property.” *Mater. Today: Proceedings*. In press. **DOI: 10.1016/j.matpr.2020.02.853**
- ✚ **Sethi, M. and Bhat, D.K.** (2019). “Electrochemical study of graphene- NiCo_2O_4 nanocomposite prepared through solvothermal approach.” *AIP Conf. Proceedings*, 2142 (1), 140027. **DOI: 10.1063/1.5122540**

Conference Paper Presentations:

- ❖ **Presented a poster** in the CRSI-ACS Symposium and 21st CRSI-National Symposium in Chemistry held at CSIR-IICT Hyderabad, India, during 13th – 16th, July 2017.
- ❖ **Presented a poster** in the INTERNATIONAL CONFERENCE ON CRYSTAL BALL VISION ON SCIENCE AND ENGINEERING FOR SOCIETAL UPLIFTMENT, IJAA-2017, held at CSIR-NIO, Goa, India, during 7th – 8th, August, 2017.
- ❖ **Presented a poster** in the 37th Annual conference of Indian Council of Chemists (ICC-2018), held at NITK Surathkal, Mangalore, India, during the period of 12th – 14th December, 2018.
- ❖ **Presented a poster** in the INTERNATIONAL CONFERENCE ON ADVANCES IN BASIC SCIENCES (ICABS19), held at GDC Memorial college, Bahal, Dist: Bhiwani, Haryana, India, during the period of 7th – 9th February, 2019.

- ❖ **Presented a poster** in the International Conference on Physics of Materials and Nanotechnology (ICPN-2019), organized by Department of Physics, Mangalore University, Mangalore, India, during the period of 19th –21st September, 2019.
- ❖ **Presented a poster** in the Second International Conference on Nanoscience and Nanotechnology (ICNAN'19) held at VIT University, Vellore, India, during the period of 29th November –1st December, 2019.
- ❖ **Oral presentation** in the Second International Conference on DESIGN, MATERIALS & MANUFACTURE (ICDEM 2019) organized by NITK, Surathkal, Mangalore, India, during the period of 6th – 8th December, 2019.
- ❖ **Oral presentation** in the second International Conference on Processing and Characterization of Materials (ICPCM-2019) held at NIT Rourkela, Rourkela, India, during the period of 12th – 14th December, 2019.

Conference/Workshop/Seminar Participation:

- ❖ **Participated** in Advances in Chemistry and their Biological and Industrial Relevance (ACBIR) organized by NIT Rourkela, Rourkela, India, January 2014.
- ❖ **Participated** in Recent Developments in Chemical Science and Technology: Young Scientist's Meet (RDCST) organized by NIT Rourkela, Rourkela, India, March 2014.
- ❖ **Participated** in Awareness Programme on “Intellectual Property Rights” for MSME'S organized by The MHRD chair on IPR and Centre for Intellectual Property Rights and Advocacy (CIPRA), and National Law School of India University on 1st September 2016 at NITK, Surathkal, Mangalore, India.
- ❖ **Participated** in NANOSTRUCTURED MATERIALS AND THEIR APPLICATIONS IN CATALYSIS & FUEL CELLS (NMCF-2016) organized by NITK Surathkal, Mangalore, India, during September 29th – October 1st, 2016.
- ❖ **Participated** in GIAN course on Novel Functional Materials for Energy Conversion organized by NITK Surathkal, Mangalore, India, during October 4th – October 7th, 2016.
- ❖ **Participated** in RECENT TRENDS IN ENVIRONMENT, HEALTH AND SAFETY MANAGEMENT IN MINING AND OTHER CORE INDUSTRIES

(REHASMMOCI-2017) organized by NITK Surathkal, Mangalore, India, during 27th – 28th, January, 2017.

Academic/Professional References:

Prof. D. Krishna Bhat (Ph.D. Supervisor)

Professor & former Head, Department of Chemistry, NITK Surathkal.

Mangalore-575025, India.

E-mail: denthajekb@gmail.com, Ph: +91-8242474000, Ext. 3202 (O).

Dr. Garudadhvaj Hota (M.Sc. Thesis Supervisor)

Associate Professor, Department of Chemistry, NIT Rourkela, Odisha, India.

E-mail: garud@nitrkl.ac.in, Ph.: 0661-2462655.

Dr. Harekrushna Sahoo (M.Sc. Faculty advisor)

Associate Professor, Department of Chemistry, NIT Rourkela, Odisha, India.

E-mail: sahooh@nitrkl.ac.in, Ph: 0661-2462665.

Declaration:

I do hereby declare that all the above information furnished by me are true and correct to the best of my knowledge.

Date: 17/06/2021

Place: Srinivasanagar



Meenaketan Sethi